

**Titre:** Deterministic Algorithms for High Accuracy Coupled Photon-Electron-Positron Transport in Radiation Therapy Planning

**Auteur:** Charles Bienvenue

**Date:** 2024

**Type:** Mémoire ou thèse / Dissertation or Thesis

**Référence:** Bienvenue, C. (2024). Deterministic Algorithms for High Accuracy Coupled Photon-Electron-Positron Transport in Radiation Therapy Planning [Thèse de doctorat, Polytechnique Montréal]. PolyPublie.  
Citation: <https://publications.polymtl.ca/61891/>

 **Document en libre accès dans PolyPublie**  
Open Access document in PolyPublie

**URL de PolyPublie:** <https://publications.polymtl.ca/61891/>  
PolyPublie URL:

**Directeurs de recherche:** Alain Hébert, & Jean-François Carrier  
Advisors:

**Programme:** Génie biomédical  
Program:

**POLYTECHNIQUE MONTRÉAL**

affiliée à l'Université de Montréal

**Deterministic Algorithms for High Accuracy Coupled Photon-Electron-Positron  
Transport in Radiation Therapy Planning**

**CHARLES BIENVENUE**

Institut de génie biomédical

Thèse présentée en vue de l'obtention du diplôme de *Philosophiæ Doctor*

Génie biomédical

Décembre 2024

**POLYTECHNIQUE MONTRÉAL**

affiliée à l'Université de Montréal

Cette thèse intitulée :

**Deterministic Algorithms for High Accuracy Coupled Photon-Electron-Positron  
Transport in Radiation Therapy Planning**

présentée par **Charles BIENVENUE**

en vue de l'obtention du diplôme de *Philosophiæ Doctor*  
a été dûment acceptée par le jury d'examen constitué de :

**Cédric BÉGUIN**, président

**Alain HÉBERT**, membre et directeur de recherche

**Jean-François CARRIER**, membre et codirecteur de recherche

**Guy MARLEAU**, membre

**Emiliano MASIELLO**, membre externe

**DEDICATION**

*To Léa-Lou,  
for everything.*



## ACKNOWLEDGEMENTS

First and foremost, I would like to express my gratitude to my advisors, Dr. Alain Hébert and Dr. Jean-François Carrier, for their invaluable guidance, support and encouragement, even though my research deviated from the pre-established scope most of the time. Thank you to Dr. Alain Hébert for inspiring my dedication to open-source research. I want to thank my colleague Ahmed Naceur for the fruitful discussions and collaborations over the years. I am grateful to my supervisors from my previous research group at INRS, Dr. Simon Vallières and Dr. Patrizio Antici, for their significant contribution to my decision to pursue graduate studies. Finally, I want to express my deepest gratitude to my family, friends, girlfriend and her family. Your unwavering support, love and encouragement have been the cornerstone of my academic journey. Without you, this thesis would have been an insurmountable challenge.

## RÉSUMÉ

Pour toute Planification de Traitement par Radiothérapie (PTR), il est essentiel d'avoir des outils pour calculer rapidement et avec exactitude les profils de dose. Bien que les solveurs de transport de rayonnement de Monte Carlo aient traditionnellement été considérés comme la référence en PTR, leur application dans les environnements cliniques est limitée en raison de leur temps d'exécution excessifs et de leur nature stochastique. Pourtant, il existe une multitude de méthodes dites déterministes capables de simuler l'ensemble des interactions physiques avec une tout aussi grande exactitude. Le solveur Acuros<sup>®</sup>, le code de Varian Medical Systems qui utilise des méthodes déterministes, est déjà utilisé pour les faisceaux de rayons X dans les systèmes de PTR. Malgré certaines avancées dans les capacités déterministes, telles que la dérivation de l'équation de Boltzmann Fokker-Planck (BFP) ou le développement du code CEPXS, les modèles déterministes existants pour la PTR présentent des limitations qui entravent leur utilisation généralisée et sans contrainte à tout faisceau de photons et d'électrons. L'objectif principal de cette thèse est d'examiner et de proposer des solutions à ces lacunes.

L'équation de Boltzmann Fokker-Planck (BFP) est au coeur de cette dissertation, car tous les développements algorithmiques qu'elle présente s'articulent autour de cette équation. Des lacunes ont été identifiées et d'innovants algorithmes ont été proposés dans trois axes de recherche, soit 1) la production de données atomiques couplées pour les photons, les électrons et les positrons, 2) la discrétisation angulaire de l'équation de BFP et 3) les relations de fermeture associées aux méthodes de Galerkin.

Jusqu'à récemment, le code CEPXS, développé en 1989, était le seul code à produire des sections efficaces multigroupes photon-électron de haute précision pour l'équation de BFP. Bien que les solveurs de Monte-Carlo aient affiné leurs modèles physiques depuis, tel qu'avec l'introduction de section efficace explicite pour les positrons et l'utilisation de données évaluées plus récentes, CEPXS n'a point évolué. De plus, des problèmes ont été identifiés dans la méthodologie de CEPXS pouvant entraîner des échecs dans les calculs de dépôt de dose. Il a été décidé de développer une alternative à CEPXS en libre accès pour améliorer à la fois les modèles physiques et la méthodologie de production de sections efficaces multigroupes, tout en offrant un outil aisément accessible pour développer et produire des sections efficaces couplées photon-électron-positron pour l'équation de BFP. La performance de ces données atomiques a été évaluée à l'aide de calculs de référence Monte-Carlo pour différents énergies, matériaux et types de faisceaux. Pour le calcul de dose, les comparaisons montrent

des différences relatives typiques de quelques pourcents, tandis que les spectres énergétiques montrent une excellente correspondance.

La méthode des ordonnées discrètes ( $S_N$ ) est une technique de discrétisation angulaire largement utilisée en génie nucléaire pour le transport de neutrons. Cependant, des études ont montré que les diffusions hautement anisotropes, comme celle des électrons et des positrons, peuvent engendrer de graves problèmes de convergence ou de précision. La méthode de quadrature Galerkin rectifie les principales lacunes de la méthode  $S_N$  avec ce type de diffusion, mais il appert que cette technique fut négligée dans les solveurs  $S_N$  en PTR. Un solveur incorporant cette méthode a été développé de manière à être compatible avec tout choix de quadrature, mais il a été observé que les diffusions hautement anisotropes génèrent d'indésirables oscillations dans la solution, distinctes de l'effet de raie. Un schéma, basé sur la méthode des différences finies, a été développé pour l'opérateur angulaire de Fokker-Planck (AFP) afin de faire face à ce problème. Le schéma est monotone, il préserve les deux premiers moments de l'opérateur AFP et est compatible avec des quadratures non orthogonales. Les résultats numériques montrent que ces méthodes permettent l'utilisation de quadrature optimale, diminuant la quantité de calcul requise pour atteindre un niveau de précision donné, tout en assurant un traitement strictement monotone, précis et stable des diffusions fortement anisotropes.

Finalement, les solutions de l'équation de BFP varient immensément en espace et en énergie. L'obtention de solutions précises à partir de la discrétisation couplée de ces deux variables est très ardue. Même avec les méthodes Galerkin discontinues et des relations de fermetures linéaires, des oscillations parasites et des négativités apparaissant dans la solution. Des relations de fermeture d'ordre supérieur furent étudiées, mais elles ne permettaient pas de résoudre les problèmes de positivité et de monotonie. Sur la base de précédentes études portant sur des schémas linéaires adaptatifs d'ordre 2, il a été postulé qu'un tel schéma pourrait produire des solutions améliorant la positivité et monotonie du schéma discontinu linéaire Galerkin. Ces schémas ont été développés pour des maillages 1D et 2D afin d'améliorer la positivité et la monotonie des solutions tout en garantissant une précision d'ordre 2. Des comparaisons entre les principales relations de fermeture, autant pour les solutions de dépôt d'énergie que pour les spectres énergétiques, montrent que ces schémas adaptatifs permettent d'obtenir des solutions positives et monotones.

## ABSTRACT

An essential requirement of Radiation Treatment Planning (RTP) is efficient and accurate dose deposition estimation capacities. While Monte Carlo radiation transport solvers have traditionally been considered the gold standard for RTP, their application in clinical environments is limited due to their significant execution time and stochastic nature. Yet, a broad family of algorithms can simulate the physics of radiation therapy with similar accuracy called deterministic methods. The solver Acuros<sup>®</sup>, from Varian Medical Systems, is one of them and is already used for X-ray beams in RTP systems. Despite breakthroughs in deterministic capacities, such as the derivation of the Boltzmann Fokker-Planck (BFP) equation or the development of CEPXS code, existing RTP deterministic models have limitations that hinder their widespread use. The main objective of this thesis is to investigate and address these shortcomings.

The Boltzmann Fokker-Planck (BFP) equation is central to this dissertation since every development in this work revolves around it. The investigations have led to innovative algorithms in three areas of research: 1) the production of coupled photon-electron-positron atomic data, 2) the angular discretization, and 3) the energy-space closure relations.

Until recently, the CEPXS code, developed in 1989, was the sole code to produce high-accuracy multigroup photon-electron cross-sections for the BFP equation and was used as the source of atomic data for transport solvers. While Monte-Carlo solvers have refined their physics models since then, such as having explicit positrons cross-sections or using more recent data, CEPXS still lacks these improvements. Moreover, issues were identified in the CEPXS methodology, which can lead to failure in energy deposition calculations. It was decided to develop an open-source alternative to CEPXS to improve both the physics models and the multigroup cross-section production methodology while offering to the research community an easily accessible tool to develop and produce coupled photon-electron-positron cross-sections for the BFP equation. Accuracy of resulting atomic data were compared using Monte-Carlo reference calculations for varying energies, materials and external beam types. The benchmark, consisting of energy deposition benchmark and energy spectra per particle species, has shown typical agreement of a few percent for energy deposition calculations and the ability of deterministic codes to replicate energy spectra.

The discrete ordinates ( $S_N$ ) method is a widely used angular discretization technique in nuclear engineering for neutron transport. However, studies have shown that highly forward-peaked scattering, such as the one of electrons and positrons, leads to severe convergence

or accuracy issues. The Galerkin quadrature method is a paramount feature to implement alongside the  $S_N$  method, tackling these issues, but it is overlooked in existing RTP discrete ordinates codes. This method was implemented to be compatible with any choice of quadrature and tested, but those tests have shown that forward-peaked elastic scattering generates spurious oscillations distinct from the well-known ray effect. A monotone and moment-preserving finite-difference scheme for the Angular Fokker-Planck (AFP) operator, compatible with nonorthogonal quadrature, is developed to grapple with this issue. Numerical results show that these methods permit optimal quadrature, which is very efficient since they reduce the computational requirement for accurate calculations while producing monotone, precise and stable treatment of forward-peaked scattering.

Finally, solutions of the BFP equation vary enormously in space and energy. Obtaining accurate solutions with the simultaneous discretization of these variables is challenging, even for Discontinuous Galerkin Finite-Element Method (DG-FEM) with coupled linear closure relations. Indeed, these solutions often exhibit spurious oscillations and negativities, which make no physical sense. At first, quadratic and higher-order closure relations were investigated, but they failed to solve the problem. Based on previous studies on adaptive 2<sup>nd</sup>-order accurate linear schemes, it was postulated that such a scheme could produce more positive and monotone solutions than the state-of-the-art linear discontinuous Galerkin scheme. These schemes were developed for 1D and 2D meshes to improve the positivity and monotonicity of the solutions while enforcing 2<sup>nd</sup>-order accuracy. Transport calculations for energy spectrum and energy deposition benchmark show that such adaptive schemes can provide positive and monotone solutions.

## TABLE OF CONTENTS

DEDICATION . . . . .	iii
ACKNOWLEDGEMENTS . . . . .	iv
RÉSUMÉ . . . . .	v
ABSTRACT . . . . .	vii
TABLE OF CONTENTS . . . . .	ix
LIST OF TABLES . . . . .	xiii
LIST OF FIGURES . . . . .	xiv
LIST OF SYMBOLS AND ACRONYMS . . . . .	xvi
LIST OF APPENDICES . . . . .	xvii
CHAPTER 1 INTRODUCTION . . . . .	1
1.1 Simulation of Ionizing Radiation in Radiation Therapy Planning . . . . .	1
1.2 Research Motivation . . . . .	3
1.3 Thesis Outline . . . . .	5
CHAPTER 2 COUPLED DETERMINISTIC PARTICLE TRANSPORT . . . . .	6
2.1 Foreword . . . . .	6
2.2 The Transport Equation . . . . .	6
2.3 Energy Discretization . . . . .	8
2.3.1 Multigroup discretization . . . . .	8
2.3.2 The Fokker-Planck approximation . . . . .	9
2.3.3 The Boltzmann Fokker-Planck equation . . . . .	11
2.4 Angular Discretization . . . . .	13
2.4.1 Discrete ordinates method . . . . .	14
2.4.2 Fixed external sources . . . . .	15
2.4.3 Ray effects . . . . .	18
2.5 Spatial Discretization . . . . .	19
2.6 Resolution of the Coupled Photon-Electron-Positron Transport Equations . .	19

2.7	Energy Deposition . . . . .	21
2.8	Charge Deposition . . . . .	23
CHAPTER 3 COUPLED PHOTON, ELECTRON AND POSITRON MULTIGROUP		
	CROSS-SECTIONS . . . . .	24
3.1	Foreword . . . . .	24
3.2	Ionizing Radiation in Radiotherapy Treatment . . . . .	25
3.3	Definitions . . . . .	26
3.4	Impact Ionization . . . . .	27
	3.4.1 Catastrophic inelastic cross-section . . . . .	29
	3.4.2 Soft stopping power . . . . .	32
3.5	Elastic Scattering for Electrons and Positrons . . . . .	33
	3.5.1 Legendre moments of the scattering cross-sections . . . . .	36
	3.5.2 Total cross-sections . . . . .	37
	3.5.3 Transport correction and elastic decomposition in soft and catastrophic components . . . . .	38
3.6	Bremsstrahlung . . . . .	39
	3.6.1 Scattering cross-sections for deflected electron or positron . . . . .	41
	3.6.2 Scattering cross-sections for produced photon . . . . .	41
	3.6.3 Catastrophic total cross-sections . . . . .	42
	3.6.4 Absorption cross-sections for incoming positrons . . . . .	42
	3.6.5 Total stopping power . . . . .	42
	3.6.6 Soft stopping powers . . . . .	42
3.7	Annihilation . . . . .	42
	3.7.1 Scattering cross-sections for the lowest energy photons . . . . .	44
	3.7.2 Scattering cross-sections for the highest energy photons . . . . .	44
	3.7.3 Total cross-sections . . . . .	45
	3.7.4 Annihilation when positrons scatter under the cutoff energy . . . . .	45
3.8	Rayleigh Scattering . . . . .	46
	3.8.1 Scattering cross-sections of the incoming photon . . . . .	47
	3.8.2 Total cross-sections . . . . .	47
3.9	Compton Scattering . . . . .	47
	3.9.1 Scattering cross-sections of the incoming photon . . . . .	48
	3.9.2 Scattering cross-sections of the produced electron . . . . .	49
	3.9.3 Total cross-sections . . . . .	49
3.10	Photoelectric Effect . . . . .	49

3.10.1	Scattering cross-sections of the produced electron . . . . .	50
3.10.2	Total cross-sections . . . . .	51
3.11	Pair Production . . . . .	51
3.11.1	Scattering cross-sections for the produced electron and positron . . .	53
3.11.2	Total cross-sections . . . . .	54
3.11.3	Absorption cross-sections . . . . .	54
3.12	Atomic Relaxation . . . . .	54
3.12.1	Scattering cross-sections of produced Auger electron or fluorescence photon . . . . .	55
3.13	Consolidated Atomic Data . . . . .	56
3.14	Results and Discussion . . . . .	59
3.14.1	An open-source alternative to CEPXS . . . . .	59
3.14.2	Comparison of Boltzmann Fokker-Planck solver with a reference Monte- Carlo solver . . . . .	60
3.14.3	Comparison with experimental energy and charge deposition benchmarks	67
3.15	Conclusion and Perspectives . . . . .	71
CHAPTER 4 ANGULAR DISCRETIZATION OF THE BOLTZMANN FOKKER- PLANCK EQUATION . . . . .		73
4.1	Foreword . . . . .	73
4.2	Methods for Discrete Ordinates Solvers . . . . .	73
4.2.1	Matrix formalism . . . . .	73
4.2.2	Quadrature over the unit sphere . . . . .	74
4.2.3	Galerkin quadrature . . . . .	76
4.3	Discretization Schemes for the Angular Fokker-Planck Operator . . . . .	78
4.3.1	1D finite-difference schemes . . . . .	80
4.3.2	2D and 3D finite-difference schemes for orthogonal quadrature . . . .	81
4.3.3	Voronoi grid on the unit sphere . . . . .	84
4.3.4	2D and 3D finite-difference schemes for nonorthogonal quadrature . .	84
4.4	Results and Discussion . . . . .	88
4.4.1	Comparison of Galerkin quadrature methods . . . . .	89
4.4.2	Comparison of Galerkin and finite-difference schemes in 1D geometry	90
4.4.3	Comparison of Galerkin and finite-difference schemes in 3D geometry	92
4.5	Conclusion and Perspectives . . . . .	93
CHAPTER 5 LINEAR ADAPTIVE ENERGY-SPACE SCHEMES . . . . .		95
5.1	Foreword . . . . .	95



5.2	Discretization by the Galerkin Method of Weighted Residuals . . . . .	95
5.2.1	Transport equation in a space-energy mesh . . . . .	96
5.2.2	Definition of the flux moments . . . . .	97
5.2.3	Coupled space-energy moment equations . . . . .	99
5.3	Closure Relations . . . . .	100
5.3.1	Review of closure relations . . . . .	101
5.3.2	Generalized static closure relations . . . . .	103
5.3.3	1D linear weighted schemes . . . . .	105
5.3.4	2D linear weighted schemes . . . . .	108
5.4	Adaptive Choice of Weights . . . . .	115
5.4.1	1D linear weighted schemes . . . . .	115
5.4.2	2D linear weighted schemes . . . . .	119
5.5	Results and Discussion . . . . .	121
5.5.1	Energy spectrum of electrons . . . . .	121
5.5.2	Energy deposition . . . . .	124
5.6	Conclusion and Perspectives . . . . .	126
CHAPTER 6	CONCLUSION . . . . .	127
6.1	Summary of Works . . . . .	127
6.2	Future Research . . . . .	128
REFERENCES	. . . . .	130
APPENDICES	. . . . .	150

# LIST OF TABLES

Table 5.1	Values of $\delta_1$ as a function of parameter $u_x^{\text{CM}}$ . . . . .	107
Table 5.2	Values of $Q_x$ as a function of parameter $\delta_1$ . . . . .	108
Table 5.3	Values of $(\delta_1, \delta_2)$ as a function of parameter $(u_x^{\text{CM}}, u_y^{\text{CM}})$ . . . . .	111
Table 5.4	Values of $(Qx, Qy, Tx, Ty)$ as a function of parameter $(\delta_1, \delta_2)$ . . . . .	112

# LIST OF FIGURES

Figure 2.1	Energy discretization. . . . .	8
Figure 2.2	Definition of the soft and catastrophic interactions at energy group boundaries. . . . .	12
Figure 2.3	Spatial discretization. . . . .	19
Figure 2.4	Sweeping process. . . . .	20
Figure 3.1	Impact ionization. . . . .	28
Figure 3.2	Elastic scattering. . . . .	34
Figure 3.3	Bremsstrahlung production. . . . .	39
Figure 3.4	Positrons annihilation. . . . .	43
Figure 3.5	Coherent scattering. . . . .	46
Figure 3.6	Compton scattering. . . . .	47
Figure 3.7	Photoelectric effect. . . . .	50
Figure 3.8	Pair production. . . . .	51
Figure 3.9	Relaxation cascades. . . . .	54
Figure 3.10	Dose and energy spectrum per particle for normally incident 1 MeV electron and photon beams on water, aluminum and gold. . . . .	61
Figure 3.11	Dose and energy spectrum per particle for normally incident 10 MeV electron and photon beams on water, aluminum and gold. The curve definition are given in Fig. 3.10. . . . .	62
Figure 3.12	Dose and energy spectrum per particle for normally incident 100 MeV electron and photon beams on water, aluminum and gold. The curve definition are given in Fig. 3.10. . . . .	63
Figure 3.13	Energy deposition compared with experimental data. . . . .	68
Figure 3.14	Energy deposition on multilayer assembly compared with experimental data. . . . .	69
Figure 3.15	Charge deposition compared with experimental data. . . . .	69
Figure 4.1	Voronoi tessellation of the product quadrature (Gauss-Legendre quadrature along $\mu$ and Chebychev quadrature along $\phi$ ), the level-symmetric quadrature (Carlson $ES_N$ quadrature) and Lebedev quadrature. . . .	75
Figure 4.2	Quadrature efficiency. . . . .	76
Figure 4.3	Voronoi tessellation of the $S_8$ Carlson's level-symmetric quadrature nodes on the positive octant of the unit sphere. . . . .	86

Figure 4.4	Comparison of two Galerkin quadrature methods for different quadrature order. . . . .	89
Figure 4.5	Comparison of energy deposition profiles using either Galerkin and finite-difference schemes for the AFP operator based on a Gauss-Lobatto quadrature in 1D Cartesian geometry. . . . .	91
Figure 4.6	Comparison of energy deposition profiles using Galerkin and finite-difference schemes for the Fokker-Planck operator based on the Lebedev quadrature in 1D Cartesian geometry. . . . .	92
Figure 4.7	Comparison of energy deposition profiles using either Galerkin and finite-difference schemes for the AFP operator based on a Lebedev quadrature in 3D Cartesian geometry. . . . .	93
Figure 5.1	Padé approximant of $e^{-1/h_x}$ . . . . .	104
Figure 5.2	Approximation of $a(h_x)$ for different schemes. . . . .	105
Figure 5.3	The 2 cases of linear-constant flux representation within a 1D Cartesian finite-element. . . . .	106
Figure 5.4	The 12 cases of flux representation within a 2D Cartesian finite-element. . . . .	109
Figure 5.5	Subdomains. . . . .	111
Figure 5.6	Values of $Q_x$ , $Q_y$ , $T_x$ and $T_y$ as a function of the centroid coordinates. . . . .	114
Figure 5.7	Centroid coordinates that enforce positivity as a function of parameter $\dot{Q}_x$ and $h_x$ . . . . .	117
Figure 5.8	Electron energy spectra at various depths: comparison of different closure relations with 40 energy groups and 40 voxels. . . . .	122
Figure 5.9	Electron energy spectra at various depths: comparison of different closure relations with 300 energy groups and 160 voxels. . . . .	123
Figure 5.10	Comparison of discretization refinements and closure relations for energy deposition in water by 10 MeV incident electron beam. . . . .	125

## LIST OF SYMBOLS AND ACRONYMS

AAA	Analytical Anisotropic Algorithm
AAPM	American Association of Physicists in Medicine
AFP	Angular Fokker-Planck
AWD	Adaptive Weighted Difference
BFP	Boltzmann Fokker-Planck
BTE	Boltzmann Transport Equation
CCC	Collapsed-Cone Convolution
CPU	Central Processing Unit
CSD	Continuous Slowing-Down
CT	Computed Tomography
DD	Diamond difference
DG	Discontinuous Galerkin
DG-FEM	Discontinuous Galerkin Finite-Element Method
DSA	Diffusion Synthetic Acceleration
EADL	Evaluated Atomic Data Library
EEDL	Evaluated Electron Data Library
ENDF	Evaluated Nuclear Data File
EPDL	Evaluated Photon Data Library
FAIR	Findability, Accessibility, Interoperability and Reuse
FCS	First Collision Source
FP	Fokker-Planck
GMRES	Generalized Minimal Residual
GPU	Graphic Processing Unit
HODD	High-order diamond difference
JENDL	Japanese Evaluated Nuclear Data Library
KBA	Koch-Baker-Alcouffe
ICRU	International Commission on Radiological Units and Measurements
LINAC	Linear Accelerator
MRI	Magnetic Resonance Imaging
RTP	Radiation Treatment Planning
SI	Source Iteration
SM	Step Moment

**LIST OF APPENDICES**

Appendix A	Polynomials . . . . .	150
Appendix B	Quadratures . . . . .	153
Appendix C	Newton-bisection method . . . . .	156

## CHAPTER 1 INTRODUCTION

### 1.1 Simulation of Ionizing Radiation in Radiation Therapy Planning

Ionizing radiation is present in a wide variety of fields, such as nuclear energy, medical imaging, radiotherapy, radiation protection, accelerator physics, food irradiation, shielding, non-destructive testing, security scanning equipment and even cultural heritage, where assessing its effect with accuracy is critical [1–3]. For a nuclear power plant, the study of neutrons transport and reaction rates in the reactor core is a requisite to determine quantities such as its energy output, its reactivity or the depletion of fissile atoms [4]. For radiotherapy, it is critical to have quality estimate of the dose distribution in the patient to adequately target the tumor while minimizing the damage to healthy tissues. Beyond technologies relying on ionizing radiation, there is an important risk assessment incentive since exposition to such radiation presents a health hazard among other things. For example, in hospital, both patient and medical personnel are exposed to some level of radiation due to proximity of nuclear technologies such as linear accelerator (LINAC) or Computed Tomography (CT) scanner. In space, astronaut are exposed to significant quantities of cosmic rays. In every house, people are exposed to various level of radon gas. These health risks have to be mitigated by taking radiation protection measures, which requires an understanding of, not only how the human body reacts to different types of ionizing radiation, but how the ionizing particles behaves inside the human body. As specified, risk assessment is not limited to health and ionizing radiation can have significant impact on inanimate entity, such as electronic devices. For satellites in orbit, cosmic rays can deposit their energy and charge in electronics components, potentially making them unusable and since repairing in space can be quite expansive, anticipating these effect beforehand is primordial.

RTP is a process to determine the treatment parameters, such as the kind of sources, the particle energies and the beam angles. Nowadays, the planning begins by acquiring 3D images of the tumour and its surroundings using CT and MRI technologies. Afterward, volumes of interest for the treatment are delineated to encompass the solid tumour, the planning volume, uncertainties and organs at risk. The International Commission on Radiological Units and Measurements (ICRU), in its reports 50 and 62, proposed a general framework which is widely used [5]. Then, treatment parameters must be found to deliver the dose to the defined volumes subject to established constraints, for example exposition limits to organs at risk. The dosimetrist relies on algorithms to estimate accurately the delivered dose to the tumour and its surroundings. The RTP is an inverse problem, in which the treatment

parameters are adjusted to provide the required dose deposition to the tumor. The American Association of Physicists in Medicine (AAPM) recommends in its report 85 that the dose calculation accuracy should be between 1 to 2% [6].

Despite advancements in computational capacities in the last decades, the complexity of the physics processes leading to dose deposition events in heterogeneous media makes accurate estimation of quantities such as energy or charge deposition challenging to obtain without time-consuming calculations. The underlying physics and the displacement of the different species of particles in matter fall under the scope of an integro-differential equation, the steady-state Boltzmann transport equation, which solution determines the particle distribution in the media. Using stochastic processes to simulate the transport of particles in matter, Monte Carlo algorithms have reached unprecedented accuracy and thus are considered the gold standard in RTP [7]. They are very flexible since general geometries and physics interactions can be implemented quickly. The leading issue with these methods is their execution times, which can easily become exceedingly long, notably when low-probability events have to be simulated or high accuracy is needed. This issue limits their application to RTP since the delay between imaging and treatment should be short enough to prevent the cancer from propagating in between. Other disadvantages of Monte Carlo include 1) the inability to get rid of statistical noise, 2) difficulty of setting important parameters like step length adapted for a specific problem in order to have a good equilibrium between accuracy and running time [8], 3) systematic error, for example at layer boundaries, can be produced by the condensed history method [1, 9] 4) its limits when applied to inverse problem such as the RTP one, since it would require solving multiples times the already time-expansive forward problem [10, 11]. Therefore, these high-accuracy Monte Carlo methods are set aside for clinical usage in favour of simpler, less accurate, but much faster semi-empirical models, such as point kernel, pencil beams, collapsed cone convolution, convolution/superposition, or confined to limited scopes of applications by simplifying physics or geometry, implementing variance reduction techniques, or using massively parallel computing architectures.

Nevertheless, there are other approaches to solving the steady-state Boltzmann transport equation with similar accuracy than Monte Carlo solvers. While there is a belief that Monte Carlo methods are superior to any deterministic ones in the medical field [12, 13], many researchers, myself included, contest that claim [9, 14]. Deterministic methods, which encompass a broad family of algorithms, have been widely used for neutron transport to describe nuclear reactors' physics since the middle of the 20<sup>th</sup> century, and many are pretty mature. Charged particle transport, which is required for RTP, had its challenges, but the more notable of them were lifted by the advent of critical developments in the eighties, notably the Boltzmann Fokker-Planck approximation [15], the multigroup cross-sections production



code CEPXS [16] and the Galerkin quadrature method [17]. At the start of the 21<sup>th</sup> century, the discrete ordinates Attila solver from Los National Laboratories was applied to external photon beam radiotherapy. Gifford et al. compared its energy deposition solution on heterogeneous media to reference Monte Carlo calculations, which showed a typical discrepancy of 2%, up to 5% at some locations [7]. Further validation has been done, showing that 99% of voxels agreed with Monte Carlo using a criterion of 3% or 3 mm distance-to-agreement [18]. This research resulted in a commercial product, Acuros<sup>®</sup> from Varian Medical Systems [19]. Over the years, it was shown to be more accurate than the analytical anisotropic algorithm (AAA) and the collapsed-cone convolution (CCC) algorithm, two semi-empirical algorithms which are widely used in planning systems [20–22]. Deterministic solvers are very advantageous when multiple beams are considered, such as with arc therapy, since it does not increase the workload as it is the case with semi-empirical and Monte-Carlo methods [19].

The advent of deterministic methods in RTP has prompted new research directions. At University of Alberta, researchers have added the magnetic component of the Lorentz force into the transport equation to treat external magnetic field, enabling its use for MRI-guided radiotherapy, for both the discrete ordinates or coupled space-angle finite-element discretization [23–27]. At Delft University of Technology, researchers have developed coupled space-angle finite-element discretization and angular refinement methods and are leading the deterministic proton RTP effort [28–31]. Outside the medical application, the SCEPTRE code of Sandia National Laboratories, whose primary purpose is radiation-driven electrical effect, is one of the most advanced codes for charged particle transport [32]. The Lorentz force, including the electric field, has been implemented [33, 34]. At Polytechnique Montréal, there is an effort to extend NJOY nuclear data code [35] capabilities to electron transport through a new module ELECTR using open source evaluated ENDF formatted data [36]. Naceur et al. have implemented and validated pure electron CEPXS models in ELECTR over the entire periodic table up to multi-GeV energies [37], while the development of ENDF mode is underway [38, 39].

## 1.2 Research Motivation

The primary motivation of this thesis is to address flaws of the Acuros<sup>®</sup> solver and to develop open source tools to make discrete ordinates solvers more reliable for RTP applications. These shortcomings are related to three areas of research regarding the BFP equation, namely 1) the production of atomic data, 2) the angular discretization and 3) the energy-space schemes. Let's discuss them separately:

1. **Production of atomic data :** From its release in 1989 to recent times, the CEPXS code from Sandia National Laboratories is technically the sole accurate tool to produce coupled multigroup electron-photon cross-sections for the BFP equation. While some coupled multigroup electron-photon cross-sections can be found in literature [40, 41], none cover as much interactions as the CEPXS code, whose cover Compton effect, photoelectric effect, pair production, annihilation, inelastic and elastic scattering of electrons, bremsstrahlung and relaxation.. It is the source of the atomic data used in Acuros<sup>®</sup>. The physics models it contains are not up-to-date with those used in Monte Carlo codes specialized in coupled photons, electron and positron transport such as GEANT4 [42], PENELOPE [43], or EGSnrc [44]. For example, it does not contain subshell-dependant inelastic electron scattering or photoelectric effect, and is valid only for low-Z atoms, as implied in [37]. It also does not have explicit positrons cross-sections, which limits its use at high-energy where pair production becomes a dominant phenomenon. While the CEPXS code is widely used, it still contains many deficiencies. It was noted that energy deposition calculations fail when a low number of energy groups are used. It was also noted that the group-based CEPXS definition of soft and catastrophic domain and the resulting arbitrary definition of group boundary's stopping power leads to noticeable errors when the number of energy groups is low. These issues can be mitigated using more energy groups, increasing the computational cost. There is also an additional limitation, which is the proprietary nature of the code that does not have an open source alternative, which hinders the development and testing of newer physics models for deterministic transport.
2. **Angular discretization :** The average scattering angle of charged particles is tiny, which means the scattering of these particles is far from being isotropic. While the classical discrete ordinates method performs very well with weak anisotropic scattering, more tools are needed with highly forward peaked scattering. Morel has shown, in a consequential paper [17], that the  $S_N$  method can give very inaccurate results (and even diverge, as pointed out by Pautz and Adams [45]) and proposed a method called Galerkin quadrature, which ensures accurate treatment of forward-peaked scattering. We have found no documentation showing that Acuros<sup>®</sup> nor its mother code Attila have implemented Galerkin quadrature [7, 9]. In a 2015 whitepaper about their product Acuros<sup>®</sup> XB, Varian Medical Systems shows an explicit formula showing that classical discrete ordinates, with level-symmetric quadrature, are used [46]. Moreover, no Galerkin quadrature method have strictly positive weights, which comes with monotonicity issues with forward-peaked scattering [17, 47]. These issues are distinct from the ray effect. These can cause, as will be shown, significant and unpredictable oscil-

lations in the solution, depending on the choice of quadrature, flux angular expansion basis, discretization order, spatial discretization and other parameters.

3. **Energy-space schemes:** It is well-known that charged particle transport generates a solution that varies strongly along both the space and energy axis, which is challenging to converge even high-order discretization [47]. Acuros<sup>®</sup> is based on a linear discontinuous Galerkin space-energy scheme. While being a significant improvement over constant schemes, this scheme produces oscillations and negativities in the flux solution, which can be passed on to the dose deposition profiles [48].

This thesis focuses on developing mathematical tools and frameworks addressing these shortcomings. Another motivation, which was not explicated yet, is to provide a state-of-the-art deterministic transport capacities in open access, which neither CEPXS nor Acuros<sup>®</sup> are. Our research group promotes the FAIR guiding principles (FAIR: Findability, Accessibility, Interoperability and Reuse) [49] and supports the idea that publicly funded research should remain available.

### 1.3 Thesis Outline

The development of the novel capacities for the Boltzmann Fokker-Planck is elaborated in the upcoming chapters. In Chapter 2, the coupled transport framework is implemented. It describes the principal discretizations, the energy deposition calculations, the BFP equation, and how to solve them. In Chapter 3, coupled photon-electron-positron multigroup cross-sections and other atomic data are produced based on an improved physics model compared to CEPXS. Validation and performance of these cross-sections are done by comparing BFP dose and energy spectrum calculations using them in Monte Carlo reference calculations. In Chapter 4, a finite-difference scheme for the Fokker-Planck operator compatible with optimal quadrature is developed and is used to mitigate monotonicity issues. In Chapter 5, adaptive linear schemes are developed for the BFP equation. Finally, Chapter 6 summarizes this thesis findings and future perspectives.

## CHAPTER 2 COUPLED DETERMINISTIC PARTICLE TRANSPORT

### 2.1 Foreword

This chapter introduces the foundation of this thesis' coupled electron-photon-positron transport solver. It describes the main discretization techniques, such as the Fokker-Planck (FP) approximation, the multigroup formalism, and the discrete ordinates method. It also explains how this equation is solved. Finally, a novel energy deposition formula is proposed as a function of the angular flux.

There is three novelty introduced in this section. First, the proposed scattering cross-section is expanded using an arbitrary subset of spherical harmonics rather than all spherical harmonics up to a specified Legendre order, as it is usually done. Second, a new definition of catastrophic and soft domain is proposed for the Boltzmann Fokker-Planck (BFP) equation, in Sect. 2.3.3. Third, energy and charge deposition cross-section formula, that take into account positron annihilation and variation of rest mass energy, defined in Sect. 2.7.

### 2.2 The Transport Equation

The linear Boltzmann Transport Equation (BTE), which describes radiation transport in a medium, is derived to enforce particle conservation. It is assumed that transported particles do not interact between themselves and that the medium has isotropic properties. Since neither the medium properties nor the sources evolve in applications covered by this thesis, only the time-independent (i.e. steady-state) transport equation is used [50].

Let  $E$  be the particle energy,  $\mathbf{r} = (x, y, z)$  be the particle position in  $\mathbb{R}^3$ ,  $\boldsymbol{\Omega} = (\mu, \phi) = (\mu, \eta, \xi)$  be the moving particle direction, where  $\mu$  is the principal direction cosine aligned with  $x$ -axis,  $\phi$  is the azimuthal angle, while  $\eta$  and  $\xi$  are the secondary direction cosines under the constraint  $\mu^2 + \eta^2 + \xi^2 = 1$ . Let

$$\mathbb{S}^2 = \left\{ \boldsymbol{\Omega} = (\mu, \eta, \xi) \in \mathbb{R}^3 : \|\boldsymbol{\Omega}\| = 1 \right\} \quad (2.1)$$

be the unit sphere. Let  $P$  be the set of all simulated particles, which in this thesis will be restricted to  $P = \{\gamma, \mathbf{e}^-, \mathbf{e}^+\}$ , corresponding to photons, electrons and positrons respectively. The steady-state linear BTE for a particle  $p \in P$  is given by [50]

$$\boldsymbol{\Omega} \cdot \nabla \Psi_p(\mathbf{r}, \boldsymbol{\Omega}, E) + \Sigma_t^p(\mathbf{r}, \boldsymbol{\Omega}, E) \Psi_p(\mathbf{r}, \boldsymbol{\Omega}, E) = Q_p^{\mathbf{B}}(\mathbf{r}, \boldsymbol{\Omega}, E) + Q_p^{\text{ext}}(\mathbf{r}, \boldsymbol{\Omega}, E), \quad (2.2)$$

where the first and second terms on the left side of the equation will respectively be referred to as the streaming and collision terms,  $Q_p^{\text{ext}}(\mathbf{r}, \boldsymbol{\Omega}, E)$  account for fixed volume sources (see Sect. 2.4.2) and the Boltzmann operator, which accounts for both particle scattering and production in the medium, is given by

$$Q_p^{\text{B}}(\mathbf{r}, \boldsymbol{\Omega}, E) = \sum_{p' \in P} \int_{\mathbb{S}^2} d^2\Omega' \int_0^\infty dE' \Sigma_s^{p' \rightarrow p}(\mathbf{r}, E' \rightarrow E, \boldsymbol{\Omega}' \rightarrow \boldsymbol{\Omega}) \Psi_{p'}(\mathbf{r}, \boldsymbol{\Omega}', E'), \quad (2.3)$$

where  $\Sigma_t^p(\mathbf{r}, E)$  is the macroscopic total cross-section for particle  $p$  and  $\Sigma_s^{p' \rightarrow p}(\mathbf{r}, E' \rightarrow E, \boldsymbol{\Omega}' \rightarrow \boldsymbol{\Omega})$  is the macroscopic double differential scattering cross-section describing the probability of a particle  $p'$  with energy  $E'$  and direction  $\boldsymbol{\Omega}'$  to yield a particle  $p$  with energy  $E$  and direction  $\boldsymbol{\Omega}$ . The solution of this equation,  $\Psi_p(\mathbf{r}, \boldsymbol{\Omega}, E)$ , is the angular flux for particle  $p$ . It is defined as the product of the population density  $n_p(\mathbf{r}, \boldsymbol{\Omega}, E)$  and the particle speed  $v_p(E)$

$$\Psi_p(\mathbf{r}, \boldsymbol{\Omega}, E) = v_p(E) n_p(\mathbf{r}, \boldsymbol{\Omega}, E). \quad (2.4)$$

The integrated flux for particle  $p$  is given by integrating the angular flux over the unit sphere

$$\Psi_p(\mathbf{r}, E) = \int_{\mathbb{S}^2} d^2\Omega \Psi_p(\mathbf{r}, \boldsymbol{\Omega}, E). \quad (2.5)$$

This integrated flux can be used to compute so-called reaction rates, such as energy or charge deposition. In the scope of this work, all materials considered have isotropic properties, which further simplify the transport equation by making the total cross-sections independent in angle, such as  $\Sigma_t^p(\mathbf{r}, \boldsymbol{\Omega}, E) = \Sigma_t^p(\mathbf{r}, E)$ , and the scattering cross-sections only dependent on the scattering angle  $\boldsymbol{\Omega} \cdot \boldsymbol{\Omega}'$ , such as  $\Sigma_s^{p' \rightarrow p}(\mathbf{r}, E' \rightarrow E, \boldsymbol{\Omega}' \rightarrow \boldsymbol{\Omega}) = \Sigma_s^{p' \rightarrow p}(\mathbf{r}, E' \rightarrow E, \boldsymbol{\Omega} \cdot \boldsymbol{\Omega}')$ . Using Legendre expansion of the scattering cross-sections in that scattering angle is common practice. The resulting Boltzmann operator is given by

$$Q_p^{\text{B}}(\mathbf{r}, \boldsymbol{\Omega}, E) = \sum_{p' \in P} \int_0^\infty dE' \sum_{q=1}^{N_q} \frac{2\ell_q + 1}{4\pi} \Sigma_{s, \ell_q}^{p' \rightarrow p}(\mathbf{r}, E' \rightarrow E) R_{\ell_q}^{m_q}(\boldsymbol{\Omega}) \Phi_{p, q}(\mathbf{r}, E'), \quad (2.6)$$

where the  $q^{\text{th}}$  moment of the angular flux is given by

$$\Phi_{p, q}(\mathbf{r}, E) = \int_{\mathbb{S}^2} d^2\Omega' R_{\ell_q}^{m_q}(\boldsymbol{\Omega}') \Psi_p(\mathbf{r}, \boldsymbol{\Omega}', E), \quad (2.7)$$

where  $\Sigma_{s, \ell}^{p' \rightarrow p}(\mathbf{r}, E' \rightarrow E)$  is the  $q^{\text{th}}$  Legendre moment of the scattering cross-section and  $R_{\ell_q}^{m_q}(\boldsymbol{\Omega})$  are the real spherical harmonics, as defined in Annex A. Each index  $q \in \{1, N_q\}$  leads to a unique pair  $(\ell_q, m_q)$  and their choice will be discussed later.

## 2.3 Energy Discretization

### 2.3.1 Multigroup discretization

The multigroup discretization divides the energy domain in  $G$  meshes, often referred to as energy group, in which particles share the same energy and averaged energy-dependant variables [50]. The convention where  $g = 1$  corresponds to the highest energy group is used. The midpoint energy of the group  $g$  is  $E_g$ , its width is  $\Delta E_g$ , and its upper and lower boundaries are respectively  $E_{g-1/2}$  and  $E_{g+1/2}$ , as shown in Fig. 2.1. The lower energy boundary of the lowest energy group,  $E_{G+1/2}$ , is called the cutoff energy. Particles that scatter or are produced under this energy cutoff are considered to be absorbed locally. It also means that charge and energy are deposited locally. This energy should be chosen carefully, being low enough to ensure that the absorbed particle mean free path is lower than the spatial meshes' width to be realistic. For electron or photon transport, which is not affected by resonance like neutrons, it is recommended to use logarithmically spaced energy groups for an energy domain stretching over several orders of magnitude. The classical multigroup discretization assumes that the angular flux is separable in energy, such that [51]

$$\Psi_p(\mathbf{r}, \boldsymbol{\Omega}, E) = \Psi_{p,g}(\mathbf{r}, \boldsymbol{\Omega}) f_g(E) \quad (2.8)$$

for  $E \in [E_{g-1/2}, E_{g+1/2}]$ , where the group-averaged flux is given by

$$\Psi_{p,g}(\mathbf{r}, \boldsymbol{\Omega}) = \int_{E_{g+1/2}}^{E_{g-1/2}} dE \Psi_p(\mathbf{r}, \boldsymbol{\Omega}, E), \quad (2.9)$$

and the weighting function  $f_g(E)$ , as it can be deduced from the two previous equations, is constrained to

$$\int_{E_{g+1/2}}^{E_{g-1/2}} dE f_g(E) = 1. \quad (2.10)$$

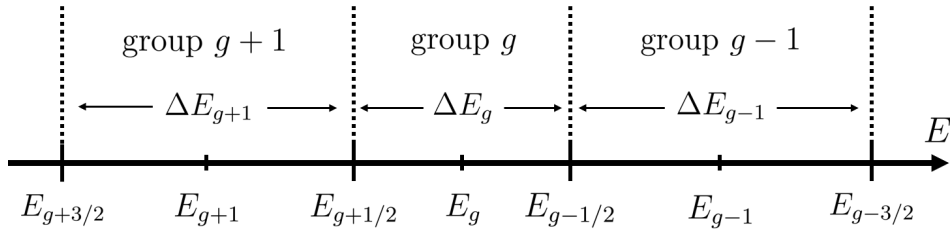


Figure 2.1 Energy discretization.

In this thesis, it is also assumed that  $f_g(E)$  is constant over each group, which results in  $f(E) = 1/\Delta E_g$ . Applying the Galerkin method of weighted residuals to the transport equation, the resulting equation is the multigroup discretized transport given by

$$\boldsymbol{\Omega} \cdot \nabla \Psi_{p,g}(\mathbf{r}, \boldsymbol{\Omega}) + \Sigma_{t,g}^p(\mathbf{r}) \Psi_{p,g}(\mathbf{r}, \boldsymbol{\Omega}) = Q_{p,g}^B(\mathbf{r}, \boldsymbol{\Omega}) + Q_{p,g}^{\text{ext}}(\mathbf{r}, \boldsymbol{\Omega}), \quad (2.11)$$

where the multigroup total cross-section is given by

$$\Sigma_{t,g}^p(\mathbf{r}) = \frac{\int_{E_{g+1/2}}^{E_{g-1/2}} dE \Sigma_t^p(\mathbf{r}, E) \Psi_p(\mathbf{r}, \boldsymbol{\Omega}, E)}{\int_{E_{g+1/2}}^{E_{g-1/2}} dE \Psi_p(\mathbf{r}, \boldsymbol{\Omega}, E)} = \frac{1}{\Delta E_g} \int_{E_{g+1/2}}^{E_{g-1/2}} dE \Sigma_t^p(\mathbf{r}, E) \quad (2.12)$$

and the multigroup  $\ell$  Legendre moment of the scattering cross-section is given by

$$\Sigma_{s,\ell,g' \rightarrow g}^{p' \rightarrow p}(\mathbf{r}) = \frac{\int_{E_{g+1/2}}^{E_{g-1/2}} dE \Sigma_{s,\ell,g'}^{p' \rightarrow p}(\mathbf{r}, E) \Phi_{p,q}(\mathbf{r}, E)}{\int_{E_{g+1/2}}^{E_{g-1/2}} dE \Phi_{p,q}(\mathbf{r}, E)} = \frac{1}{\Delta E_g} \int_{E_{g+1/2}}^{E_{g-1/2}} dE \Sigma_{s,\ell,g'}^{p' \rightarrow p}(\mathbf{r}, E), \quad (2.13)$$

with

$$\Sigma_{s,\ell,g'}^{p' \rightarrow p}(\mathbf{r}, E) = 2\pi \int_{E'_{g+1/2}}^{E'_{g-1/2}} dE' \int_{-1}^1 d\mu P_\ell(\mu) \Sigma_s^{p' \rightarrow p}(\mathbf{r}, E' \rightarrow E, \mu), \quad (2.14)$$

where  $P_\ell(\mu)$  is the  $\ell$ -order Legendre polynomial. The generalized multigroup method consists of an  $M_E$ -order expansion of the angular flux in energy within each energy group [52]. It results in a set  $M_E$  moment equations to solve. This method is more accurate since it can better deal with highly varying solutions from one group to another. Such a method will be partially applied in this work, in Chap. 5.

### 2.3.2 The Fokker-Planck approximation

While it is very successful with neutral particles such as neutrons and photons in reactor physics, the multigroup Boltzmann equation becomes inefficient in dealing with charged particles. This failure is due to the highly forward-peaked scattering of charged particles, the large amount of scattering events due to interactions with atomic electrons in the medium, and the small energy lost in each of these scattering events. For example, Berger and Wang estimated that slowing-down electron from 500 to 250 keV requires 4000 diffusions in aluminum and 7000 in gold, while it reduces to a few dozen for neutral particles such as photons or neutrons [53]. An accurate discretization of the energy domain would require an astronomical number of energy meshes to capture these small energy losses effectively [16].

Under the assumption of forward-peaked and small energy-loss processes, it is possible to derive an alternate form of the Boltzmann operator. Indeed, using Taylor expansion in the angles and energy variables, the Boltzmann operator reduces to the FP operator. The steady-state FP equation for a particle  $p \in P$ , where  $P$  is the set of all simulated particles, is given by [54, 55]

$$\boldsymbol{\Omega} \cdot \nabla \Psi_p(\mathbf{r}, \boldsymbol{\Omega}, E) + \Sigma_a^p(\mathbf{r}, E) \Psi_p(\mathbf{r}, \boldsymbol{\Omega}, E) = Q_p^{\text{FP}}(\mathbf{r}, \boldsymbol{\Omega}, E) + Q_p^{\text{ext}}(\mathbf{r}, \boldsymbol{\Omega}, E), \quad (2.15)$$

where  $\Sigma_a^p(\mathbf{r}, E)$  is the macroscopic absorption cross-section for particle  $p$  and where the FP operator is given by

$$Q_p^{\text{FP}}(\mathbf{r}, \boldsymbol{\Omega}, E) = Q_p^{\text{CSD}}(\mathbf{r}, \boldsymbol{\Omega}, E) + Q_p^{\text{AFP}}(\mathbf{r}, \boldsymbol{\Omega}, E), \quad (2.16)$$

where the Continuous Slowing-Down (CSD) operator is given by

$$Q_p^{\text{CSD}}(\mathbf{r}, \boldsymbol{\Omega}, E) = \frac{\partial}{\partial E} \left[ S^p(\mathbf{r}, E) \Psi_p(\mathbf{r}, \boldsymbol{\Omega}, E) \right] \quad (2.17)$$

and the Angular Fokker-Planck (AFP) operator is given by

$$Q_p^{\text{AFP}}(\mathbf{r}, \boldsymbol{\Omega}, E) = T^p(\mathbf{r}, E) \left[ \frac{\partial}{\partial \mu} (1 - \mu^2) \frac{\partial}{\partial \mu} + \frac{1}{1 - \mu^2} \frac{\partial^2}{\partial \phi^2} \right] \Psi_p(\mathbf{r}, \boldsymbol{\Omega}, E). \quad (2.18)$$

where  $S^p(\mathbf{r}, E)$  is the stopping power and  $T^p(\mathbf{r}, E)$  is the momentum transfer, which are given [55]

$$S^p(\mathbf{r}, E) = 2\pi \int_0^\infty dE' \int_{-1}^1 d\mu (E - E') \Sigma_s^{p \rightarrow p}(\mathbf{r}, E' \rightarrow E, \mu) \quad (2.19)$$

and

$$T^p(\mathbf{r}, E) = \pi \int_0^\infty dE' \int_{-1}^1 d\mu (1 - \mu) \Sigma_s^{p \rightarrow p}(\mathbf{r}, E' \rightarrow E, \mu). \quad (2.20)$$

A higher-order FP term from the Taylor expansion is often kept, which is the energy straggling operator, and is important to obtain more accurate results [54, 56]. Generalized FP operators have also been developed [41, 57, 58]. The presented form, which is fairly minimal, is sufficient for the needs of this work because of the method presented in the following section. While this equation performs well with very fast or heavily charged particles [56], electrons and positrons often change direction when interacting. These large deflections often come with large energy transfers, which cannot be ignored without making significant errors.

While the multigroup discretization of the AFP is straightforward, it is more complicated with the CSD term, which has a derivative in energy. This discretization is describes in



detail in Chap. 5. The stopping powers at boundaries of group  $g$  for particle  $p$ , which will be required to solve the BFP equation, are

$$S_{g+1/2}^p(\mathbf{r}) = S^p(\mathbf{r}, E_{g+1/2}) \quad \text{and} \quad S_{g-1/2}^p(\mathbf{r}) = S^p(\mathbf{r}, E_{g-1/2}), \quad (2.21)$$

while the group-averaged stopping powers of group  $g$  for particle  $p$ , used in the energy deposition cross-sections calculations, are

$$S_g^p(\mathbf{r}) = \frac{\int_{E_{g+1/2}}^{E_{g-1/2}} dE S^p(\mathbf{r}, E) \Psi_p(\mathbf{r}, \mathbf{\Omega}, E)}{\int_{E_{g+1/2}}^{E_{g-1/2}} dE \Psi_p(\mathbf{r}, \mathbf{\Omega}, E)} = \frac{1}{\Delta E_g} \int_{E_{g+1/2}}^{E_{g-1/2}} dE S^p(\mathbf{r}, E) \quad (2.22)$$

and the group-averaged momentum transfers in group  $g$  for particle  $p$  are

$$T_g^p(\mathbf{r}) = \frac{\int_{E_{g+1/2}}^{E_{g-1/2}} dE T^p(\mathbf{r}, E) \Psi_p(\mathbf{r}, \mathbf{\Omega}, E)}{\int_{E_{g+1/2}}^{E_{g-1/2}} dE \Psi_p(\mathbf{r}, \mathbf{\Omega}, E)} = \frac{1}{\Delta E_g} \int_{E_{g+1/2}}^{E_{g-1/2}} dE T^p(\mathbf{r}, E). \quad (2.23)$$

### 2.3.3 The Boltzmann Fokker-Planck equation

In order to have the best of both worlds, Przybylski and Ligou proposed to divide the scattering events into two domains: soft, which consists of small change of direction and energy-loss, and catastrophic, for large change of direction and energy-loss [15]. The catastrophic interactions are treated with the Boltzmann operator, while the soft interactions are treated with the FP operator. The two domains are defined as a function of the particle energy  $E$  by a function  $E_c(E) \leq E$ , over which interactions are considered soft and under which they are considered catastrophic. The steady-state Boltzmann Fokker-Planck (BFP) equation is given by

$$\mathbf{\Omega} \cdot \nabla \Psi_p(\mathbf{r}, \mathbf{\Omega}, E) + \Sigma_t^p(\mathbf{r}, E) \Psi_p(\mathbf{r}, \mathbf{\Omega}, E) = Q_p^B(\mathbf{r}, \mathbf{\Omega}, E) + Q_p^{\text{FP}}(\mathbf{r}, \mathbf{\Omega}, E) + Q_p^{\text{ext}}(\mathbf{r}, \mathbf{\Omega}, E). \quad (2.24)$$

The mathematical structures of the Boltzmann source  $Q_p^B$  or the FP source  $Q_p^{\text{FP}}$  remains the same as in the BTE and FP equations. The BFP can be seen as a generalized form for these equations. However, it should be clear that the definitions of the cross-sections, stopping powers, and momentum transfer differ from the BTE and FP equations. Their complete definitions are given in Chap. 3. It should be assumed that these new definitions overwrite their previous definition in the following sections and chapters.

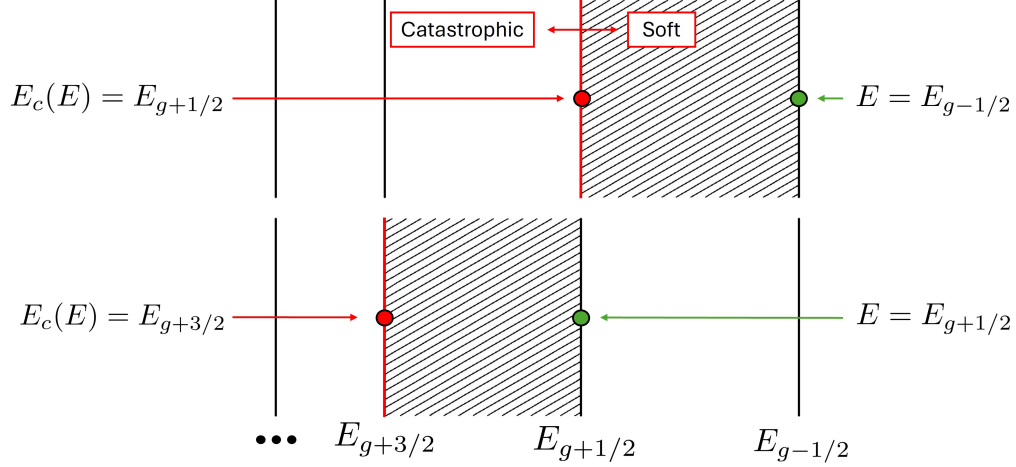


Figure 2.2 Definition of the soft and catastrophic interactions at energy group boundaries. The green dots represent the energy of the incident particle which interact with the medium, while the red dots correspond to the cutoff energies between soft and catastrophic energy domains. The cutoff energy corresponding to any incident particle energy anywhere in group  $g$ , or between  $E_{g-1/2}$  and  $E_{g+1/2}$ , is given by Eq. 2.26.

The energy separating the soft and catastrophic domains on the energy spectrum,  $E_c(E)$ , is a function of  $E$ , the incident particle in a given interaction. There are two limiting cases: 1) if  $E_c(E) = 0$ , the BFP reduces to the FP equation, and 2) if  $E_c(E) = E$ , it reduces to the Boltzmann transport equation. A choice can be made between these two limiting cases to fully use the potential of the BFP. In CEPXS, the catastrophic interactions are defined as the ones in which the particle in group  $g$  down-scatter into a non-adjacent energy group, with energy lower than  $E_{g+3/2}$ , while with soft interactions, the particle down-scatter in the adjacent energy group [16]. In other words, for  $E \in [E_{g-1/2}, E_{g+1/2}]$ , the energy  $E_c(E)$  is given by

$$E_c(E) = E_{g+3/2}. \quad (2.25)$$

This definition is problematic since it leads to ambiguous definitions of the soft stopping powers at group boundaries because the definition of the soft stopping power  $S_{g+1/2}^p$  differs whether it is viewed from the energy group  $g$  or  $g+1$ . Lorence et al. address this challenge by averaging these two definitions, which is somewhat arbitrary and lacks consistency with the BFP equation. This method produces numerical errors in the solution of the BFP equation, which are exacerbated with rough energy discretization. For example, the relative difference between the two stopping power definitions, in each group, range between 3% and 25% for impact ionization in aluminum, while it ranges between 72% and 862% for bremsstrahlung, with 80 logarithmically spaced energy groups between 1 keV and 10.58 MeV, and based on the

stopping powers defined later. A more robust definition can be proposed in order to solve such ambiguity. The definition of soft and catastrophic domains on the energy spectrum at group boundaries are shown in Fig. 2.2, where two points  $(E, E_c(E))$  are defined as  $(E_{g-1/2}, E_{g+1/2})$  and  $(E_{g+1/2}, E_{g+3/2})$  for any group  $g$ , with the additional definition  $E_{G+3/2} = 0$ . A smooth transition between these two coordinates is required and is set to be linear in  $E$ . The resulting energy dividing the soft and catastrophic domains, for  $E \in [E_{g-1/2}, E_{g+1/2}]$ , is given by

$$E_c(E) = \left( \frac{E_{g+1/2} - E_{g+3/2}}{E_{g-1/2} - E_{g+1/2}} \right) E - \frac{E_{g+1/2}^2 - E_{g-1/2}E_{g+3/2}}{E_{g-1/2} - E_{g+1/2}} \quad (2.26)$$

for any  $1 \leq g \leq G$ . This new definition solves the ambiguity of the definition of soft stopping powers, cancelling out the numerical issues it could generate.

## 2.4 Angular Discretization

Many methods have been developed to discretize the angular domain. For charged particle transport, which deals with strong anisotropy, there are three major methods:

1. **The discrete ordinates ( $S_N$ ) method:** The  $S_N$  method only enforces the transport equation along a discrete set of directions. This method is very flexible since it is easily extendable to multidimensional geometries, keeps the angular and spatial discretization separated, and is well-suited for parallelization in angle. It also leaves the spatial domain easily parallelizable [59] and can deal with highly anisotropic scattering. However it generates ray-effect with point sources in weakly diffusive media. This flaw is discussed in Sect. 2.4.3.
2. **The spherical harmonics ( $P_N$ ) method:** This  $P_N$  method consists of representing the flux as a truncated linear combination of spherical harmonics, substituting it in the transport equation, which is multiplied by the spherical harmonics and integrated over the whole angular domain [50]. It generates an intricate coupling between angular and spatial unknowns, which is ineffective in multidimensional (2D and 3D) geometries, albeit a simplified  $P_N$  ( $SP_N$ ) method exists that is useful for slightly anisotropic flux [60]. The SCEPTRE code, specialized in electron transport, contains different  $P_N$  methods [61] and does not exhibit ray effect like the  $S_N$  method.
3. **The discontinuous Galerkin finite-element method (DG-FEM):** The flux, expanded in space and angle using a polynomial basis, is substituted in the transport equation, multiplied by the basis function and integrated over a discretized space-angle

mesh. This method gives highly intricate space-angle relations, that depend on the discretization choice of the angular domain [24, 28, 29].

Since the  $S_N$  method is easily parallelizable, it is a significant argument to go with this method rather than the others to achieve the fast and accurate solution goal, required in RTP. As will be shown in this thesis, most of the flaws of the  $S_N$  method can be mitigated, even the infamous ray-effect issue.

### 2.4.1 Discrete ordinates method

The discrete ordinates or  $S_N$  method is one of the most efficient angular discretizations of the transport equation [62]. It is a discretization of the angular domain, the unit sphere  $\mathbb{S}^2$ , in  $N_d$  directions  $\mathbf{\Omega}_n$  with  $n = 1, N_d$ . Numerical quadratures are used to deal with integrals over  $\mathbb{S}^2$  using weights  $\omega_n$  associated with each direction  $\mathbf{\Omega}_n$ . Each of these weights can be conceived as the area of an angular mesh, or solid angle, over  $\mathbb{S}^2$ , with

$$\omega_n = \int_{\mathbf{\Omega}_n} d^2\Omega \quad (2.27)$$

such that the integration over the unit sphere gives the area of the unit sphere, i.e.

$$\int_{\mathbb{S}^2} d^2\Omega = \sum_{n=1}^{N_d} \int_{\mathbf{\Omega}_n} d^2\Omega = \sum_{n=1}^{N_d} \omega_n = 4\pi. \quad (2.28)$$

The angular flux along the  $\mathbf{\Omega}_n$  direction is given by  $\Psi_n = \Psi(\mathbf{\Omega}_n)$ . The  $S_N$  equation is obtained by enforcing the one-speed transport equation, in group  $g$ , to hold when evaluated at each direction  $\mathbf{\Omega} = \mathbf{\Omega}_n$  such as

$$\mathbf{\Omega}_n \cdot \nabla \Psi_{g,n}^p(\mathbf{r}) + \Sigma_{t,g}^p \Psi_{g,n}^p(\mathbf{r}) = Q_{p,g,n}^{\text{CSD}}(\mathbf{r}) + Q_{p,g,n}^{\text{AFP}}(\mathbf{r}) + Q_{p,g,n}^{\text{B}}(\mathbf{r}) + Q_{p,g,n}^{\text{ext}}(\mathbf{r}), \quad (2.29)$$

for  $n = 1, N_d$ . The AFP operator discretization is given in Chap. 4, while the energy-discretized CSD operator  $Q_{p,g,n}^{\text{CSD}}(\mathbf{r})$  is given in Chap. 5. The Boltzmann operator is given by

$$Q_{p,g,n}^{\text{B}}(\mathbf{r}) = \sum_{p' \in P} \sum_{g'=1}^{N_{g,p}} \sum_{q=1}^{N_q} \frac{2\ell_q + 1}{4\pi} \Sigma_{s,\ell_q,g' \rightarrow g}^{p' \rightarrow p}(\mathbf{r}) R_{\ell_q}^{m_q}(\mathbf{\Omega}_n) \Phi_{g',q}^{p'}(\mathbf{r}), \quad (2.30)$$

where the moments of the angular flux are given by

$$\Phi_{g',q}^p(\mathbf{r}) = \sum_{n=1}^{N_d} \omega_n R_{\ell_q}^{m_q}(\mathbf{\Omega}_n) \Psi_{g',n}^p(\mathbf{r}). \quad (2.31)$$

In a transport solver, it is inevitable to decompose the Boltzmann operator into three components to avoid costly recalculation. The elastic component ( $g' = g$  and  $p' = p$ )

$$Q_{p,g,n}^{\text{B,el}}(\mathbf{r}) = \sum_{q=1}^{N_q} \frac{2\ell_q + 1}{4\pi} \Sigma_{s,\ell_q,g \rightarrow g}^{p \rightarrow p}(\mathbf{r}) R_{\ell_q}^{m_q}(\boldsymbol{\Omega}_n) \Phi_{g,q}^p(\mathbf{r}), \quad (2.32)$$

also called within group scattering or self-scattering by the nuclear engineering community [50], has to be updated before each sweeping step until convergence of the one-speed transport equation in group  $g$ . The inelastic component ( $g' \neq g$  and  $p' = p$ )

$$Q_{p,g,n}^{\text{B,inel}}(\mathbf{r}) = \sum_{\substack{g'=1 \\ g' \neq g}}^{N_{g,p}} \sum_{q=1}^{N_q} \frac{2\ell_q + 1}{4\pi} \Sigma_{s,\ell_q,g' \rightarrow g}^{p \rightarrow p}(\mathbf{r}) R_{\ell_q}^{m_q}(\boldsymbol{\Omega}_n) \Phi_{g',q}^p(\mathbf{r}) \quad (2.33)$$

also called up- and down-scattering, has to be computed only once before solving each one-speed transport equation in the group  $g$ . The particle production component ( $p' \neq p$ )

$$Q_{p,g,n}^{\text{B,pp}}(\mathbf{r}) = \sum_{\substack{p' \in P \\ p' \neq p}} \sum_{g'=1}^{N_{g,p}} \sum_{q=1}^{N_q} \frac{2\ell_q + 1}{4\pi} \Sigma_{s,\ell_q,g' \rightarrow g}^{p' \rightarrow p}(\mathbf{r}) R_{\ell_q}^{m_q}(\boldsymbol{\Omega}_n) \Phi_{g',q}^{p'}(\mathbf{r}) \quad (2.34)$$

has to be calculated only once before solving the transport equation for a specific particle  $p$ . The Boltzmann operator is given by the sum of these components, i.e.

$$Q_{p,g,n}^{\text{B}}(\mathbf{r}) = Q_{p,g,n}^{\text{B,el}}(\mathbf{r}) + Q_{p,g,n}^{\text{B,inel}}(\mathbf{r}) + Q_{p,g,n}^{\text{B,pp}}(\mathbf{r}). \quad (2.35)$$

The discrete ordinates methods and their limits are further discussed in Sect. 4.2.

### 2.4.2 Fixed external sources

For radiotherapy applications, two kinds of fixed sources are of interest, namely 1) boundary monodirectional sources and 2) volume isotropic sources. On the one hand, with a combination of boundary monodirectional sources, it is possible to reconstruct the profile of external particle sources from the so-called phase space [63] of medical linear accelerator (LINAC) or radioisotope such as cobalt-60. On the other hand, volume isotropic sources can represent radioactive sources inside the patient, such as iodine-125 or cesium-137 [5].

## Boundary monodirectionnal sources

The definition of monodirectional for the discrete ordinates transport equation is not straightforward. Let  $V$  be the volume of the spatial domain, which is divided into orthogonal meshes along the Cartesian system axis. Let  $N_{\text{dim}} \in \{1, 2, 3\}$  be the geometry dimension. The boundary monodirectional sources will take the form

$$Q^{\text{ext}}(\mathbf{r}, \boldsymbol{\Omega}, E) = \mathcal{I} \delta(\boldsymbol{\Omega} - \boldsymbol{\Omega}_0) \delta(\mathbf{r}_a - \mathbf{r}_a^s) \quad (2.36)$$

for  $a \neq b \neq c$ , with  $s \in \{1, N_a\}$ , such as  $\mathbf{r}_a^1$  and  $\mathbf{r}_a^{N_a}$  corresponding to the leftmost and rightmost boundaries respectively along axis  $a$ , and

$$\begin{cases} a = x & \text{if } N_{\text{dim}} = 1 \\ a, b \in \{x, y\} & \text{if } N_{\text{dim}} = 2 \\ a, b, c \in \{x, y, z\} & \text{if } N_{\text{dim}} = 3 \end{cases} \quad (2.37)$$

and where

$$\begin{cases} \mathcal{I} = \mathcal{I}(E) & \text{if } N_{\text{dim}} = 1 \\ \mathcal{I} = \mathcal{I}(\mathbf{r}_b, E) & \text{if } N_{\text{dim}} = 2 \\ \mathcal{I} = \mathcal{I}(\mathbf{r}_b, \mathbf{r}_c, E) & \text{if } N_{\text{dim}} = 3 \end{cases} \quad (2.38)$$

$\mathcal{I}$  is the intensity [in  $\text{cm}^{1-N_{\text{dim}}\text{s}^{-1}}$ ] and  $\boldsymbol{\Omega}_0$  is the source particle direction. The main difficulty encountered is that the direction  $\boldsymbol{\Omega}_0$  may not be in the set of discrete direction  $\boldsymbol{\Omega}_n$  for  $n = 1, N_d$ , meaning that simply evaluating Eq. 2.36 will result in the absence of source in the discrete ordinates formulation. An inverse distance weighting is established, such as the source term is given by

$$Q^{\text{ext}}(\mathbf{r}, \boldsymbol{\Omega}, E) = \mathcal{I} \delta(\mathbf{r}_a - \mathbf{r}_a^s) \sum_{n=1}^N \mathcal{W}_n \delta(\boldsymbol{\Omega} - \boldsymbol{\Omega}_n), \quad (2.39)$$

where the inverse distance weight, normalized over the quadrature nodes such that the intensity is conserved, is given by

$$\mathcal{W}_n = \begin{cases} \frac{1}{\|\boldsymbol{\Omega}_0 - \boldsymbol{\Omega}_n\|^r \sum_{m=1}^m \omega_m \sum_{k=1}^N \frac{\delta(\boldsymbol{\Omega}_m - \boldsymbol{\Omega}_k)}{\|\boldsymbol{\Omega}_0 - \boldsymbol{\Omega}_k\|^r}} & \text{if } \boldsymbol{\Omega}_0 \notin \{\boldsymbol{\Omega}_n : n = 1, N_d\} \\ \delta(\boldsymbol{\Omega}_n - \boldsymbol{\Omega}_0) & \text{otherwise} \end{cases}, \quad (2.40)$$

where  $r \geq 2$  establishes the penalty strength to being far from the source direction  $\mathbf{\Omega}_0$ . In this research work,  $r = 3$  is chosen, to enforce a strong penalty for quadrature directions that are far from the given source particle direction. The discrete ordinates monodirectional source is therefore given by

$$Q_n^{\text{ext}}(\mathbf{r}, E) = \mathcal{W}_n \mathcal{I} \delta(\mathbf{r}_a - \mathbf{r}_a^s). \quad (2.41)$$

The discretized source is given by integrating this term over the corresponding energy group and voxel. In 1D Cartesian geometry ( $N_{\text{dim}} = 1$ ), the discretized monodirectional source is given by

$$Q_{n,g,i}^{\text{ext},s} = \begin{cases} \mathcal{W}_n \int_{E_{g+1/2}}^{E_{g-1/2}} dE \mathcal{I}(E) & \text{if } i = s \\ 0 & \text{otherwise} \end{cases}, \quad (2.42)$$

while for 2D Cartesian geometry ( $N_{\text{dim}} = 2$ ),

$$Q_{n,g,i,j}^{\text{ext},s} = \begin{cases} \mathcal{W}_n \int_{E_{g+1/2}}^{E_{g-1/2}} dE \int_{\mathbf{r}_{b,j-1/2}}^{\mathbf{r}_{b,j+1/2}} d\mathbf{r}_b \mathcal{I}(E, \mathbf{r}_b) & \text{if } i = s \\ 0 & \text{otherwise} \end{cases} \quad (2.43)$$

and in 3D Cartesian geometry ( $N_{\text{dim}} = 3$ ),

$$Q_{n,g,i,j,k}^{\text{ext},s} = \begin{cases} \mathcal{W}_n \int_{E_{g+1/2}}^{E_{g-1/2}} dE \int_{\mathbf{r}_{b,j-1/2}}^{\mathbf{r}_{b,j+1/2}} d\mathbf{r}_b \int_{\mathbf{r}_{c,k-1/2}}^{\mathbf{r}_{c,k+1/2}} d\mathbf{r}_c \mathcal{I}(E, \mathbf{r}_b, \mathbf{r}_c) & \text{if } i = s \\ 0 & \text{otherwise} \end{cases}. \quad (2.44)$$

This source is added to the transport equation as boundary conditions.

### Volume isotropic sources

A volume isotropic sources will take the form

$$Q^{\text{ext}}(\mathbf{r}, \mathbf{\Omega}, E) = \mathcal{I}(\mathbf{r}, E), \quad (2.45)$$

where  $\mathcal{I}(\mathbf{r}, E)$  is the intensity [in  $\text{cm}^{-N_{\text{dim}}} \text{s}^{-1}$ ], where  $N_{\text{dim}}$  is the geometry dimension. The Legendre moments of the isotropic sources are given by

$$Q_\ell^{\text{ext}}(\mathbf{r}, E) = \begin{cases} \mathcal{I}(\mathbf{r}, E) & \ell = 0 \\ 0 & \text{otherwise} \end{cases} \quad (2.46)$$

and the discretized form is given by integrating space and energy. This term is added to the transport equation as a source term.

### 2.4.3 Ray effects

An important flaw of the discrete ordinates method is the ray effect [64]. Since the  $S_N$  method only enforces the fulfillment of the transport equation along a discrete set of directions, it forces the radiation to travel along these directions. Without significant scattering in the medium, the flux remains aligned with the discrete directions. The ray effect manifests on the solution as artificial streaks along the discrete directions, deteriorating the accuracy of the local solutions. The most straightforward way to address this issue is to increase the quadrature order, but it is computationally expansive and still produces numerical artifacts [50]. While there are finite-element methods for angular discretization, it results in intricate coupling of the angular and spatial variables in a dense system of equations, which becomes very expensive to solve [28]. There is an incentive to keep the discrete ordinates formalism for efficiency and to develop ray effect mitigation compatible with that approach.

An important ray effect mitigation technique is the first collision source (FCS) method, which divides the flux into uncollided and collided components [65]. Since the uncollided flux is often the dominant source of ray effect and the uncollided flux equation is less complicated than the full transport equation, the uncollided flux can be computed using methods that do not produce or produce less ray effect, such as ray tracing, low-order  $S_N$  or  $P_N$  methods [66]. The uncollided flux solution can then be used as a source in the collided flux equation, which is solved using the discrete ordinates method. For the BFP equation, the uncollided equation includes the CSD operator, which requires ray tracing through not only space but through space and energy domain [67–69]. Additional preoccupations can arise with FCS methods, such as ensuring that ray tracing remains conservative [70], ensuring compatibility with unstructured meshes [71], dealing with different kinds of sources, such as omnidirectional boundary and isotropic sources, and keeping computational time reasonable. Other ray effects mitigation has been proposed, such as adding a quadrature rotation step [72] or an artificial source [73], for example.

Despite all these efforts, ray effect mitigation remains a significant challenge. In RTP, electron transport solutions do not suffer much from the ray effect since electrons scatter a lot, but photons travel long distances before interacting with the medium and, therefore, notably suffer from it. While this issue is not addressed in this work, ray mitigation techniques will be required to efficiently treat external photon beams and brachytherapy’s localized isotropic sources.



## 2.5 Spatial Discretization

The most straightforward spatial discretization is obtained by dividing the spatial domain into voxels, which are 3D box meshes defined on a Cartesian grid. A good deal of research work resort to unstructured meshes [7, 74], because that kind of meshes offer greater flexibility to fit interface boundaries, such as the skin surface and the air, and it can ensure thinner discretization is a critical subpart of the spatial domain without needlessly over-discretizing another part of the domain, contrary to structured geometries. However, they complicate the sweeping and parallelization procedures, whereas these procedure are straightforward to implement in Cartesian geometry. Moreover, since a typical CT scan generates a 3D Cartesian grid of  $128^3$  voxels, whose size varies from 0.5 to 1.5 mm, there is already a bias toward a Cartesian representation in imaging. Therefore, in this work, the spatial domain is assumed to be discretized along Cartesian coordinates.

The spatial domain along an axis  $x$  ( $y$  or  $z$ ) is divided in  $N_x$  ( $N_y$  or  $N_z$ ) mesh. The midpoint of the mesh  $i$  ( $j$  or  $k$ ) is  $x_i$  ( $y_j$  or  $z_k$ ), its width is  $\Delta x_i$  ( $\Delta y_j$  or  $\Delta z_k$ ), and its upper and lower boundaries are respectively  $x_{i-1/2}$  ( $y_{j-1/2}$  or  $z_{k-1/2}$ ) and  $x_{i+1/2}$  ( $y_{j+1/2}$  or  $z_{k+1/2}$ ), as shown in Fig. 2.3. The transport equation is then discretized using the Galerkin method of weighted residuals, which development is continued in Chap. 5.

## 2.6 Resolution of the Coupled Photon-Electron-Positron Transport Equations

The resolution of the coupled system of three BFP equations, one per particle, is done by solving the transport equation individually for each particle. By obtaining the flux solution for a particle, it can be used to compute the production of the other two particles based on the corresponding scattering cross-sections (see Chap. 3). The resulting source term is then added to the following particle equation. This iterative loop between particle can be continued until convergence or a predetermined number of generations  $N_{\text{gen}}$ . For a given particle, the cumulative flux solution is given by the sum of the  $N_{\text{gen}}$  flux solution of that

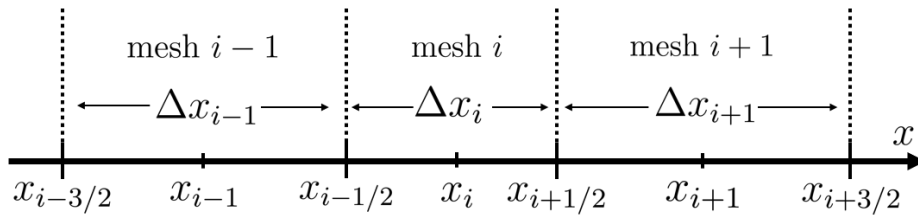


Figure 2.3 Spatial discretization.

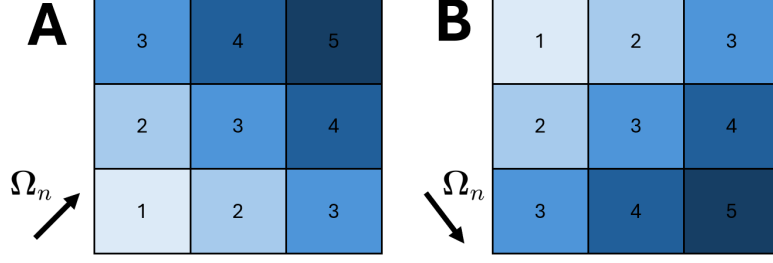


Figure 2.4 Sweeping process assuming A)  $\mu > 0$  and  $\eta > 0$  and B)  $\mu > 0$  and  $\eta < 0$ . The numbers indicate the order in which calculations can take place.

particle. It should be noted that fixed sources for a given particle are used only the first time the BFP is solved for that specific particle.

The BFP has to be solved for each particle. Neither the electron, the positron, nor the photon has an upscattering interaction; they encounter no interaction in which the particle itself acquires energy. Therefore, the multigroup transport equation is solved by sweeping for the highest energy group,  $g = 1$ , to the lowest energy group only once. In each group, the transport equation is solved by Source Iteration (SI). The angular flux is computed along each direction  $\Omega_n$  by sweeping through the domain from the geometry side to the other following the direction of  $\Omega_n$ , as shown in Fig. 2.4. The source terms are then actualized for subsequent sweeping and so on. The sweeping procedure is repeated until the convergence of the angular flux. The speed of convergence is given by the spectral radius  $\rho$ , which can be estimated by [47]

$$\rho = \lim_{\ell \rightarrow \infty} \frac{\|\Psi^{(\ell)} - \Psi^{(\ell-1)}\|}{\|\Psi^{(\ell-1)} - \Psi^{(\ell-2)}\|}, \quad (2.47)$$

where  $\ell$  is the iteration index. A spectral radius  $\rho \ll 1$  is associated with fast convergence, which slows as  $\rho$  approach one and if  $\rho \geq 1$ , then the SI process do not converge. A Fourier analysis shows that the spectral radius of the SI is given by the ratio of the elastic scattering cross-section to the total cross-section [47]. Therefore, the more elastic scattering is the dominant process over absorption and out-of-group scattering, the slower the convergence. As shown in Chap. 3, the electron and positron elastic interactions are very dominant, and calculations can become extremely slow. Many methods have been developed to accelerate the convergence. The most important one for electron and positron is the transport correction, given in Sect. 3.5.3, which reduces the magnitude of elastic cross-sections while leaving the solution intact [17]. The diffusion synthetic acceleration (DSA) method is a well-known and widely used method to reduce the number of iterations until convergence [75]. Unfortunately, the DSA method becomes ineffective for highly anisotropic forward-peaked scattering. Morel

and Manteuffel have developed an acceleration method that reduces the scattering ratio to 0.6 in the Fokker-Planck scattering limit for 1D geometries [76], but an extension of this method to multidimensional geometries was inconclusive [47]. Livolant acceleration, based on the minimization of residuals, was used in this thesis to accelerate the iterative process [50]. Krylov subspace methods like Generalized minimal residual (GMRES) and its low-memory form GMRES(m) can be very efficient and stable techniques to accelerate convergence. While they were not used in this work, Krylov's methods are powerful tools to reduce drastically the number of iterations for convergence.

The discrete ordinates method produces an inherently parallel problem since the calculation along each direction can be performed simultaneously without interference. The sweeping procedure can be further accelerated in 2D and 3D Cartesian geometries. As shown in Fig. 2.4, meshes that share the same number can be performed simultaneously since they only depend on previous mesh information. Therefore, the sweeping procedure can be performed along waves using the Koch-Baker-Alcouffe (KBA) method [59,77–79]. These calculations can be distributed to multiples Central Processing Unit (CPU) or Graphic Processing Unit (GPU) threads, or both, on a personal laptop or distributed over several computers. The KBA procedure has to be optimized for each of these choices to account for communication delay between threads, which is far from being trivial [80]. Parallelization methods will be essential to achieving highly efficient dose calculation solvers.

## 2.7 Energy Deposition

The solution of the BFP for each particle  $p$ , in each voxel  $j$  of volume  $V_j$  and in each energy group  $g$  is given by the integrated flux  $\Psi_{g,j}^p$ . Such integrated fluxes can be used to compute reaction rates such as energy deposition or charge deposition. The volume  $V_j$  is given in  $\text{cm}^{N_{\text{dim}}}$ , with  $N_{\text{dim}}$  is the geometry dimension. The total energy deposition in voxel  $j$ , in  $\text{m}_e c^2/\text{g} \times \text{cm}^{3-N_{\text{dim}}}$ , is given by [16,81]

$$D_j = \frac{1}{\rho V_j} \sum_{p \in P} \left\{ \sum_{g=1}^G \Sigma_{e,g,j}^p \Psi_{g,j}^p + \Sigma_{e,G+1,j}^p \Psi_{G+1/2,j}^p \right\} \quad \text{with} \quad \Sigma_{e,g,j}^p = \sum_x \Sigma_{e,g,j}^{p,x}, \quad (2.48)$$

where  $\rho$  is the medium density in  $\text{g}/\text{cm}^3$ .  $\Psi_{G+1/2,j}^p$  is the flux evaluated at the cutoff energy  $E_{G+1/2}$ , which is computed using an energy closure relation as defined in Chap. 5. The first term of the total energy deposition formula correspond to the net energy deposited in each energy group, while the second term is required with the BFP equation, due to the CSD operator, to take into account particle slowing-down to the energy cutoff [81]. The energy

deposition cross-sections,  $\Sigma_{e,g,j}^p$ , is the sum of the  $\Sigma_{e,g,j}^{p,x}$  for each interaction  $x$  in energy group  $g$  for incident particle  $p$ . The energy deposition cross-sections for a given interaction  $x$ , which characterize the net energy gain or loss following that interaction, is given by

$$\begin{aligned} \Sigma_{e,g}^{p,x} = & S_g^{p,x} + \frac{1}{\Delta E_g} \int_{E_{g+1/2}}^{E_{g-1/2}} dE \left\{ (E - \Delta Q_x) \Sigma_t^{p,x}(E) \right. \\ & \left. - \sum_{p' \in P} \left[ \int_{E_{G+1/2}}^E dE' E' \Sigma_{s,0}^{p \rightarrow p',x}(E \rightarrow E') \right] - \Sigma_{uc}^{p,x}(E) \right\}, \end{aligned} \quad (2.49)$$

for  $1 \leq g \leq G$ . It encompasses the CSD energy-loss in the group, the kinetic energy of the interaction's incident particle in the group, the kinetic energy of the particle leaving the interaction, and the variation of rest mass energy of the nucleus and the elementary particle, given by  $\Delta Q_x$  ( $\Delta Q_x > 0$  for increase in mass,  $\Delta Q_x < 0$ , for a decrease in mass) [13]. For example, the pair production interaction causes an electron and a positron to appear, which correspond to  $\Delta Q_x = 2 m_e c^2$ . Conversely, the annihilation interaction makes the incoming positron and an atomic electron to disappear, resulting in a decrease of mass of  $\Delta Q_x = -2 m_e c^2$ . In interaction such as Compton or elastic scattering, no change of mass occurs, i.e.  $\Delta Q_x = 0$ . The last term,  $\Sigma_{uc}^{p,x}(E)$ , corresponds to the particle production from processes occurring under the cutoff energy, which is restricted to positron annihilation in this work. Physically, positrons always end up annihilating by producing two photons. Three interactions can scatter or produce positrons under the energy cutoff  $E_{G+1/2}$ , following either 1) catastrophic impact ionization positron interactions, 2) catastrophic positron-induced Bremsstrahlung interactions, or 3) following pair production. To take the annihilation of these positrons, which scatter under the cutoff, into account, the following contribution,

$$\Sigma_{uc}^{p,x}(E) = \int_0^{E_{G+1/2}} dE' (\Delta Q' + \Delta Q_x + E') \Sigma_{s,0}^{p \rightarrow p',x'}(E \rightarrow E'), \quad (2.50)$$

should be added to the energy deposition, with  $p' = \gamma$  and  $\Delta Q' = -2 m_e c^2$ , corresponding respectively to the annihilation photon and to the loss of rest mass energy in annihilation. The annihilation cross-sections under the cutoff energy are given in Sect. 3.7.4. There is another contribution to energy deposition with the BFP equation due to soft interaction, which causes particles to slow-down until it reaches the cutoff, where they are absorbed locally. The energy deposition cross-sections at the cutoff energy is given by [2, 81]

$$\Sigma_{e,G+1}^{p,x} = E_{G+1/2} \frac{S_{G+1/2,j}^p}{\Delta E_G}, \quad (2.51)$$

where  $S_{G+1/2,j}^p$  is the soft stopping power at the cutoff energy.

## 2.8 Charge Deposition

The total charge deposition in voxel  $j$ , in  $\text{cm}^{3-N_{\text{dim}}}/\text{g}$ , is given by [2, 16]

$$C_j = \frac{1}{\rho V_j} \sum_{p \in P} \left\{ \sum_{g=1}^G \Sigma_{c,g,j}^p \Psi_{g,j}^p + \Sigma_{c,G+1,j}^p \Psi_{G+1/2,j}^p \right\} \quad \text{with} \quad \Sigma_{c,g,j}^p = \sum_x \Sigma_{c,g,j}^{p,x}, \quad (2.52)$$

where the charge deposition cross-sections for a given interaction  $x$  is given by

$$\Sigma_{c,g}^{p,x} = -\frac{1}{\Delta E_g} \int_{E_{g+1/2}}^{E_{g-1/2}} dE \left\{ q_p \Sigma_t^{p,x}(E) - \sum_{p' \in P} \delta_x q_{p'} \left[ \int_{E_{G+1/2}}^E dE' \Sigma_{s,0}^{p \rightarrow p',x}(E \rightarrow E') \right] \right\} \quad (2.53)$$

for  $1 \leq g \leq G$ , where  $q_p$  is the particle charge given by

$$q_p = \begin{cases} -1 & \text{if } p = \text{e}^- \\ 0 & \text{if } p = \gamma \\ 1 & \text{if } p = \text{e}^+ \end{cases} \quad (2.54)$$

and where  $\delta_x$  is a parameter to account for particle that are neither extracted from the medium nor deposited in it. For pair production, it is given by  $\delta_x = 0$  since the electron-positron pair does not change the net charge of the medium. Otherwise,  $\delta_x = 1$ . As for dose deposition, there is a charge deposition component at the cutoff energy due to soft interaction. The charge deposition cross-sections at the cutoff energy is given by [2]

$$\Sigma_{c,G+1}^{p,x} = -q_p \frac{S_{G+1/2,j}^p}{\Delta E_G}. \quad (2.55)$$

## CHAPTER 3    COUPLED PHOTON, ELECTRON AND POSITRON MULTIGROUP CROSS-SECTIONS

### 3.1 Foreword

The main motivation in this chapter is to close the gap between deterministic and Monte Carlo physics models. Coupled photon-electron-positron multigroup cross-section models compatible with the BFP equation are developed based on 9 interaction kinds, namely impact ionization, elastic scattering of leptons, bremsstrahlung, annihilation, Rayleigh scattering, Compton scattering, photoelectric effect, pair production and relaxation cascades. This work led to the development of RADIANT, an open-source alternative to CEPXS for deterministic coupled photon-electron cross-sections. A comparative study is conducted between RADIANT and Monte Carlo calculation results, consisting of energy deposition and energy spectrum per particle species at varying depths.

My original contributions to cross-section production include the introduction of updated models that advance beyond the state-of-the-art CEPXS code, as well as the explicit incorporation of positron cross-sections. I have also introduced novel methodologies, such as the efficient analytic integration of elastic scattering Legendre moments and improved energy deposition cross-section calculation. Additionally, I have developed a new open-source code, RADIANT, capable of generating comprehensive photon-electron-positron cross-section libraries. The developments discussed in this section, along with the innovations presented in the preceding section, have been submitted to the Journal of Computational Physics on May 1<sup>st</sup>, 2024 [82]. The manuscript has undergone peer review and is currently under revision (major revisions required). I have also contributed to a peer-reviewed Scientific Reports paper on pure high-energy electron determinist cross-section library validation [37].

Sect. 3.2 presents the particle species present during conventional radiotherapy treatment. Sect. 3.3 establishes some definitions for the upcoming sections. Sect. 3.4 to 3.12 describes the 9 interaction kinds and their multigroup models. In Sect. 3.13, the atomic models of the previous section are consolidated. Sect. 3.14 proposes a comparison of the solutions of the BFP equation using these cross-sections to the reference Monte Carlo ones and discuss its findings. Sect. 3.15 concludes the chapter by looking at perspectives.

### 3.2 Ionizing Radiation in Radiotherapy Treatment

The goal of radiotherapy is to use the properties of ionizing radiation to deliver energy to tumorous cells to kill them, either directly or through the production of highly reactive, thus damaging, free radicals [13]. This ionizing radiation usually takes the form of subatomic particles such as photons, electrons, protons or ions. The range of energies for conventional radiation therapy, which relies on photons or electron sources, scales from 10 keV to 25 MeV [13]. Nonetheless, this range will likely expand in the following decades to encompass very-high energy electron beams (50 MeV to 300 MeV) and ultra-high energy electron beams (300 MeV - few GeV) [37]. These energetic electrons can treat deep-seated tumours as demonstrated in many publications [83–85]. On the other end of the spectrum, researchers are pushing to improve understanding of microdosimetry under 10 keV. GEANT4-DNA, for example, is a project to develop a simulation of low-energy ionizing radiation, down to a few eV, and of the radiation-induced DNA damage [86]. Evaluating the impact of low doses can help assess its health effects. To this day, radiation protection for these low energy deposition events is based on extrapolation of epidemiology data assuming no threshold [87]. Such an approach implies that any dose poses a risk, and caution is always required. This hypothesis is still controversial to this day since it can lead people to avoid medical imaging, therefore missing cancer detection due to radiophobia [88]. Under the muons pair production threshold of 211 MeV [89], in a medium exempt from fissile atoms, only three particles are of interest using either photons or electrons sources: photons, electrons and positrons. Therefore, this section proposes models of interactions of these three particles with matter over energies ranging from 1 keV to 211 MeV, compatible with the multigroup BFP equation. This thesis does not evaluate the validity of the models for transport calculations over 211 MeV, neglecting muons production.

Photons are massless and uncharged particles carrying electromagnetic energy. The ones that possess enough energy to ionize matter are often called X-rays and gamma-rays. In the defined energy range, these ionizing photons can have 4 dominant interactions: Rayleigh scattering, Compton scattering, photoelectric effect and pair production. The photoelectric effect is the dominant effect for low energies up to hundreds of keV; the Compton interaction dominates at intermediate energies between hundreds of keV and about 10 MeV, while the pair production is the most important interaction at higher energies. Due to their lack of charge, photons pass through matter without interacting much, making them particularly useful for penetrative radiotherapy treatment. The energy lost during either Compton or photoelectric interaction is almost totally transferred to an atomic electron, becoming a new receptacle to transport energy in the medium. Extracting an inner-shell atomic electron can

trigger relaxation cascades that produce more ionizing radiation, namely fluorescence and Auger electrons. When a pair production interaction occurs, the photon energy is transferred to the newly produced electron and positron.

Electrons, the negatively charged particles with mass, play a significant role in energy transport. The total energy they carry is a combination of their kinetic energy and mass. In the defined energy range, electrons interact with matter in three major ways: elastic scattering, impact ionization, and bremsstrahlung. Impact ionization is the dominant energy-loss process up to about 10 MeV, while bremsstrahlung production takes over at high energies. Elastic interaction, unlike photons, is a dominant phenomenon. As discussed in the previous chapter, electrons lose their energy either following the CSD approximation or in catastrophic large energy-loss events. The CSD approximation is used for both impact ionization and bremsstrahlung interaction. In a catastrophic impact ionization event, almost all the kinetic energy lost by the incoming electron is transferred to an ionized atomic electron. Such interaction can also trigger relaxation cascades, producing fluorescence and Auger electrons. In catastrophic bremsstrahlung interactions, a significant part of the electron's energy is transferred to a bremsstrahlung photon.

Positrons, the positively charged particles that share the same mass as their antiparticles, the electrons, have a unique fate. In the defined energy range, they interact with matter in four major ways: elastic scattering, impact ionization, bremsstrahlung interaction, and annihilation. While positron elastic, impact ionization, and bremsstrahlung interactions share many similarities with their electron counterparts, positrons are the only ones that always end up annihilating with an atomic electron into two photons. This annihilation process becomes inevitable as the kinetic energy of the positron approaches zero. The relevance of positron transport is only significant if photons of 1.022 MeV or more are present, which is the threshold for pair production.

### 3.3 Definitions

A few constants, variables, units, and parameters, which will be used in the following sections, need to be defined. In this chapter, the energies are given in reduced electron energy (in  $m_e c^2$ ), where  $m_e c^2 \approx 0.510999$  MeV is the electron rest energy, the length unit is the centimetre (cm), and the unit of mass is the gram (g) unless noted otherwise. The classical electron radius is given by  $r_e \approx 2.81794 \times 10^{-13}$  cm. The ratio of the particle velocity on the speed of



light and the Lorentz factor are respectively given by

$$\beta^2 = \frac{E(E+2)}{(E+1)^2} \quad \text{and} \quad \gamma = E+1. \quad (3.1)$$

The Avogadro constant is given by  $N_a \approx 6.022094 \times 10^{23}$  u/g, where u is the atomic mass unit. The following section's atomic data calculations apply to any compound material of  $N_e$  constituent elements. The density of a monoelemental material is given by

$$\mathcal{N}_{n,i} = \frac{\rho N_a}{A_i}, \quad (3.2)$$

where  $i$  is the element atomic number,  $\rho$  is the compound density (in g/cm<sup>3</sup>) and  $A_i$  is the atomic weight (in u) of the  $i^{\text{th}}$ -element of the compound. The weight fraction of the  $i^{\text{th}}$ -element of a compound is given by  $f_i$ , which can be used to compute the density of the  $i^{\text{th}}$ -element in that compound, given by  $f_i \mathcal{N}_{n,i}$ .

The function  $\mathcal{H}_b$  is introduced to simplify the notation of integrals greatly. This special function, which can be defined only inside an integral, acts as a Heaviside function on the difference between upper and lower integral bounds, i.e.

$$\int_a^b dx f(x) \mathcal{H}_b \equiv \int_a^b dx f(x) H(b-a), \quad (3.3)$$

where  $H(x)$  is the Heaviside function such as

$$H(x) = \begin{cases} 1 & x \geq 0 \\ 0 & \text{otherwise} \end{cases}. \quad (3.4)$$

Many tables are used to generate multigroup atomic data. Any interpolation over these tables is done using the monotone cubic Hermite spline interpolation from Fritsch and Carlson [90].

### 3.4 Impact Ionization

When travelling through the medium, an electron or a positron ionizes atomic electrons in impact ionization. When an inner-shell electron is ionized, a relaxation cascade is initiated (see Sect. 3.12). A schematic representation of this interaction is presented in Fig. 3.1. This interaction is the dominant energy-loss phenomenon up to a few MeV for electrons and positrons [91]. In CEPXS, the Møller cross-section, assuming unbounded atomic electrons, describes the inelastic interactions of incoming electrons [16, 92]. In medical physics,

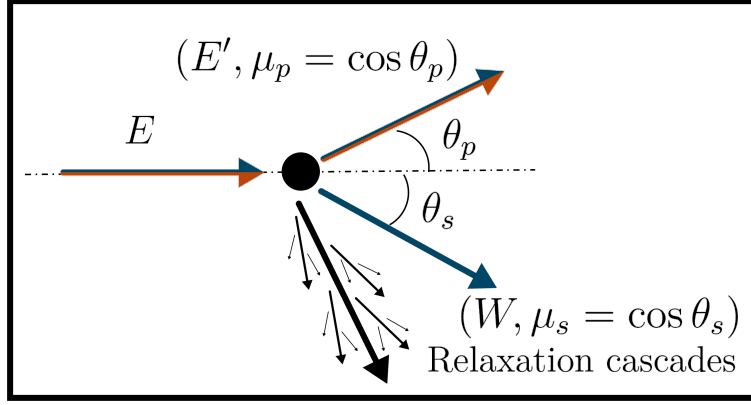


Figure 3.1 Impact ionization by incoming electrons (in blue) or positrons (in orange).

an inelastic interaction is a collision where the particle loses energy, which differ from the definition in [50]. While adequate for low- $Z$  medium and fast incoming electrons, such an approximation fails when the incoming electron energy is not significantly greater than the electron binding energy, which can be really important for inner subshells of high- $Z$  material. For example, the  $K$  subshell of gold ( $Z = 79$ ) has a binding energy of 80.96 keV [93], an energy greater than usual energy cutoffs in both Monte Carlo and determinist transport codes. The Møller cross-section diverges as the energy-loss approach zero, dealt with in CEPXS by dividing the domain into soft and catastrophic components and employing an alternate model for soft interactions. This alternate models consist of tabulated stopping powers values from Bethe theory [94], to which the semi-empirical density correction from Sternheimer [95] and an empirical low-energy correction under 10 keV are applied (see [16]). The atomic relaxation from the inelastic collision is taken into account using subshell-dependant impact ionization models, such as Kolbenstvedt [96], or Gryzinski [97] models, which means that impact ionization and its relaxation are uncorrelated in CEPXS. In this thesis, the BFP formalism is also used to treat impact ionization. The catastrophic cross-sections are defined by subshell-dependant Møller [92] and Bhabha [98] models, for electrons and positrons respectively, based on models developed by Seltzer [99,100] and Salvat et al. [91,101]. The soft stopping powers are developed based on the state-of-the-art stopping power models of Salvat and Andreo [102]. The following models represent an advancement over CEPXS by accounting for subshell-dependent catastrophic cross-sections essential for high- $Z$  material transport. In contrast to CEPXS, which only offers electron models, the proposed models also include explicit positron cross-sections and stopping powers. These models utilize cutting-edge stopping powers, incorporating shell correction and an analytic form of the Fermi density effect, thereby replacing the semi-empirical methods used in CEPXS. Additionally, atomic relaxation is directly linked to the inelastic cross-sections. The new soft and catastrophic domain

definition, presented in Sect. 2.3.3, is applied.

### 3.4.1 Catastrophic inelastic cross-section

The total inelastic cross-section describes the interaction of an incoming electron ( $p' = \mathbf{e}-$ ) or positron ( $p' = \mathbf{e}+$ ) with an atomic electron. Such interaction results in the scattering of the incoming particle ( $p' = \mathbf{e}-$  or  $p' = \mathbf{e}+$ ) and the production of knock-on electrons ( $p' = \mathbf{e}-$ ). The impact ionization is the sum of three components: the close collisions, the distance collisions and a density effect term [100]. Distance collisions consist of the interaction of the incident electron or positron perturbing field, which can ionize atomic electrons and be interpreted as virtual photons producing photoionization [99]. Since catastrophic collisions do not deal with small energy losses and distant collisions result in such energy transfer, they are neglected in the catastrophic cross-section model [103]. The density effect component accounts for the material dielectric polarization and can also be neglected in catastrophic cross-sections since by inspection, the corresponding Scofield cross-section [100,104] is important only when small energy losses occur.

The collisional inelastic differential cross-section in energy of the knock-on electron in a monoelemental material  $i$  is given by the sum of the differential cross-section per electron subshell  $k$  [16,43,105]

$$\sigma_s^i(E \rightarrow W) = \sum_{k=1}^{N_{\text{shells}}} Z_{i,k} \sigma_s^{i,k}(E \rightarrow W), \quad (3.5)$$

where  $Z_{i,k}$  is the mean number of electrons in subshells  $k$  for element  $i$ ,  $E$  is the incoming electron or positron energy,  $E'$  is the scattered electron or positron energy and  $W = E - U_{i,k} - E'$  is the knock-on electron energy, where  $U_{i,k}$  is the binding energy of the  $k^{\text{th}}$  subshell. The values of  $Z_{i,k}$  and  $U_{i,k}$  are extracted from the Evaluated Atomic Data Library (EADL) [93]. The close interaction cross-section is given by

$$\sigma_s^{i,k}(E \rightarrow W) = \frac{2\pi r_e^2}{\beta^2} F_{i,k}^{\pm}(E, W), \quad (3.6)$$

where the subshell-dependant Møller factor, for electrons, is given by [92,99]

$$F_{i,k}^-(E, W) = \frac{1}{(W + U_{i,k})^2} + \frac{1}{(E - W)^2} + \frac{1}{(E + 1)^2} - \frac{(2E + 1)}{(E + 1)^2(E - W)(W + U_{i,k})} \quad (3.7)$$

and the subshell-dependant Bhabha factor, for positrons, is given by [98]

$$F_{i,k}^+(E, W) = \frac{1}{(W + U_{i,k})^2} \left[ 1 - b_1 \left( \frac{W + U_{i,k}}{E} \right) + b_2 \left( \frac{W + U_{i,k}}{E} \right)^2 - b_3 \left( \frac{W + U_{i,k}}{E} \right)^3 + b_4 \left( \frac{W + U_{i,k}}{E} \right)^4 \right], \quad (3.8)$$

with

$$b_1 = \left( \frac{\gamma - 1}{\gamma} \right)^2 \frac{2(\gamma + 1)^2 - 1}{\gamma^2 - 1}, \quad b_2 = \left( \frac{\gamma - 1}{\gamma} \right)^2 \frac{3(\gamma + 1)^2 + 1}{(\gamma + 1)^2}, \quad (3.9)$$

$$b_3 = \left( \frac{\gamma - 1}{\gamma} \right)^2 \frac{2\gamma(\gamma - 1)}{(\gamma + 1)^2}, \quad b_4 = \left( \frac{\gamma - 1}{\gamma} \right)^2 \frac{(\gamma - 1)^2}{(\gamma + 1)^2}.$$

The scattering angles for the incoming particle and knock-on electron are respectively [16]

$$\mu_p = \sqrt{\frac{E'(E + 2)}{E(E' + 2)}} \quad \text{and} \quad \mu_s = \sqrt{\frac{W(E + 2)}{E(W + 2)}}, \quad (3.10)$$

and their double differential cross-sections are respectively given by

$$\sigma_s(E \rightarrow E', \mu) = \frac{1}{2\pi} \sigma_s(E \rightarrow E') \delta(\mu - \mu_p) \quad (3.11)$$

and

$$\sigma_s(E \rightarrow W, \mu) = \frac{1}{2\pi} \sigma_s(E \rightarrow W) \delta(\mu - \mu_s). \quad (3.12)$$

The maximum energy of knock-on for incoming electron and positron, which results from classical kinematics and the indistinguishability of electrons, are given respectively by

$$W_{\max}^- = \frac{E - U_{i,k}}{2} \quad \text{and} \quad W_{\max}^+ = E - U_{i,k}. \quad (3.13)$$

### Scattering cross-sections for incoming electrons or positrons

The Legendre moments of the differential scattering cross-sections are given by

$$\sigma_{s,\ell}^{i,k}(E \rightarrow E') = 2\pi \int_{-1}^1 d\mu P_\ell(\mu) \sigma_s^{i,k}(E \rightarrow E', \mu) = P_\ell(\mu_p) \sigma_s^{i,k}(E \rightarrow E'). \quad (3.14)$$

The macroscopic Legendre moments of the scattering cross-sections for particle scattering from group  $g'$  are therefore given by

$$\Sigma_{s,\ell,g'}^{\mathbf{e}\pm\rightarrow\mathbf{e}\pm}(E) = \sum_{i=1}^{N_e} \mathcal{N}_{n,i} f_i \sum_{k=1}^{N_{\text{shells}}} Z_{i,k} \int_{\max\{E'_{g+1/2}, W_{\max}^{\pm}\}}^{\min\{E'_{g-1/2}, E_c(E), E-U_{i,k}\}} dE' \sigma_{s,\ell}^{i,k}(E \rightarrow E') \mathcal{H}_b, \quad (3.15)$$

where  $E_c(E)$  is given by Eq 2.26. This equation is evaluated using numerical quadrature.

### Scattering cross-sections for knock-on electrons

The Legendre moments of the differential scattering cross-sections are given by

$$\sigma_{s,\ell}^{i,k}(E \rightarrow W) = 2\pi \int_{-1}^1 d\mu P_\ell(\mu) \sigma_s^{i,k}(E \rightarrow W, \mu) = P_\ell(\mu_s) \sigma_s^{i,k}(E \rightarrow W). \quad (3.16)$$

The multigroup Legendre moments of the scattering cross-sections are therefore given by

$$\Sigma_{s,\ell,g'}^{\mathbf{e}\pm\rightarrow\mathbf{e}^-}(E) = \sum_{i=1}^{N_e} \mathcal{N}_{n,i} f_i \sum_{k=1}^{N_{\text{shells}}} Z_{i,k} \int_{E'_{g+1/2}}^{\min\{E'_{g-1/2}, W_{\max}^{\pm}\}} dW \sigma_{s,\ell}^{i,k}(E \rightarrow W) \mathcal{H}_b. \quad (3.17)$$

This equation is integrated using numerical quadrature.

### Catastrophic total cross-sections

The catastrophic inelastic total cross-sections are defined by

$$\Sigma_t^{\mathbf{e}\pm}(E) = \sum_{i=1}^{N_e} \mathcal{N}_{n,i} f_i \sum_{k=1}^{N_{\text{shells}}} Z_{i,k} \int_{E-E_c(E)}^{W_{\max}^{\pm}} dW \sigma_{s,0}^{i,k}(E \rightarrow W) \mathcal{H}_b, \quad (3.18)$$

which is evaluated analytically.

### Absorption cross-sections for incoming positrons

The inelastic catastrophic absorption cross-sections for inelastic interaction with incoming positrons, which include both soft and catastrophic contributions and are required for annihilation calculations, are given by

$$\Sigma_a^{\text{inel}}(E) = \sum_{i=1}^{N_e} \mathcal{N}_{n,i} f_i \sum_{k=1}^{N_{\text{shells}}} Z_{i,k} \int_{E-\min\{E_{G+1/2}, E_c\}}^{W_{\max}^+} dW \sigma_{s,0}^{i,k}(E \rightarrow W) \mathcal{H}_b, \quad (3.19)$$

which is evaluated analytically.

### 3.4.2 Soft stopping power

#### Total stopping power

The total collisional stopping powers of electron and positron for any compound, in  $m_e c^2 \times \text{cm}^{-1}$ , are given by the density- and shell-corrected Bethe formula [106]

$$S_t(E) = \frac{2\pi r_e^2}{\beta^2} \mathcal{N}_e^{\text{eff}} \left[ \ln \left\{ \frac{E+2}{2} \left( \frac{E}{I^{\text{eff}}} \right)^2 \right\} + f^{(\pm)} - \delta_F - 2\mathcal{C}(E) \right], \quad (3.20)$$

where  $E$  is the energy of the incoming electron or positron,  $\mathcal{N}_e^{\text{eff}}$  is the effective electron density in the medium given by

$$\mathcal{N}_e^{\text{eff}} = \sum_{i=1}^{N_e} \mathcal{N}_{n,i} f_i Z_i, \quad (3.21)$$

with  $f_i$  is the weight percent of the  $i^{\text{th}}$ -element of the compound,  $Z_i$  is the atomic number of the  $i^{\text{th}}$ -element of the compound.  $\delta_F$  is the Fermi density effect, defined in the next subsection, and  $\mathcal{C}(E)$  is the shell correction, extracted from SBETHE program files [106], a state-of-the-art program to compute stopping power of charged particle.  $I^{\text{eff}}$  is the effective mean excitation energy of the compound is given by [43]

$$I^{\text{eff}} = \exp \left\{ \frac{1}{Z^{\text{eff}}} \sum_{i=1}^{N_e} f_i Z_i \log(I_i) \right\} \quad \text{with} \quad Z^{\text{eff}} = \sum_{i=1}^{N_e} f_i Z_i, \quad (3.22)$$

where the mean excitation energy of the  $i^{\text{th}}$ -element of the compound is  $I_i$  (tabulated by Seltzer and Berger [107]), unless more accurate value is provided. For water,  $I^{\text{eff}} = 78$  eV is used, as recommended by the ICRU report 90 [102, 108]. The electron factor  $f^{(-)}$  is given by [109]

$$f^{(-)} = 1 - \beta^2 - \frac{(2E+1)}{(E+1)^2} \ln(2) + \frac{1}{8} \left( \frac{E}{E+1} \right)^2 \quad (3.23)$$

and the positron factor  $f^{(+)}$  is given by

$$f^{(+)} = 2 \ln(2) - \frac{\beta^2}{12} \left[ 23 + \frac{14}{E+2} + \frac{10}{(E+2)^2} + \frac{4}{(E+2)^3} \right]. \quad (3.24)$$

#### Fermi density effect

The following calculation of the Fermi density effect is the same as described in SBETHE and the same used in the Monte Carlo transport code PENELOPE [43]. It is based on the

formula from Fano [110,111], which is

$$\delta_F = \frac{1}{Z^{\text{eff}}} \sum_{i=1}^{N_e} \sum_{k=1}^{N_{\text{shells}}} f_i Z_{i,k} \ln \left( 1 + \frac{L^2}{W_{i,k}^2} \right) - \frac{L^2}{\Omega_p^2} (1 - \beta^2), \quad (3.25)$$

where  $L$  is given by solving

$$(1 - \beta^2) = \frac{\Omega_p^2}{Z^{\text{eff}}} \sum_{i=1}^{N_e} \sum_{k=1}^{N_{\text{shells}}} \frac{f_i Z_{i,k}}{W_{i,k}^2 + L^2}. \quad (3.26)$$

which can be done using the Newton-bisection method presented in Annex C. The plasma energy is given by

$$\Omega_p^2 = 4\pi \mathcal{N}_e^{\text{eff}} \hbar^2 c^2 r_e^2 \quad (3.27)$$

and the resonance energy in the  $i^{\text{th}}$ -subshell is [95]

$$W_{i,k} = \sqrt{(aU_{i,k})^2 + \frac{2}{3} \frac{Z_{i,k}}{Z_i} \Omega_p^2}, \quad (3.28)$$

where  $a$  is given by solving

$$Z_i \ln(I^{\text{eff}}) = \sum_{k=1}^{N_{\text{shells}}} Z_{i,k} \ln \left( \sqrt{(aU_{i,k})^2 + \frac{2}{3} \frac{Z_{i,k}}{Z_i} \Omega_p^2} \right), \quad (3.29)$$

again using the Newton-bisection method.

### Soft stopping powers

The inelastic collisional soft stopping power,  $S^{\text{e}\pm}(E)$ , is given by removing the catastrophic stopping power from the total stopping power. It is given by

$$S^{\text{e}\pm}(E) = S_t(E) - \sum_{i=1}^{N_e} \mathcal{N}_{n,i} f_i \sum_{k=1}^{N_{\text{shells}}} Z_{i,k} \int_{E-E_c(E)}^{W_{\text{max}}^{\pm}} dW (W + U_{i,k}) \sigma_{s,0}^{i,k}(E \rightarrow W) \mathcal{H}_b, \quad (3.30)$$

which is evaluated analytically.

### 3.5 Elastic Scattering for Electrons and Positrons

An interaction in which the particle changes direction without losing energy is said to be elastic. Elastic interaction of electron and positron with matter, as pictured in Fig. 3.2, is of utmost importance to accurately model the distribution of this particle in the medium up

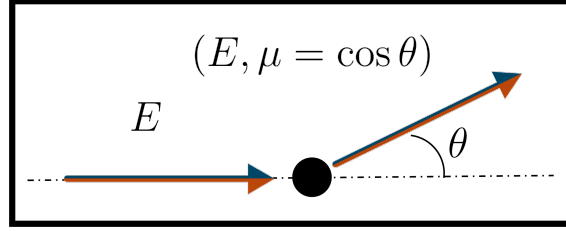


Figure 3.2 Elastic scattering for electrons (in blue) and positrons (in orange).

to hundreds of MeV. In CEPXS, a combination of Mott [112] and Rutherford [113] cross-sections, with Molière screening [114], is employed over 256 keV, while Riley cross-sections [115] are employed under that threshold down to 1 keV [16]. The same approach is used in MCNP Monte Carlo for elastic electron cross-sections [116]. The Mott cross-sections, which take into account spin and relativistic effects, are obtained under the assumption of an unscreened point-like nuclei. Adding screening by combination of the Mott and the screened Rutherford cross-sections seems a common practice [44, 117]. Riley cross-sections are computed by solving the partial-wave solution of the Dirac equation for an electron in the screened Coulomb potential of the atom [115, 118], which makes it more precise than the Mott-Rutherford marriage. Seltzer has proposed a semi-empirical correction of the Molière screening for the Mott-Rutherford cross-sections to fit partially the ones of Riley at lower energies [118]. GEANT4 uses Urban's multiple scattering model under 100 MeV and a mixed single/multiple scattering model over 100 MeV [119]. While it is efficient and accurate, both PENELOPE and EGSnrc outperform it in accuracy [120]. The PENELOPE code computes cross-sections using ELSEPA [121], a state-of-the-art program made for elastic cross-section calculations from partial-wave solutions of the Dirac equation. The EGSnrc code uses Mott-Rutherford cross-sections down to 1 keV to which a correction term is added to take into account sub-threshold inelastic scattering by atomic electrons while enforcing coherence with the knock-on production model [44, 122]. In this thesis, a similar approach to EGSnrc is employed. A combined Molière screened Mott-Rutherford cross-section is employed, based on an interpolation formula and data proposed by Lijian et al. [117, 123], jointly with the knock-on dependent correction from Kawrakow [122] and Seltzer's adjustment to Molière screening factor [118]. It has a few improvements compared to CEPXS. Contrary to CEPXS, the methodology and its tabulation are available in open source. Seltzer's correction is an alternative to the mixed use of two disjoint physical models. Analytical Legendre moments of the elastic cross-sections are proposed, which is very useful since numerical integration on very anisotropic cross-sections is highly inefficient and slow. Finally, explicit positron elastic cross-sections are produced.



The Mott cross-section describes the elastic interaction of an incoming electron ( $p = p' = \mathbf{e}^-$ ) or positron ( $p = p' = \mathbf{e}^+$ ) with the Coulomb field of an atom. The microscopic differential scattering cross-section in a monoelemental material  $i$  is given by

$$\sigma_s^i(E, \mu) = \frac{2\pi Z_i(Z_i + \xi_i^\pm)r_e^2}{\beta^2 E(E+2)} \frac{1}{(1 - \mu + 2\eta_i)^2} \mathcal{R}_{\text{Mott}}^i, \quad (3.31)$$

with  $\eta_i$ , the Molière screening factor with Seltzer's adjustment, obtained by [16, 114, 118]

$$\eta_i = \frac{\alpha^2 Z_i^{2/3} \left( 1.13 + 3.76 \left( \frac{Z_i \alpha}{\beta} \right)^2 \sqrt{\frac{E}{E+1}} \right)}{4 \left( \frac{9\pi^2}{128} \right)^{2/3} E(E+2)}, \quad (3.32)$$

where  $\alpha \approx 1/137$  is the fine structure constant. Note that when the incoming electron or positron has increasingly more kinetic energy,  $\eta_i$  becomes tiny, and the scattering cross-section becomes increasingly large as  $\mu$  tends to 1, producing highly forward-peaked scattering. Lijian et al. [123] proposed the following interpolation formula for  $\mathcal{R}_{\text{Mott}}^i$ , the ratio of the unscreened Mott differential cross-section to Rutherford's cross-section:

$$\mathcal{R}_{\text{Mott}}^i = \sum_{j=0}^4 a_{i,j} (1 - \mu)^{j/2}, \quad \text{where} \quad a_{i,j} = \sum_{k=1}^6 b_{k,j}(Z_i) (\beta - \bar{\beta})^{k-1} \quad (3.33)$$

and  $\bar{\beta} = 0.7181287$ . Boschini et al. [117] have generated  $b_{k,j}(Z_i)$  parameters for any  $Z_i \leq 118$ , for both electron and positron, and these are valid for energies between 1 keV and 900 MeV.

For incoming electrons or positrons, to take into account atomic electron contribution to the multiple scattering of charged particle transport,  $Z^2$  is often replaced by  $Z(Z+1)$  [124]. However, a double counting issue was observed in Monte Carlo codes due to an overlap with knock-on electrons [125], which are already taken into account by the Møller and Bhabha models (see Sect. 3.4.1). Kawrakow proposed a correction for this issue, which is significant for low  $Z$  material or when cutoff energy  $E_{G+1/2}$  is low [122]. This correction is given by

$$\xi_i^\pm = 1 - \frac{g_{\text{inel},i}^\pm}{g_{\text{el},i}}, \quad (3.34)$$

with  $g_{\text{el},i}$ , which is calculated using methodology described by Kawrakow for the Mott cross-sections rather than the screened Rutherford ones, is given by

$$g_{\text{el},i} = \frac{\tilde{\sigma}_{s,0}^i(E) - \tilde{\sigma}_{s,2}^i(E)}{3}, \quad (3.35)$$

where  $\tilde{\sigma}_{s,\ell}^i(E)$  is given by Eq. 3.38, and with  $g_{\text{inel},i}$  is given by

$$g_{\text{inel},i}^{\pm} = \sum_{k=1}^{N_{\text{shells}}} \frac{Z_{i,k}}{Z_i} E(E+2) \int_{E_{G+1/2}}^{W_{\text{max}}^{\pm}} dW (1 - \mu_p^2) F_{i,k}^{\pm}(E, W) \mathcal{H}_b, \quad (3.36)$$

where  $E_{G+1/2}$  is the minimum energy transfer to knock-on electron,  $W_{\text{max}}^{\pm}$  is given by Eq. 3.13,  $\mu_p$ , by Eq. 3.10 and  $F_{i,k}^{\pm}(E, W)$ , by Eq. 3.7-3.8. This equation is evaluated analytically.

### 3.5.1 Legendre moments of the scattering cross-sections

For deterministic transport calculations, the Legendre moments of the elastic cross-sections are required, namely

$$\Sigma_{s,\ell}^{\mathbf{e}\pm \rightarrow \mathbf{e}\pm}(E) = \sum_{i=1}^{N_e} \mathcal{N}_{n,i} f_i \int_{-1}^1 d\mu P_{\ell}(\mu) \sigma_s^i(E, \mu) = \sum_{i=1}^{N_e} \mathcal{N}_{n,i} f_i \frac{2\pi Z_i (Z_i + \xi_i^{\pm}) r_e^2}{\beta^2 E(E+2)} \tilde{\sigma}_{s,\ell}^i(E), \quad (3.37)$$

with the following definition

$$\tilde{\sigma}_{s,\ell}^i(E) = \int_{-1}^1 d\mu P_{\ell}(\mu) \frac{\mathcal{R}_{\text{Mott}}^i}{(1 - \mu + 2\eta_i)^2}. \quad (3.38)$$

Calculating these Legendre moments using numerical quadrature is highly inefficient due to the near singularity that often occurs at  $\mu = 1$ , when  $\eta_i$  is small. As demonstrated in the following lines, the integration can be fast, done analytically and in a way that ensures numerical stability.

First, the Legendre polynomial can be expressed as a sum of powers of  $\mu$  as [126]

$$P_{\ell}(\mu) = \frac{1}{2^{\ell}} \sum_{k=0}^{\lfloor \ell/2 \rfloor} C_{\ell,k} \mu^{\ell-2k}, \quad \text{where} \quad C_{\ell,k} = \frac{(-1)^k (2\ell - 2k)!}{k! (\ell - k)! (\ell - 2k)!}, \quad (3.39)$$

and therefore, the Legendre moments can be expressed as

$$\tilde{\sigma}_{s,\ell}^i(E) = \frac{1}{2^{\ell}} \sum_{k=0}^{\lfloor \ell/2 \rfloor} C_{\ell,k} \int_{-1}^1 d\mu \frac{\mathcal{R}_{\text{Mott}}^i}{(1 - \mu + 2\eta_i)^2} \mu^{\ell-2k} = \frac{1}{2^{\ell}} \sum_{k=0}^{\lfloor \ell/2 \rfloor} C_{\ell,k} \sum_{r=1}^2 I_r^{\ell,k}, \quad (3.40)$$

where  $I_1^{\ell,k}$  is given by

$$\begin{aligned} I_1^{\ell,k} &= \int_{-1}^1 d\mu \frac{\mu^{\ell-2k}}{(1 - \mu + 2\eta_i)^2} [\alpha_{i,0} + \alpha_{i,1}\mu + \alpha_{i,2}\mu^2] \\ &= \sum_{j=0}^2 \alpha_{i,j} \left( \mathcal{G}_1^{\ell-2k+j}(1 + 2\eta_i, -1, 1) - \mathcal{G}_1^{\ell-2k+j}(1 + 2\eta_i, -1, -1) \right) \end{aligned} \quad (3.41)$$

and  $I_2^{\ell,k}$  is given by

$$\begin{aligned} I_2^{\ell,k} &= \int_{-1}^1 d\mu \frac{\mu^{\ell-2k} \sqrt{(1-\mu)}}{(1-\mu+2\eta)^2} [\alpha_3 + \alpha_4 \mu] \\ &= 2 \sum_{j=0}^1 \alpha_{i,j+3} \sum_{g=0}^{\ell-2k+j} (-1)^g \frac{(\ell-2k+j)!}{g!(\ell-2k+j-g)!} \mathcal{G}_2^{2+2g}(2\eta_i, 1, \sqrt{2}), \end{aligned} \quad (3.42)$$

with  $\alpha_{i,0} = a_{i,0} + a_{i,2} + a_{i,4}$ ,  $\alpha_{i,1} = -(a_{i,2} + 2a_{i,4})$ ,  $\alpha_{i,2} = a_{i,4}$ ,  $\alpha_{i,3} = a_{i,1} + a_{i,3}$  and  $\alpha_{i,4} = -a_{i,3}$ . The first integral is obtained using the following integral from Gradshteyn et al. (Eq. 4, Sect. 2.111) [127]

$$\mathcal{G}_1^n(a, b, x) = \sum_{g=1}^{n-1} (-1)^{g-1} \frac{ga^{g-1}x^{n-g}}{(n-g)b^{g+1}} + (-1)^{n-1} \frac{a^n}{b^{n+1}(a+bx)} + (-1)^{n+1} \frac{na^{n-1}}{b^{n+1}} \ln(a+bx), \quad (3.43)$$

while the second integral is evaluated by applying the change of variable  $u = \sqrt{1-\mu}$ , using the binomial theorem and then formulae from Gradshteyn et al. (Sect. 2.172, Eq. 1 Sect. 2.173 and Eq. 1 Sect. 2.174)

$$\mathcal{G}_2^n(a, b, x) = \begin{cases} \frac{x}{2aR} + \frac{1}{2a\sqrt{ab}} \arctan\left(\frac{bx}{\sqrt{ab}}\right) & n = 0 \\ -\frac{x^{n-1}}{(3-n)bR} + \frac{(n-1)a}{(3-n)b} \mathcal{G}_2^{n-2}(a, b, x) & n \text{ even} > 0 \end{cases}. \quad (3.44)$$

This fully analytical solution can be numerically unstable, because of catastrophic cancellations for high-order Legendre terms when  $\eta_i$  is large ( $> 1$ ), which happens when the elastic scattering is becoming more or less isotropic, notably at low energies. Since an isotropic flux is characterized by  $\ell \geq 1$  Legendre moments equal to zero, the following correction for  $\ell_x \geq 1$  is proposed:

$$\text{if } \left| \sigma_{s,\ell_x}^i(E) \right| > \left| \sigma_{s,0}^i(E) \right| \quad \text{then} \quad \sigma_{s,\ell}^i(E) = 0 \quad \forall \ell \geq \ell_x, \quad (3.45)$$

which are based on the upper bound of high-order Legendre moments, found in Annex A.

### 3.5.2 Total cross-sections

The elastic total cross-sections are simply given by

$$\Sigma_t^{\mathbf{e}\pm}(E) = \Sigma_{s,0}^{\mathbf{e}\pm \rightarrow \mathbf{e}\pm}(E). \quad (3.46)$$

### 3.5.3 Transport correction and elastic decomposition in soft and catastrophic components

The elastic scattering cross-sections can be decomposed into soft and catastrophic components [128]. Let  $L$  be the order of the cross-sections Legendre expansion and  $\Sigma_{s,\ell,g \rightarrow g}^{\mathbf{e}\pm \rightarrow \mathbf{e}\pm}$  be the  $\ell$ -order Legendre moment of the elastic scattering cross-section in group  $g$ . Let  $L_{\max} \leq L$  be the last non-zero Legendre moments of the scattering in group  $g$ . The Legendre moments of the soft are assumed to be given by

$$\Sigma_{s,\ell,g \rightarrow g}^{\mathbf{e}\pm \rightarrow \mathbf{e}\pm, \text{soft}} = \Sigma_{s,0,g \rightarrow g}^{\mathbf{e}\pm \rightarrow \mathbf{e}\pm, \text{soft}} - T_g \ell(\ell + 1) \quad (3.47)$$

for  $\ell \in \{1, \dots, L_{\max}\}$ . This expression is obtained by establishing equality between the eigenvalues of the Boltzmann and the AFP operator applied to the Legendre polynomials [54]. This method sets a relation, which depends on two undefined parameters  $\Sigma_{s,0,g \rightarrow g}^{\mathbf{e}\pm \rightarrow \mathbf{e}\pm, \text{soft}}$  and  $T_g$ , such as moments of the Boltzmann operator are preserved by the Fokker-Planck operator. Landesman and Morel proposed to equate  $\Sigma_{s,L_{\max}-1}^{\mathbf{e}\pm \rightarrow \mathbf{e}\pm, \text{soft}} = \Sigma_{s,L_{\max}-1,g \rightarrow g}^{\mathbf{e}\pm \rightarrow \mathbf{e}\pm}$  and  $\Sigma_{s,L_{\max},g \rightarrow g}^{\mathbf{e}\pm \rightarrow \mathbf{e}\pm, \text{soft}} = \Sigma_{s,L_{\max},g \rightarrow g}^{\mathbf{e}\pm \rightarrow \mathbf{e}\pm}$  to define these parameters, which results in

$$T_g = \frac{\Sigma_{s,L_{\max}-1,g \rightarrow g}^{\mathbf{e}\pm \rightarrow \mathbf{e}\pm} - \Sigma_{s,L_{\max},g \rightarrow g}^{\mathbf{e}\pm \rightarrow \mathbf{e}\pm}}{2L_{\max}}, \quad (3.48)$$

and

$$\Sigma_{s,0,g \rightarrow g}^{\mathbf{e}\pm \rightarrow \mathbf{e}\pm, \text{soft}} = \Sigma_{s,L_{\max},g \rightarrow g}^{\mathbf{e}\pm \rightarrow \mathbf{e}\pm} + T_g L_{\max}(L_{\max} + 1). \quad (3.49)$$

The soft component of the elastic cross-sections should then be withdrawn from cross-sections, since the AFP operator, jointly with the momentum transfer given by Eq. 3.48, is used to treat that soft scattering. The total elastic cross-sections are redefined as

$$\Sigma_{t,g} \leftarrow \Sigma_{t,g} - \Sigma_{s,L_{\max},g \rightarrow g}^{\mathbf{e}\pm \rightarrow \mathbf{e}\pm} - T_g L_{\max}(L_{\max} + 1), \quad (3.50)$$

and the  $\ell$ -order Legendre moment of the scattering cross-sections are redefined as

$$\Sigma_{s,\ell,g \rightarrow g}^{\mathbf{e}\pm \rightarrow \mathbf{e}\pm} \leftarrow \Sigma_{s,\ell,g \rightarrow g}^{\mathbf{e}\pm \rightarrow \mathbf{e}\pm} - \Sigma_{s,L_{\max},g \rightarrow g}^{\mathbf{e}\pm \rightarrow \mathbf{e}\pm} - T_g [L_{\max}(L_{\max} + 1) - \ell(\ell + 1)]. \quad (3.51)$$

The goal of this operation is to transfer the handling of forward-peaked scattering from the Boltzmann operator, which encounters monotonicity issues with such scattering [47], to the Fokker-Planck operator, which can be tackled by finite-difference discretization schemes (see Chap. 4).

This method, as presented, includes the extended transport correction [50, 68, 129]. The

transport correction is a method that reduces the amplitude of the elastic cross-sections for the BFP solver while leaving intact the flux solution, which requires the use of Galerkin quadrature [47], as described in Sect. 4.2.3. This amplitude reduction aims to reduce the scattering ratio, which is very close to one in charged particle transport. Without this correction, the source iteration process would require an astounding number of iterations, thus a long time, to converge [17].

### 3.6 Bremsstrahlung

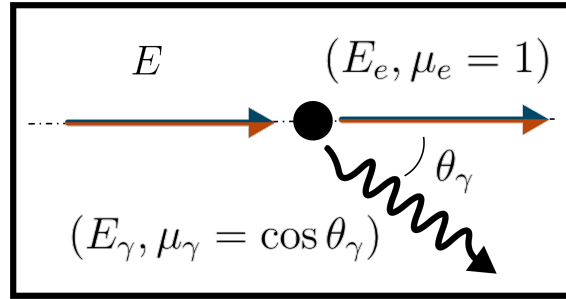


Figure 3.3 Bremsstrahlung production (in black) by incoming electrons (in blue) or positrons (in orange).

The bremsstrahlung interaction occurs when an incoming electron or positron interacts with the field of the atomic nucleus and its electrons. This interaction, vital at high energies, slows the incoming particle by producing a bremsstrahlung photon. CEPXS uses a weighted sum of bremsstrahlung formulas from Koch and Motz [130], as prescribed by Berger and Seltzer [131], with Sommerfield angular distribution of photons, to describe catastrophic events [16]. Soft events are characterized based on Berger's radiative stopping powers [37, 94]. The PENELOPE code uses tables from Seltzer and Berger [132] for both differential cross-sections and stopping powers, which are still considered the most accurate and comprehensive energy-dependent bremsstrahlung data available [102], with a modified dipole distribution of emitted photons distribution [133, 134]. This code also uses a formula to convert electron cross-sections or stopping powers to positron ones [106]. The bremsstrahlung model presented in this work is almost identical to the one of PENELOPE but has a different angular photon distribution. The presented model is an improvement over CEPXS since it uses the more recent data from Seltzer and Berger, uses open-source models, improves the angular distribution of photons, and generates explicit positron data.

The bremsstrahlung cross-section describes the interaction of an incoming electron ( $p' = e^-$ ) or positron ( $p' = e^+$ ) with the field of the atomic nucleus and its electrons. The incoming

particle scatter ( $p = e^-$  or  $p = e^+$ ), while photon are produced ( $p = \gamma$ ). Seltzer and Berger proposed tables to compute the differential cross-section as a function of the energy of the produced photon, which includes both electron-nucleus and electron-electron interactions, and for monoelemental material  $i$ , it is given by [132]

$$\sigma_s^i(E \rightarrow E_\gamma) = \begin{cases} \frac{F_{p,i}^\pm Z_i^2 \tilde{\sigma}_s(Z_i, E, E_\gamma)}{E_\gamma \beta^2} & E_\gamma \leq E \\ 0 & \text{otherwise} \end{cases}, \quad (3.52)$$

where  $E$  is incoming electron or positron energy,  $E_\gamma$  is the produced photon energy and  $\tilde{\sigma}_s(Z_i, E, E_\gamma)$  is the total scaled bremsstrahlung energy-weighted cross-section, given in  $\text{cm}^2$ , from interpolation of the Seltzer and Berger tables [132]. These cross-sections are defined for  $Z_i \leq 100$  and energies between 1 keV and 10 GeV. The factor  $F_{p,i}^\pm$  is given by [106]

$$F_{p,i}^+ = 1 - \exp \left\{ -1.2359 \times 10^{-1} t_i + 6.1274 \times 10^{-2} t_i^2 - 3.1516 \times 10^{-2} t_i^3 + 7.7446 \times 10^{-3} t_i^4 \right. \\ \left. - 1.0595 \times 10^{-3} t_i^5 + 7.0568 \times 10^{-5} t_i^6 - 1.8080 \times 10^{-6} t_i^7 \right\}, \quad (3.53)$$

with

$$t_i = \ln \left( 1 + \frac{10^6 E}{Z_i^2} \right) \quad (3.54)$$

for incoming positrons, which is based on the tabulated positron-to-electron ratios from Kim et al. [135], and  $F_{p,i}^- = 1$  for incoming electrons. The double differential cross-sections are given by [16]

$$\sigma_s^i(E \rightarrow E_e, \mu) = \frac{1}{2\pi} \sigma_s^i(E \rightarrow E_e) \delta(\mu - 1) \quad \text{and} \quad \sigma_s^i(E \rightarrow E_\gamma, \mu) = \frac{1}{2\pi} \sigma_s^i(E \rightarrow E_\gamma) \Theta(E, \mu), \quad (3.55)$$

where it is assumed, as in CEPXS [16], that the incoming electron does not deflect from its trajectory after interaction ( $\mu_e = 1$ ). The bremsstrahlung photon angular distribution, greatly inspired by the modified dipole distribution from Acosta et al. [133, 136], is given by

$$\Theta(E, E_\gamma, \mu) = \frac{3(1 - C^2)}{4(2A + B)(1 - \mu C)^2} \left[ (A + B) + (A - B) \left( \frac{\mu - C}{1 - \mu C} \right)^2 \right], \quad (3.56)$$

where the parameters  $A = A(E, E_\gamma)$ ,  $B = B(E, E_\gamma)$  and  $C = C(E, E_\gamma)$ , which have values strictly between 0 and 1, are adjusted by least-square method to fit the shape function from Pořkus [137] for  $E \leq 3$  MeV, and are set to give the dipole distribution ( $A = 1$ ,  $B = 0$  and  $C = \beta$ ) for energy  $E > 3$  MeV. This approach is similar to the one used in the PENELOPE

code, where a 500 keV threshold is applied rather than 3 MeV [136], and where the shape functions are extracted from Kissel et al. [134] rather than the more recent and comprehensive work from Pořkus.

### 3.6.1 Scattering cross-sections for deflected electron or positron

The bremsstrahlung Legendre moments of the differential scattering cross-sections for the incoming lepton are given by

$$\sigma_{s,\ell}^i(E \rightarrow E_e) = 2\pi \int_{-1}^1 d\mu P_\ell(\mu) \sigma_s^i(E \rightarrow E_e, \mu) = \sigma_s^i(E \rightarrow E_e). \quad (3.57)$$

The multigroup Legendre moments of the scattering cross-sections are therefore given by

$$\Sigma_{s,\ell,g'}^{\mathbf{e}\pm \rightarrow \mathbf{e}\pm}(E) = \sum_{i=1}^{N_e} \mathcal{N}_{n,i} f_i \int_{E'_{g+1/2}}^{\min\{E'_{g-1/2}, E_c(E)\}} dE_e \sigma_{s,\ell}^i(E \rightarrow E_e) \mathcal{H}_b. \quad (3.58)$$

This equation is evaluated using numerical quadrature.

### 3.6.2 Scattering cross-sections for produced photon

The Legendre moments of the differential scattering cross-sections for the produced bremsstrahlung photon are given by

$$\sigma_{s,\ell}^i(E \rightarrow E_\gamma) = 2\pi \int_{-1}^1 d\mu P_\ell(\mu) \sigma_s^i(E \rightarrow E_\gamma, \mu) = \sigma_s^i(E \rightarrow E_\gamma) \Theta_\ell(E), \quad (3.59)$$

where the moment of the angular distribution,

$$\Theta_\ell(E) = \int_{-1}^1 d\mu P_\ell(\mu) \Theta(E, \mu), \quad (3.60)$$

are calculated analytically based on the same reasoning than in the Sect. 3.5.1, with Legendre expansion in power of  $\mu$ . The multigroup Legendre moments of the scattering cross-sections are therefore given by

$$\Sigma_{s,\ell,g'}^{\mathbf{e}\pm \rightarrow \gamma}(E) = \sum_{i=1}^{N_e} \mathcal{N}_{n,i} f_i \int_{E'_{g+1/2}}^{\min\{E'_{g-1/2}, E\}} dE_\gamma \sigma_{s,\ell}^i(E \rightarrow E_\gamma) \mathcal{H}_b. \quad (3.61)$$

This equation is evaluated using numerical quadrature.

### 3.6.3 Catastrophic total cross-sections

The catastrophic bremsstrahlung total cross-sections are defined by

$$\Sigma_t^{\text{e}\pm}(E) = \sum_{i=1}^{N_e} \mathcal{N}_{n,i} f_i \int_0^{E_c(E)} dE_e \sigma_{s,0}^i(E \rightarrow E_e) \quad (3.62)$$

and are evaluated using numerical quadrature.

### 3.6.4 Absorption cross-sections for incoming positrons

The bremsstrahlung catastrophic absorption cross-sections, for annihilation calculations, are given by

$$\Sigma_a^{\text{brem}}(E) = \sum_{i=1}^{N_e} \mathcal{N}_{n,i} f_i \int_0^{E_{G+1/2}} dE_e \sigma_{s,0}^i(E \rightarrow E_e) \quad (3.63)$$

and are evaluated using numerical quadrature.

### 3.6.5 Total stopping power

The radiative stopping powers of electron are given by

$$S_t(E) = \alpha r_e^2 (E + 1) \sum_{i=1}^{N_e} \mathcal{N}_{n,i} f_i F_{p,i}^{\pm} Z_i^2 \phi_{\text{rad}}(Z_i, E), \quad (3.64)$$

where  $\phi_{\text{rad}}(Z_i, E)$  are also given by the tables of Selzer and Berger [132].

### 3.6.6 Soft stopping powers

The soft radiative stopping powers,  $S^{\text{e}\pm}(E)$ , are given by removing catastrophic bremsstrahlung stopping powers from total stopping powers. They are given by

$$S^{\text{e}\pm}(E) = S_t(E) - \sum_{i=1}^{N_e} \mathcal{N}_{n,i} f_i \int_0^{E_c(E)} dE_e (E - E_e) \sigma_{s,0}^i(E \rightarrow E_e), \quad (3.65)$$

where the integral is evaluated with numerical quadrature.

## 3.7 Annihilation

The annihilation interaction consists of an incoming positron that annihilates with an atomic electron to produce two photons, as shown in Fig. 3.4. The combined photon's energy



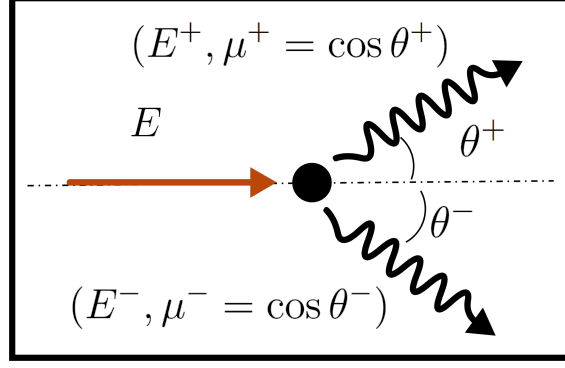


Figure 3.4 Annihilation of positrons (in orange) and production of two photons (in black).

is equivalent to the sum of kinetic and mass energies of the annihilated atomic electron and incoming positron. As the kinetic energy of an incoming positron approaches zero, this interaction becomes inevitable. In CEPXS, there is no explicit positron interaction. It is, however, considered by annihilation photon production at the moment positrons are produced by pair production, which is equivalent to annihilating the positron on the spot. This technique neglects the other mechanisms in which the energy can be dissipated through the medium. The model of Nelson et al. [138], used in both PENELOPE and EGSnrc, is employed in this thesis. The presented annihilation model is an improvement over CEPXS since it is explicitly defined as a positron cross-section.

The following cross-sections describe the annihilation of an incoming positron ( $p' = e^+$ ) with an atomic electron producing two photons ( $p = \gamma$ ), assuming that the electrons are free and at rest. The differential cross-sections in the energy of the lowest energy photon [105, 139]

$$\sigma_s(E \rightarrow E_{\gamma_-}) = \frac{\pi r_e^2}{(\gamma + 1)^2(\gamma^2 - 1)} \left[ S(\zeta) + S(1 - \zeta) \right] \quad (3.66)$$

with

$$S(\zeta) = -(\gamma + 1)^2 + (\gamma^2 + 4\gamma + 1) \frac{1}{\zeta} - \frac{1}{\zeta^2}, \quad (3.67)$$

where  $E$  is the incoming positron energy,  $E_{\gamma_-}$  is the lowest photon energy,  $E_{\gamma_+} = E + 2 - E_{\gamma_-}$  is the highest photon energy and  $\zeta = E_{\gamma_-}/(E + 2)$  is the ratio of the lowest energy photon to the total (kinetic + mass) energy. The value of the lowest photon energy is bounded by

$$E^{\max} = \frac{\gamma + 1}{2} \quad \text{and} \quad E^{\min} = \frac{\gamma + 1}{\gamma + 1 + \sqrt{\gamma^2 - 1}}. \quad (3.68)$$

The scattering angles of the lowest and highest energy photons are respectively

$$\mu_- = \frac{1}{\sqrt{\gamma^2 - 1}} \left[ \gamma + 1 - \frac{1}{\zeta} \right] \quad \text{and} \quad \mu_+ = \frac{1}{\sqrt{\gamma^2 - 1}} \left[ \gamma + 1 - \frac{1}{1 - \zeta} \right], \quad (3.69)$$

and the double differential cross-sections for the lowest and highest energy photons are given by

$$\sigma_s(E \rightarrow E_{\gamma_-}, \mu) = \frac{1}{2\pi} \sigma_s(E \rightarrow E_{\gamma_-}) \delta(\mu - \mu_-) \quad (3.70)$$

and

$$\sigma_s(E \rightarrow E_{\gamma_+}, \mu) = \frac{1}{2\pi} \sigma_s(E \rightarrow E_{\gamma_+}) \delta(\mu - \mu_+). \quad (3.71)$$

### 3.7.1 Scattering cross-sections for the lowest energy photons

The annihilation Legendre moments of the differential scattering cross-sections for the lowest energy photons are given by

$$\sigma_{s,\ell}(E \rightarrow E_{\gamma_-}) = 2\pi \int_{-1}^1 d\mu P_\ell(\mu) \sigma_s(E \rightarrow E_{\gamma_-}, \mu) = P_\ell(\mu_-) \sigma_s(E \rightarrow E_{\gamma_-}). \quad (3.72)$$

The multigroup Legendre moments of the scattering cross-sections are therefore given by

$$\Sigma_{s,\ell,g'}^{\mathbf{e}^+ \rightarrow \gamma}(E) = \sum_{i=1}^{N_e} \mathcal{N}_{n,i} f_i Z_i \int_{\max\{E_{g+1/2}^\gamma, E^{\min}\}}^{\min\{E_{g-1/2}^\gamma, E^{\max}\}} dE_{\gamma_-} \sigma_{s,\ell}(E \rightarrow E_{\gamma_-}) \mathcal{H}_b. \quad (3.73)$$

This equation is evaluated using numerical quadrature.

### 3.7.2 Scattering cross-sections for the highest energy photons

The annihilation Legendre moments of the differential scattering cross-sections for the highest energy photons are given by

$$\sigma_{s,\ell}(E \rightarrow E_{\gamma_+}) = 2\pi \int_{-1}^1 d\mu P_\ell(\mu) \sigma_s(E \rightarrow E_{\gamma_+}, \mu) = P_\ell(\mu_+) \sigma_s(E \rightarrow E_{\gamma_+}). \quad (3.74)$$

The multigroup Legendre moments of the scattering cross-sections are therefore given by

$$\Sigma_{s,\ell,g'}^{\mathbf{e}^+ \rightarrow \gamma}(E) = \sum_{i=1}^{N_e} \mathcal{N}_{n,i} f_i Z_i \int_{\max\{E_{g+1/2}^\gamma, E^{\max}\}}^{\min\{E_{g-1/2}^\gamma, (\gamma+1) - E^{\min}\}} dE_{\gamma_+} \sigma_{s,\ell}(E \rightarrow E_{\gamma_+}) \mathcal{H}_b. \quad (3.75)$$

This equation is integrated using numerical quadrature.

### 3.7.3 Total cross-sections

The annihilation total cross-sections are defined by

$$\Sigma_t^{\mathbf{e}^+}(E) = \sum_{i=1}^{N_e} \mathcal{N}_{n,i} f_i Z_i \int_{E^{\min}}^{E^{\max}} dE_{\gamma-} \sigma_{s,0}(E \rightarrow E_{\gamma-}) \quad (3.76)$$

and are evaluated analytically.

### 3.7.4 Annihilation when positrons scatter under the cutoff energy

Positrons ( $p' = \mathbf{e}^+$ ) will inevitably annihilate with atomic electrons and produce two photons ( $p = \gamma$ ). Therefore, all positrons scattered under the cutoff energy  $E_{G+1/2}$  should annihilate. The positron energy under the cutoff is small enough that the annihilation photon can be assumed to have isotropic scattering, as done in GEANT4 [140]. It is then assumed that two 511 keV photons are produced. The positrons are scattered under the cutoff following either an inelastic interaction or a bremsstrahlung interaction, and positrons can also be produced under the cutoff following pair production interaction. The  $\ell = 0$  Legendre moments of the scattering cross-sections are given by

$$\Sigma_{s,0,g' \rightarrow g}^{\mathbf{e}^+ \rightarrow \gamma} = 2 \left[ \Sigma_{a,g'}^{\text{inel}} + \Sigma_{a,g'}^{\text{brem}} \right] \times \begin{cases} 1 & 1 \in [E'_{g+1/2}, E'_{g-1/2}] \\ 0 & \text{otherwise} \end{cases} \quad (3.77)$$

and

$$\Sigma_{s,0,g' \rightarrow g}^{\gamma \rightarrow \gamma} = 2 \Sigma_{a,g'}^{\text{pp}} \times \begin{cases} 1 & 1 \in [E'_{g+1/2}, E'_{g-1/2}] \\ 0 & \text{otherwise} \end{cases}, \quad (3.78)$$

where the absorption cross-sections are given by integration of Eqs. 3.19, 3.63 and 3.111 over group  $g'$  and where the  $\ell \geq 1$  moments are equal to zero since scattering is isotropic. While these scattering cross-sections account for catastrophic impact ionization interactions, they do not include positrons reaching the cutoff energy by soft impact ionization interactions. In order to accurately estimate the production of annihilation photons following all impact ionization interactions, the lower bounds of integrals over energy loss  $W$  (Eq. 3.19) should be  $E - E_{G+1/2}$  rather than  $E - \min \{E_{G+1/2}, E_c\}$ , because the latter excluding soft interactions. However, the Bhabha-based impact ionization model is inaccurate for small energy losses, i.e. for soft interaction, and it can lead to substantial error in the solution when used to describe such interactions. Since these soft events require an improved impact ionization model for positron, which would required enormous effort, the annihilation photons produced by absorption of positrons at the cutoff energy are neglected. This will result in an underesti-

mation of the production of annihilation photon, which have an impact on the accuracy of transport calculations.

### 3.8 Rayleigh Scattering

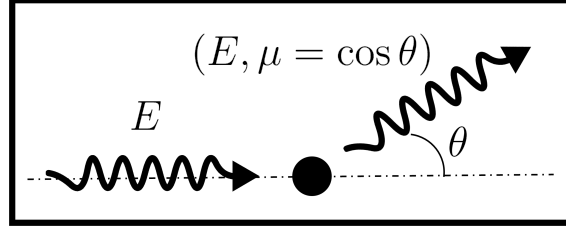


Figure 3.5 Coherent scattering of photons (in black).

Rayleigh scattering, also often called coherent scattering, consists of the elastic change of direction of an incoming photon by atomic electrons, as shown in Fig. 3.5. This interaction is not considered in CEPXS because it is assumed to be negligible compared to the other photon interactions [16]. The Rayleigh scattering model from PENELOPE [43], which is based on atomic form factors [141] and anomalous scattering factors [142], is used in this thesis. The presented Rayleigh scattering model is an improvement over CEPXS since it is omitted in CEPXS.

The Rayleigh cross-sections, which described the elastic scattering of photons ( $p = p' = \gamma$ ) are given by [141–143]

$$\sigma_s^i(E, \mu) = \pi r_e^2 (1 + \mu^2) \left[ \left( F_i(E, \mu) + f_i'(E) \right)^2 + \left( f_i''(E) \right)^2 \right], \quad (3.79)$$

where  $F_i(E, \mu)$  is the atomic form factor for the  $i^{\text{th}}$ -element, where the factors  $f_i'(E)$  and  $f_i''(E)$  respectively are the real and imaginary parts of the anomalous scattering factors for the  $i^{\text{th}}$ -element, which are all tabulated by the Japanese evaluated nuclear data library (JENDL-5) [144], which are based on the EPDL library [145]. The double differential cross-sections are given by

$$\sigma_s^i(E \rightarrow E', \mu) = \sigma_s^i(E, \mu) \delta(E' - E). \quad (3.80)$$

### 3.8.1 Scattering cross-sections of the incoming photon

The Rayleigh Legendre moments of the differential scattering cross-sections of the incoming photon are simply given by

$$\Sigma_{s,\ell}^{\gamma \rightarrow \gamma}(E) = \sum_{i=1}^{N_e} \mathcal{N}_{n,i} f_i \int_{-1}^1 P_\ell(\mu) \sigma_s^i(E, \mu), \quad (3.81)$$

which are integrated using numerical quadrature.

### 3.8.2 Total cross-sections

The Rayleigh total cross-sections are given by

$$\Sigma_{s,\ell}^\gamma(E) = \Sigma_{s,0}^{\gamma \rightarrow \gamma}(E). \quad (3.82)$$

## 3.9 Compton Scattering

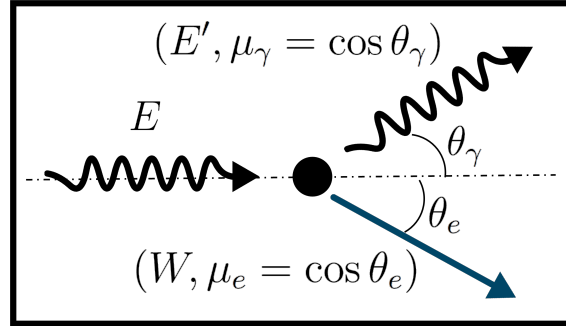


Figure 3.6 Compton scattering by an incoming photon (in black) and production of electron (in blue).

The Compton scattering, often called incoherent scattering, consists of the ionization of an atomic electron by an incoming photon, which loses energy in the process, as shown in Fig. 3.6. This interaction is dominant for intermediate energies ranging from the hundreds of keV to a few MeV. In CEPXS, the Klein-Nishina model, which assumes interaction with an unbounded electron at rest, is used to describe this interaction [16]. This model neglects the binding effects and Doppler broadening because electrons are not at rest. Penelope and EGSnrc models are based on the subshell-dependent relativistic impulse approximation from Brusa et al. [146]. While using this model is desirable for multigroup deterministic transport, it is challenging to implement to have fast and accurate results. The production of Legendre

moments of these cross-sections is an outstanding challenge since two very challenging integrations, in angle and energy of the scattered photon, must be performed, one following the other, in an accurate and fast enough way. Therefore, until such multigroup cross-sections can be developed, the proposed model uses the Waller-Hartree incoherent function, which is applied to the Klein-Nishina cross-section, in order to encompass most electron binding effects [146]. The presented Compton scattering model is an improvement over CEPXS since it includes the Waller-Hartree incoherent function, which includes bindings effects.

The Compton cross-section describes the interaction of an incoming photon ( $p' = \gamma$ ) with atomic electrons, resulting in a scattered photon ( $p = \gamma$ ) and a produced electron ( $p = e^+$ ). The Klein-Nishina differential cross-section in the energy of the scattered photon for a single interaction with an assumed free atomic electron is given by [16, 139]

$$\sigma_s(E \rightarrow E') = \frac{\pi r_e^2}{E^2} \left[ \frac{E}{E'} + \frac{E'}{E} - 2 \left( \frac{1}{E'} - \frac{1}{E} \right) + \left( \frac{1}{E'} - \frac{1}{E} \right)^2 \right], \quad (3.83)$$

where  $E$  is the incoming photon energy,  $E'$  is the scattered photon energy and  $W = E - E'$  is the produced electron energy. The scattering angles for the scattered photon and the produced electron are respectively

$$\mu_\gamma = 1 + \frac{1}{E} - \frac{1}{E'} \quad \text{and} \quad \mu_e = \frac{1 + E}{E} \left[ 1 + \frac{2}{W} \right]^{-\frac{1}{2}}. \quad (3.84)$$

The double differential cross-sections for the scattered photon and the produced electron, with an incoherent scattering factor  $S_i(E, \mu)$  extracted from JENDL-5 library [144] taking into account some binding effects [146], are given by

$$\sigma_s^i(E \rightarrow E', \mu) = \frac{1}{2\pi} S_i(E, \mu) \sigma_s(E \rightarrow E') \delta(\mu - \mu_\gamma) \quad (3.85)$$

and

$$\sigma_s^i(E \rightarrow W, \mu) = \frac{1}{2\pi} S_i(E, \mu) \sigma_s(E \rightarrow W) \delta(\mu - \mu_e). \quad (3.86)$$

### 3.9.1 Scattering cross-sections of the incoming photon

The Compton Legendre moments of the differential scattering cross-sections of the incoming photon are given by

$$\sigma_{s,\ell}^i(E \rightarrow E') = 2\pi \int_{-1}^1 d\mu P_\ell(\mu) \sigma_s^i(E \rightarrow E', \mu) = P_\ell(\mu_\gamma) S_i(E, \mu_\gamma) \sigma_s(E \rightarrow E'). \quad (3.87)$$

The multigroup Legendre moments of the scattering cross-sections are therefore given by

$$\Sigma_{s,\ell,g'}^{\gamma \rightarrow \gamma}(E) = \sum_{i=1}^{N_e} \mathcal{N}_{n,i} f_i \int_{\max\left\{E'_{g+1/2}, \frac{E}{1+2E}\right\}}^{\min\left\{E'_{g-1/2}, E\right\}} dE' \sigma_{s,\ell}^i(E \rightarrow E'), \quad (3.88)$$

which are integrated by numerical quadrature.

### 3.9.2 Scattering cross-sections of the produced electron

The Compton Legendre moments of the differential scattering cross-sections of the produced electron are given by

$$\sigma_{s,\ell}^i(E \rightarrow W) = 2\pi \int_{-1}^1 d\mu P_\ell(\mu) \sigma_s^i(E \rightarrow W, \mu) = P_\ell(\mu_e) S_i(E, \mu_e) \sigma_s(E \rightarrow W). \quad (3.89)$$

The multigroup Legendre moments of the scattering cross-sections are therefore given by

$$\Sigma_{s,\ell,g'}^{\gamma \rightarrow e^-}(E) = \sum_{i=1}^{N_e} \mathcal{N}_{n,i} f_i \int_{E'_{g+1/2}}^{\min\left\{E'_{g-1/2}, \frac{2E^2}{1+2E}\right\}} dW \sigma_\ell^i(E \rightarrow W), \quad (3.90)$$

which are integrated by numerical quadrature.

### 3.9.3 Total cross-sections

The Compton total cross-sections are defined by

$$\Sigma_t^\gamma(E) = \sum_{i=1}^{N_e} \mathcal{N}_{n,i} f_i \int_{\frac{E}{1+2E}}^E dE' S_i(E, \mu_\gamma) \sigma_{s,0}(E \rightarrow E'), \quad (3.91)$$

which are integrated by numerical quadrature.

## 3.10 Photoelectric Effect

The photoelectric effect consists of the emission of electrons by absorption of photons, as shown in Fig. 3.7. In CEPXS, the total macroscopic cross-sections are computed using energy interpolation of data from Biggs and Lighthill tables [147]. Subshell-dependant cross-sections, for the K, L1, L2, L3, M (averaged) and N (effective) subshells, are extracted using by approximating the photoeffect efficiencies from the cross-sections themselves [16]. The angular distribution of photoelectron is given by the Fischer distribution for low-energy electrons and the Sauter distribution for high-energy electrons. Relaxation cascades are

taken into account for these interactions. Penelope uses tables from the subshell-dependent Evaluated Photon Data Library (EPDL) [148], while the Sauter distribution is used regardless of the electron energy. This is the model used in this thesis. The presented photoelectric model is an improvement over CEPXS since it includes subshell-dependent microscopic cross-sections, from a more recent evaluated data library. The Fischer distribution, not used for the angular distribution model, could be of interest for low-energy electrons.

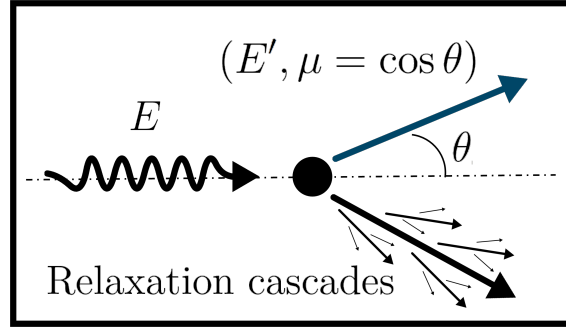


Figure 3.7 Photoelectric effect by an incoming photon (in black) and production of electron (in blue).

The photoelectric cross-section describes the absorption of an incoming photon ( $p' = \gamma$ ) and the emission of an atomic electron ( $p = e^-$ ). The microscopic absorption cross-sections are given by

$$\sigma_a^i(E) = \sum_{k=1}^{N_{\text{shells}}} \sigma_a^{i,k}(E), \quad (3.92)$$

where  $\sigma_a^{i,k}(E)$  is given by linear interpolation of the data given by the absorption cross-sections per subshells from the JENDL-5 library [144], which are available for  $Z_i \leq 100$  and for energies up to 100 GeV.

### 3.10.1 Scattering cross-sections of the produced electron

The photoelectric scattering cross-sections are given by

$$\sigma_s^{i,k}(E \rightarrow E', \mu) = \sigma_a^{i,k}(E) \delta(E' - E + U_{i,k}) \Theta(E, \mu), \quad (3.93)$$

where  $E'$  is the energy of the photo-electron,  $U_{i,k}$  is the binding energy of the  $k^{\text{th}}$  shell and the Sauter cross-section for the K-shell, normalized over the angular domain, is given by [149]

$$\Theta(E, \mu) = \Gamma(E) \frac{1 - \mu^2}{(1 - \beta\mu)^4} \left[ 1 + \frac{\gamma(\gamma - 1)(\gamma - 2)}{2} (1 - \beta\mu) \right], \quad (3.94)$$



where the normalization factor is

$$\Gamma(E) = \left\{ \frac{4}{3(1-\beta^2)^2} + \frac{\gamma(\gamma-1)(\gamma-2)}{2\beta^3} \left[ \frac{2\beta}{1-\beta^2} - \ln \left( \frac{1+\beta}{1-\beta} \right) \right] \right\}^{-1}. \quad (3.95)$$

The Legendre moments of the normalized Sauter cross-section are given by

$$\Theta_\ell(E) = \int_{-1}^1 d\mu P_\ell(\mu) \Theta(E, \mu), \quad (3.96)$$

which are integrated analytically based on the same reasoning presented in the Sect. 3.5.1, with Legendre expansion in power of  $\mu$ . The scattering cross-sections are given by

$$\Sigma_{s,\ell,g'}^{\gamma \rightarrow e^-}(E) = \sum_{i=1}^{N_e} \mathcal{N}_{n,i} f_i \int_{E'_{g+1/2}}^{E'_{g-1/2}} dE' \sum_{k=1}^{N_{\text{shells}}} \sigma_{s,\ell}^{i,k}(E \rightarrow E'), \quad (3.97)$$

which can be rewritten as

$$\Sigma_{s,\ell,g'}^{\gamma \rightarrow e^-}(E) = \sum_{i=1}^{N_e} \mathcal{N}_{n,i} f_i \sum_{k=1}^{N_{\text{shells}}} \sigma_a^{i,k}(E) \Theta_\ell(E) \times \begin{cases} 1 & E - U_{i,k} \in [E'_{g+1/2}, E'_{g-1/2}] \\ 0 & \text{otherwise} \end{cases}. \quad (3.98)$$

### 3.10.2 Total cross-sections

The photoelectric total cross-sections are simply

$$\Sigma_t^\gamma(E) = \sum_{i=1}^{N_e} \mathcal{N}_{n,i} f_i \sigma_a^i(E). \quad (3.99)$$

## 3.11 Pair Production

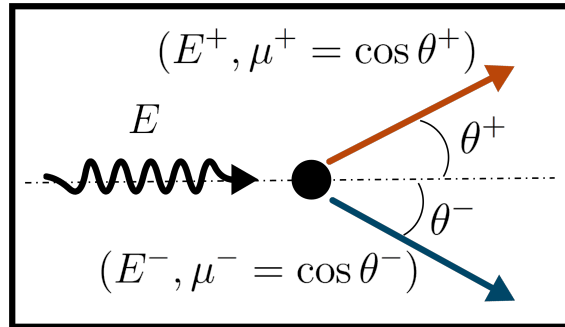


Figure 3.8 Pair production by an incoming photon (in black) and production of an electron (in blue) and a positron (in orange).

An electron-positron pair is produced from the incoming photon energy in the neighbours of the atom, as shown in Fig. 3.8. The threshold for pair production is approximately 1.022 MeV, the required energy to constitute at least the electron and positron mass energy, the extra energy going into their kinetic energies. This phenomenon is the dominant photon process at high energy, about 10 MeV and more. In CEPXS, the macroscopic photon absorption cross-sections related to pair production are given by interpolations and data from Biggs and Lighthill [16,150], while it uses the Sommerfield angular distribution for the pair production. Penelope uses the model of Baró et al. [151], based on the screening function of Tsai [152]. The proposed model is similar to the one of PENELOPE, but it uses tabulated data of the EPDL [148] to match the total cross-sections. It is an improvement over CEPXS since it proposes microscopic cross-sections based on more recent models and data.

The pair production cross-section describes the absorption of a photon ( $p' = \gamma$ ) and the production of an electron ( $p = e^-$ ) and a positron ( $p = e^+$ ). A variation of the semi-empirical model of Baró [151] is used and, in a monoelemental material  $i$ , the differential cross-section is given by

$$\sigma_s^i(E \rightarrow E') = \begin{cases} A(Z_i, E) \left[ 2 \left( \frac{1}{2} - \frac{E' + 1}{E} \right)^2 \phi_{i,1}(E') + \phi_{i,2}(E') \right] & E > 2 \\ 0 & \text{otherwise} \end{cases}, \quad (3.100)$$

where  $E$  is the incoming photon energy and  $E'$  is the outgoing electron or positron energy. The screening function, derived from the one of Tsai [152], are given by

$$\phi_{i,1}(E') = \max \{g_{i,1}(E') + g_{i,0}, 0\} \quad \text{and} \quad \phi_{i,2}(E') = \max \{g_{i,2}(E') + g_{i,0}, 0\}, \quad (3.101)$$

where

$$\begin{aligned} g_{i,1}(E') &= \frac{7}{3} - 2 \ln(1 + b_i^2) - 6b_i \arctan\left(\frac{1}{b_i}\right) - b_i^2 \left[ 4 - 4b_i \arctan\left(\frac{1}{b_i}\right) - 3 \ln\left(1 + \frac{1}{b_i^2}\right) \right], \\ g_{i,2}(E') &= \frac{11}{6} - 2 \ln(1 + b_i^2) - 3b_i \arctan\left(\frac{1}{b_i}\right) - \frac{b_i^2}{2} \left[ 4 - 4b_i \arctan\left(\frac{1}{b_i}\right) - 3 \ln\left(1 + \frac{1}{b_i^2}\right) \right], \end{aligned} \quad (3.102)$$

$$g_{i,0} = 4 \ln(r_{s,i}) - 4f_{C,i}, \quad (3.103)$$

with

$$b_i = \frac{r_{s,i}}{2} \frac{E}{(E' + 1)(E - E' - 1)}. \quad (3.104)$$

The variable  $r_{s,i}$  corresponds to the reduced screening radius, tabulated in Baró [151] for

$Z_i \leq 92$  and extended up to  $Z_i \leq 99$  in PENELOPE [43]. The high-energy Coulomb correction  $f_{C,i}$  is given by [153]

$$f_{C,i} = \alpha^2 Z_i^2 \sum_{k=1}^{\infty} \frac{1}{k(k^2 + \alpha^2 Z_i^2)}. \quad (3.105)$$

As it is done in EGSnrc [44], a normalization factor  $A(Z_i, E)$  is added to the pair production cross-section, which is defined as the ratio between the total cross-sections obtained with  $A(Z_i, E) = 1$  and the tabulated values from JENDL-5 for the pair production in both the nuclear and electron field [144]

$$A(Z_i, E) = \frac{\sigma_t^{\text{JENDL-5}}(Z_i, E)}{\sigma_t(Z_i, E)|_{A=1}}. \quad (3.106)$$

Since pair production and bremsstrahlung are closely related through a substitution rule, the same angular distribution can be used for the electron and positron emission [16, 152]. The double differential cross-section is given by

$$\sigma_s^i(E \rightarrow E', \mu) = \frac{1}{2\pi} \sigma_s^i(E \rightarrow E') \Theta(E, \mu). \quad (3.107)$$

This distribution  $\Theta(E, \mu)$  is defined by Eq. 3.56.

### 3.11.1 Scattering cross-sections for the produced electron and positron

The pair production Legendre moments of the differential scattering cross-sections for the produced leptons are given by

$$\sigma_{s,\ell}^i(E \rightarrow E') = 2\pi \int_{-1}^1 d\mu P_\ell(\mu) \sigma_s^i(E \rightarrow E', \mu) = \sigma_s^i(E \rightarrow E') \Theta_\ell(E), \quad (3.108)$$

where the values of  $\Theta_\ell(E)$  are given by Eq. 3.60. The multigroup Legendre moments of the scattering cross-sections are therefore given by

$$\Sigma_{s,\ell,g'}^{\gamma \rightarrow e^\pm}(E) = \sum_{i=1}^{N_e} \mathcal{N}_{n,i} f_i \int_{E'_{g+1/2}}^{\min\{E'_{g-1/2}, E-2\}} dE_e \sigma_{s,\ell}^i(E \rightarrow E') \mathcal{H}_b, \quad (3.109)$$

which are integrated by numerical quadrature.

### 3.11.2 Total cross-sections

The pair production total cross-sections are defined by

$$\Sigma_t^\gamma(E) = \sum_{i=1}^{N_e} \mathcal{N}_{n,i} f_i \int_0^{E-2} dE' \sigma_{s,0}^i(E \rightarrow E') \mathcal{H}_b \quad (3.110)$$

and are integrated using numerical quadrature.

### 3.11.3 Absorption cross-sections

The pair production absorption cross-sections, which are required for annihilation calculations, are given by

$$\Sigma_a^{\text{pp}}(E) = \sum_{i=1}^{N_e} \mathcal{N}_{n,i} f_i \int_0^{\min\{E-2, E_{G+1/2}\}} dE' \sigma_{s,0}^i(E \rightarrow E') \mathcal{H}_b \quad (3.111)$$

and are integrated using numerical quadrature.

## 3.12 Atomic Relaxation

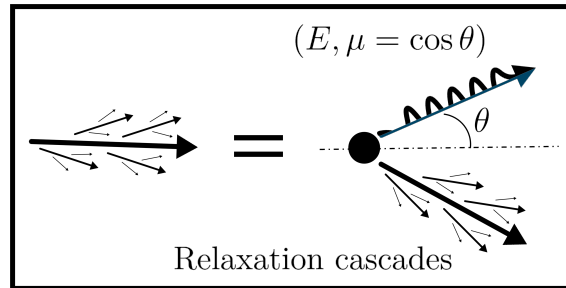


Figure 3.9 A step of the relaxation cascades recursive process, with production of fluorescence (in black) or Auger electron (in blue).

The ionization of an atomic electron in shell  $k$  by an incoming particle leaves behind a vacancy in the atom's electronic structure  $i$ . The inner-shell vacancy in an atom is filled by an outer-shell electron, leading to the emission of a fluorescence photon or the ejection of an Auger electron. This process leaves additional vacancies in outer shells, triggering the production of more photons or electrons, resulting in a recursive process. A step of the recursive process is shown in Fig. 3.9. These intricate relaxation processes are often referred to as relaxation cascades, for which a simplified visual diagram can be found in Lorence et al. [16] and Naceur et al. [37]. Because such calculation can be rather intensive for high-Z atoms, only particle

productions with a probability of occurrence following an initial ionization event greater than 0.1 % are included in this work. Finally, only the  $N_t$  specific electron cascade transitions which result in electron or photon with energy greater than the cutoff energy  $E_{G+1/2}$  are kept for the following calculations.

The differential cross-sections corresponding to the production of either fluorescence ( $p' = \gamma$ ) or Auger electron ( $p' = e^-$ ) following a specific electron cascade transition  $j$ , where  $1 \leq j \leq N_t$ , with the produced particle energy,  $\Delta E_{i,k,j}$ , and the probability of occurrence of the  $j$  electron cascade,  $\eta_{i,k,j}^{p'}$ , is given by

$$\sigma_s^{i,k,j,p \rightarrow p'}(E \rightarrow E') = \eta_{i,k,j}^{p'} \delta(E' - \Delta E_{i,k,j}^{p'}) \sigma_t^{i,k,p}(E), \quad (3.112)$$

where  $\sigma_t^{i,k,p}(E)$  is the  $k$ -shell cross-sections of either inelastic electron ( $p = e^-$ ), inelastic positron ( $p = e^+$ ) or photoelectric interaction ( $p = \gamma$ ) given in previous sections. The values of  $\Delta E_{i,k,j}^{p'}$  and  $\eta_{i,k,j}^{p'}$  are computed using the relaxation data from the JENDL-5 library [144], based on the EADL library [93], as proposed by Hébert and Naceur [38]. The data is available for  $Z \in \{6, 100\}$  for subshells K, L1 to L3, M1 to M5, N1 to N7, O1 to O7, P1 to P3 and Q1. For  $Z \leq 5$ , the produced relaxation radiation energy is very low and can be ignored in transport calculations. The production of fluorescence photon and Auger electron is assumed to be isotropic. Contrary to CEPXS, the relaxation is correlated with the inelastic model [16].

### 3.12.1 Scattering cross-sections of produced Auger electron or fluorescence photon

The relaxation  $\ell = 0$  Legendre moments of the differential scattering cross-sections of the produced Auger electron or fluorescence photon are given by

$$\sigma_{s,0,g'}^{i,p \rightarrow p'}(E) = \sum_{k=1}^{N_{\text{shells}}} \sigma_t^{i,k,p}(E) \sum_{j=1}^{N_t} \eta_{i,k,j}^{p'} \int_{E'_{g+1/2}}^{E'_{g-1/2}} dE' \delta(E' - \Delta E_{i,k,j}^{p'}), \quad (3.113)$$

where the  $\ell \geq 1$  moments are equal to zero since scattering is isotropic. The resulting cross-section is given by

$$\Sigma_{s,0,g'}^{p \rightarrow p'}(E) = \sum_{i=1}^{N_e} \mathcal{N}_{n,if_i} \sum_{k=1}^{N_{\text{shells}}} \sigma_t^{i,k,p}(E) \sum_{j=1}^{N_t} \eta_{i,k,j}^{p'} \times \begin{cases} 1 & \Delta E_{i,k,j}^{p'} \in [E'_{g+1/2}, E'_{g-1/2}] \\ 0 & \text{otherwise} \end{cases}. \quad (3.114)$$

### 3.13 Consolidated Atomic Data

The total cross-sections, the Legendre moments of the scattering cross-sections, the stopping powers and the momentum transfers for each interaction, presented in Sect. 3.4 to Sect. 3.12, are combined.

The consolidated Legendre moments of the scattering cross-sections are given for every particle-to-particle transition:

- **Electron-to-electron:** They are given by the sum of 5 contributions: 1) the scattered electron following impact ionization, 2) the ionized atomic electron (knock-on electron) following impact ionization, 3) the scattered electron following elastic scattering, 4) the slowed-down electron following bremsstrahlung emission and 5) the produced Auger electron following impact ionization, such as

$$\Sigma_{s,\ell,g'}^{e^- \rightarrow e^-}(E) = \underbrace{\left(\text{Eq. 3.15}\right)}_{\text{collisional scattering}} + \underbrace{\left(\text{Eq. 3.17}\right)^1}_{\text{knock-on production}} + \underbrace{\left(\text{Eq. 3.37}\right)}_{\text{elastic scattering}} + \underbrace{\left(\text{Eq. 3.58}\right)}_{\text{radiative scattering}} + \underbrace{\left(\text{Eq. 3.114}\right)}_{\text{auger electron production}}. \quad (3.115)$$

- **Electron-to-photon:** They are given by the sum of 2 contributions: 1) the produced bremsstrahlung photon and 2) the produced fluorescence following impact ionization, such as

$$\Sigma_{s,\ell,g'}^{e^- \rightarrow \gamma}(E) = \underbrace{\left(\text{Eq. 3.61}\right)}_{\text{bremsstrahlung production}} + \underbrace{\left(\text{Eq. 3.114}\right)}_{\text{fluorescence production}}. \quad (3.116)$$

- **Electron-to-positron:** There is no electron interaction that produces positron and, then,

$$\Sigma_{s,\ell,g'}^{e^- \rightarrow e^+}(E) = 0. \quad (3.117)$$

- **Photon-to-electron:** They are given by the sum of 4 contributions: 1) the ionized atomic electron following Compton interaction, 2) the produced photo-electron, 3) the generated electron following pair production interaction and 4) the produced Auger

---

<sup>1</sup>Note that the elastic scattering is transport corrected and its soft component is extracted, as defined by Sect. 3.5.3.

electrons following photoelectric interaction, such as

$$\Sigma_{s,\ell,g'}^{\gamma \rightarrow e^-}(E) = \underbrace{\left( \text{Eq. 3.90} \right)}_{\text{compton production}} + \underbrace{\left( \text{Eq. 3.98} \right)}_{\text{photoelectric production}} + \underbrace{\left( \text{Eq. 3.109} \right)}_{\text{pair production}} + \underbrace{\left( \text{Eq. 3.114} \right)}_{\text{auger electron production}}. \quad (3.118)$$

- **Photon-to-photon:** They are given by the sum of 4 contributions: 1) the photons from the annihilation of positrons generated under the cutoff by pair production interaction, 2) the scattered photon following elastic scattering, 3) the scattered photon following Compton interaction and 4) the produced fluorescence following photoelectric interaction, such as

$$\Sigma_{s,\ell,g'}^{\gamma \rightarrow \gamma}(E) = \underbrace{\left( \text{Eq. 3.78} \right)}_{\text{annihilation production}} + \underbrace{\left( \text{Eq. 3.81} \right)}_{\text{Rayleigh scattering}} + \underbrace{\left( \text{Eq. 3.88} \right)}_{\text{Compton scattering}} + \underbrace{\left( \text{Eq. 3.114} \right)}_{\text{fluorescence production}}. \quad (3.119)$$

- **Photon-to-positrons:** They have only one contribution: 1) the produced positron following pair production, such as

$$\Sigma_{s,\ell,g'}^{\gamma \rightarrow e^+}(E) = \underbrace{\left( \text{Eq. 3.109} \right)}_{\text{pair production}}. \quad (3.120)$$

- **Positron-to-electron:** They are given by the sum of 2 contributions: 1) the produced knock-on electron following impact ionization and 2) the produced Auger electron following impact ionization, such as

$$\Sigma_{s,\ell,g'}^{e^+ \rightarrow e^-}(E) = \underbrace{\left( \text{Eq. 3.17} \right)}_{\text{knock-on production}} + \underbrace{\left( \text{Eq. 3.114} \right)}_{\text{auger electron production}}. \quad (3.121)$$

- **Positron-to-photon:** They are given by the sum of 5 contributions: 1) the produced bremsstrahlung photon, 2) the highest-energy photon produced by annihilation of positrons, 3) the lowest-energy photon produced by annihilation of positrons, 4) the photons produced by annihilation of positrons scattering under the energy cutoff following either impact ionization or bremsstrahlung interaction and 5) the produced

fluorescence following impact ionization, such as

$$\Sigma_{s,\ell,g'}^{e^+ \rightarrow \gamma}(E) = \underbrace{\left(\text{Eq. 3.61}\right)}_{\text{bremsstrahlung production}} + \underbrace{\left(\text{Eq. 3.73}\right) + \left(\text{Eq. 3.75}\right) + \left(\text{Eq. 3.77}\right)}_{\text{annihilation interaction}} + \underbrace{\left(\text{Eq. 3.114}\right)}_{\text{fluorescence production}}. \quad (3.122)$$

- **Positron-to-positrons:** They are given by the sum of 3 contributions: 1) the scattered positrons following impact ionization, 2) the scattered positron following elastic scattering and 3) the slowed-down positron following bremsstrahlung production, such as

$$\Sigma_{s,\ell,g'}^{e^+ \rightarrow e^+}(E) = \underbrace{\left(\text{Eq. 3.15}\right)}_{\text{collisional scattering}} + \underbrace{\left(\text{Eq. 3.37}\right)^1}_{\text{elastic scattering}} + \underbrace{\left(\text{Eq. 3.58}\right)}_{\text{radiative scattering}}. \quad (3.123)$$

The electron consolidated total cross-sections are given by the sum of 3 contributions: 1) the impact ionization, 2) the elastic scattering and 3) the bremsstrahlung interaction, such as

$$\Sigma_t^{e^-}(E) = \underbrace{\left(\text{Eq. 3.18}\right)}_{\text{impact ionization}} + \underbrace{\left(\text{Eq. 3.46}\right)^1}_{\text{elastic scattering}} + \underbrace{\left(\text{Eq. 3.62}\right)}_{\text{bremsstrahlung scattering}}, \quad (3.124)$$

the photon consolidated total cross-sections are given by the sum of 4 contributions: 1) the Rayleigh scattering, 2) the Compton scattering, 3) the photoelectric effect and 4) the pair production interaction, such as

$$\Sigma_t^{\gamma}(E) = \underbrace{\left(\text{Eq. 3.82}\right)}_{\text{impact ionization}} + \underbrace{\left(\text{Eq. 3.91}\right)}_{\text{Compton scattering}} + \underbrace{\left(\text{Eq. 3.99}\right)}_{\text{photoelectric interaction}} + \underbrace{\left(\text{Eq. 3.110}\right)}_{\text{pair production}}, \quad (3.125)$$

and the positron consolidated total cross-sections are given by the sum of 4 contributions: 1) the impact ionization, 2) the elastic scattering and 3) the bremsstrahlung interaction and 4) the annihilation interaction, such as

$$\Sigma_t^{e^+}(E) = \underbrace{\left(\text{Eq. 3.18}\right)}_{\text{impact ionization}} + \underbrace{\left(\text{Eq. 3.46}\right)^1}_{\text{elastic scattering}} + \underbrace{\left(\text{Eq. 3.62}\right)}_{\text{bremsstrahlung scattering}} + \underbrace{\left(\text{Eq. 3.76}\right)}_{\text{annihilation interaction}}. \quad (3.126)$$

The electron and positron consolidated stopping powers are given by the sum of 2 contribu-



tions: 1) the impact ionization and 2) the bremsstrahlung interaction, such as

$$S^{\text{e}\pm}(E) = \underbrace{\left(\text{Eq. 3.30}\right)}_{\text{impact ionization}} + \underbrace{\left(\text{Eq. 3.65}\right)}_{\text{bremsstrahlung scattering}}, \quad (3.127)$$

and there is no photon stopping powers and, then,

$$S^\gamma(E) = 0. \quad (3.128)$$

The only momentum transfer contribution, for electron and positron, comes from the soft components of the elastic cross-sections such as

$$T^{\text{e}\pm}(E) = \underbrace{\left(\text{Eq. 3.48}\right)}_{\text{soft elastic component}}, \quad (3.129)$$

while there is none for photon and, then,

$$T^\gamma(E) = 0. \quad (3.130)$$

## 3.14 Results and Discussion

### 3.14.1 An open-source alternative to CEPXS

The construction of these multigroup cross-sections has led to the development of RADIANT [154], an open-source alternative to CEPXS. The RADIANT package contains coupled photon-electron-positron multigroup cross-sections and discrete ordinates capabilities. It is written in 100% pure Julia, an open-source programming language providing Python-like readability and flexibility, combined with execution times comparable to those of C++ and FORTRAN [155]. Such a choice is unconventional since deterministic and Monte Carlo codes are generally written in C++ or FORTRAN, but it was made for research purposes. By proposing an open-source, easily readable and writable code, the aim is to accelerate the implementation and the testing of new models to close the gap between Monte Carlo and deterministic algorithms. An oriented-object framework has been implemented to make the code user-friendly. Large atomic datasets, such as Boschini et al. parameters for elastic cross-sections [117] or Seltzer and Berger scaled cross-sections [132], are saved in files based on Hierarchical Data Format 5 (HDF5) [156] using JLD2.jl package <sup>2</sup>, which allows the reg-

---

<sup>2</sup>JLD2.jl package: <https://github.com/JuliaIO/JLD2.jl>

istry of complex Julia data structures. All these datasets' size is less than 100 Mo, which is relatively small for today's computers. Small datasets, such as atomic weights or subshells energies, are written directly in the Julia code. All atomic datasets are publicly available in literature or public databases such as the Evaluated Nuclear Data File (ENDF) database <sup>3</sup>. Comprehensive documentation of the code is still ongoing.

The RADIANT package can be found in a public GitHub repository <sup>4</sup>. It is also registered in the Julia programming language General registry.

### 3.14.2 Comparison of Boltzmann Fokker-Planck solver with a reference Monte-Carlo solver

#### Numerical results

In order to test the aforementioned models, the energy spectrum per particle and the energy deposition profile calculated with RADIANT will be compared to the ones in the Monte Carlo calculations. Such results offer a comprehensive overview of its algorithms' performance and limitations. We are considering normally incident electron and photon beams on water (H<sub>2</sub>O), aluminum (Al) and gold (Au). The incident beam has energies of 1 MeV, 10 MeV and 100 MeV, which correspond respectively to Fig. 3.10, Fig. 3.11 and Fig. 3.12.

The spatial domain, along the principal axis, is two times the range of electrons in the material at the incident beam energy, while the transverse size is assumed to be infinite. This assumption greatly simplifies the BFP transport equation [37, 157]. Nonetheless, it reduces the source of error related to multidimensional transport with discrete ordinates solver, notably the ray effect. The spatial domain is divided into 80 equal-size voxels. The energy domain is divided into 80 logarithmically spaced energy groups, where the mean energy  $E_1$  of the most energetic group is the incident beam energy, and the cutoff energy is given by  $E_{G+1/2} = 1$  keV, which is the lowest energy bound available by the developed models. To deal with the derivative in space and energy, a 2<sup>nd</sup>-order accurate adaptive coupled space-energy scheme, developed in Chap. 5 and presented at M&C 2023 conference [158], is employed. It produces mainly positive and monotone solutions and, therefore, more physical solutions. For angular discretization, the discrete ordinates' method with Galerkin quadrature methodology, as developed by Morel [17], is used, while the angular Fokker-Planck term, which deals with the momentum transfer, is treated using a finite-difference approach which ensures 2<sup>nd</sup> order accurate, positive and monotone treatment of forward scattering [128, 159]. Since the beam under consideration is normally incident, the choice was made to utilize a 16-point Gauss-

---

<sup>3</sup>ENDF database: <https://www-nds.iaea.org/exfor/endl.htm>

<sup>4</sup>Radiant.jl package: <https://github.com/CBienvenue/Radiant.jl>

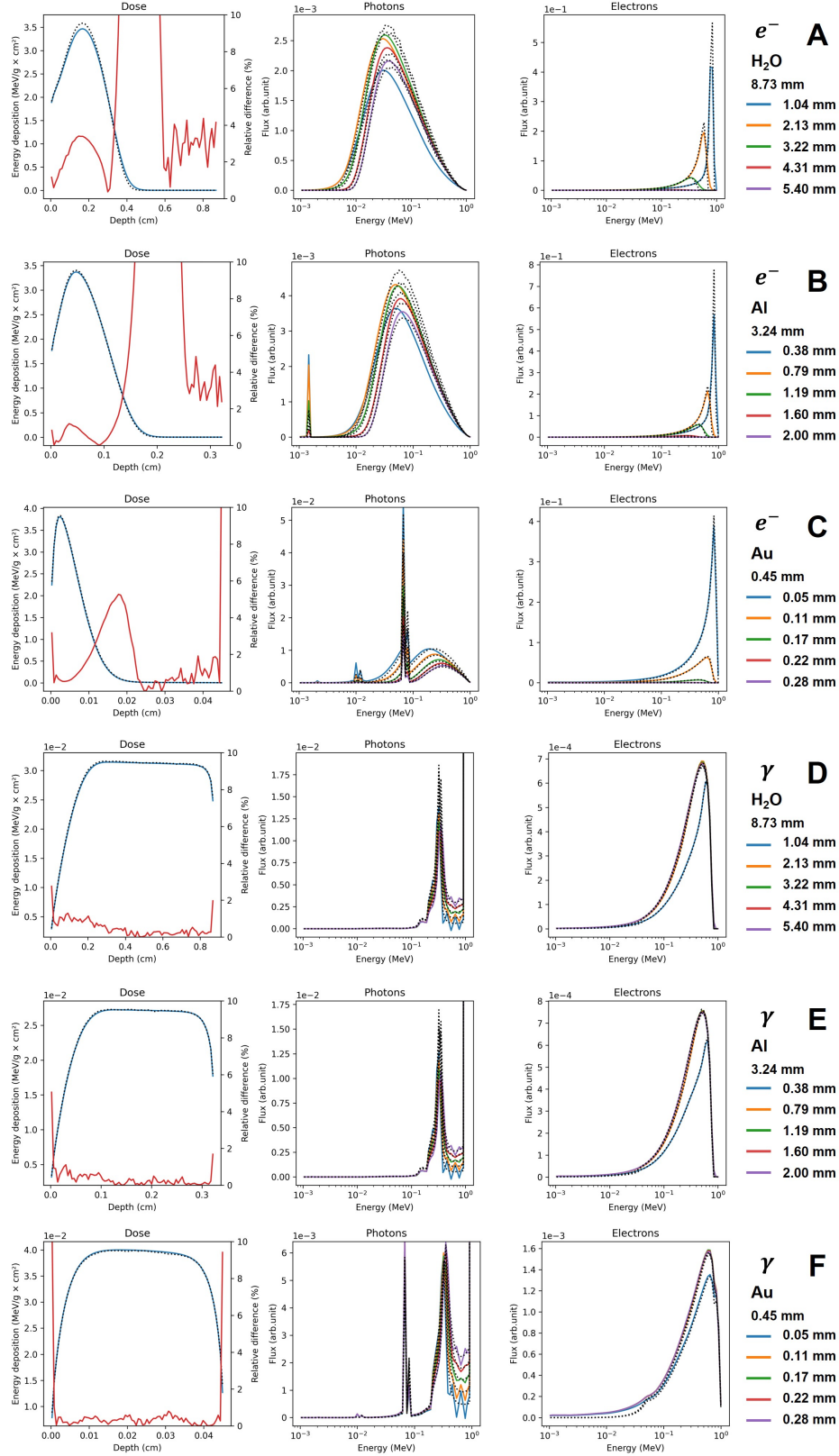


Figure 3.10 Dose and energy spectrum per particle for normally incident 1 MeV electron and photon beams on water, aluminum and gold. Dotted black curves are from GEANT4, while coloured curves are from our deterministic Boltzmann Fokker-Planck algorithms. The length of the slab is indicated on the right, as well as the depth at which each energy spectrum curves are extracted. Relative differences in dose deposition are given in red.

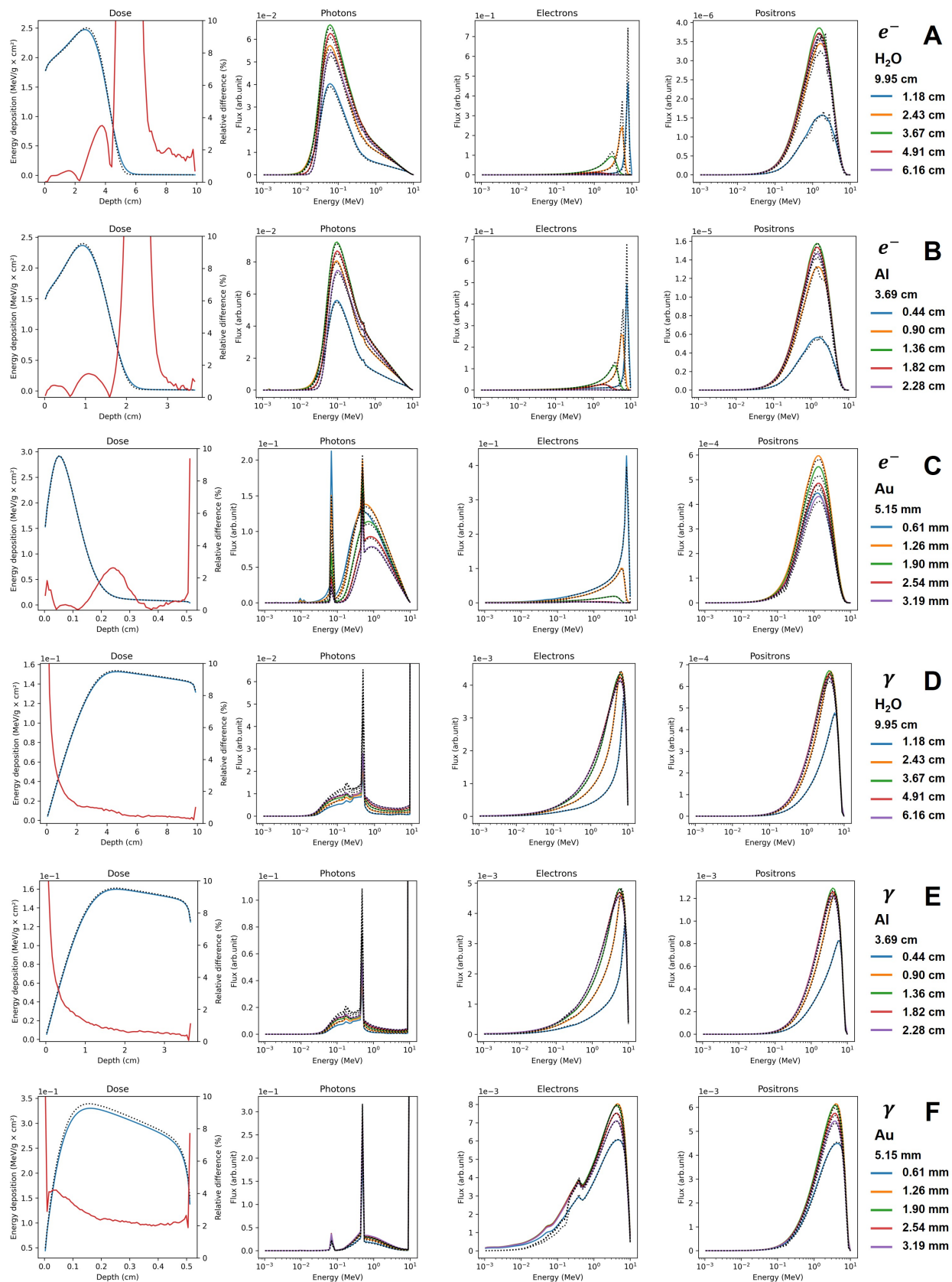


Figure 3.11 Dose and energy spectrum per particle for normally incident 10 MeV electron and photon beams on water, aluminum and gold. The curve definition are given in Fig. 3.10.

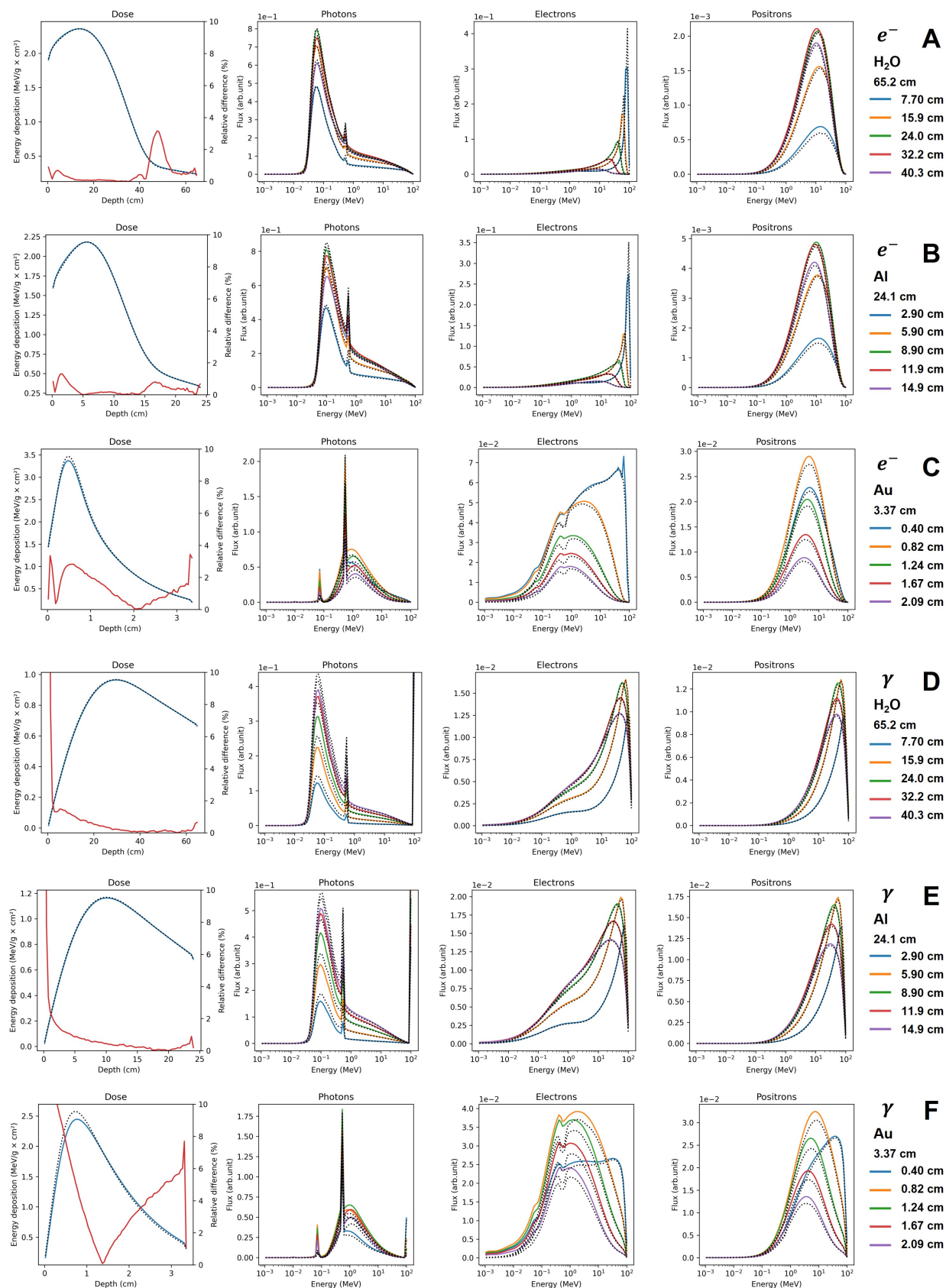


Figure 3.12 Dose and energy spectrum per particle for normally incident 100 MeV electron and photon beams on water, aluminum and gold. The curve definition are given in Fig. 3.10.

Lobatto quadrature, as it incorporates an integration point along  $\mu = 0$ . Galerkin quadrature has a restriction concerning the Legendre order, which has to be  $L = 15$ . This methodology is presented in further detail in Chap. 4.

The reference Monte Carlo solutions are obtained from GEANT4 package [42, 160], using the G4EmPenelope constructor [43], based on PENELOPE physics models, which are widely recognized as a state-of-the-art for electron, positron and photon transport. In order to extract the energy spectrum in GEANT4, the occurrence of a type of particle in an energy group and a voxel is counted and saved in a matrix  $\mathcal{M}$  of size  $3 \times 80 \times 80$ . At each step of particle interaction and transport, the particle's kinetic energy and its pre- and post-step positions are measured. Then, for each voxel  $j$  the particle crosses, for the particle  $i$  with kinetic energy in energy group  $k$ , the particle travel length during the step, divided by the total number of voxels crossed by the particle, is added to the counting matrix  $\mathcal{M}_{i,j,k}$ . For calculations, 100 million incident particles are simulated for 1 MeV and 10 MeV beams and 10 million for 100 MeV ones. Scoring cells of the same size as the discretized space and energy domains of RADIANT deterministic algorithms and the same 1 keV cutoff are used. While the transverse width cannot be set to infinity in GEANT4, setting 100 meters width, which is exceedingly more than the electron range, practically gives the same results.

## Discussion

Beforehand, a Monte Carlo solution's numerical limitation must be emphasized. For electrons or positrons, in their energy spectrum curves at a specific energy, the Monte Carlo curves exhibit a sudden drop, while RADIANT curves remain smooth and regular. This discrepancy is evident in the electron spectrum depicted in Fig. 3.10F around 50 keV or Fig. 3.11F around 100 keV. The reason behind this difference lies in the modelling choices of the PENELOPE algorithm, as implemented in GEANT4, which opts not to generate knock-on electrons below a specific threshold [140]. This method is typical of mixed, or class II, Monte Carlo algorithms [43, 161], which distinguishes between soft and catastrophic scattering events. In contrast, the knock-on energy cutoff in RADIANT is set at the cutoff energy  $E_{G+1/2}$  and the methodology outlined by Karakow [122] is adopted to ensure compatibility between the elastic model and this choice of cutoff to avoid double counting issues. Consequently, RADIANT transports low-energy knock-on electrons and the particles they produce upon interaction with matter, potentially resulting in differences in particle distribution at low energies. Otherwise, the Monte Carlo energy spectrum curves should accurately represent the particles' distribution in the medium.

That said, the results, presented in Fig. 3.10 to Fig. 3.12, underline the potential of dis-

crete ordinates solver for general-purpose coupled photon-electron-positron transport. Our algorithms' energy deposition profiles remain close to the Monte Carlo ones, with a typical relative difference of a few percent, except in a few parts of the spatial domain, usually where the energy deposition is low. These differences will be analyzed in the following paragraphs. A brief examination of the energy spectrum per particle at different depths is sufficient to recognize that RADIANT estimations of the energy distribution of every particle species in any depth in the material are comparable with the Monte Carlo ones. Analyzing the energy spectrum is a valuable tool to assess the quality of the cross-sections.

For energy deposition, the most obvious deviation from reference is the relative difference peak between the maximum of the dose curve and the bremsstrahlung tail for electrons beams (Fig. 3.10 to Fig. 3.12, A to C), which is more dominant at low  $Z$  and low energy. This error is solely caused by the coupled space-energy discretization of the BFP equation, which struggles with the highly varying solution in space and energy that occurs with charged particle transport, and not by the cross-sections models and discretization [47, 158]. For example, while the employed adaptive schemes overestimate the dose in that region, the linear discontinuous scheme underestimates the energy deposition and even produces a negative dip in that same region [48]. The impact of different choices of coupled energy-space schemes is analyzed in Sect. 5.5.2, showing that the difficulty of converging the high variations of the solution in the coupled space-energy grid is the issue. It could be significantly reduced either by increasing the number of voxels and of energy groups or by using higher-order coupled space-energy schemes [48, 157, 162], while full mitigation of the error in that regions will require innovative work.

For 1 MeV electron beam (Fig. 3.10, A to C), substantive relative differences are observable in the curve's tail, which reaches 5% in water and aluminum. Moreover, the photon spectrum is shifted to the left-bottom compared to the Monte Carlo ones. These disparities are related to the interaction that results in energy deposition that far in the medium, mainly by the electron produced by bremsstrahlung photons. The photon spectrum shows that RADIANT curves do not match the reference ones, and while this difference could be attributed to the photon interaction, they seem to perform well in incoming photon benchmark (Fig. 3.10, D to F), besides the oscillatory behaviour which will be explained shortly. The origin of the discrepancies is likely related to the production of bremsstrahlung photons, but we failed to isolate the root cause. Both PENELOPE and EGSnrc documentations recommend using and use, an interpolation table with increased granularity compared to the one of the Seltzer and Berger [44, 132, 136] and interpolation methods that differ from the one used through this work, namely the monotone cubic Hermite spline method [90]. In the GEANT4 implementation of PENELOPE [163], the angular distribution of the bremsstrahlung photon is, like

RADIANT, based on the tables of Pořkus [137] rather than the more scarce tables of Kissel et al. [134]. Further investigations will be required to assess the quality of the bremsstrahlung emission modelization of both RADIANT and GEANT4.

For 1 MeV photon beam (Fig. 3.10 D to F), the photon spectrum shows nonphysical oscillation and even negativities. It is known that the integration of Klein-Nishina Legendre moments is a challenging task due to catastrophic cancellations [164] and, while suitable Legendre moments are enforced by setting higher moments upper bounds, further work will be required to get rid of these artifacts. Nonetheless, while adding a Waller-Hartree incoherent scattering factor to the Klein-Nishina helps consider bindings effects, it omits Doppler broadening and its consequences on angular deviation and energy loss. Brusa et al. proposed a relativistic impulse approximation description of Compton scattering, which formulation is subshell-based like the photoelectric or inelastic model, and such model is implemented in state-of-the-art Monte Carlo code such as PENELOPE and EGSnrc [146]. The production of Legendre moments of these cross-sections is not easy since two layers of integrations have to be done, which is difficult to do analytically but would be too slow to evaluate numerically. Given that such a model is implemented, relaxation could be directly correlated with Compton ionization in the same way as presented in this work. It would be great if such subshell-based Compton cross-sections could be added to the Evaluated Photon Data Library (EPDL), the source of most of the photon cross-sections in this work. Another improvement to Compton scattering could be to divide scattering interactions into soft and catastrophic components, like the impact ionization and Bremsstrahlung cross-sections.

The pair production models could also be greatly improved if provided with tables similar to the one of Bremsstrahlung rather than the proposed approximate analytic model normalized by tabulated total cross-sections [165]. Moreover, explicit triplet production cross-sections would be preferable to the current approach, since such a phenomenon results in an electron ionization event and relaxation cascades. As for both photoelectric and coherent cross-sections, which data is given by the Evaluated Photon Data Library, seems pretty efficient.

In the energy spectrum, the location of the fluorescence and Auger electron production peaks and the annihilation peaks at 511 keV correspond to the Monte Carlo reference ones. Note that the relaxation peaks, especially the annihilation peak, overestimate the particle production compared to Monte Carlo. This overshooting should be expected because the high Monte Carlo knock-on electron cutoff decreases the low-energy electron contribution to relaxation processes. The use of the Evaluated Atomic Data Library comprehensive dataset of atomic transitions, correlated with ionizing interactions such as photoelectric effect and inelastic interactions, can be very efficient in deterministic calculations. For the annihilation peak,



there is a blind spot. The rate of positrons that scatter under the cutoff energy is estimated using the catastrophic impact ionization and bremsstrahlung cross-sections. However, it neglects that an important source of annihilation photon comes from positrons continuously slowing down to the cutoff energy. For impact ionization, which produces the vast majority of such positrons, a major improvement would be to develop an accurate soft absorption cross-section for positrons in the same way soft stopping powers are produced independently from the catastrophic models that are unprecise for small energy losses. Until then, the annihilation photon production is underestimated, resulting in a local deposition of energy and charge, rather than transporting that energy and charge further via annihilation photons.

Elastic cross-sections at low energies should be investigated more. GEANT4, using the G4EmPenelope constructor, uses Urban's model of multiple scattering under 100 MeV and a mixed scattering model over 100 MeV, which was shown to be less accurate than both EGSnrc and PENELOPE approach [120]. Since the deterministic model is based on the EGSnrc approach, the GEANT4 reference may be less accurate. Nonetheless, the Riley model in CEPXS is likely more accurate than the Mott model with Seltzer correction, but it does not contain the Kawrakow correction to avoid double counting issues with knock-on electrons. Evaluating the exactness of the elastic model and its compatibility with the knock-on electron model is not as easy of a task as it seems, but it should be done.

As for the impact ionization model, while the stopping power should be very accurate for energies down to 1 keV, the catastrophic models could be improved further. These models, while taking into account binding energies, are based on Møller and Bhabha cross-sections which are theoretical models for impact ionization with free electrons, neglecting any screening effect due to the electronic structure of the atom. These become increasingly inaccurate to represent inner-shells ionization, notably in high-Z atoms like gold. Bote et al. have proposed interpolation formula and data, based on the mixed uses of the relativistic plane-wave and distorted-wave Born approximation, for inner-shells ionization [166, 167]. The implementation of such a model should be considered to improve impact ionization cross-sections, but also to provide a soft absorption cross-section for positrons to estimate accurately the production of annihilation photons.

### 3.14.3 Comparison with experimental energy and charge deposition benchmarks

#### Numerical results

To further establish the performance of the proposed physics models, energy and charge deposition profiles from incident electron beams for different materials and energies are com-

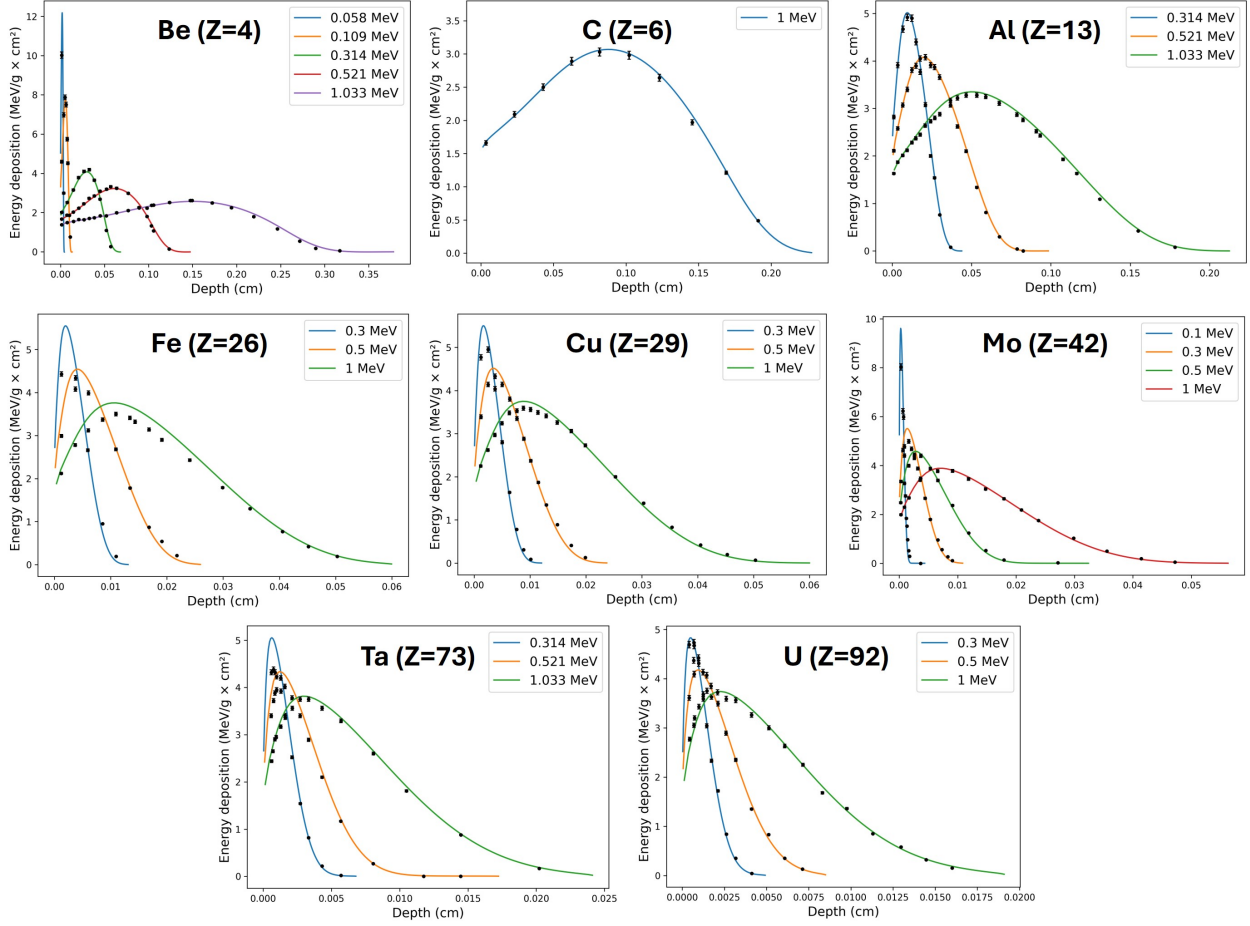


Figure 3.13 Energy deposition for normally incident electron beams on beryllium, carbon, aluminum, iron, copper, molybdenum, tantalum and uranium. The experimental data comes from Lockwood et al. [168].

pared with experimental data. For the following comparison, the spatial domain, along the principal axis, is 1.2 times the depth of the last experimental data, while the transverse size is assumed to be infinite. The spatial domain is divided into 80 equal-size voxels. The energy domain is divided into 80 logarithmically spaced energy groups, where the mean energy  $E_1$  of the most energetic group is the incident beam energy, and the cutoff energy is given by  $E_{G+1/2} = 1$  keV, which is the lowest energy bound available in the developed models. To deal with the derivative in space and energy, a 3<sup>rd</sup>-order accurate discontinuous Galerkin coupled space-energy scheme is employed. For angular discretization, the discrete ordinates method with Galerkin quadrature methodology is used. Since the beam under consideration is normally incident, the choice was made to utilize a 14-point Gauss-Lobatto quadrature, as it incorporates an integration point along  $\mu = 0$ .

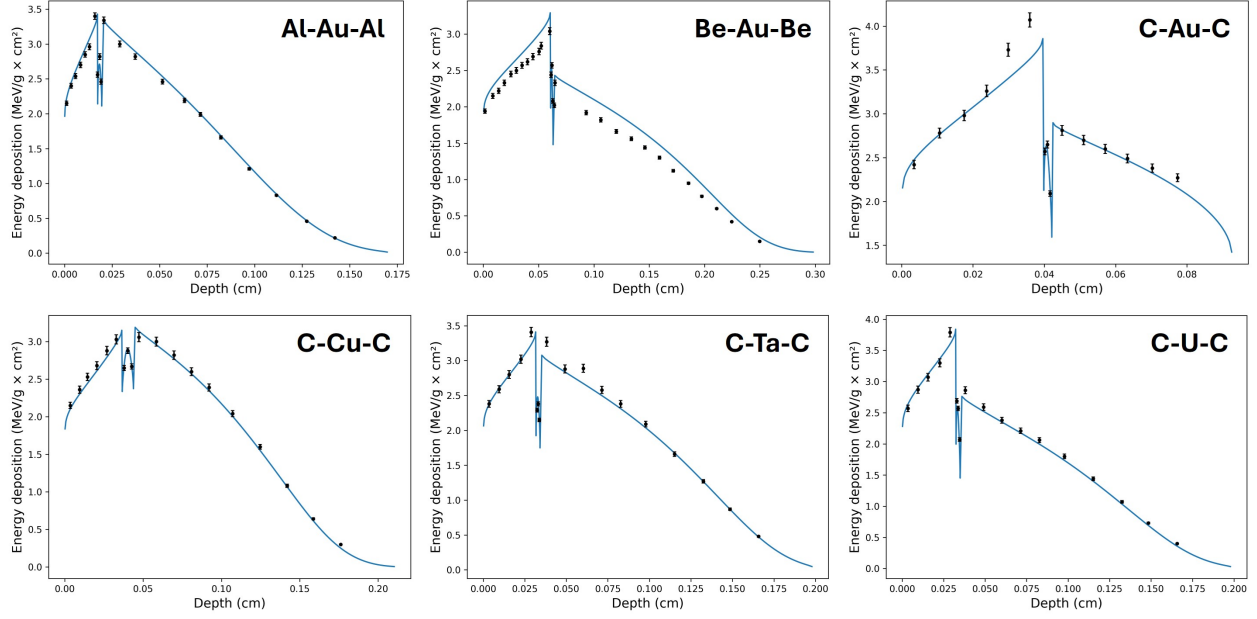


Figure 3.14 Energy deposition for 1 MeV normally incident electron beams on multilayer assembly. The experimental data comes from Lockwood et al. [168].

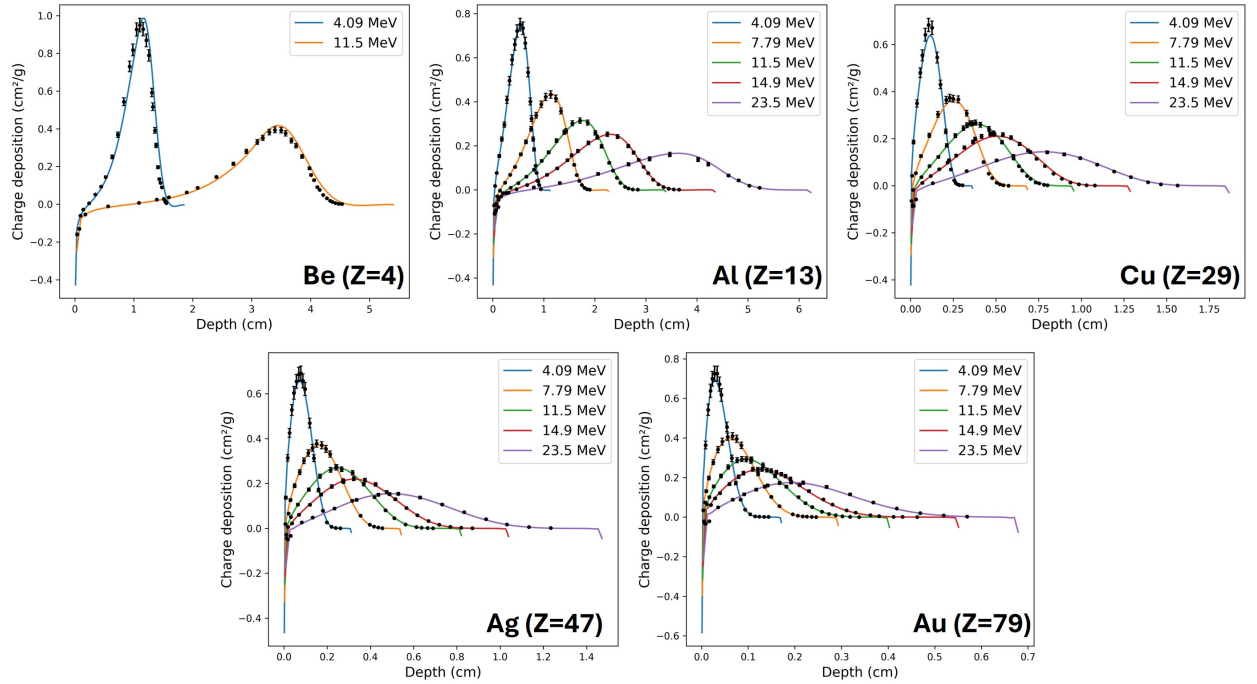


Figure 3.15 Charge deposition for normally incident electron beams on beryllium, aluminum, copper, silver and gold. The experimental data comes from Tabata et al. papers [169–171].

Lockwood et al. [168] has produced an extensive set of experimental energy deposition measurements. That work gives such measurements in beryllium, carbon, aluminum, iron, copper, molybdenum, tantalum and uranium for electron beams of 58 keV to 1.033 MeV. Nonetheless, it also provides measurement in a multilayer medium, exhibiting high-Z/low-Z interfaces, which is very useful to attest to the quality of the scattering modelization. The layer interstices are located at 0.0854 cm and 0.1396 cm (Al-Au-Al), 0.21031 cm and 0.26619 cm (Be-Au-Be), 0.184197 cm and 0.24093 cm (C-Au-C), 0.169475 cm and 0.272868 cm (C-Cu-C), 0.14674 cm and 0.2 cm (C-Ta-C), 0.15 cm and 0.2086 cm (C-U-C). These values, not provided in Lockwood's work, are obtained by estimating these boundaries' location directly in the graph and should be close enough to the actual value. The energy deposition results for monoelemental material are shown in Fig. 3.13, while they are shown in Fig. 3.14 for multilayer medium.

Tabata et al. [170] gives experimental measurements of charge deposition in beryllium, aluminum, copper, silver and gold for electron beams of 4.09 MeV, 7.79 MeV, 11.5 MeV, 14.9 MeV and 23.5 MeV. However, these values are given as the net charge deposited to the total charge of the absorbed electrons, not as the net charge deposited to the total charge of the incident electrons. The following equation can be used to convert between the two definitions [170]

$$D_c^{\text{incident electrons}}(Z, x, E) = \left(1 - \eta(Z, E)\right) D_c^{\text{absorbed electrons}}(Z, x, E), \quad (3.131)$$

where  $Z$  is the atomic number,  $x$  is the depth,  $E$  is the kinetic energy of the incident electron and  $\eta(Z, E)$  is the backscattering coefficient. Tabata et al. [171] proposed an empirical equation to compute backscattering coefficients for  $Z \geq 6$ . This equation is used for all materials but beryllium ( $Z = 4$ ), for which backscattering coefficients are extracted from tables in [169, 170]. The charge deposition results are shown in Fig. 3.15.

## Discussion

Overall, these results show that the proposed physics models and the coupled photon-electron-positron discrete ordinates solver can reproduce experimental energy and charge deposition profiles rather accurately. While the quality of the results in some materials is excellent, such as in aluminum or uranium, the difference between experimental measurement and simulation can be exacerbated in iron or copper for example. Such deviation seems to be due to limits in the physics models rather than in the discretization methods since similar deviations are observed when these same Lockwood's benchmarks are compared with Monte-

Carlo results from TIGER [168] or MCNP6 [172]. GEANT4 models also have been compared to this experimental data [173] and, while they perform better on iron and copper than RADIANT, they are worse in molybdenum and uranium. Such results underline the limit of comparing Monte-Carlo and determinist solvers between themselves, which is widely done in the literature. While such an approach is great at first to develop a cross-section library such as the one presented in this section, it can be misleading when attempting to improve the models. However, experimental energy and charge deposition in a semi-infinite medium are rather scarce in the literature, restricted to a few atoms over a limited range of energies. It would be very useful to have such tabulated experimental data for electron or photon beams, systematically for every atom and some compounds (e.g. water), for energies ranging from a few keV to a few GeV. This could have a major impact on the development of combined cross-section models for both Monte-Carlo and deterministic solvers.

### 3.15 Conclusion and Perspectives

In this chapter, coupled photon-electron-positron multigroup cross-sections were developed for the BFP equation. The models and their multigroup representation were developed for nine kinds of interactions: impact ionization, elastic scattering of leptons, bremsstrahlung production, annihilation, Rayleigh scattering, Compton scattering, photoelectric effect, pair production and relaxation cascades. Comparative analysis is presented, confronting the discrete ordinates BFP equation, fed with the coupled cross-sections, with reference Monte Carlo code GEANT4. The benchmark consists of three materials (water, aluminum and gold), two kinds of incoming beams (photon and electron), and three energies (1 MeV, 10 MeV and 100 MeV). The results compare energy deposition and energy spectrum profiles. It shows that the determinist and the Monte Carlo calculations give similar results, with a typical discrepancy of a few percent for dose deposition profiles but in a few isolated parts of the domain. The main discrepancy between the deterministic and Monte Carlo solutions is then discussed, and improvements are proposed. Nonetheless, the deterministic calculations are compared with experimental data for energy and charge deposition. Comparisons show that RADIANT can predict accurately the deposition of charge and energy in the medium.

St-Aubin et al. [23, 24] and Pautz et al. [34] have developed capacities to treat external magnetic and electric fields, which can be useful in medical applications such as MRI-guided radiotherapy or for radiation effect on electronic devices. In its work, based on CEPXS, St-Aubin et al. have assumed that positrons can be treated as electrons. This approximation can be acceptable if the population of positrons is small compared with the electron ones. However, as shown in Fig. 3.11 and Fig. 3.12, the population of electrons is not an order

of magnitude greater than the population of positrons in many cases, notably with photon beams greater than pair production threshold and high-Z materials. Since electrons and positrons deflect in different directions due to the application of external magnetic or electric fields, it is important to explicitly transport positrons.

These developments have resulted in the foundation of RADIANT, an open-source alternative to CEPXS for generating coupled photon-electron-positron cross-sections. It enables the development and testing of newer, faster, and more accurate models using the methodology presented in this chapter without much constraint. The aim is for this tool to close the gap between deterministic and Monte Carlo methods, seriously undermining the perceived preeminence of Monte Carlo methods in RTP.

## CHAPTER 4    ANGULAR DISCRETIZATION OF THE BOLTZMANN FOKKER-PLANCK EQUATION

### 4.1 Foreword

The motivation behind the following methods was to provide fast, robust and flexible angular discretization of the transport equation in the presence of highly anisotropic scattering, such as that encountered with charged particle transport. Monotone and moment-preserving schemes for the AFP operator are developed, compatible with nonorthogonal quadrature on the unit sphere, permitting the use of optimal quadrature, which minimizes the number of sweeping through the spatial domain to achieve a specific accuracy. For transport calculations based on the BFP equation, numerical results show that spurious oscillations in flux solution related to anisotropic scattering can be eliminated with such discretization.

My original contribution to the angular discretization of the transport equation involves the utilization of the AFP operator to address the positivity and monotonicity challenges associated with the Boltzmann operator in the presence of anisotropic scattering. To this end, I have developed a novel monotone and moment-preserving finite-difference scheme, which is based on the Voronoi tessellation of the unit sphere and is compatible with nonorthogonal quadrature. The work presented here has been submitted to Nuclear Science and Engineering on August 13<sup>th</sup>, 2024 [174].

In Sect. 4.2, discrete ordinates limitations and improvement, such as the Galerkin quadrature method, are discussed. In Sect. 4.3, discretization for the angular Fokker-Planck are proposed, notably finite-difference ones. The performance of the new discretization techniques are then presented in Sect. 4.4.

### 4.2 Methods for Discrete Ordinates Solvers

#### 4.2.1 Matrix formalism

The discrete ordinates method, described in Sect. 2.4.1, can be expressed in matrix form. The  $N_d$  discrete angular fluxes in  $\mathbf{\Psi}_g^p = (\Psi_{g,1}^p, \Psi_{g,2}^p, \dots, \Psi_{g,N_d}^p)$  have to be converted in  $N_q$  spherical harmonics flux moments in  $\mathbf{\Phi}_g^{p'} = (\Phi_{g,1}^{p'}, \Phi_{g,2}^{p'}, \dots, \Phi_{g,N_q}^{p'})$  and vice-versa. These conversion operations can be expressed in matrix form using both the discrete-to-moment (**D**) and the

moment-to-discrete ( $\mathbf{M}$ ) matrices, i.e.

$$\Phi_g^p = \mathbf{D}\Psi_g^{p'} \quad \text{and} \quad \Psi_g^p = \mathbf{M}\Phi_g^{p'}. \quad (4.1)$$

Their components are given by

$$D_{q,n} = w_n R_{\ell_q}^{m_q}(\Omega_n) \quad \text{and} \quad M_{n,q} = \frac{2\ell_q + 1}{4\pi} R_{\ell_q}^{m_q}(\Omega_n), \quad (4.2)$$

for  $n = 1, N_d$  and  $q = 1, N_q$ , where both indices  $\ell_q$  and  $m_q$  are function of their index  $q$ . In 1D Cartesian geometry, these components reduce to

$$D_{q,n} = w_n P_{\ell_q}(\mu_n) \quad \text{and} \quad M_{n,q} = \frac{2\ell_q + 1}{2} P_{\ell_q}(\mu_n), \quad (4.3)$$

where  $P_{\ell_q}(\mu_n)$  are Legendre polynomials and  $\ell_q = q - 1$ . The quadrature on the unit sphere reduces to a quadrature over the director cosine  $\mu$  domain, which spans from -1 to 1. With these matrices, the vector containing the  $N_d$  Boltzmann sources,  $\mathbf{Q}_{p,g}^B = (Q_{p,g,1}^B, Q_{p,g,2}^B, \dots, Q_{p,g,N_d}^B)$ , is given by

$$\mathbf{Q}_{p,g}^B = \sum_{p' \in P} \sum_{g'=1}^{N_{g,p}} \mathbf{M} \Sigma^{g' \rightarrow g, p' \rightarrow p} \mathbf{D} \Psi_{g'}, \quad (4.4)$$

where  $\Sigma^{g' \rightarrow g, p' \rightarrow p}$  is a  $N_q \times N_q$  diagonal matrix with each component associated with  $\ell_q$ -order Legendre moments of the scattering cross-section ( $\Sigma_{q,q}^{g' \rightarrow g, p' \rightarrow p} = \Sigma_{s,\ell_p,g' \rightarrow g}^{p' \rightarrow p}$ ). The definition of indexes  $\ell_q$  and  $m_q$  depending on index  $q$  can seem messy, but it is a compact and versatile notation that enables any choice of a subset of spherical harmonics. For instance, based on Reed's  $S_2$  suitable interpolation basis for level-symmetric quadrature in 2D Cartesian geometry [175], composed of  $R_0^0$ ,  $R_1^0$ ,  $R_1^1$  and  $R_2^1$ , the corresponding indexes are given by  $\ell = (0, 1, 1, 2)$  and  $\mathbf{m} = (0, 0, 1, 1)$ , and the diagonal of the  $\Sigma^{g' \rightarrow g, p' \rightarrow p}$  matrix is given by  $(\Sigma_{s,0,g' \rightarrow g}^{p' \rightarrow p}, \Sigma_{s,1,g' \rightarrow g}^{p' \rightarrow p}, \Sigma_{s,1,g' \rightarrow g}^{p' \rightarrow p}, \Sigma_{s,2,g' \rightarrow g}^{p' \rightarrow p})$ .

#### 4.2.2 Quadrature over the unit sphere

The efficiency of a quadrature defined over the unit sphere with  $N_d$  nodes that integrate a subspace of spherical harmonics of maximum degree  $N$  is given by [176]

$$\eta = \frac{(N+1)^2}{3N_d}. \quad (4.5)$$

A quadrature set is optimal if  $\eta \approx 1$ , while it is suboptimal if  $\eta < 1$ . For discrete ordinates transport, using an optimal quadrature is desirable since the multiplication of nodes increases



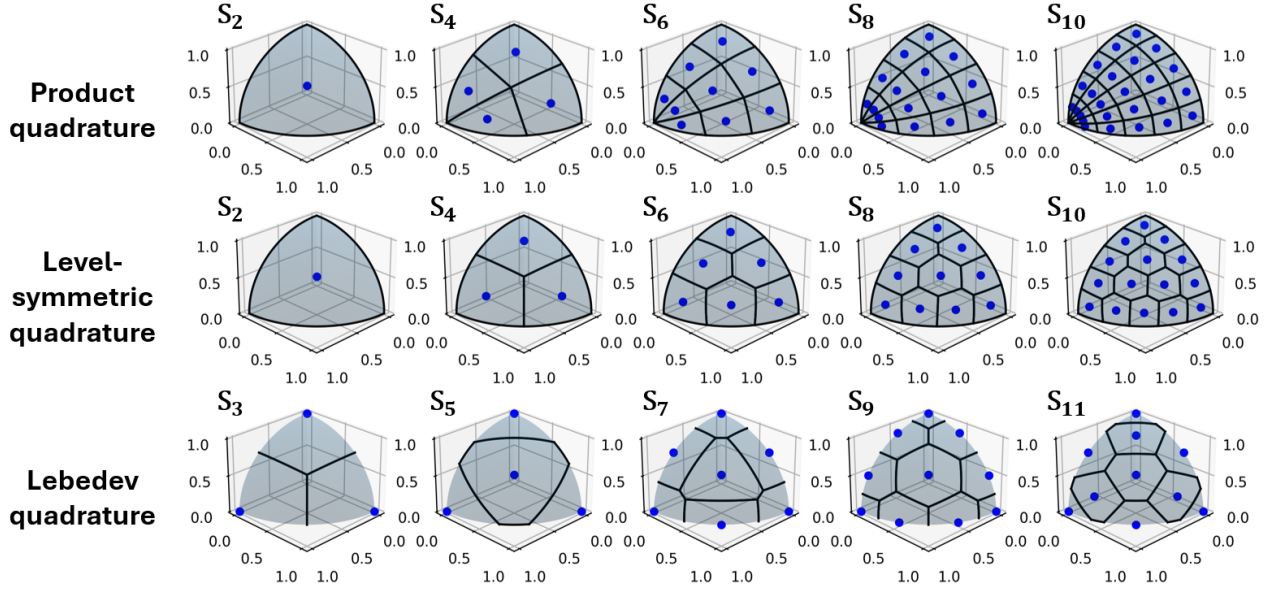


Figure 4.1 Voronoi tessellation of the product quadrature (Gauss-Legendre quadrature along  $\mu$  and Chebychev quadrature along  $\phi$ ), the level-symmetric quadrature (Carlson  $ES_N$  quadrature) and Lebedev quadrature.

the number of required sweepings over the spatial domain per iteration to achieve a specific accuracy. The most straightforward quadrature set over the sphere is a product quadrature, which consists of the product of two quadrature sets, over line segment, defined along the  $\mu$  and  $\phi$  coordinates. This quadrature with  $N_d = 2N^2$  nodes divides the angular domain in orthogonal meshes, but accurate calculations with such quadrature set are exceedingly expensive since the quadrature efficiency is a constraint between  $\eta = 1/6$  ( $N \rightarrow \infty$ ) and  $\eta = 3/8$  ( $N = 2$ ). The node distribution over the sphere is far from uniform with dense pileups of nodes near  $\mu = \pm 1$  while it also lacks 4-fold ( $C_4$ ) rotational symmetry, as it can be seen in Fig. 4.1. In order to deal with these issues, so-called level-symmetric quadrature was developed. For example, Carlson's  $ES_N$  quadrature [177], which present a more uniform nodes distribution and  $C_4$  rotational symmetry. It has  $N_d = N(N + 2)$  nodes, and the resulting efficiency of this type of quadrature still is a constraint between  $\eta = 1/3$  ( $N \rightarrow \infty$ ) and  $\eta = 3/8$  ( $N = 2$ ). Fortunately, optimal, or slightly optimal, quadrature do exist, such as the ones of Lebedev [178–180], Ahrens [181], Heo and Xu [182] or Bellet et al. [183]. Lebedev quadrature possesses octahedral rotation and inversion symmetry and has, as the Gauss-Lobatto in 1D, nodes along the Cartesian reference system axis. While these nodes along the axis help treat normally incident beams, they lead to an asymmetric subset of spherical harmonics for the Galerkin quadrature methods, which is not ideal [184].

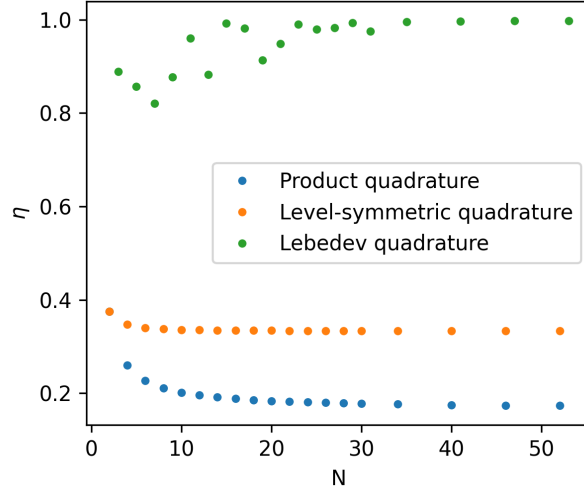


Figure 4.2 Quadrature efficiency of the product quadrature (Gauss-Legendre quadrature along  $\mu$  and Chebychev quadrature along  $\phi$ ), the level-symmetric quadrature (Carlson  $ES_N$  quadrature) and Lebedev quadrature.

### 4.2.3 Galerkin quadrature

It is well known that there is an equivalence in 1D Cartesian or spherical geometry between the discrete ordinates solution, using  $N$ -order Gauss-Legendre quadrature with Legendre expansion of degree  $N - 1$ , and the  $(N - 1)$ -order spherical harmonics (or  $P_N$ ) solution using Mark boundary conditions [50, 54]. In such case, the conversion matrices  $\mathbf{D}$  and  $\mathbf{M}$  are the inverse of each other, which is desirable for multiple reasons. This property ensures, assuming that scattering is described by a Dirac delta function,

$$\Sigma_{s,g \rightarrow g}^{p \rightarrow p}(\mu) = \delta(\mu - 1), \quad (4.6)$$

that discretized Boltzmann operator gives the exact analytic result [17]. That scattering leaves the angular flux unchanged  $Q_{p,g}^{\mathbf{B}, \mathbf{e}1}(\mu) = \Psi_g^p(\mu)$ . The moments of this scattering cross-section are given by

$$\Sigma_{s,\ell,g \rightarrow g}^{p \rightarrow p} = \int_{-1}^1 d\mu P_\ell(\mu) \Sigma_{s,g \rightarrow g}^{p \rightarrow p}(\mu) = 1 \quad (4.7)$$

since  $P_\ell(1) = 1$  for any  $\ell$ . Then, the matrix  $\Sigma^{g \rightarrow g, p \rightarrow p}$  is equal to the identity matrix  $I$ . Since  $\mathbf{M} = \mathbf{D}^{-1}$ , then Eq. 4.4 reduces to

$$\mathbf{Q}_{p,g}^{\mathbf{B}, \mathbf{e}1} = \Psi_g^p \quad (4.8)$$

which is equivalent to write

$$Q_{p,g}^{\mathbf{B}, \mathbf{e}1}(\mu_n) = \Psi_g^p(\mu_n) \quad (4.9)$$

for  $n = 1, N_d$ , which is the exact solution. Such property ensures that the Boltzmann operator will accurately treat anisotropic scattering regardless of its strength. It is essential for charged particle transport, which deals with highly forward-peaked scattering. Nonetheless, the fact that  $\mathbf{M} = \mathbf{D}^{-1}$  also ensures that the transport correction leaves the  $S_N$  solution invariant. This correction reduces the Legendre moments of the cross-sections for charged particle transport by many orders of magnitude, significantly accelerating the source iteration process. Unfortunately, in multidimensional geometries, there is no known quadrature set on the unit sphere and choice of polynomial expansion such as  $\mathbf{M} = \mathbf{D}^{-1}$ . Therefore, the  $S_N$  method can lead to inaccurate and non-physical solutions, particularly with anisotropic scattering. Moreover, as shown by Pautz and Adams [45], the source iteration process can even diverge, especially in a scattering-dominated medium where the scattering ratio is already close to one. Defining the in-group scattering ratio matrix as

$$\mathbf{C}^{p,g} = \frac{1}{\Sigma_{t,g}^p} \mathbf{D} \mathbf{M} \Sigma^{g \rightarrow g, p \rightarrow p}, \quad (4.10)$$

which is a diagonal matrix whose components are scattering ratios. If  $\mathbf{M} = \mathbf{D}^{-1}$ , then the scattering ratio will be given by

$$\mathbf{C}_{q,q}^{p,g} = \frac{\Sigma_{s,\ell_q,g \rightarrow g}^{p \rightarrow p}}{\Sigma_{t,g}^p} = \frac{\Sigma_{s,\ell_q,g \rightarrow g}^{p \rightarrow p}}{\Sigma_{s,0,g \rightarrow g}^{p \rightarrow p} + \Sigma_{a,g}^p} \leq \frac{\Sigma_{s,0,g \rightarrow g}^{p \rightarrow p}}{\Sigma_{s,0,g \rightarrow g}^{p \rightarrow p} + \Sigma_{a,g}^p} \leq 1. \quad (4.11)$$

Otherwise, the scattering ratio will differ from these values and can potentially exceed one. This has significant consequences, as it introduces a non-physical multiplicative factor in the medium. This can lead to the divergence of the iterative process and the generation of unusable non-physical solutions, highlighting the potential concerns associated with the classical  $S_N$  method.

The Galerkin quadrature method, developed by Morel, solves the most critical issues of classical  $S_N$  method [17]. It ensures the exact integration of a Dirac scattering and, corollary that the transport correction leaves the solution of the transport equation invariant [47]. It ensures that the scattering ratio remains under one and, therefore, proper convergence of the source iteration process [45]. The Galerkin method, however, does not offer a solution to artifacts related to scattering positivity [17] and no Galerkin quadrature method with positive weights have been found [47]. A Galerkin quadrature is obtained by inverting either the discrete-to-moment or the moment-to-discrete matrix, which is evaluated using Eqs. 4.3 or 4.2, i.e.

$$\mathbf{D} = \mathbf{M}^{-1} \quad \text{or} \quad \mathbf{M} = \mathbf{D}^{-1} \quad (4.12)$$

This requires that  $\mathbf{D}$  and  $\mathbf{M}$  are square and invertible matrices. If we can compute  $\mathbf{M}$  with these two properties, it can be inverted to find  $\mathbf{D}$ , or vice-versa, to obtain a Galerkin quadrature [17, 185]. For these matrices to be square, the number of directions  $N_d$  (nodes of the quadrature) has to be strictly equal to the number of basis functions used in the angular flux expansion. The matrix columns must be linearly independent for them to be invertible, which is not the case for any choice of basis functions.

For 1D Cartesian geometries, the Legendre polynomial can be used as a basis function. For a quadrature with  $N_d$  nodes, the Legendre polynomial up to order  $N_d - 1$  should be chosen as the basis function of the angular flux expansion. Then, the discrete-to-moment matrix ( $\mathbf{D}$ ) could be computed using Eqs. 4.3 and inverted to obtain the moment-to-discrete matrix ( $\mathbf{M}$ ), or vice-versa, without any additional difficulties since the previously stated choice of Legendre polynomial yield square and invertible matrices. The Galerkin quadrature method permits the use of Gauss-Lobatto quadrature, which is very useful when dealing with normally incident particle sources because of its two nodes aligned with the Cartesian reference system axis ( $\mu = -1$  and  $\mu = 1$ ) [47].

For multidimensional geometries, the real spherical harmonics are used as basis functions. For a quadrature with  $N_d$  nodes, a subset of spherical harmonics must be chosen, knowing that no subset leads to an invertible discrete-to-moment matrix (or vice-versa). While rules for a suitable subset of spherical harmonics exist with product or level-symmetric quadrature (see [17, 184]), a Gram-Schmidt procedure is proposed by Drumm et al. to choose a subset of spherical harmonics such as the columns of  $\mathbf{D}$  (or  $\mathbf{M}$ ) are linearly independent, irrespective of the choice of quadrature [32, 186]. This procedure, for either the discrete-to-moment matrix ( $\mathbf{D}$ ) or the moment-to-discrete matrix ( $\mathbf{M}$ ) to be invertible, is shown at Alg. 1. It should be noted that quadrature on the unit sphere and real spherical harmonics basis functions can also be used in 1D geometry.

### 4.3 Discretization Schemes for the Angular Fokker-Planck Operator

The  $N_d$  AFP sources are given by

$$\mathbf{Q}_{p,g,n}^{\text{AFP}} = T_g^p \mathcal{M} \Psi_{p,g,n}, \quad (4.13)$$

where  $T_g^p$  is the momentum transfer and the square  $N_d \times N_d$  mapping matrix  $\mathcal{M}$  define the FP scattering between  $N_d$  angular flux. Leaving the forward-peaked part of the elastic scattering in the cross-sections to be dealt with the Boltzmann operator is equivalent to extracting the

---

**Algorithm 1** Gram-Schmidt procedure to choose a suitable subset of spherical harmonics for the discrete-to-moment matrix ( $\mathbf{D}$ ) or the moment-to-discrete matrix ( $\mathbf{M}$ ) to be invertible.

---

```

1:  $(\ell[1], \mathbf{m}[1]) \leftarrow (0, 0)$ 
2: for  $\ell \in [1, N_d]$  do
3:    $\mathbf{D}[1, n] \leftarrow \omega_n R_0^0(\Omega_n)$  or  $\mathbf{M}[n, 1] \leftarrow \frac{1}{4\pi} R_0^0(\Omega_n)$ 
4:    $\mathbf{v}_1[n] \leftarrow R_0^0(\Omega_n)$ 
5:    $\mathbf{u}_1[n] \leftarrow \mathbf{v}_1[n] / \|\mathbf{v}_1\|$ 
6: end for
7:  $i \leftarrow 1$ 
8: for  $\ell \in [1, \infty]$  do
9:   if  $N_{\text{dim}} = 2$  then  $m_{\min} = 0$  else if  $N_{\text{dim}} = 3$  then  $m_{\min} = -\ell$  end if
10:  for  $m \in [m_{\min}, \ell]$  do
11:    for  $\ell \in [1, N_d]$  do
12:       $\mathbf{v}_{i+1}[n] \leftarrow R_\ell^m(\Omega_n)$ 
13:    end for
14:     $\mathbf{v}_{i+1} \leftarrow \mathbf{v}_{i+1} - \sum_{n=1}^i \langle \mathbf{u}_n, \mathbf{v}_{i+1} \rangle \mathbf{u}_n$ 
15:    if  $\|\mathbf{v}_{i+1}\| > \epsilon$  then
16:       $(\ell[i+1], \mathbf{m}[i+1]) \leftarrow (\ell, m)$ 
17:      for  $\ell \in [1, N_d]$  do
18:         $\mathbf{D}[i+1, n] = \omega_n R_\ell^m(\Omega_n)$  or  $\mathbf{M}[n, i+1] \leftarrow \frac{2\ell+1}{4\pi} R_\ell^m(\Omega_n)$ 
19:         $\mathbf{u}_{i+1}[n] = \mathbf{v}_{i+1}[n] / \|\mathbf{v}_{i+1}\|$ 
20:      end for
21:       $i \leftarrow i + 1$ 
22:    end if
23:    if  $i = N_d$  then return ( $\mathbf{D}$  or  $\mathbf{M}$ ,  $\ell$  and  $\mathbf{m}$ ) end if
24:  end for
25: end for

```

---

momentum transfer  $T_g^p$  from cross-sections and using the following mapping matrix [128, 187]

$$\mathcal{M} = \mathbf{M} \Sigma^{\text{AFP}} \mathbf{D}, \quad \text{with} \quad \Sigma_{n,q}^{\text{AFP}} = \begin{cases} -\ell_q(\ell_q + 1) & \text{if } n = q \\ 0 & \text{otherwise} \end{cases}. \quad (4.14)$$

With the Galerkin method,  $\mathbf{M} = \mathbf{D}^{-1}$ , and this will be referred to as the Galerkin scheme. It preserves the moments of the AFP operator with the selected subset of spherical harmonics [47], but it does not yield a monotone mapping matrix  $\mathcal{M}$  as the following finite-difference schemes, which is characterized by positive components along the diagonal and negative ones elsewhere [188].

### 4.3.1 1D finite-difference schemes

Morel has developed a finite-difference scheme for the 1D AFP operator that preserves both the zeroth and first angular moments of the analytical AFP operator [128, 159]. The integration of the AFP operator can be either described as the sum over the  $N_d$  interval corresponding to each  $\mu_n$ , between  $\mu_{n-1/2}$  and  $\mu_{n+1/2}$ , or the numerical quadrature over  $\mu$  domain, such as

$$\int_{-1}^1 d\mu Q_{p,g}^{\text{AFP}}(\mu) = \sum_{n=1}^{N_d} \int_{\mu_{n-1/2}}^{\mu_{n+1/2}} d\mu Q_{p,g}^{\text{AFP}}(\mu) = \sum_{n=1}^{N_d} \omega_n Q_{p,g,n}^{\text{AFP}}, \quad (4.15)$$

where  $Q_{p,g,n}^{\text{AFP}}$  is the discretized AFP operator which, by association, can be expressed as

$$Q_{p,g,n}^{\text{AFP}} = \frac{1}{\omega_n} \int_{\mu_{n-1/2}}^{\mu_{n+1/2}} d\mu Q_{p,g}^{\text{AFP}}(\mu). \quad (4.16)$$

Integrating this expression and applying a centred finite-difference scheme to describe derivative at region boundaries becomes

$$Q_{p,g,n}^{\text{AFP}} = \frac{T_g^p}{\omega_n} \left[ \gamma_{n+1/2} \left( \frac{\Psi_{n+1} - \Psi_n}{\mu_{n+1} - \mu_n} \right) - \gamma_{n-1/2} \left( \frac{\Psi_n - \Psi_{n-1}}{\mu_n - \mu_{n-1}} \right) \right], \quad (4.17)$$

where  $\gamma_{n+1/2} = (1 - \mu_{n+1/2}^2)$  and  $\gamma_{n-1/2} = (1 - \mu_{n-1/2}^2)$ . Since Legendre polynomials are eigenfunctions of the Legendre differential equation [128], i.e.

$$\frac{\partial}{\partial \mu} \left[ (1 - \mu^2) \frac{\partial}{\partial \mu} \right] P_\ell(\mu) = -\ell(\ell + 1) P_\ell(\mu), \quad (4.18)$$

the preservation of the Legendre moments of the AFP operator requires the enforcement of

$$\int_{-1}^1 d\mu P_\ell(\mu) Q_{p,g}^{\text{AFP}}(\mu) = -T_g^p \ell(\ell + 1) \int_{-1}^1 d\mu P_\ell(\mu) \Psi(\mu). \quad (4.19)$$

The zeroth and the first moments of the AFP operator are therefore given by

$$\int_{-1}^1 d\mu Q_{p,g}^{\text{AFP}}(\mu) = 0 \quad \text{and} \quad \int_{-1}^1 d\mu \mu Q_{p,g}^{\text{AFP}}(\mu) = -2T_g^p \int_{-1}^1 d\mu \mu \Psi(\mu) \quad (4.20)$$

and should be preserved by the discretized AFP operator, such as,

$$\sum_{n=1}^{N_d} \omega_n Q_{p,g,n}^{\text{AFP}} = 0 \quad \text{and} \quad \sum_{n=1}^{N_d} \omega_n \mu_n Q_{p,g,n}^{\text{AFP}} = -2T_g^p \sum_{n=1}^{N_d} \mu_n \Psi_n. \quad (4.21)$$

Eq. 4.17 do not enforce the preservation of the first moment of the analytic AFP operator. However, setting the  $\gamma_{n+1/2}$  and  $\gamma_{n-1/2}$  as free parameters, Morel has found values for them, such as the zeroth and first moments of the discretized AFP are the same as the analytic operator [159]. The resulting mapping matrix is a tridiagonal matrix in which components are given by

$$\mathcal{M}_{n,m} = \begin{cases} -C_n & \text{if } n = m \\ C_n^- & \text{if } n = m + 1 \\ C_n^+ & \text{if } n = m - 1 \\ 0 & \text{otherwise} \end{cases}, \quad (4.22)$$

where the terms are defined by

$$C_n^- = \frac{C_{n-1/2}}{w_n(\mu_n - \mu_{n-1})}, \quad C_n^+ = \frac{C_{n+1/2}}{w_n(\mu_{n+1} - \mu_n)} \quad \text{and} \quad C_n = C_n^- + C_n^+, \quad (4.23)$$

with the recursion formula

$$C_{n+1/2} = C_{n-1/2} - 2\mu_n w_n \quad \text{and} \quad C_{1/2} = 0. \quad (4.24)$$

The matrix  $\mathcal{M}$  is negative semidefinite (real eigenvalues less or equal to zero), monotone (negative diagonal and positive off-diagonal elements) and diagonally dominant (sum of absolute value of non-diagonal row components is equal to the absolute value of the diagonal component). This discretization scheme can be described as positive since it will yield positive AFP sources given positive angular flux [47, 159]. This scheme is compatible with any 1D quadrature set.

### 4.3.2 2D and 3D finite-difference schemes for orthogonal quadrature

Morel et al. have extended the 1D finite-difference AFP scheme to multidimensional geometries [47, 188]. However, the proposed scheme is constrained to product quadrature, in which angular mesh boundaries are aligned with director cosine  $\mu$  and azimuthal angle  $\phi$ , greatly simplifying the construction of finite-difference methods. It allows computing free parameters independently along  $\mu$  and  $\phi$ , which would not be possible with a nonorthogonal grid on the unit sphere. The discretized AFP operator using the finite-difference method is

given by [188]

$$Q_{p,g,n}^{\text{AFP}} = T_g^p \left[ \frac{\gamma_{i+1/2}}{\omega_i} \left( \frac{\Psi_{i+1,j} - \Psi_{i,j}}{\mu_{i+1} - \mu_i} \right) - \frac{\gamma_{i-1/2}}{\omega_i} \left( \frac{\Psi_{i,j} - \Psi_{i-1,j}}{\mu_i - \mu_{i-1}} \right) \right] \\ + \frac{1}{1 - \mu_i^2} \left[ \frac{\gamma_{i,j+1/2}}{w_j} \left( \frac{\Psi_{i,j+1} - \Psi_{i,j}}{\phi_{j+1} - \phi_j} \right) - \frac{\gamma_{i,j-1/2}}{w_j} \left( \frac{\Psi_{i,j} - \Psi_{i,j-1}}{\phi_j - \phi_{j-1}} \right) \right], \quad (4.25)$$

where  $\omega_i$  and  $w_j$  are respectively the weights of the quadrature along  $\mu$  and  $\phi$ , while index  $i$  and  $j$  correspond to the position along each axis  $\mu$  and  $\phi$  and then are function of  $n$ . The flux  $\Psi_{i,j}$  correspond to the flux at direction  $\Omega_n$ , which corresponds to the pair  $(i, j)$ . The parameters  $\gamma_{i+1/2}$ ,  $\gamma_{i-1/2}$ ,  $\gamma_{i,j+1/2}$  and  $\gamma_{i,j-1/2}$  are used as free parameters to find moment-preserving scheme. Their values are found using method like the 1D techniques of the previous section along each axis  $\mu$  and  $\phi$ . For the 2D AFP operator, the mapping matrix  $\mathcal{M}$  is given by

$$\mathcal{M}_{x,y} = \begin{cases} -C_n - D_{n,i} & \text{if } n = m \text{ and } i = j \\ C_n^- & \text{if } n = m + 1 \text{ and } i = j \\ C_n^+ & \text{if } n = m - 1 \text{ and } i = j \\ D_{n,i}^- & \text{if } n = m \text{ and } i = j + 1 \\ D_{n,i}^+ & \text{if } n = m \text{ and } i = j - 1 \\ 0 & \text{otherwise} \end{cases}, \quad (4.26)$$

with  $x = i + N(n - 1)$  and  $y = j + N(m - 1)$ , where the  $C$ -term are defined by Eq. 4.23 and the  $D$ -terms are defined by

$$D_{n,i}^- = \frac{\gamma_n}{w(\omega_i - \omega_{i-1})(1 - \mu_n^2)}, \quad (4.27)$$

$$D_{n,i}^+ = \frac{\gamma_n}{w(\omega_{i+1} - \omega_i)(1 - \mu_n^2)} \quad (4.28)$$

and

$$D_{n,i} = D_{n,i}^- + D_{n,i}^+ \quad (4.29)$$

The weights of the Chebychev quadrature are given by

$$w = \frac{\pi}{N} \quad \text{and} \quad \omega_i = \frac{(2i - 1)\pi}{2N}, \quad (4.30)$$



while the coefficients  $\gamma_n$  are given by

$$\gamma_n = \frac{\pi^2}{2N \left(1 - \cos\left(\frac{\pi}{N}\right)\right)} \left[ 2(1 - \mu_n^2) + \frac{\sqrt{1 - \mu_n^2}}{\omega_n} \left( C_{n+1/2} d_{n+1/2} - C_{n-1/2} d_{n-1/2} \right) \right], \quad (4.31)$$

with

$$d_{n+1/2} = \frac{\sqrt{1 - \mu_{n+1}^2} - \sqrt{1 - \mu_n^2}}{\mu_{n+1} - \mu_n}. \quad (4.32)$$

For the 3D AFP operator, the mapping matrix  $\mathcal{M}$  is given by

$$\mathcal{M}_{x,y} = \begin{cases} -C_n - E_{n,i} & \text{if } n = m \text{ and } i = j \\ C_n^- & \text{if } n = m + 1 \text{ and } i = j \\ C_n^+ & \text{if } n = m - 1 \text{ and } i = j \\ E_{n,i}^- & \text{if } n = m \text{ and } \{i = j + 1 \text{ or } (i = 1 \text{ and } j = 2N)\} \\ E_{n,i}^+ & \text{if } n = m \text{ and } \{i = j - 1 \text{ or } (i = 2N \text{ and } j = 1)\} \\ 0 & \text{otherwise} \end{cases}, \quad (4.33)$$

with  $x = i + 2N(n - 1)$  and  $y = j + 2N(m - 1)$ , where the  $C$ -term are defined by Eq. 4.23 and where the  $E$ -terms are defined by

$$E_{n,i}^- = \begin{cases} \frac{\gamma_n}{w(\omega_i - \omega_{i-1})(1 - \mu_n^2)} & \text{if } i \neq 1 \\ \frac{\gamma_n}{w(2\pi + \omega_1 - \omega_{2N})(1 - \mu_n^2)} & \text{otherwise} \end{cases}, \quad (4.34)$$

$$E_{n,i}^+ = \begin{cases} \frac{\gamma_n}{w(\omega_{i+1} - \omega_i)(1 - \mu_n^2)} & \text{if } i \neq 2N \\ \frac{\gamma_n}{w(2\pi + \omega_1 - \omega_{2N})(1 - \mu_n^2)} & \text{otherwise} \end{cases} \quad (4.35)$$

and

$$E_{n,i} = E_{n,i}^- + E_{n,i}^+. \quad (4.36)$$

As in the 1D case, these mapping matrices are negative semidefinite and monotone and yield positive sources. When the product quadrature is constructed with the Chebychev azimuthal quadrature, it enforces the preservation of the zeroth and the three first angular moments of the AFP operator. In comparison, it preserves only two out of three first angular moments with other azimuthal quadrature choices. Unfortunately, as underlined in the previous section, product quadrature sets are far from optimal quadrature; their nodes are unevenly distributed on the sphere, and they lack  $\mathbf{C}_4$  rotational symmetry. Using such quadrature in

transport calculations is hugely inefficient due to the enormous number of nodes  $\mathbf{\Omega}_n$  required to achieve a specific accuracy level, which involves sweeping over the spatial domain for each of these directions. The approach has been extended to address nonorthogonal quadrature on the unit sphere in order to tackle these limitations.

### 4.3.3 Voronoi grid on the unit sphere

The following discretization is based on the Voronoi tessellation of the unit sphere by a finite set of points on the sphere. With the resulting grid, a random point  $\mathbf{\Omega}_k$  on the unit sphere is contained in the mesh formed around the point  $\mathbf{\Omega}_n$  such as the distance between the two coordinates over the unit sphere,

$$d_{n,k} = \arccos(\mathbf{\Omega}_n \cdot \mathbf{\Omega}_k) , \quad (4.37)$$

is lower than the distance of point  $\mathbf{\Omega}_k$  with any other point of the set. A vertex, which is a mesh corner, is shared by at least 3 points  $\mathbf{\Omega}_n$ ,  $\mathbf{\Omega}_m$  and  $\mathbf{\Omega}_k$ . The vertex coordinates are given by the intersection of two bisector planes and the unit sphere, given by

$$\begin{cases} x^2 + y^2 + z^2 &= 1 \\ (\mu_n - \mu_m)x + (\eta_n - \eta_m)y + (\xi_n - \xi_m)z &= \mu_n^2 - \mu_m^2 + \eta_n^2 - \eta_m^2 + \xi_n^2 - \xi_m^2 \\ (\mu_n - \mu_k)x + (\eta_n - \eta_k)y + (\xi_n - \xi_k)z &= \mu_n^2 - \mu_k^2 + \eta_n^2 - \eta_k^2 + \xi_n^2 - \xi_k^2 \end{cases} . \quad (4.38)$$

These equations are solved using Newton's root-finding algorithm. The vertices forming the smaller mesh around each point  $\mathbf{\Omega}_n$  are isolated. For the AFP discretization, the Voronoi grid serves only one purpose, that is to establish the neighbors of the mesh generated around point  $\mathbf{\Omega}_n$ , that is all the point  $\mathbf{\Omega}_m$  which mesh share an edge with  $\mathbf{\Omega}_n$  mesh.

### 4.3.4 2D and 3D finite-difference schemes for nonorthogonal quadrature

The AFP operator can be expressed as [29, 189]

$$Q_{p,g}^{\text{AFP}}(\mathbf{\Omega}) = T_g^p \nabla^2 \Psi(\mathbf{\Omega}) = T_g^p \nabla_t \cdot \nabla_t \Psi(\mathbf{\Omega}) , \quad (4.39)$$

where  $\nabla^2$  is the Laplace operator and  $\nabla_t$  is the tangential gradient on the unit sphere  $\mathbb{S}^2$  given by

$$\nabla_t \Psi(\mathbf{\Omega}) = \nabla \Psi(\mathbf{\Omega}) - [\nabla \Psi(\mathbf{\Omega}) \cdot \mathbf{n}(\mathbf{\Omega})] \mathbf{n}(\mathbf{\Omega}) , \quad (4.40)$$

where  $\nabla$  is the usual gradient in  $\mathbb{R}^3$  and  $\mathbf{n}(\boldsymbol{\Omega})$  is the unit normal vector on  $\mathbb{S}^2$  at  $\boldsymbol{\Omega}$ . The integration of the AFP operator over the unit sphere can be described either as the sum of the integral over  $N_d$  non-overlapping regions  $\boldsymbol{\Omega}_n$  covering the totality of  $\mathbb{S}^2$  or by numerical quadrature on  $\mathbb{S}^2$ , such as

$$\int_{\mathbb{S}^2} d^2\Omega Q_{p,g}^{\text{AFP}}(\boldsymbol{\Omega}) = \sum_{n=1}^{N_d} \int_{\boldsymbol{\Omega}_n} d^2\Omega Q_{p,g}^{\text{AFP}}(\boldsymbol{\Omega}) = \sum_{n=1}^{N_d} \omega_n Q_{p,g,n}^{\text{AFP}}, \quad (4.41)$$

where  $\omega_n$  are the quadrature weights and  $Q_{p,g,n}^{\text{AFP}}$  the discretized AFP operator. This discretized operator can be deduced by association from the previous equation, and integral over region  $\boldsymbol{\Omega}_n$  can be simplified using divergence theorem over the spherical domain [29, 190]

$$Q_{p,g,n}^{\text{AFP}} = \frac{1}{\omega_n} \int_{\boldsymbol{\Omega}_n} d^2\Omega Q_{p,g}^{\text{AFP}}(\boldsymbol{\Omega}) = \frac{T_g^p}{\omega_n} \oint_{\delta\boldsymbol{\Omega}_n} d\ell \nabla_t \Psi(\boldsymbol{\Omega}) \cdot \mathbf{n}_\ell, \quad (4.42)$$

where  $\delta\boldsymbol{\Omega}_n$  is the boundary of the region  $\boldsymbol{\Omega}_n$  and  $\mathbf{n}_\ell$  is the normal vector at region boundary on  $\mathbb{S}^2$ . Assuming that the region  $\boldsymbol{\Omega}_n$  is a polygon with  $J_n$  sides, then the integral can be rewritten as the sum of the  $J_n$  integrals over the edges of the  $n^{\text{th}}$  region

$$Q_{p,g,n}^{\text{AFP}} = \frac{T_g^p}{\omega_n} \sum_{j=1}^{J_n} \int_{\delta\boldsymbol{\Omega}_{n,j}} d\ell \nabla_t \Psi(\boldsymbol{\Omega}) \cdot \mathbf{n}_\ell. \quad (4.43)$$

The central finite-difference is used to approximate the previous expression, and the following form is obtained

$$Q_{g,n}^{\text{AFP}} = \frac{T_g^p}{\omega_n} \sum_{j=1}^{J_n} \ell_{n,j} \left[ \frac{\Psi_{g,m_{n,j}} - \Psi_{g,n}}{\Delta x_{n,j}} \right], \quad (4.44)$$

where  $\ell_{n,j}$  is the length of the  $j^{\text{th}}$  edge, which is an arc on the unit sphere,  $\Psi_{g,n} = \Psi_g(\boldsymbol{\Omega}_n)$  is the angular flux along node  $n$ ,  $\Psi_{g,m_{n,j}}$  is the angular flux of the node  $m_{n,j}$  that share the edge  $j$  with the node  $n$  and  $\Delta x_{n,j}$  is the length of the arc between the two nodes  $n$  and  $m$ . Let introduce a general parameter  $\gamma_{n,m_{n,j}}$ , which includes both  $\ell_{n,j}$  and  $\Delta x_{n,j}$ , that is associated with the shared edge between the nodes  $n$ . The property  $\gamma_{n,m} = \gamma_{m,n}$  is enforced, such as each edge is associated with a unique coefficient  $\gamma_{n,m}$  with  $n < m$ . The discretized AFP operator takes the form

$$Q_{g,n}^{\text{AFP}} = \frac{T_g^p}{\omega_n} \sum_{j=1}^{J_n} \gamma_{n,m_{n,j}} [\Psi_{g,m_{n,j}} - \Psi_{g,n}]. \quad (4.45)$$

Fig. 4.3 shows how these relations are defined between adjacent regions on the unit sphere. To define which regions share which edge, a Voronoi tessellation, based on the set of quadrature

nodes, is constructed over the unit sphere such as an arbitrary point on  $\mathbb{S}^2$  belongs to the closest node  $\Omega_n$ , based on the distance defined over  $\mathbb{S}^2$ . Voronoi grids for product, level-quadrature and Lebedev quadrature are shown in Fig. 4.1.

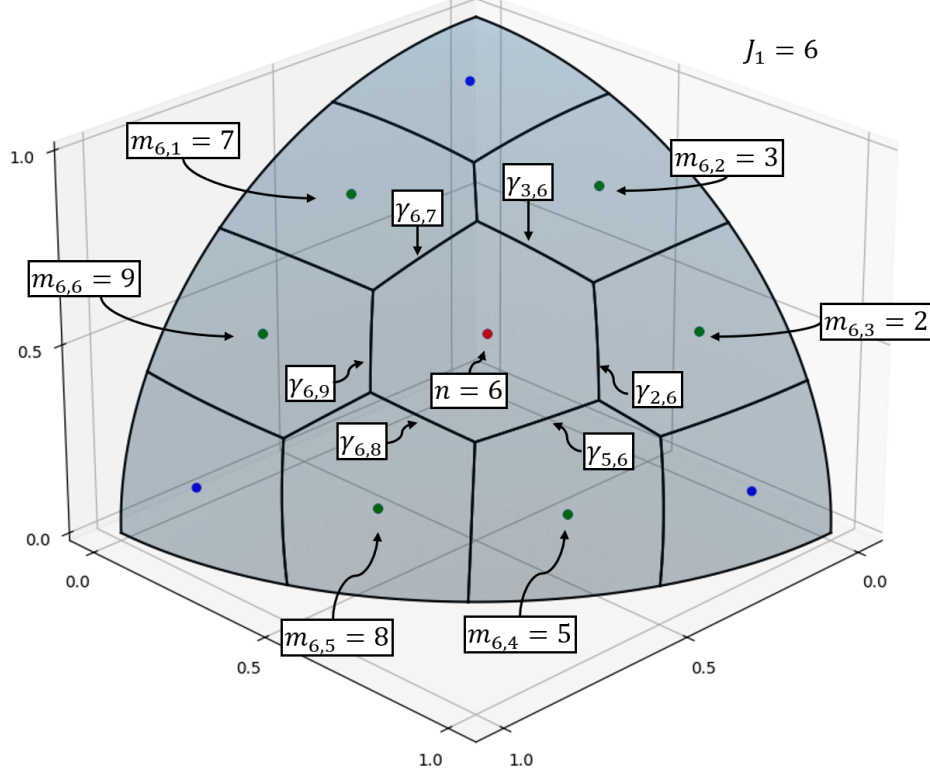


Figure 4.3 Voronoi tessellation of the  $S_8$  Carlson's level-symmetric quadrature nodes on the positive octant of the unit sphere. The red point corresponds to the node  $n = 6$ , and the green ones correspond to the nodes that share one of the  $J_1 = 6$  edges of the region formed by the 6<sup>th</sup> node.

The values of the  $\gamma_{n,m}$  coefficients will be fixed to enforce the preservation of the zeroth and first moments of the flux. Regardless of the value of  $\gamma_{n,m}$ , the discretized AFP operator preserves the null space, meaning that any isotropic angular flux leads to zero. Following that, the spherical harmonics are eigenfunctions of the Laplace operator [188],

$$\nabla^2 R_\ell^m(\Omega) = -\ell(\ell + 1)R_\ell^m(\Omega), \quad (4.46)$$

the preservation of the spherical harmonics moments of the AFP operator requires the enforcement of

$$\int_{\mathbb{S}^2} d^2\Omega R_\ell^m(\Omega) Q_{p,g}^{\text{AFP}}(\mu) = -T_g^p \ell(\ell + 1) \int_{\mathbb{S}^2} d^2\Omega R_\ell^m(\Omega) \Psi(\Omega). \quad (4.47)$$

The zeroth and the three first moments of the AFP operator are, therefore, given by

$$\int_{\mathbb{S}^2} d^2\Omega Q_{p,g}^{\text{AFP}}(\mu) = 0 \quad \text{and} \quad \int_{\mathbb{S}^2} d^2\Omega \Omega Q_{p,g}^{\text{AFP}}(\mu) = -2T_g^p \int_{\mathbb{S}^2} d^2\Omega \Omega \Psi(\Omega) \quad (4.48)$$

and should be preserved by the discretized AFP operator, such as

$$\sum_{n=1}^{N_d} \omega_n Q_{p,g,n}^{\text{AFP}} = 0 \quad \text{and} \quad \sum_{n=1}^{N_d} \omega_n \Omega_n Q_{p,g,n}^{\text{AFP}} = -2T_g^p \sum_{n=1}^{N_d} \omega_n \Omega_n \Psi_n, \quad (4.49)$$

with  $\Omega_n = (\mu_n, \eta_n, \xi_n)$ . The finite-difference scheme is given by Eq. 4.45 to preserve the zeroth moment of the AFP operator for any value of  $\gamma_{n,m}$ . The methodology proposed by Morel et al. [188] is used to find the parameters  $\gamma_{n,m}$  that preserve the three discretized first moments of the flux. Explicit equations for  $\gamma_{n,m}$  are obtained by defining the following complete basis

$$\Psi_{g,k} = (\delta_{1,k}, \delta_{2,k}, \dots, \delta_{N_d,k}), \quad (4.50)$$

where  $\delta_{n,k}$  is the Kronecker delta. Substituting it and Eq. 4.45 in the rightmost expression in Eqs. 4.49 for each  $k = 1, N_d$ , one obtain  $N_d$  equations of the form

$$\sum_{j=1}^{J_k} \gamma_{k,m_{k,j}} [\Omega_{m_{k,j}} - \Omega_k] = -4\omega_k \Omega_k, \quad (4.51)$$

where  $\Omega_{m_{k,j}}$  is the coordinates of the node that share the edge  $j$  with node  $k$ , for a total of  $3N_d$  equations. Regardless of the choice of quadrature, it leads to an overdetermined linear system of equations since the number of unknown parameters  $\gamma_{n,m}$  with  $n < m$ , which is equal to the total number of edges between nodes  $N_{\text{edges}}$ , is smaller than the total number of equations,  $3N_d$ . From Euler's polyhedron formula, which states that the sum of vertices  $N_{\text{vertices}}$ , edges  $N_{\text{edges}}$  and faces  $N_d$  in a convex polyhedron, which the quadrature nodes are forming, is given by Euler characteristic  $\chi = 2$  and from the fact that there are at least three edges connecting at each vertex such as  $2N_{\text{edges}} \geq 3N_{\text{vertices}}$  [191], it follows that

$$N_{\text{edges}} = N_d + N_{\text{vertices}} - 2 \leq 3N_d - 6 \leq 3N_d. \quad (4.52)$$

Fortunately, with any quadrature set we have tested, ranging from product, level-symmetric, and Lebedev quadrature, the resulting system contains redundant equations, likely due to symmetry in these quadrature sets. Solving this system using the Moore-Penrose inverse, also called pseudoinverse, gives an exact solution for  $\gamma_{n,m}$  such that all the  $3N_d$  equations are simultaneously satisfied. The solution is unique since the system's matrix has full column rank. It is observed that all values of  $\gamma_{n,m}$  are positive and respect the quadrature set

symmetries. These observations will require further investigations to assert the properties of quadrature (e.g. required symmetries) compatible with our approach, i.e. leading to an exact solution rather than an inexact least squares solution, which is usually expected with the pseudoinverse.

Using the calculated zeroth and first moment-preserving coefficients  $\gamma_{n,m}$ , the resulting mapping matrix is given by

$$\mathcal{M}_{n,m} = \begin{cases} -\frac{1}{\omega_n} \sum_{j=1}^{J_n} \gamma_{n,m_{n,j}} & \text{if } n = m \\ \frac{\gamma_{n,m}}{\omega_n} & \text{if } m \in \{m_{n,j} : j = 1, J_n\} \\ 0 & \text{otherwise} \end{cases} \quad (4.53)$$

The produced matrix is negative semidefinite and monotone. The presented methodology, applied to product quadrature with Chebychev azimuthal quadrature, reproduces the mapping matrix of the scheme from Morel et al. [188].

#### 4.4 Results and Discussion

This results section has no graph comparison of solutions between the Galerkin quadrature and classical  $S_N$  methods. For example, in 1D geometry, with Gauss-Lobatto quadrature and external sources, the classical  $S_N$  method for electron or positron transport was observed to be either highly inaccurate or unable to converge. While the Gauss-Legendre quadrature naturally generates a Galerkin quadrature, multidimensional transport has no such quadrature. The same problems with 1D Gauss-Lobatto quadrature were observed with multidimensional quadrature, notably with product, level-symmetric and Lebedev quadrature. As discussed in the previous sections, the Galerkin quadrature is not a mere improvement; it should be the foundation of any  $S_N$  solver, nothing less.

The benchmarks are based on pure electron transport in a water slab exposed by an infinitely wide, normally incident 10 MeV electron beam, unless noted otherwise. Elastic, collisional inelastic and Bremsstrahlung interactions, as described in Chap. 3 are considered. Based on Mott cross-sections, the elastic model becomes highly forward-peaked as the particle energy increases, providing an interesting study case for the presented angular discretization models. The energy domain is divided logarithmically into 40 energy groups, where the midpoint of the highest energy group is 10 MeV, and the cutoff energy is 1 keV. Linear discontinuous schemes are used to deal with both space and energy derivatives. Convergence criterion of  $10^{-5}$  is used. Void boundary conditions are applied to the geometry boundaries.

#### 4.4.1 Comparison of Galerkin quadrature methods

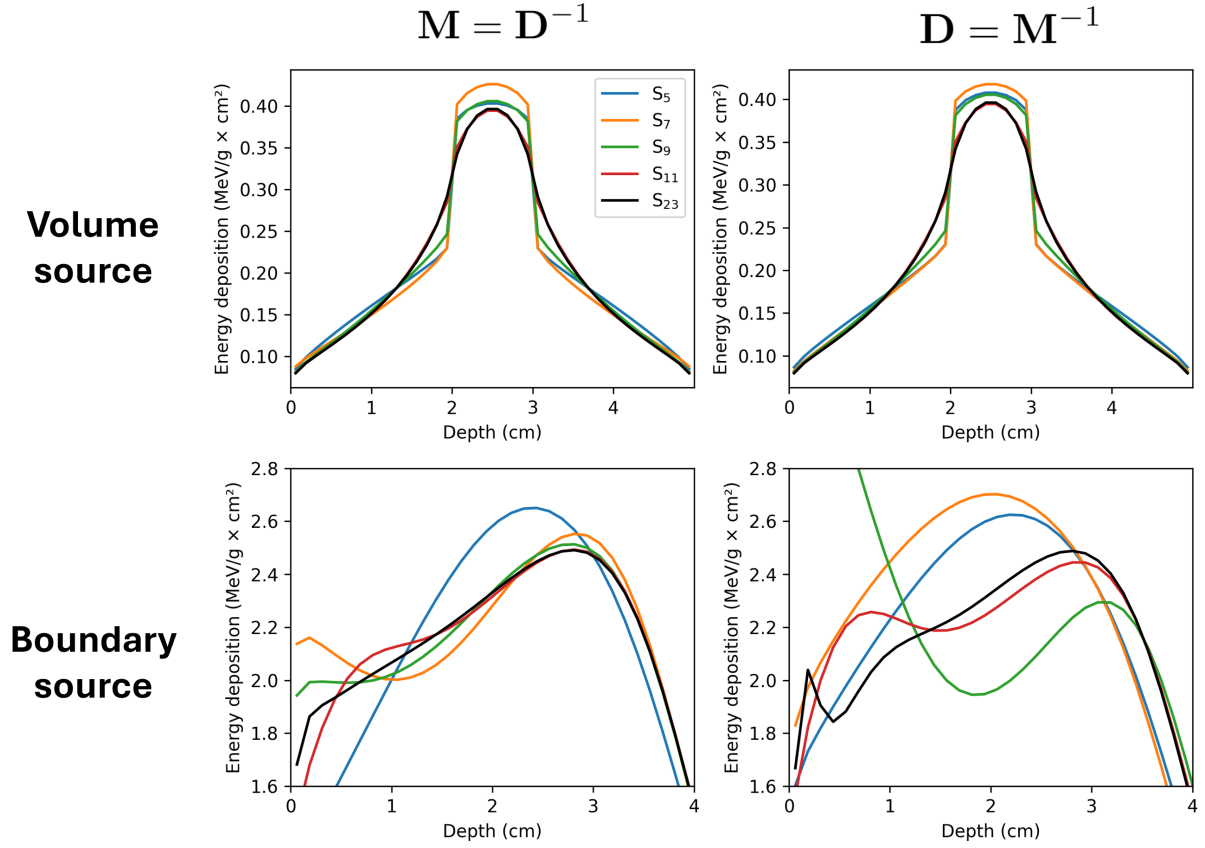


Figure 4.4 Comparison of two Galerkin quadrature methods for different quadrature order for benchmark with isotropic source (top) or normally incident source (bottom).

In a conference paper [185], Morel et al. compared two Galerkin quadratures methods for a product quadrature defined over the unit sphere, which consist of inverting either the discrete-to-moment ( $D$ ) and the moment-to-discrete ( $M$ ). Their results show that these methods give similar flux solutions, for a benchmark in which an isotropic boundary source is defined. However, it was observed that one method is superior in some cases with quadrature defined over the unit sphere.

The 1D Cartesian geometry is used with the Lebedev quadrature. The geometry domain, an infinitely wide 5 cm slab, is divided into 40 voxels. The Galerkin scheme is used for the AFP operator. The first comparison consists of a benchmark with a 10 MeV isotropic source defined between 2 and 3 cm, while the second one uses a normally incident 10 MeV beam. As shown in Fig. 4.4, for isotropic sources, both methods give similar results for any quadrature order. This is coherent with the result in Morel et al. [185]. However, for the

normally incident boundary source, the  $\mathbf{D} = \mathbf{M}^{-1}$  energy deposition results are less accurate than the  $\mathbf{M} = \mathbf{D}^{-1}$  ones at any quadrature order. Notably, the  $S_9$  solution presents a huge overestimation of the deposited energy between 0 and 1 cm depth. Even at high quadrature order ( $S_{23}$ ), while seemingly converging toward the  $\mathbf{M} = \mathbf{D}^{-1}$  solution, the  $\mathbf{D} = \mathbf{M}^{-1}$  solution still exhibits significant spurious oscillations. The  $\mathbf{M} = \mathbf{D}^{-1}$  Galerkin quadrature method is therefore used for the following results.

#### 4.4.2 Comparison of Galerkin and finite-difference schemes in 1D geometry

The first benchmark compares Galerkin and the monotone finite-difference discretization of the AFP term in 1D Cartesian geometry using Gauss-Lobatto quadrature. The geometry domain, an infinitely wide 5 cm slab, is divided into 40 voxels. The Galerkin and finite-difference mapping matrix of the  $S_6$  case, provided to highlight their properties, are respectively given by

$$\mathcal{M}_6^g = \begin{bmatrix} 0.0 & 20.2828 & -8.07237 & 4.48937 & -2.69983 & 1.0 \\ 3.57273 & 5.0 & 8.22289 & -2.67431 & 1.35425 & -0.475562 \\ -0.969902 & 5.60893 & 5.0 & 6.64575 & -1.82418 & 0.539401 \\ 0.539401 & -1.82418 & 6.64575 & 5.0 & 5.60893 & -0.969902 \\ -0.475562 & 1.35425 & -2.67431 & 8.22289 & 5.0 & 3.57273 \\ 1.0 & -2.69983 & 4.48937 & -8.07237 & 20.2828 & 0.0 \end{bmatrix} \quad (4.54)$$

and

$$\mathcal{M}_6^{fd} = \begin{bmatrix} -8.51264 & 8.51264 & 0.0 & 0.0 & 0.0 & 0.0 \\ 1.49946 & -5.42257 & 3.92311 & 0.0 & 0.0 & 0.0 \\ 0.0 & 2.676 & -5.92681 & 3.25081 & 0.0 & 0.0 \\ 0.0 & 0.0 & 3.25081 & -5.92681 & 2.676 & 0.0 \\ 0.0 & 0.0 & 0.0 & 3.92311 & -5.42257 & 1.49946 \\ 0.0 & 0.0 & 0.0 & 0.0 & 8.51264 & -8.51264 \end{bmatrix}. \quad (4.55)$$

The finite-difference matrix is clearly monotone, since the row's off-diagonal components are positive and the diagonal components are negative, and it is diagonally dominant, since the sum of the row's off-diagonal components is equal to the absolute value of the diagonal components. These properties are not shared by the Galerkin matrix. Along each line  $n$ , the main scattering events are  $n \rightarrow n - 1$  (for  $n \neq 1$ ) and  $n \rightarrow n + 1$  (for  $n \neq N_d$ ), as in the finite-difference case, but farther away from the diagonal, the values sign oscillates. The negative sign for a non-diagonal element  $m \neq n$  is not desirable since it implies that



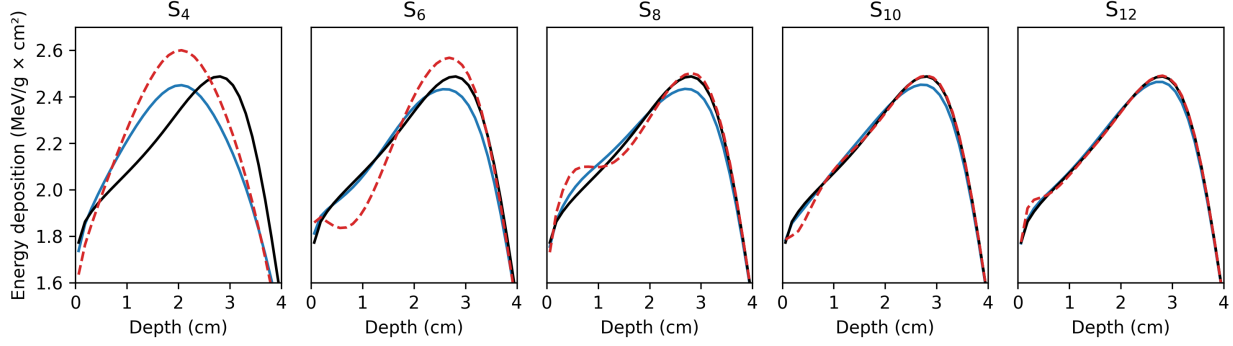


Figure 4.5 Comparison of energy deposition profiles using either Galerkin (in red) and finite-difference (in blue) schemes for the AFP operator based on a Gauss-Lobatto quadrature in 1D Cartesian geometry. The given reference (in black) is the solution using  $S_{26}$  finite-difference scheme.

the flux  $\Psi_n$  along the direction  $\mu_n$  scatter such as there is a reduction along the direction  $\mu_m$ , which does not make any physical sense. On the contrary, the finite-difference matrix is more physically robust, since the flux  $\Psi_n$  along the direction  $\mu_n$  scatter such as the flux lost at  $m = n$  is redistributed along the directions  $m \neq n$ .

The energy deposition solutions for quadrature order varying from 4 to 12 are shown in Fig. 4.5. The reference solution is obtained with the  $S_{26}$  finite-difference scheme. The solution using Galerkin scheme present significant non-physical oscillations, due to the discussed lack of monotonicity of the mapping matrix  $\mathcal{M}$ . These oscillations can be damped by increasing the quadrature order, but some artifacts can be persistent, as shown by the  $S_{12}$  case near  $x = 0$  cm. This scheme, used jointly with the Galerkin quadrature method, preserved  $N_d$  moments of the AFP operator [47]. It makes the Galerkin scheme a more accurate moment representation of the AFP operator than the finite-difference scheme that preserve only the zeroth and first moments. This explains the better agreement of low-order Galerkin scheme near  $x = 3$  cm between the reference solution. The finite-difference is more robust for any quadrature order, since it eliminates the spurious oscillations in the solution. As the quadrature order increases, both the Galerkin and finite-difference schemes tend toward the same solution.

The second benchmark compares Galerkin and the multidimensional finite-difference discretization of the AFP term in 1D Cartesian geometry using Lebedev quadrature. The geometry domain, an infinitely wide 5 cm slab, is divided into 40 voxels. The energy deposition solutions for quadrature order varying from 5 to 13 are shown in Fig. 4.6. The solution using the Galerkin scheme exhibits oscillations, similar to the one with the Gauss-

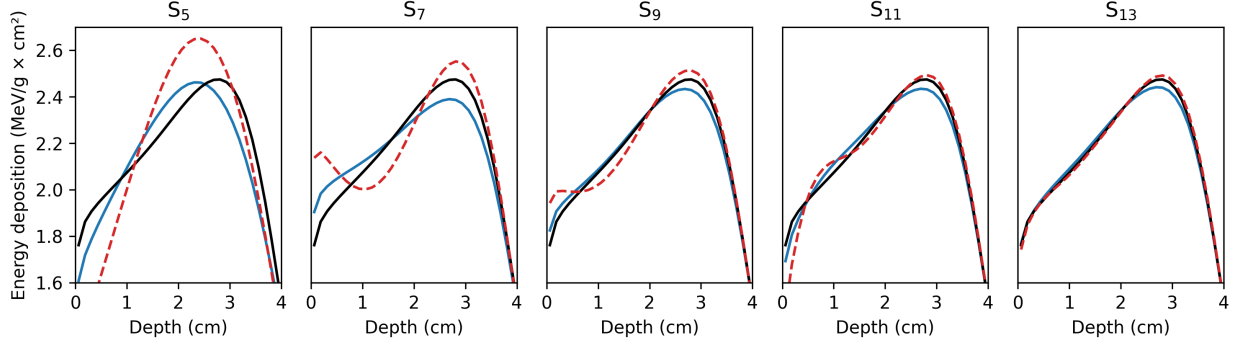


Figure 4.6 Comparison of energy deposition profiles using Galerkin (in red) and finite-difference (in blue) schemes for the Fokker-Planck operator based on the Lebedev quadrature in 1D Cartesian geometry. The reference solution (in black) is obtained using the  $S_{23}$  finite-difference scheme.

Lobatto, but at different locations. It shows that such behavior is difficult to predict for a given quadrature choice. As the 1D AFP finite-difference scheme, the multidimensional AFP one provide a solution free of such oscillations, at the cost of the enforcement of high-order spherical harmonics moments of the AFP operator.

#### 4.4.3 Comparison of Galerkin and finite-difference schemes in 3D geometry

The third benchmark compares the Galerkin and the finite-difference discretization of the AFP term in 3D Cartesian geometry using the Lebedev quadrature. The Cartesian geometry domain, whose size is  $5 \times 5 \times 1.5$  cm along each axis, is divided into 20, 20 and 6 voxels. The Galerkin and finite-difference mapping matrix have respectively the same properties than in the 1D case. The energy deposition solution for quadrature order varying from 5 to 13 is shown in Fig. 4.7. The solution using Galerkin scheme present, as expected, non-physical oscillation along both  $x$  and  $y$  spatial axis. As in the 1D case, increasing the quadrature order improve the overall monotonicity, but do not restore it. The finite-difference method, which preserve the zeroth and the three first moments of the AFP operator, eliminate any spurious oscillations of the Galerkin scheme at the cost of higher-order enforcement.

The newly developed method permits monotonicity-enforcing AFP operator treatment with optimal quadrature. This is very useful for particle transport, since it diminishes greatly the number of direction required to achieve a specific angular accuracy and then improving running times. For example, the speedup of Lebedev quadrature, for  $S_5$ ,  $S_9$  and  $S_{17}$ , compared to product quadrature, for  $S_4$ ,  $S_8$  and  $S_{16}$  are respectively 2.3, 3.5 and 4.7. Lebedev quadrature also offer a better distribution of nodes and desirable symmetries. It should be

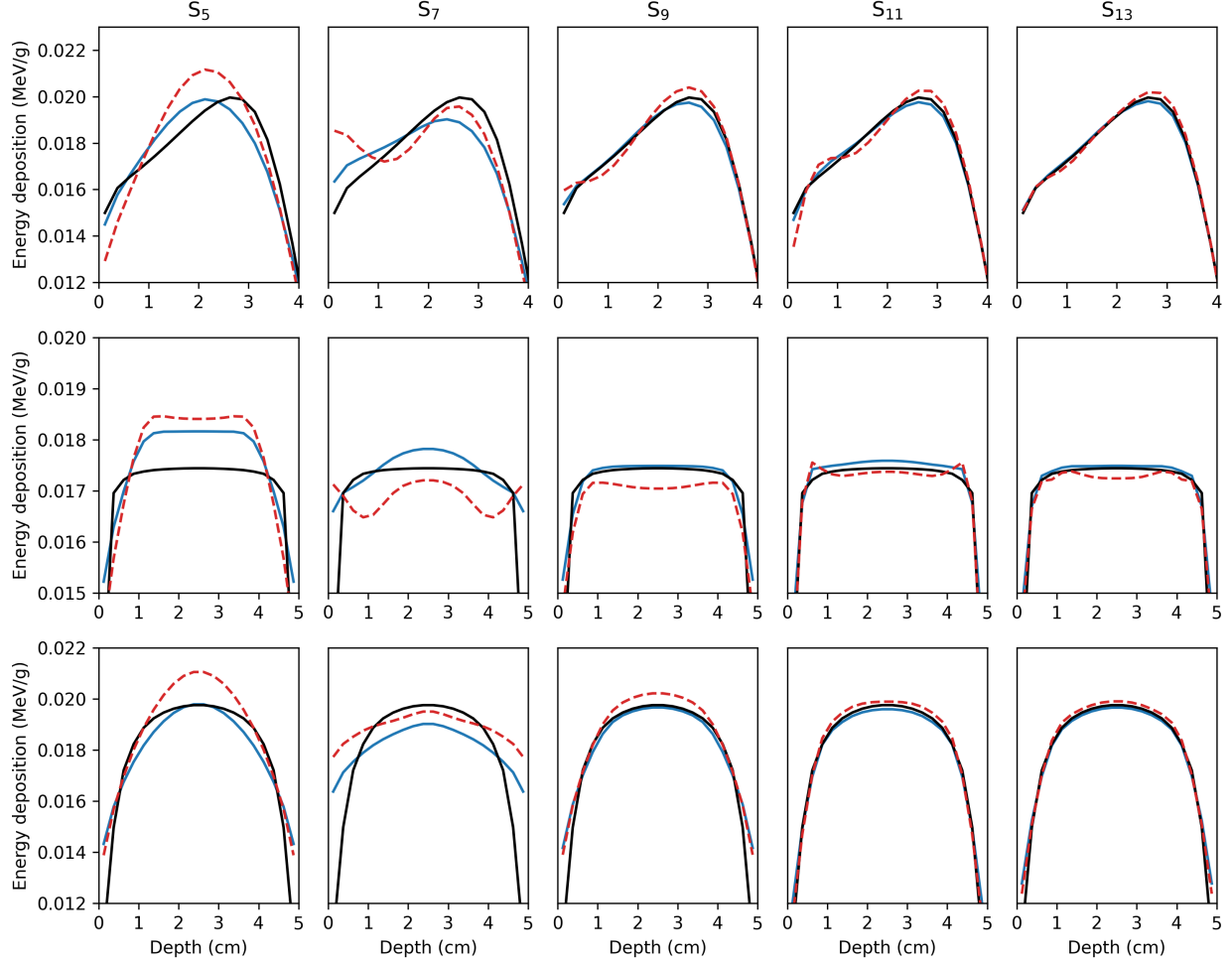


Figure 4.7 Comparison of energy deposition profiles along A)  $y = 2.5$  cm, B)  $x = 1.25$  cm and C)  $x = 2.5$  cm using either Galerkin (in red) and finite-difference (in blue) schemes for the AFP operator based on a Lebedev quadrature in 3D Cartesian geometry. The given reference (in black) is the solution using  $S_{19}$  finite-difference scheme.

noted that this method does not address the issues related to ray effect, another sources of angular spurious oscillations that occur with localized isotropic sources or in case particle scattering is low.

#### 4.5 Conclusion and Perspectives

In this chapter, a methodology was proposed to developed finite-difference schemes for the AFP operator in discrete ordinates calculations, in particular for nonorthogonal quadrature in multidimensional geometries. The proposed finite-difference schemes are monotone, and preserve the zeroth and first moments of the AFP operator. This discretization scheme

is very useful to deal with monotonicity issues related to forward-peaked scattering in the transport equation. Results for 1D and 3D geometries calculations shows that such scheme eliminates spurious oscillation related to forward-peaked scattering. Further investigations will be required to assess the properties of the quadrature set compatible with the proposed approach. It is conjectured is that the quadrature should respect at least  $\mathbf{C}_4$  rotational symmetry around an axis and  $\mathbf{C}_2$  rotational symmetry around the two others, which correspond to the product quadrature symmetries.

## CHAPTER 5 LINEAR ADAPTIVE ENERGY-SPACE SCHEMES

### 5.1 Foreword

The work in this chapter aims to address positivity and monotonicity issues related to coupled energy-space discretization. Charged particle transport solutions vary immensely from one spatial or energy mesh to the next. Even with high-order schemes proposed in the literature, negativities remain present in the dose deposition profile, and oscillations are predominant in the energy spectrum. Linear adaptive schemes are developed to tackle these issues while enforcing 2<sup>nd</sup>-order accuracy.

My original contribution in this section consists in the development of a new weighted linear schemes in 2D mesh, the adaptive choice of weights for 1D and 2D meshes and its application to the coupled discretization of the spatial and energy derivatives in the BFP equation. It follows from initial investigations of high-order schemes, such as the High-Order Diamond Difference (HODD) schemes, to tackle the highly varying energy-space solution in charged particle transport. This section work have been partially presented in form of peer-reviewed papers and presentation at the International Conference on Physics of Reactors (PHYSOR 2022) [192] and at the International Conference on Mathematics and Computational Methods Applied to Nuclear Science and Engineering (M&C 2023) [158], and published in the peer-reviewed journal *Annals of Nuclear Energy* [157].

First, the discretization of both space and energy domain using the Galerkin Method of Weighted Residuals is described in Sect. 5.2. Then, in Sect. 5.3, widely used closure relations are reviewed and weighted second-order linear schemes are developed. In Sect. 5.4, adaptive choices of weighting parameters are proposed to improve positivity and monotonicity. The newly developed adaptive schemes are then tested against Monte-Carlo reference for energy deposition and energy spectrum benchmarks in Sect 5.5 and these results are discussed. Conclusive remarks and perspectives are shared in Sect. 5.6.

### 5.2 Discretization by the Galerkin Method of Weighted Residuals

A discretization of the energy and space domain can be obtained using the Galerkin method of weighted residuals, applied to every local finite element in which the angular flux is expanded as a linear combination of basis function [193]. This method is versatile and powerful; it permits reaching high-order accuracy and modularity by confining the discretization in each finite element. The following section depicts the application of this method to the transport

equation for approximation of any order.

### 5.2.1 Transport equation in a space-energy mesh

The discrete ordinates transport equation along each direction, which index are omitted for simplicity, can be expressed as

$$\sum_{k=1}^K \frac{\partial}{\partial \mathbf{x}_k} \left[ f_k(\mathbf{x}) \Psi(\mathbf{x}) \right] + \Sigma(\mathbf{x}) \Psi(\mathbf{x}) = Q(\mathbf{x}), \quad (5.1)$$

where the vector  $\mathbf{x}$  contains spatial and/or energy variables, such as  $\mathbf{x}_k \in \{E, x, y, z\}$ . The source  $Q(\mathbf{s})$  includes the Boltzmann, the AFP and fixed external sources. The derivative term can represent the streaming term, with  $\mathbf{x}_k = x$  and  $f_k(\mathbf{x}) = \mu$  in 1D Cartesian geometry, or the CSD term, with  $\mathbf{x}_k = E$  and  $f_k(\mathbf{x}) = -S(\mathbf{x})$ . For every  $\mathbf{x}_k$  coordinates in  $\mathbf{x}$ , the domain along axis  $\mathbf{x}_k$  is divided into  $N_{\mathbf{x}_k}$  meshes, with the mesh-edge values in the  $i_k^{\text{th}}$ -cell denoted  $\mathbf{x}_{k,i_k \pm 1/2}$ . The following change of variable is applied in the  $i_k^{\text{th}}$ -cell

$$u_{\mathbf{x}_k} = \frac{2\mathbf{x}_k - \mathbf{x}_{k,i_k+1/2} - \mathbf{x}_{k,i_k-1/2}}{2\Delta\mathbf{x}_{k,i_k}}, \quad (5.2)$$

where  $\Delta\mathbf{x}_{k,i_k} = \mathbf{x}_{k,i_k+1/2} - \mathbf{x}_{k,i_k-1/2}$  is the mesh size. This new variable is defined over the support  $u_{\mathbf{x}_{i_k}} \in [-1/2, 1/2]$ . This leads to the  $S_N$  equation in the  $K$ -dimensional mesh defined by indexes  $\mathbf{i} = (i_1, i_2, \dots, i_K)$ , i.e.

$$\sum_{k=1}^K s_k h_{k,\mathbf{i}} \frac{\partial \Psi_{\mathbf{i}}}{\partial u_{\mathbf{x}_k}}(\mathbf{u}) + \Psi_{\mathbf{i}}(\mathbf{u}) = \tilde{Q}_{\mathbf{i}}(\mathbf{u}), \quad (5.3)$$

where  $\mathbf{u} = (u_{\mathbf{x}_1}, u_{\mathbf{x}_2}, \dots, u_{\mathbf{x}_K})$ ,

$$\tilde{Q}_{\mathbf{i}} = \frac{Q_{\mathbf{i}}}{\Sigma_{\mathbf{i}}} \quad \text{and} \quad h_{k,\mathbf{i}} = \frac{f_{k,i_k}}{\Delta\mathbf{x}_{k,i_k} \Sigma_{\mathbf{i}}}. \quad (5.4)$$

For the streaming, the terms  $f_{k,i_k}$  as a function of the axis  $k$  are given by

$$f_{x,i_x} = |\mu|, \quad f_{y,i_y} = |\eta|, \quad f_{z,i_z} = |\xi| \quad \text{and} \quad f_{E,i_E} = \frac{S_{i_E}^+ + S_{i_E}^-}{2} \quad (5.5)$$

and

$$s_x = \text{sign}(\mu), \quad s_y = \text{sign}(\eta), \quad s_z = \text{sign}(\xi) \quad \text{and} \quad s_E = -1. \quad (5.6)$$

For the following development, it is assumed that  $f_{E,i_E}$  and  $\Sigma_{\mathbf{i}}$  are constant in the cell. The implication of this choice is discussed in Sect. 5.6.

### 5.2.2 Definition of the flux moments

The in-cell flux, defined over  $u_{\mathbf{x}_k} \in ]-1/2, 1/2[$ , is expanded using normalized Legendre polynomials along each axis  $k$  and up to order  $M_k$  such as

$$\Psi_{\mathbf{i}}(\mathbf{u}) = \sum_{\mathcal{M}} \left\{ \prod_{k=1}^K \tilde{P}_{m_k}(u_{\mathbf{x}_k}) \right\} \Psi_{\mathbf{i}}^{(\mathbf{m})}, \quad (5.7)$$

where  $\mathbf{m} = (m_1, m_2, \dots, m_K)$  with  $m_k \in \{0, 1, \dots, M_k\}$ . The moments of the in-cell flux are given by

$$\Psi_{\mathbf{i}}^{(\mathbf{m})} = \int_{\mathcal{D}} d\mathcal{D} \left\{ \prod_{k=1}^K \tilde{P}_{m_k}(u_{\mathbf{x}_k}) \right\} \Psi_{\mathbf{i}}(\mathbf{u}). \quad (5.8)$$

The summation and integral notation indicate nested summation and integral, i.e.

$$\sum_{\mathcal{M}} \equiv \sum_{m_1=0}^{M_1} \sum_{m_2=0}^{M_2} \dots \sum_{m_K=0}^{M_K} \quad (5.9)$$

and

$$\int_{\mathcal{D}} d\mathcal{D} \equiv \int_{-1/2}^{1/2} du_{\mathbf{x}_1} \int_{-1/2}^{1/2} du_{\mathbf{x}_2} \dots \int_{-1/2}^{1/2} du_{\mathbf{x}_K}. \quad (5.10)$$

This expansion enforces coupling of high-order ( $m_k \geq 1$ ) moments between axes, which is not always maintained. Indeed, whereas this expansion generate moments of the form  $\Psi^{(n,m)}$  with  $n \geq 1$  for any  $m$ , for example, one could choose to ignore  $\Psi^{(n,m)}$  with  $n \geq 1$  for  $m \neq 0$ . This can reduce the size of the resulting system of equations, but at the cost of some accuracy.

The source term is similarly expanded, such as

$$\tilde{Q}_{\mathbf{i}}(\mathbf{u}) = \sum_{\mathcal{M}} \left\{ \prod_{k=1}^K \tilde{P}_{m_k}(u_{\mathbf{x}_k}) \right\} \tilde{Q}_{\mathbf{i}}^{(\mathbf{m})}, \quad (5.11)$$

where  $\mathbf{m} = (m_1, m_2, \dots, m_K)$  with  $m_k \in \{0, 1, \dots, M_k\}$ . The moment of the in-cell flux are given by

$$\tilde{Q}_{\mathbf{i}}^{(\mathbf{m})} = \int_{\mathcal{D}} d\mathcal{D} \left\{ \prod_{k=1}^K \tilde{P}_{m_k}(u_{\mathbf{x}_k}) \right\} \tilde{Q}_{\mathbf{i}}(\mathbf{u}). \quad (5.12)$$

The flux at mesh boundaries along  $k$ , defined at  $u_{\mathbf{x}_k} = \pm 1/2$ , is expanded along each axis but  $k'$  such as

$$\Psi_{\mathbf{i}}(\mathbf{u}_{k'}^{\pm}) = \sum_{\mathcal{M}_{k'}} \left\{ \prod_{\substack{k=1 \\ k \neq k'}}^K \tilde{P}_{m_k}(u_{\mathbf{x}_k}) \right\} \Psi_{\mathbf{i}, \mathbf{x}'_k}^{\pm(\mathbf{m}_{k'})}, \quad (5.13)$$

where the  $\Psi_k^{\pm(\mathbf{m}_k)}$  are the boundary flux moments along  $k$  given by

$$\Psi_{\mathbf{i}, \mathbf{x}'_k}^{\pm(\mathbf{m}_{k'})} = \int_{\mathcal{D}_{k'}} d\mathcal{D}_{k'} \left\{ \prod_{\substack{k=1 \\ k \neq k'}}^K \tilde{P}_{m_k}(u_{\mathbf{x}_k}) \right\} \Psi_{\mathbf{i}}(\mathbf{u}_{k'}^{\pm}). \quad (5.14)$$

The vector corresponding to the boundary positions along  $k$  is given by

$$\mathbf{u}_{k'}^{\pm} = \mathbf{u} \Big|_{u_{k'} = \pm 1/2} = (u_{\mathbf{x}_1}, \dots, u_{\mathbf{x}_{k'-1}}, \pm 1/2, u_{\mathbf{x}_{k'+1}}, \dots, u_{\mathbf{x}_K}), \quad (5.15)$$

while the vector of indexes of the boundary moment is given by the vector  $\mathbf{m}$  to which the  $k$  component is removed, such as

$$\mathbf{m}_{k'} = (m_1, \dots, m_{k'-1}, m_{k'+1}, \dots, m_K). \quad (5.16)$$

The nested sum over  $\mathcal{M}_{k'}$  is the same as Eq. 5.9, but without the summation over  $m_{k'}$  variable, and the nested integral over  $\mathcal{D}_{k'}$  is the same as Eq. 5.10, but without the integral over  $u_{\mathbf{x}_{k'}}$ .

Finally, the moments of the flux derivative along axis  $k \in \{1, 2, \dots, K\}$  is given by

$$\dot{\Psi}_{\mathbf{i}, \mathbf{x}_k}^{(\mathbf{m})} = \int_{\mathcal{D}} d\mathcal{D} \left\{ \prod_{k'=1}^K \tilde{P}_{m_{k'}}(u_{\mathbf{x}_{k'}}) \right\} \frac{\partial \Psi_{\mathbf{i}}(\mathbf{u})}{\partial u_{\mathbf{x}_k}}. \quad (5.17)$$

The flux derivative moments can be rewritten as

$$\dot{\Psi}_{\mathbf{i}, \mathbf{x}_k}^{(\mathbf{m})} = \int_{-1/2}^{1/2} du_{\mathbf{x}_k} \tilde{P}_{m_k}(u_{\mathbf{x}_k}) \frac{\partial \Psi_{\mathbf{i}}^{(\mathbf{m}_k)}(u_{\mathbf{x}_k})}{\partial u_{\mathbf{x}_k}}, \quad (5.18)$$

where

$$\Psi_{\mathbf{i}}^{(\mathbf{m}_k)}(u_{\mathbf{x}_k}) = \int_{\mathcal{D}_k} d\mathcal{D}_k \left\{ \prod_{\substack{k'=1 \\ k' \neq k}}^K \tilde{P}_{m_{k'}}(u_{\mathbf{x}_{k'}}) \right\} \Psi_{\mathbf{i}}(\mathbf{u}). \quad (5.19)$$

A change of variable can be applied to the integral to transform the normalized Legendre polynomials to the usual Legendre polynomials, such as

$$\dot{\Psi}_{\mathbf{i}, \mathbf{x}_k}^{(\mathbf{m})} = \sqrt{2m_k + 1} \int_{-1}^1 d\nu P_{m_k}(\nu) \frac{\partial \Psi_{\mathbf{i}}^{(\mathbf{m}_k)}(\nu)}{\partial \nu}. \quad (5.20)$$



Using integration per parts, this expression can take the form

$$\begin{aligned} \dot{\Psi}_{\mathbf{i}, \mathbf{x}_k}^{(\mathbf{m})} = \sqrt{2m_k + 1} \left\{ P_{m_k}(1) \Psi_{\mathbf{i}}^{(\mathbf{m}_k)}(1) - P_{m_k}(-1) \Psi_{\mathbf{i}}^{(\mathbf{m}_k)}(-1) \right. \\ \left. - \int_{-1}^1 d\nu \frac{\partial P_{m_k}(\nu)}{\partial \nu} \Psi_{\mathbf{i}}^{(\mathbf{m}_k)}(\nu) \right\}. \end{aligned} \quad (5.21)$$

This can be further simplified using Legendre polynomial properties, namely (from [194], Eq. 15.9)

$$P_n(1) = 1, \quad P_n(-1) = (-1)^n \quad (5.22)$$

and (from [194], combining Eq. 15.23 and Eq. 15.24)

$$\frac{\partial P_n(x)}{\partial x} = \sum_{k=0}^{n-1} \frac{2k+1}{2} P_k(x) [1 + (-1)^{n-k-1}] \quad (5.23)$$

for any  $n$ . The flux derivative moments, using definition of the in-cell and boundary flux moments given by Eqs. 5.8 and 5.14, is

$$\dot{\Psi}_{\mathbf{i}, \mathbf{x}_k}^{(\mathbf{m})} = \sqrt{2m_k + 1} \left\{ \Psi_{\mathbf{i}}^{+(\mathbf{m}_k)} - (-1)^{m_k} \Psi_{\mathbf{i}}^{-(\mathbf{m}_k)} - \sum_{j=0}^{m_k-1} \sqrt{2j+1} [1 - (-1)^{m_k-j}] \Psi_{\mathbf{i}}^{(\mathbf{m}_{k,j})} \right\}, \quad (5.24)$$

where the vector of indexes  $\mathbf{m}_{k,j}$  is given by the vector  $\mathbf{m}$  for which the  $k$  component is equal to index  $j$ , i.e.

$$\mathbf{m}_{k,j} = \mathbf{m}|_{m_k=j} = (m_1, \dots, m_{k-1}, j, m_{k+1}, \dots, m_K). \quad (5.25)$$

### 5.2.3 Coupled space-energy moment equations

The Bubnov-Galerkin method is employed, where the trial functions are the basis functions used to expand the flux solution [193]. The moment's equations are given by multiplying the transport equation Eq. 5.3 by the trial function, the normalized Legendre polynomials, and integrating over the mesh domain, i.e.

$$\int_{\mathcal{D}} d\mathcal{D} \left\{ \prod_{k=1}^K \tilde{P}_{n_k}(u_k) \right\} \left( \sum_{k=1}^K s_k h_{k,i_k} \frac{\partial \Psi_{\mathbf{i}}}{\partial u_{\mathbf{x}_k}}(\mathbf{u}) + \Psi_{\mathbf{i}}(\mathbf{u}) - \tilde{Q}_{\mathbf{i}}(\mathbf{u}) \right) = 0 \quad (5.26)$$

for all  $0 \leq n_k \leq m_k$ . Using the definition of in-cell moments Eq. 5.8 and of flux derivative moments Eq. 5.24, this equation takes the following form

$$\sum_{k=1}^K \sqrt{2n_k + 1} s_k h_{k,i_k} \left\{ \Psi_{\mathbf{i}}^{+(\mathbf{n}_k)} - (-1)^{n_k} \Psi_{\mathbf{i}}^{-(\mathbf{n}_k)} - \sum_{j=0}^{n_k-1} \sqrt{2j+1} [1 - (-1)^{n_k-j}] \Psi_{\mathbf{i}}^{(\mathbf{n}_{k,j})} \right\} + \Psi_{\mathbf{i}}^{(\mathbf{n})} - \tilde{Q}_{\mathbf{i}}^{(\mathbf{n})} = 0, \quad (5.27)$$

where  $\mathbf{n} = (n_1, \dots, n_K)$ . In each cell, this equation will be solved by sweeping through the domain using the incoming boundary flux moments collected from calculations from the previous cells or by geometry boundary conditions, such as boundary sources (see Sect 2.4.2). Let  $s_k = \pm 1$  define the sweeping direction, where  $s_k = 1$  corresponds to sweeping from smaller to higher value along  $k$ , while  $s_k = -1$  is the inverse. For spatial domain, it is given by  $s_x = \text{sign}(\mu)$ ,  $s_y = \text{sign}(\eta)$  and  $s_z = \text{sign}(\xi)$ , while for energy domain, by  $s_E = -1$ . Let  $\phi_{\mathbf{x}_k}^{-(\mathbf{n}_k)}$  and  $\phi_{\mathbf{x}_k}^{+(\mathbf{n}_k)}$  be, respectively, the incoming and outgoing boundary flux moments such as

$$\phi_{\mathbf{x}_k}^{-(\mathbf{n}_k)} = \begin{cases} \Psi_{\mathbf{x}_k}^{-(\mathbf{n}_k)} & s_k = 1 \\ \Psi_{\mathbf{x}_k}^{+(\mathbf{n}_k)} & s_k = -1 \end{cases} \quad \text{and} \quad \phi_{\mathbf{x}_k}^{+(\mathbf{n}_k)} = \begin{cases} \Psi_{\mathbf{x}_k}^{+(\mathbf{n}_k)} & s_k = 1 \\ \Psi_{\mathbf{x}_k}^{-(\mathbf{n}_k)} & s_k = -1 \end{cases}. \quad (5.28)$$

The equation can be rewritten to take into account the sweeping direction

$$\sum_{k=1}^K \sqrt{2n_k + 1} s_k h_{k,i_k} \left\{ s_k^{n_k-1} \phi_{\mathbf{i}}^{+(\mathbf{n}_k)} - (-1)^{n_k} s_k^{n_k-1} \phi_{\mathbf{i}}^{-(\mathbf{n}_k)} - \sum_{j=0}^{n_k-1} \sqrt{2j+1} [1 - (-1)^{n_k-j}] \Psi_{\mathbf{i}}^{(\mathbf{n}_{k,j})} \right\} + \Psi_{\mathbf{i}}^{(\mathbf{n})} - \tilde{Q}_{\mathbf{i}}^{(\mathbf{n})} = 0. \quad (5.29)$$

To solve this equation in mesh  $\mathbf{i}$ , a closure relation has to be established between the outgoing boundary flux moments, and the in-cell flux and/or the incoming boundary flux moments.

### 5.3 Closure Relations

The Galerkin method of weighted residuals results in an undetermined linear equation system and must be closed by a closure relation. The outgoing flux can be expressed as a linear combination of the incoming flux and of the flux moments, i.e.

$$\phi_{\mathbf{i}}^{+(\mathbf{n}_k)} = \omega_k^- \phi_{\mathbf{i}}^{-(\mathbf{n}_k)} + \sum_{m=0}^{M_k} \sqrt{2m+1} s_k^m \omega_k^{(m)} \Psi_{\mathbf{i}}^{(\mathbf{n}_{k,m})}, \quad (5.30)$$

where  $\omega_k^-$  and  $\omega_k^{(m)}$  are weighting factors. These factors are computed to enforce moment-preservation or geometric constraints, for example. The choice of these weighting factors is the core of this chapter. The substitution of this closure relation in Eq. 5.29 gives an equation system of the form

$$\mathcal{S}\Psi = \mathcal{Q} \quad \Rightarrow \quad \Psi = \mathcal{S}^{-1}\mathcal{Q}, \quad (5.31)$$

where  $\Psi$  contains the in-cell flux moments. The sweeping process evaluates these in-cell flux moments  $\Psi$ , using them to compute the outgoing flux moments with Eq. 5.30 and repeat the process on the following adjacent meshes.

### 5.3.1 Review of closure relations

Many closure relations have been developed to solve Eq. 5.29. The 1<sup>st</sup>-order accurate step (DG<sub>0</sub>) and the 2<sup>nd</sup>-order accurate diamond difference (DD<sub>0</sub>) schemes are obtained assuming a constant flux in the mesh and discontinuity at boundaries. This scheme results in the most straightforward equation system since  $\mathcal{S}$  and  $\mathcal{Q}$  reduce to single values, the lowest memory requirements and the fastest execution per mesh. The DG<sub>0</sub> is strictly positive and monotone, but its lack of accuracy makes it very inefficient when the solution varies significantly from one mesh to the next, even when many meshes are employed. This method does not have a thick diffusion limit, so it will not likely yield good results for diffusive problems [195]. The DD<sub>0</sub> scheme 2<sup>nd</sup>-order accuracy produces a more helpful solution with fewer meshes, but it is known to have a propensity to produce negative flux and generous spurious oscillations [47, 157]. In order to enforce positivity, many resorts to the set-to-zero fix-up, which consists of setting, if negative, the outgoing flux to zero and recomputing the in-cell flux moment [51]. However, such methods come with accuracy degradation; they perform poorly with acceleration methods and converge slowly in diffusive problems [196]. A more robust method was introduced by Carlson for the 1D meshes, using a weighted diamond difference scheme (AWD<sub>0</sub>) [177]. It uses weights varying from the DD<sub>0</sub> to the DG<sub>0</sub> that vary based on the estimation of the flux gradient in the cell to enforce positivity. It was later expanded to multidimensional geometries by Voloschenko and Alcouffe [197, 198]. While the AWD<sub>0</sub> scheme strictly enforces positivity, it fails to deliver 2<sup>nd</sup>-order accuracy and non-physical oscillations remain unavoidable (see Sect. 5.3.2 for detailed explanation). Hence, since the diamond difference scheme possesses the maximum accuracy achievable with constant flux representation [199], it is not possible to address positivity while mitigating monotonicity issues and enforcing 2<sup>nd</sup>-order accuracy.

Higher-order polynomial flux representation can be used to overcome these limitations. The 3<sup>rd</sup>-order accurate linear discontinuous Galerkin (DG<sub>1</sub>) scheme introduced by Reed and Hill

[200] is nowadays among the most used scheme for robust  $S_N$  calculations [47]. It is based on a linear flux representation in the mesh and discontinuity at boundaries. It does not inherit the intense oscillatory behaviour of the diamond difference schemes. Its increased accuracy over the  $DD_0$  generally reduces its propensity to generate negative fluxes for a given discretization grid. However, in many cases, such as with sharply increasing solution in the sweeping direction, it can produce negative flux, whereas the  $DG_0$  scheme enforces positivity [48] while also being monotone. It is possible to reach 4<sup>th</sup>-order accuracy with the linear diamond difference ( $DD_1$ ) [201–203], but it suffers, although attenuated, from the same oscillatory issues than the  $DD_0$  scheme [158]. There is another scheme that can be obtained with a linear flux representation in the cell, the step moment ( $SM_1$ ) scheme [204]. This 2<sup>rd</sup>-order accurate scheme performs better than the  $DG_1$  scheme, with improved positivity and monotonicity when flux sharply decreases in the sweeping direction [199]. As with constant flux expansion, set-to-zero fix-up was proposed for these linear methods to enforce positivity, with similar setbacks [199, 205]. Higher-order polynomial flux representations have been developed for both DD [202, 203] and DG schemes [162]. The closure relations for any order's DD, DG and SM schemes are given in Sect. 5.3.2.

In an attempt to extend the adaptive scheme of Carlson to linear flux representation, Germogenova et al. proposed a linear adaptive scheme in 1D Cartesian geometries, but it fails to enforce 2<sup>nd</sup>-order accuracy [204]. Voloschenko later greatly improved the adaptive weighted scheme based on a composite constant-linear flux representation in the 1D mesh that strictly enforces 2<sup>nd</sup>-order accuracy [199]. This weighting scheme used in this chapter, based on a normalized Legendre polynomials expansion, is given by

$$\phi_x^+ = P_x \phi_x^- + (1 - P_x) \Psi_x^{(0)} + \sqrt{3} s_x (P_x + Q_x) \Psi_x^{(1)} \quad (5.32)$$

and varies between the  $DD_1$  [ $(P_x, Q_x) = (1, 1)$ ],  $DG_1$  [ $(P_x, Q_x) = (0, 1)$ ],  $SM_1$  [ $(P_x, Q_x) = (0, 1/3)$ ] and  $DD_0$  [ $(P_x, Q_x) = (0, \infty)$ ] in order to counterbalance the defect of each of these schemes. While providing a great improvement, the proposed weighting factors formulas do not ensure strict positivity or monotonicity. The work of Germogenova, Voloschenko et al. yet contains the clearest formulation of positivity with the linear scheme, including an important one that established a relation between the first and the zeroth moment of the flux, closely related to the monotonicity. Voloschenko has extended this adaptive weighted scheme to 2D Cartesian geometries based again on linear-constant flux representation. However, this scheme has many issues. The most important one is the fact that the presented 2D weighted scheme is unstable for some choice of weighting factors ( $Q_x$  or  $Q_y \geq 4/3$ ), meaning it is unusable in this part of the domain. The method is not analytic, and a 2D Newton root-

finding method has to be applied to each mesh. It was observed that there are multiple close roots, and converging to the good one requires keeping a large matrix of initial values in memory. This method lacks compatibility with spatial parallelization, such as the KBA algorithm, since this matrix should be distributed to each voxel, which would be inefficient. Maginot et al. have developed 1D and 2D linear schemes based on constant-linear flux representation [196]. These schemes enforce positivity of the zeroth moment of the flux and of the outgoing flux, but the positivity constraint on high-order flux moments of Germogenova et al. is not considered, which would result in oscillation in the solution when flux strongly increases or decreases. The proposed solution for multidimensional geometry also depends on Newton's root-finding method, which can be expensive to compute in each mesh. The 1D and 2D adaptive schemes from Voloschenko et al. are revisited and improved in the following section.

### 5.3.2 Generalized static closure relations

The generalized diamond difference scheme is obtained assuming that the  $M_k + 1$  flux derivative moments, given by Eq. 5.24, is equal to zero [202] such as

$$\phi_{\mathbf{i}}^{+(\mathbf{n}_k)} = (-1)^{M_k+1} \phi_{\mathbf{i}}^{-(\mathbf{n}_k)} + \sum_{m=0}^{M_k} \sqrt{2m+1} s_k^m \left[ 1 - (-1)^{M_k+1-m} \right] \Psi_{\mathbf{i}}^{(\mathbf{n}_k, m)}. \quad (5.33)$$

Compared with the general expression from Eq. 5.30, it gives the following weighting factors

$$\omega_k^- = (-1)^{M_k+1} \quad \text{and} \quad \omega_k^{(m)} = \left[ 1 - (-1)^{M_k+1-m} \right]. \quad (5.34)$$

These generalized diamond difference schemes are  $(2M_k + 2)^{\text{th}}$ -order accurate [157]. With  $M_k = 0$ , the scheme reduces to the classical diamond difference (DD<sub>0</sub>) scheme. The generalized discontinuous Galerkin scheme is obtained assuming continuity between the in-cell flux evaluated at outgoing boundary and outgoing flux moments, i.e.

$$\phi_{\mathbf{i}}^{+(\mathbf{n}_k)} = \Psi_{\mathbf{i}}(\mathbf{u})|_{u_k=s_x/2} = \sum_{m=0}^{M_k} \sqrt{2m+1} s_k^m \Psi_{\mathbf{i}}^{(\mathbf{n}_k, m)}, \quad (5.35)$$

which gives the following weighting factors

$$\omega_k^- = 0 \quad \text{and} \quad \omega_k^{(m)} = 1. \quad (5.36)$$

These generalized discontinuous Galerkin schemes are  $(2M_k + 1)^{\text{th}}$ -order accurate [162]. With  $M_k = 0$ , the scheme reduces to the step scheme (DG<sub>0</sub>), while  $M_k = 1$  gives the linear dis-

$\begin{array}{c} p \\ \backslash q \end{array}$	0	1	2	3	4
0	1	$\frac{h_x}{h_x + 1}$	$\frac{2h_x^2}{2h_x^2 + 2h_x + 1}$	<b>X</b>	<b>X</b>
1	<b>X</b>	$\frac{2h_x - 1}{2h_x + 1}$	$\frac{6h_x^2 - 2h_x}{6h_x^2 + 4h_x + 1}$	$\frac{24h_x^3 - 6h_x^2}{24h_x^3 + 18h_x^2 + 6h_x + 1}$	<b>X</b>
2	<b>X</b>	<b>X</b>	$\frac{12h_x^2 - 6h_x + 1}{12h_x^2 + 6h_x + 1}$	$\frac{60h_x^3 - 24h_x^2 + 3h_x}{60h_x^3 + 36h_x^2 + 9h_x + 1}$	$\frac{360h_x^4 - 120h_x^3 + 12h_x^2}{360h_x^4 + 240h_x^3 + 72h_x^2 + 12h_x + 1}$
3	<b>X</b>	<b>X</b>	<b>X</b>	$\frac{120h_x^3 - 60h_x^2 + 12h_x - 1}{120h_x^3 + 60h_x^2 + 12h_x + 1}$	$\frac{840h_x^4 - 360h_x^3 + 60h_x^2 - 4h_x}{840h_x^4 + 480h_x^3 + 120h_x^2 + 16h_x + 1}$
4	<b>X</b>	<b>X</b>	<b>X</b>	<b>X</b>	$\frac{1680h_x^4 - 840h_x^3 + 180h_x^2 - 20h_x + 1}{1680h_x^4 + 840h_x^3 + 180h_x^2 + 20h_x + 1}$




Figure 5.1 Padé approximant,  $a(h_x)$ , of  $e^{-1/h_x}$ .

continuous scheme (DG<sub>1</sub>). The following weighting factors give the generalized step moment schemes

$$\omega_k^- = 0, \quad \omega_k^{(m)} = \begin{cases} 1 & m < M_k \\ \frac{M_k}{2M_k + 1} & m = M_k \end{cases}. \quad (5.37)$$

These generalized discontinuous Galerkin schemes are  $(2M_k)^{\text{th}}$ -order accurate, for  $M_k \geq 1$ . With  $M_k = 1$ , the scheme reduces to the step moment scheme (SM<sub>1</sub>) from Germogenova et al. [204].

The properties of the aforementioned schemes can be depicted in a simple case for which the analytical solution is known. In a 1D mesh and assuming that there are no volume sources, i.e.  $\tilde{Q}_x^{(m)} = 0$  for  $m \geq 0$ , then the ratio of outgoing on incoming flux is given by

$$a(h_x) = \frac{\phi_x^+}{\phi_x^-} = e^{-1/h_x}. \quad (5.38)$$

Solving the transport equation in the 1D mesh using the previously presented closure relations leads to Padé approximant,  $a(h_x)$ , of this exponential function [162, 204]. A Padé approximant  $(p, q)$  gives the best approximation of a given function for the ratio of polynomials of degree  $p$  and degree  $q$ . The generalized DD <sub>$p-1$</sub>  scheme, also known as HODD schemes [202],

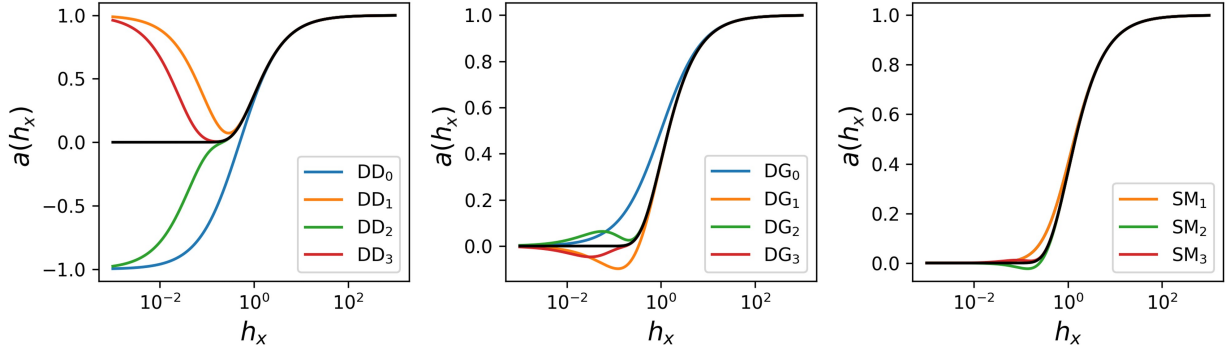


Figure 5.2 Approximation of  $a(h_x)$  for different schemes. The analytic exponential solution correspond to the black curve.

corresponds to the diagonal  $(p, p)$  Padé approximant of the exponential function as shown in Fig. 5.1. The diagonal  $(p, p)$  Padé approximant gives the solution of maximum accuracy achievable with polynomials of order  $p$ ; this means the generalized DD is the best accuracy that can be reached for a polynomial expansion of a specific order, as noted by Voloschenko who referred to this scheme as "linear best" [199]. These DD scheme are A-acceptable, i.e.  $a(h_x) \leq 1$ , but they have a false asymptotic as  $h_x \rightarrow 0$  with  $a(0) = (-1)^p$ , as shown in Fig. 5.2 [206, 207]. This is likely the root cause of the oscillation produced by the DD scheme. For spatial discretization, because  $h_x = |\mu| / (\Sigma \Delta x)$ , the issue at  $h_x \rightarrow 0$  does not fade away as the mesh shrinks in size [208]. The generalized  $DG_{p-1}$  scheme correspond to the first subdiagonal  $(p, p-1)$  Padé approximant, while the generalized  $SM_{p-1}$  scheme correspond to the second subdiagonal  $(p, p-2)$  Padé approximant. These two approximations have the correct asymptotic behaviour as  $h_x \rightarrow 0$  as shown in Fig. 5.2. Such approximations are considered L-acceptable, and these two sub-diagonal Padé approximants are likely the only L-acceptable approximations [207]. This is coherent with the reduced DG and SM propensity to generate spurious oscillations in the flux solution. In Fig. 5.2, it can be seen that increasing the scheme's accuracy order shifts the fork's location, where the exact solution and the approximate one secede. It also shows that, for a given polynomial order, the SM scheme stays closer to the exact solution, at its maximum deviation, than the DG scheme, which suggests improved stability over variation of  $h_x$ .

### 5.3.3 1D linear weighted schemes

The 1D linear weighted scheme is similar to the one developed by Voloschenko [199] but uses the normalized Legendre polynomials as the basis function. The flux in the 1D finite element

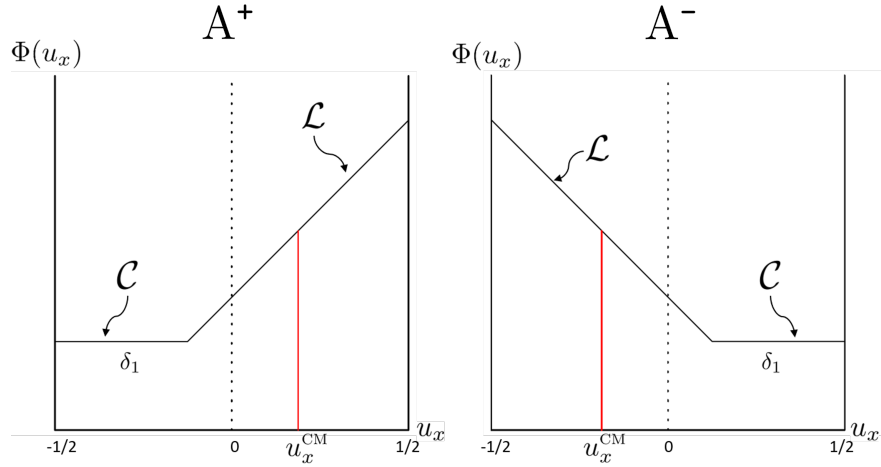


Figure 5.3 The 2 cases of linear-constant flux representation within a 1D Cartesian finite-element with  $s_x = 1$ . The red lines denote the positions of the  $\mathcal{L}$  domain centroid. Figure reproduced from [158].

is expended using a linear expansion along the  $x$ -axis. The in-cell linear flux expansion is given by

$$\Psi(u_x) = \Psi^{(0)} + 2\sqrt{3}u_x\Psi^{(1)}, \quad (5.39)$$

where the in-cell flux moments are defined by

$$\Psi^{(n)} = \int_{-1/2}^{1/2} du_x \tilde{P}_n(u_x) \Psi(u_x). \quad (5.40)$$

The flux in the 1D Cartesian finite element is defined as a composite linear-constant function of the form

$$\Psi(u_x) = \begin{cases} \phi_0 + 2\sqrt{3}u_x\phi_1 & \forall u_x \in \mathcal{L} \\ \phi_c & \forall u_x \in \mathcal{C} \end{cases}, \quad (5.41)$$

where  $\phi_0$ ,  $\phi_1$  and  $\phi_c$  are constant values.  $\mathcal{L}$  and  $\mathcal{C}$  represent, respectively, the linear and constant domains of the finite element. As shown in Fig. 5.3, there are two cases of linear-constant representation of the flux in the cell identified as  $A^+$  and  $A^-$ . Continuity is assumed between  $\mathcal{L}$  and  $\mathcal{C}$  parts, which happen at

$$u_x^\times = \begin{cases} -1/2 + \delta_1 & \text{if } A^+ \\ 1/2 - \delta_1 & \text{if } A^- \end{cases}, \quad (5.42)$$

where  $\delta_1$  is the length of the  $\mathcal{C}$  parts of the domain. Continuity is also assumed between the outgoing flux moments,  $\phi_x^+$ , and the in-cell flux moments evaluated at the outgoing cell



boundary,  $\Psi(1/2)$ . With these assumptions and enforcing in-cell flux moments, the outgoing flux can be expressed as

$$\phi_x^+ = \Psi^{(0)} + \sqrt{3}s_x Q_x \Psi^{(1)}, \quad (5.43)$$

where  $Q_x \in [1/3, \infty[$  is a weighting factor. The value of  $Q_x$  can be given as a function of  $\delta_1$  given that the subdomain ( $A^+$  or  $A^-$ ) is specified. The value of  $Q_x$  are entirely and uniquely defined by the  $\mathcal{L}$  part centroid position,  $u_x^{\text{CM}}$ , which lifts the need to specify the subdomain. Indeed, if  $u_x^{\text{CM}} \geq 0$ , then the subdomain  $A^+$  is implied, and if  $u_x^{\text{CM}} < 0$ , then the subdomain  $A^-$  is implied. For a given value of  $u_x^{\text{CM}}$ , the value of  $Q_x$  is given following these steps:

1. The first step is to identify the subdomain corresponding to the center of mass  $u_x^{\text{CM}}$ , which is given by

$$\begin{cases} A^+ & \text{if } 0 \leq u_x^{\text{CM}} \leq \frac{1}{2} \\ A^- & \text{otherwise} \end{cases}. \quad (5.44)$$

2. Then, the value of the geometric parameter  $\delta_1$  is calculated using the center of mass as prescribe in Tab. 5.1, with the following definition:

$$\delta_A(u_x^{\text{CM}}) = 2u_x^{\text{CM}}. \quad (5.45)$$

3. Finally, the value of  $Q_x$  can be calculated using  $\delta_1$  as prescribe in Tab. 5.2, with the following definition:

$$Q_A^+(\delta_1) = \frac{1 + \delta_1}{(1 - \delta_1)(1 + 2\delta_1)} \quad \text{and} \quad Q_A^-(\delta_1) = \frac{1}{1 + 2\delta_1}. \quad (5.46)$$

Substituting this scheme in the moment equations, the zeroth and first moments of the in-cell

Table 5.1 Values of  $\delta_1$  as a function of parameter  $u_x^{\text{CM}}$ .

Subdomain of $u_x^{\text{CM}}$	$\delta_1$
$A^+$	$\delta_A(u_x^{\text{CM}})$
$A^-$	$\delta_A(-u_x^{\text{CM}})$

Table 5.2 Values of  $Q_x$  as a function of parameter  $\delta_1$ .

Subdomain of $u_x^{\text{CM}}$	$Q_x$
$A^+$	$Q_A^+(\delta_1)$
$A^-$	$Q_A^-(\delta_1)$

flux are given by

$$\underbrace{\begin{bmatrix} \Psi^{(0)} \\ \Psi^{(1)} \end{bmatrix}}_{\Psi} = \underbrace{\begin{bmatrix} h_x + 1 & \sqrt{3}Q_x s_x h_x \\ -\sqrt{3}s_x h_x & 3Q_x h_x + 1 \end{bmatrix}^{-1}}_{S^{-1}} \underbrace{\begin{bmatrix} \tilde{Q}^{(0)} & + & h_x \Psi_x^- \\ \tilde{Q}^{(1)} & - \sqrt{3} & h_x s_x \Psi_x^- \end{bmatrix}}_{\mathcal{Q}}. \quad (5.47)$$

For any value of  $u_x^{\text{CM}} \in [-1/2, 1/2]$ , this scheme enforces at least 2<sup>nd</sup>-order accuracy. When  $u_x^{\text{CM}} = 0$  (or  $Q_x = 1$ ), the scheme reduces to the DG<sub>1</sub> scheme, when  $u_x^{\text{CM}} = -1/2$  (or  $Q_x = 1/3$ ), it reduces to the SM<sub>1</sub> scheme, and when  $u_x^{\text{CM}} = 1/2$  (or  $Q_x \rightarrow \infty$ ), it reduces to the DD<sub>0</sub> scheme, in a sense that it produces the same zeroth and first moments of the flux as the DD<sub>0</sub>. The properties of the scheme as a function of the choice of  $u_x^{\text{CM}}$  are discussed in Sect. 5.4.1.

### 5.3.4 2D linear weighted schemes

The flux in the 2D finite element is expanded using a linear expansion along the  $x$ - and  $y$ -axis. The in-cell linear flux expansion is given by

$$\Psi(u_x, u_y) = \Psi^{(0,0)} + 2\sqrt{3}u_x\Psi^{(1,0)} + 2\sqrt{3}u_y\Psi^{(0,1)} + 12u_xu_y\Psi^{(1,1)}, \quad (5.48)$$

where the in-cell flux moments are defined by

$$\Psi^{(n,m)} = \int_{-1/2}^{1/2} du_x \int_{-1/2}^{1/2} du_y \tilde{P}_n(u_x) \tilde{P}_m(u_y) \Psi(u_x, u_y). \quad (5.49)$$

Other than the use of normalized Legendre polynomials, this flux expansion still differs from the one of Voloschenko in which the term containing  $\Psi^{(1,1)}$  is absent [199]. The flux in the 2D Cartesian finite element is defined as a linear-constant piecewise function of the form

$$\Psi(u_x, u_y) = \begin{cases} \phi_{0,0} + u_x\phi_{1,0} + u_y\phi_{0,1} + u_xu_y\phi_{1,1} & \forall (u_x, u_y) \in \mathcal{L} \\ \phi_c & \forall (u_x, u_y) \in \mathcal{C} \end{cases}, \quad (5.50)$$

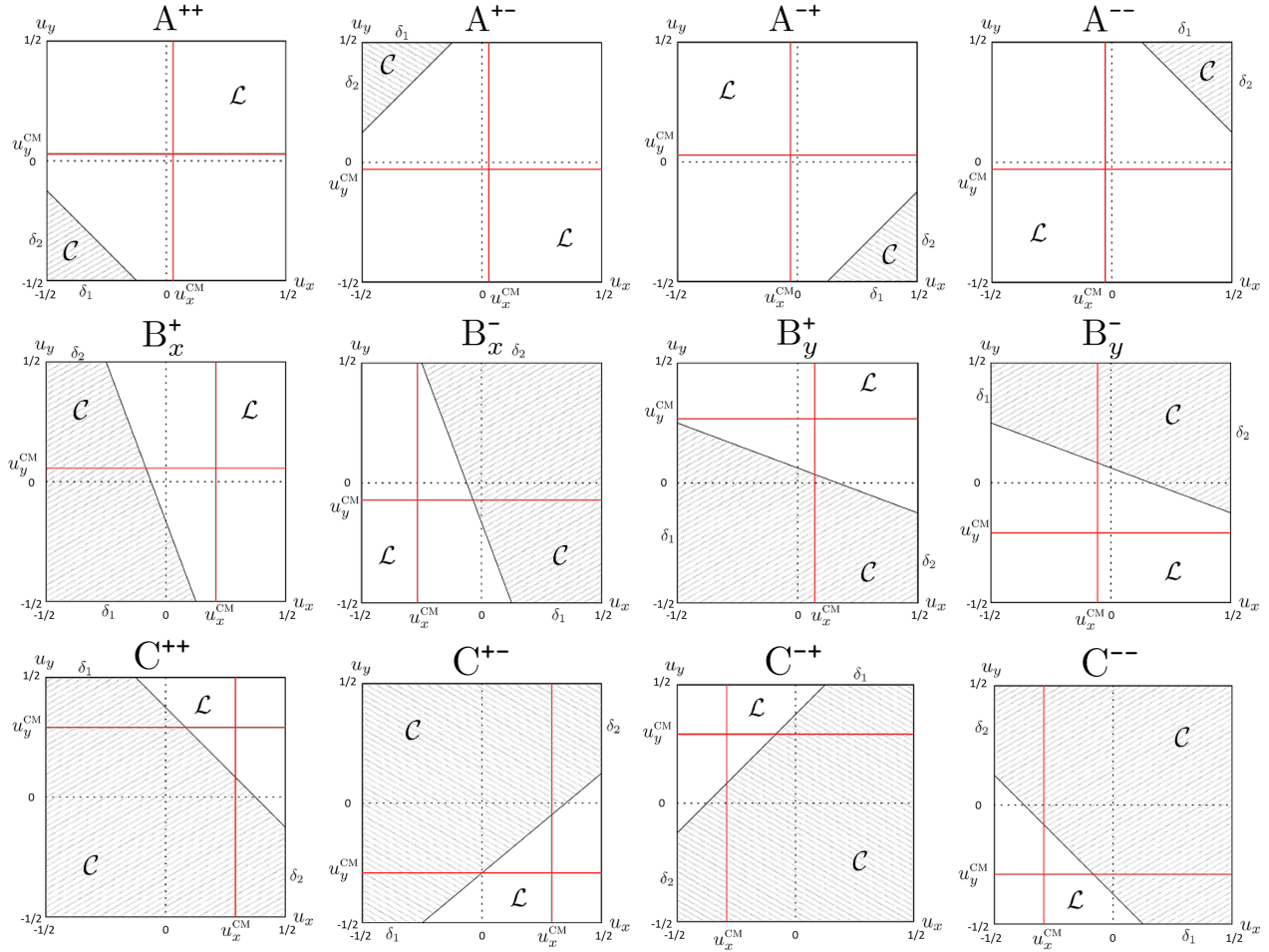


Figure 5.4 The 12 cases of flux representation within a 2D Cartesian finite-element with  $s_x = 1$  and  $s_y = 1$ . The red lines denote the positions of the  $\mathcal{L}$  domain centroid.

where  $\phi_{0,0}$ ,  $\phi_{1,0}$ ,  $\phi_{0,1}$ ,  $\phi_{1,1}$  and  $\phi_c$  are constant values.  $\mathcal{L}$  and  $\mathcal{C}$  represent, respectively, the linear and constant domains of the finite element. As shown in Fig. 5.4, there are 12 cases of linear-constant representation of the flux in the cell. Continuity is assumed between  $\mathcal{L}$  and  $\mathcal{C}$  parts intersecting along a line crossing the finite element. These lines are defined by the geometric parameters  $\delta_1$  and  $\delta_2$  for a specified subdomain, as shown in Fig. 5.4. Continuity between the outgoing flux moments,  $\phi_x^{+(m)}$  and  $\phi_y^{+(n)}$ , and the in-cell flux moments evaluated at the corresponding cell boundary, i.e.

$$\phi_x^{+(m)} = \int_{-1/2}^{1/2} du_y \tilde{P}_m(u_y) \Psi(1/2, u_y) \quad \text{and} \quad \phi_y^{+(n)} = \int_{-1/2}^{1/2} du_x \tilde{P}_n(u_x) \Psi(u_x, 1/2), \quad (5.51)$$

With these assumptions and enforcing in-cell flux moments, the outgoing flux can be expressed as

$$\begin{cases} \phi_x^{+(0)} = \Psi^{(0,0)} + \sqrt{3}s_x Q_x \Psi^{(1,0)} \\ \phi_x^{+(1)} = \Psi^{(0,1)} + \sqrt{3}s_x Q_x \Psi^{(1,1)} + s_x s_y T_x \Psi^{(1,0)} \end{cases} \quad (5.52)$$

and

$$\begin{cases} \phi_y^{+(0)} = \Psi^{(0,0)} + \sqrt{3}s_y Q_y \Psi^{(0,1)} \\ \phi_y^{+(1)} = \Psi^{(1,0)} + \sqrt{3}s_y Q_y \Psi^{(1,1)} + s_x s_y T_y \Psi^{(0,1)} \end{cases}, \quad (5.53)$$

where  $Q_x$ ,  $Q_y$ ,  $T_x$  and  $T_y$  are weighting factor, with  $Q_x, Q_y \in [1/3, \infty[$ ,  $|T_x| < 0.53 Q_x$  and  $|T_y| < 0.53 Q_y$ . The values of  $Q_x$ ,  $Q_y$ ,  $T_x$  and  $T_y$  are entirely and uniquely defined by the linear part centroid  $(u_x^{\text{CM}}, u_y^{\text{CM}})$ . As it can be deduced from Fig. 5.4, the position of the centroid is associated with a unique subdomain. For given values of centroid coordinates, the value of  $Q_x$ ,  $Q_y$ ,  $T_x$  and  $T_y$  are given following these steps:

1. The first step is to define the subdomain corresponding to the centroid  $(u_x^{\text{CM}}, u_y^{\text{CM}})$ . The Fig. 5.5 define the 12 subdomains as a function of the centroid coordinates. The red curve is defined by

$$u_y^{\text{red}}(u_x) = \frac{3u_x(1 - 2u_x)}{6u_x + 1} \quad (5.54)$$

and the blue curves are simply the symmetric curve with respect to the  $u_x$ - and  $u_y$ -axis, and with the  $u_x = u_y$  line.

2. Then, the value of the geometric parameters of  $\delta_1$  and  $\delta_2$  are calculated using centroid coordinates as prescribe in Tab. 5.3, with the following definition:

$$\begin{aligned} \delta^A(x, y) &= -\frac{1}{3a} \left( b + \zeta + \frac{\Delta_0}{\zeta} \right), \\ \delta^B(x, y) &= \frac{12y^2 + (6 - 12x)y + 2x}{12y^2 + 1}, \\ \delta^C(x) &= 3x - \frac{1}{2}, \end{aligned} \quad (5.55)$$

where

$$\zeta = -\left(\frac{1 + i\sqrt{3}}{2}\right)^3 \sqrt{\frac{\Delta_1^2 + \sqrt{\Delta_1^2 - 4\Delta_0^3}}{2}}, \quad (5.56)$$

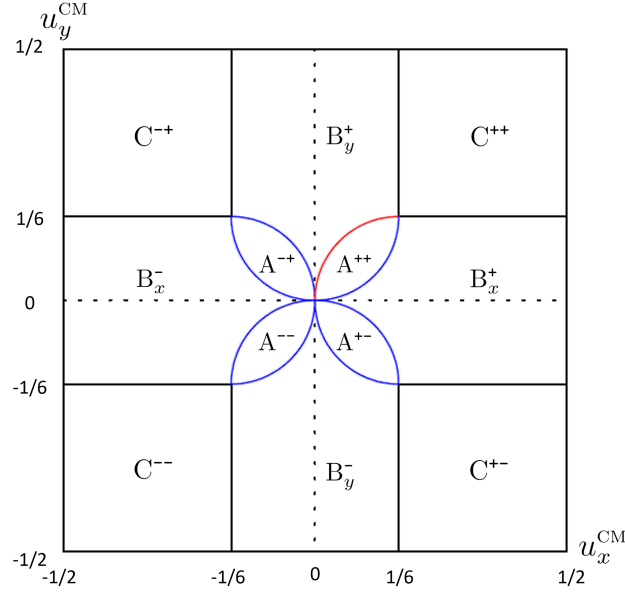


Figure 5.5 Subdomains.

Table 5.3 Values of  $(\delta_1, \delta_2)$  as a function of parameter  $(u_x^{\text{CM}}, u_y^{\text{CM}})$ .

Subdomain of $(u_x^{\text{CM}}, u_y^{\text{CM}})$	$\delta_1$	$\delta_2$
$A^{++}$	$\delta^A(u_x^{\text{CM}}, u_y^{\text{CM}})$	$\delta^A(u_y^{\text{CM}}, u_x^{\text{CM}})$
$A^{+-}$	$\delta^A(u_x^{\text{CM}}, -u_y^{\text{CM}})$	$\delta^A(-u_y^{\text{CM}}, u_x^{\text{CM}})$
$A^{-+}$	$\delta^A(-u_x^{\text{CM}}, u_y^{\text{CM}})$	$\delta^A(u_y^{\text{CM}}, -u_x^{\text{CM}})$
$A^{--}$	$\delta^A(-u_x^{\text{CM}}, -u_y^{\text{CM}})$	$\delta^A(-u_y^{\text{CM}}, -u_x^{\text{CM}})$
$B_x^+$	$\delta^B(u_x^{\text{CM}}, u_y^{\text{CM}})$	$\delta^B(u_x^{\text{CM}}, -u_y^{\text{CM}})$
$B_x^-$	$\delta^B(-u_x^{\text{CM}}, u_y^{\text{CM}})$	$\delta^B(-u_x^{\text{CM}}, -u_y^{\text{CM}})$
$B_y^+$	$\delta^B(u_y^{\text{CM}}, u_x^{\text{CM}})$	$\delta^B(u_y^{\text{CM}}, -u_x^{\text{CM}})$
$B_y^-$	$\delta^B(-u_y^{\text{CM}}, u_x^{\text{CM}})$	$\delta^B(-u_y^{\text{CM}}, -u_x^{\text{CM}})$
$C^{++}$	$\delta^C(u_x^{\text{CM}})$	$\delta^C(u_y^{\text{CM}})$
$C^{+-}$	$\delta^C(u_x^{\text{CM}})$	$\delta^C(-u_y^{\text{CM}})$
$C^{-+}$	$\delta^C(-u_x^{\text{CM}})$	$\delta^C(u_y^{\text{CM}})$
$C^{--}$	$\delta^C(-u_x^{\text{CM}})$	$\delta^C(-u_y^{\text{CM}})$

and

$$\begin{cases} a = \frac{2y}{x} \\ b = -\frac{x}{6y} - 6y + 3 \\ c = \frac{9y}{2x} - 9x + 9y - \frac{9}{2} \\ d = 12x \end{cases}, \quad \begin{cases} \Delta_0 = b^2 - 3ac \\ \Delta_1 = 2b^3 - 9abc + 27a^2d \end{cases}. \quad (5.57)$$

Table 5.4 Values of  $(Qx, Qy, Tx, Ty)$  as a function of parameter  $(\delta_1, \delta_2)$ .

Subdomain of $(u_x^{\text{CM}}, u_y^{\text{CM}})$	$Q_x$	$Q_y$	$T_x$	$T_y$
$A^{++}$	$Q_A^+(\delta_1, \delta_2)$	$Q_A^+(\delta_2, \delta_1)$	$T_A^+(\delta_1, \delta_2)$	$T_A^+(\delta_2, \delta_1)$
$A^{+-}$	$Q_A^+(\delta_1, \delta_2)$	$Q_A^-(\delta_2, \delta_1)$	$-T_A^+(\delta_1, \delta_2)$	$-T_A^-(\delta_2, \delta_1)$
$A^{-+}$	$Q_A^-(\delta_1, \delta_2)$	$Q_A^+(\delta_2, \delta_1)$	$-T_A^-(\delta_1, \delta_2)$	$-T_A^+(\delta_2, \delta_1)$
$A^{--}$	$Q_A^-(\delta_1, \delta_2)$	$Q_A^-(\delta_2, \delta_1)$	$T_A^-(\delta_1, \delta_2)$	$T_A^-(\delta_2, \delta_1)$
$B_x^+$	$Q_B^+(\delta_1, \delta_2)$	$Q_B^+(\delta_1, \delta_2)$	$T_B^+(\delta_1, \delta_2)$	$T_B^+(\delta_1, \delta_2)$
$B_x^-$	$Q_B^-(\delta_1, \delta_2)$	$Q_B^+(\delta_1, \delta_2)$	$T_B^-(\delta_1, \delta_2)$	$-T_B^+(\delta_1, \delta_2)$
$B_y^+$	$Q_B^+(\delta_1, \delta_2)$	$Q_B^+(\delta_1, \delta_2)$	$T_B^+(\delta_1, \delta_2)$	$T_B^+(\delta_1, \delta_2)$
$B_y^-$	$Q_B^+(\delta_1, \delta_2)$	$Q_B^-(\delta_1, \delta_2)$	$-T_B^+(\delta_1, \delta_2)$	$T_B^-(\delta_1, \delta_2)$
$C^{++}$	$Q_C^+(\delta_1)$	$Q_C^+(\delta_2)$	$T_C^+(\delta_1, \delta_2)$	$T_C^+(\delta_2, \delta_1)$
$C^{+-}$	$Q_C^+(\delta_1)$	$Q_C^-(\delta_2)$	$-T_C^+(\delta_1, \delta_2)$	$-T_C^-(\delta_2, \delta_1)$
$C^{-+}$	$Q_C^-(\delta_1)$	$Q_C^+(\delta_2)$	$-T_C^-(\delta_1, \delta_2)$	$-T_C^+(\delta_2, \delta_1)$
$C^{--}$	$Q_C^-(\delta_1)$	$Q_C^-(\delta_2)$	$T_C^-(\delta_1, \delta_2)$	$T_C^-(\delta_2, \delta_1)$

3. Finally, the value of  $(Q_x, Q_y)$  and  $(T_x, T_y)$  can be calculated using  $(\delta_1, \delta_2)$  as prescribe in Tab. 5.4, with the following definition:

$$Q_A^+(\delta_i, \delta_j) = \left(\frac{2}{3}\right) \frac{3 - \delta_i^2 \delta_j}{\delta_i^3 \delta_j + 2(1 - \delta_i^2 \delta_j)}, \quad (5.58)$$

$$Q_A^-(\delta_i, \delta_j) = \left(\frac{2}{3}\right) \frac{3(1 - \delta_i \delta_j) + \delta_i^2 \delta_j}{\delta_i^3 \delta_j + 2(1 - \delta_i^2 \delta_j)}, \quad (5.59)$$

$$Q_B^+(\delta_i, \delta_j) = \left(\frac{2}{3}\right) \frac{3 - (\delta_i^2 + \delta_i \delta_j + \delta_j^2)}{(\delta_i^3 + \delta_i^2 \delta_j + \delta_i \delta_j^2 + \delta_j^3) + 2(1 - \delta_i^2 - \delta_i \delta_j - \delta_j^2)}, \quad (5.60)$$

$$Q_B^-(\delta_i, \delta_j) = \left(\frac{2}{3}\right) \frac{3(1 - \delta_i - \delta_j) + (\delta_i^2 + \delta_i \delta_j + \delta_j^2)}{(\delta_i^3 + \delta_i^2 \delta_j + \delta_i \delta_j^2 + \delta_j^3) + 2(1 - \delta_i^2 - \delta_i \delta_j - \delta_j^2)}, \quad (5.61)$$

$$Q_B^*(\delta_i, \delta_j) = \left(\frac{2}{3}\right) \frac{\delta_i + 2\delta_j - 3}{\delta_i + \delta_j - 2}, \quad (5.62)$$

$$Q_C^+(\delta_i) = \left(\frac{2}{3}\right) \frac{2 + \delta_i}{1 - \delta_i^2}, \quad (5.63)$$

$$Q_C^-(\delta_i) = \left(\frac{2}{3}\right) \frac{1}{1 + \delta_i}, \quad (5.64)$$

and

$$T_A^+(\delta_i, \delta_j) = -\delta_i^2 \delta_j \frac{\delta_i^3 \delta_j^2 + 12\delta_i \delta_j - 30\delta_i - 20\delta_j + 40}{5(\delta_i^3 \delta_j + 2(1 - \delta_i^2 \delta_j))^2}, \quad (5.65)$$

$$T_A^-(\delta_i, \delta_j) = -\delta_i \delta_j \frac{\delta_i^4 \delta_j^2 - 8\delta_i^3 \delta_j^2 + 10\delta_i^2 \delta_j^2 - 12\delta_i^2 \delta_j + 30\delta_i^2 + 40\delta_i \delta_j - 80\delta_i - 40\delta_j + 60}{5(\delta_i^3 \delta_j + 2(1 - \delta_i^2 \delta_j))^2}, \quad (5.66)$$

$$T_B^+(\delta_i, \delta_j) = -\frac{(\delta_i - \delta_j)}{5((\delta_i^3 + \delta_i^2 \delta_j + \delta_i \delta_j^2 + \delta_j^3) + 2(1 - \delta_i^2 - \delta_i \delta_j - \delta_j^2))^2} \\ \times \left[ (\delta_i^4 + 4\delta_i^3 \delta_j + 10\delta_i^2 \delta_j^2 + 4\delta_i \delta_j^3 + \delta_j^4) - 6(3\delta_i^2 + 4\delta_i \delta_j + 3\delta_j^2) + 20(\delta_i + \delta_j) \right], \quad (5.67)$$

$$T_B^-(\delta_i, \delta_j) = \frac{(\delta_i - \delta_j)}{5((\delta_i^3 + \delta_i^2 \delta_j + \delta_i \delta_j^2 + \delta_j^3) + 2(1 - \delta_i^2 - \delta_i \delta_j - \delta_j^2))^2} \\ \times \left[ (\delta_i^4 + 4\delta_i^3 \delta_j + 10\delta_i^2 \delta_j^2 + 4\delta_i \delta_j^3 + \delta_j^4) - 8(\delta_i^3 + 4\delta_i^2 \delta_j + 4\delta_i \delta_j^2 + \delta_j^3) \right. \\ \left. + 4(7\delta_i^2 + 16\delta_i \delta_j + 7\delta_j^2) - 40(\delta_i + \delta_j) + 20 \right], \quad (5.68)$$

$$T_B^*(\delta_i, \delta_j) = -(\delta_i - \delta_j) \frac{\delta_i^2 + 6\delta_i \delta_j + 3\delta_j^2 - 8\delta_i - 12\delta_j + 10}{5(\delta_i + \delta_j - 2)^2}, \quad (5.69)$$

$$T_C^+(\delta_i, \delta_j) = -\frac{(\delta_j - 1)(\delta_i^2 + 6\delta_i + 3)}{5(\delta_i - 1)(1 + \delta_i)^2}, \quad (5.70)$$

$$T_C^-(\delta_i, \delta_j) = -\frac{(\delta_i - 1)(\delta_j - 1)}{5(1 + \delta_i)^2}. \quad (5.71)$$

The weighting factors' values in the centroid coordinates' function are shown in Fig. 5.6. It should be noted that the expression for  $Q_x$  and  $Q_y$  as a function of  $\delta_1$  and  $\delta_2$  are the same as the one of Voloschenko, but it is not the case for  $T_x$  and  $T_y$ . This difference, resulting from the inclusion of the term  $\Psi^{(1,1)}$  in the flux expansion, solves the stability issues underlined by Voloschenko when  $Q_x, Q_y \geq 4/3$  ( $u_x^{\text{CM}}, u_y^{\text{CM}} \geq 1/6$ ) [199]. Nonetheless, the scheme is analytically defined as a function of two variables, the centroid coordinates.

Substituting this scheme in the moment equations, the zeroth and first moments of the in-cell

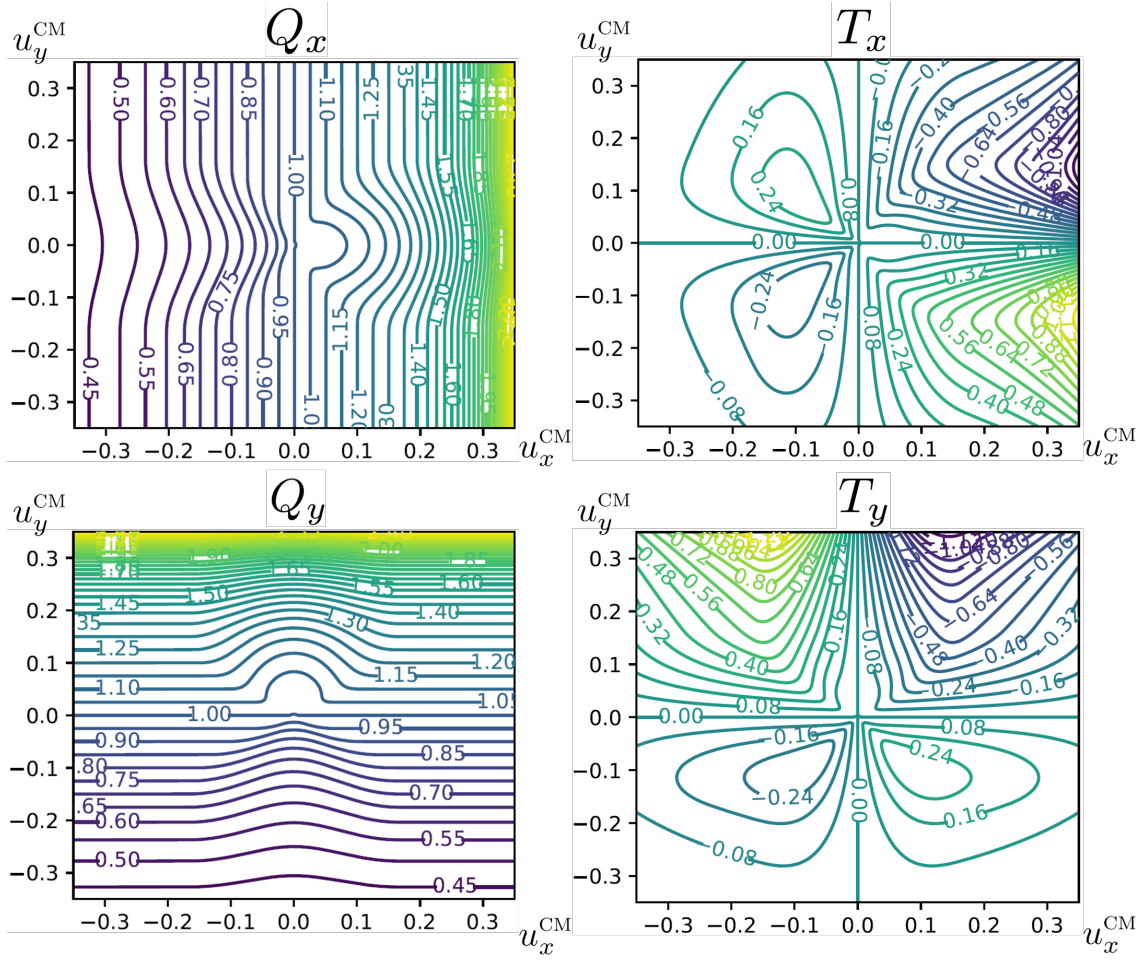


Figure 5.6 Values of  $Q_x$ ,  $Q_y$ ,  $T_x$  and  $T_y$  as a function of the centroid coordinates.

flux are given by

$$\underbrace{\begin{bmatrix} \Psi^{(0,0)} \\ \Psi^{(1,0)} \\ \Psi^{(0,1)} \\ \Psi^{(1,1)} \end{bmatrix}}_{\Psi} = \underbrace{\begin{bmatrix} h_x + h_y + 1 & \sqrt{3}Q_x s_x h_x & \sqrt{3}Q_y s_y h_y & 0 \\ -\sqrt{3}s_x h_x & 3Q_x h_x + h_y + 1 & s_x s_y T_y h_y & \sqrt{3}Q_y s_y h_y \\ -\sqrt{3}s_y h_y & s_x s_y T_x h_x & 3Q_y h_y + h_x + 1 & \sqrt{3}Q_x s_x h_x \\ 0 & -\sqrt{3}s_y (h_y - h_x T_x) & -\sqrt{3}s_x (h_x - h_y T_y) & 3Q_x h_x + 3Q_y h_y + 1 \end{bmatrix}}_{S^{-1}}^{-1} \\
 \times \underbrace{\begin{bmatrix} \tilde{Q}^{(0,0)} + h_x \Psi_x^{-(0)} + h_y \Psi_y^{-(0)} \\ \tilde{Q}^{(1,0)} - \sqrt{3} h_x s_x \Psi_x^{-(0)} + h_y \Psi_y^{-(1)} \\ \tilde{Q}^{(0,1)} + h_x \Psi_x^{-(1)} - \sqrt{3} h_y s_y \Psi_y^{-(0)} \\ \tilde{Q}^{(1,1)} - \sqrt{3} h_x s_x \Psi_x^{-(1)} - \sqrt{3} h_y s_y \Psi_y^{-(1)} \end{bmatrix}}_{Q}.$$

(5.72)



For any value of  $u_x^{\text{CM}}, u_y^{\text{CM}} \in [-1/2, 1/2]$ , this scheme enforces at least 2<sup>nd</sup>-order accuracy. When  $u_x^{\text{CM}}, u_y^{\text{CM}} = (0, 0)$ , the scheme reduced to the 3<sup>rd</sup>-order accurate DG<sub>1</sub> scheme applied along both axis. When  $u_x^{\text{CM}} = -1/2$ , it is equivalent to applying the SM<sub>1</sub> scheme along the axis  $u_x$ , and when  $u_x^{\text{CM}} = 1/2$ , it is equivalent to applying the DD<sub>0</sub> scheme along that axis. The properties of the scheme as a function of the choice of  $u_x^{\text{CM}}$  are discussed in Sect. 5.4.2.

## 5.4 Adaptive Choice of Weights

The main interest of the weighted scheme presented in the previous section is constructing adaptive schemes that enforce 2<sup>nd</sup>-order accuracy. The constant adaptive scheme from Carlson chose weights that maximize the accuracy (closer to DD<sub>0</sub> than DG<sub>0</sub>) while enforcing positivity [177]. With the proposed linear adaptive schemes, the idea remains essentially the same and can be expressed as an optimization problem as

$$\min_{u_{\mathbf{x}_k}^{\text{CM}} \in [-\frac{1}{2}, \frac{1}{2}]} \sum_{k=1}^K \left(u_{\mathbf{x}_k}^{\text{CM}}\right)^2 \quad (5.73)$$

subject to some positivity and monotonicity constraints. If  $u_{\mathbf{x}_k}^{\text{CM}} = 0$  fulfill every one of these constraints for every value  $k = 1, K$ , then the scheme reduces to the 3<sup>rd</sup>-order accurate DG<sub>1</sub> scheme, which is the maximum accuracy achievable with the weighted scheme.

### 5.4.1 1D linear weighted schemes

The flux solution to the transport equation should be strictly positive since a negative particle density makes no physical sense. Negativities are solely produced by the numerical methods employed, generating oscillations in the solution. The 1D optimization problem

$$\min_{u_x^{\text{CM}} \in [-\frac{1}{2}, \frac{1}{2}]} \left(u_x^{\text{CM}}\right)^2, \quad (5.74)$$

is subject to the following positivity constraints. Positivity is achieved if [199]

1. the mean in-cell source is positive, i.e.

$$Q^{(0)} \geq 0, \quad (5.75)$$

2. the mean flux at each incoming boundary is positive, i.e.

$$\Psi_x^{-(0)} \geq 0, \quad (5.76)$$

3. the second moment(s) of the in-cell source is bounded, such as

$$\left|Q^{(1)}\right| \leq \sqrt{3}Q^{(0)}, \quad (5.77)$$

then

1. the mean in-cell flux is positive, i.e.

$$\Psi^{(0)} \geq 0, \quad (5.78)$$

2. the mean flux at each outgoing boundary is positive, i.e.

$$\Psi_x^{+(0)} \geq 0, \quad (5.79)$$

3. the second moment(s) of the in-cell flux is bounded, such as

$$\left|\Psi^{(1)}\right| \leq \sqrt{3}\Psi^{(0)}. \quad (5.80)$$

The first and second positivity constraints are rather trivial, while the third one is derived from the upper bound on high-order Legendre flux moments of a positive function, see Eq. A.11 in Annex A. Omitting this constraint, as in the work of Maginot et al. [196], results in non-physical oscillations of the flux solution.

To solve the 1D optimization problem, let's first define the parameter

$$\dot{Q}_x = \sqrt{3}s_x \frac{\mathcal{Q}^{(1)}}{\mathcal{Q}^{(0)}} = \sqrt{3}s_x \left[ \frac{\tilde{Q}^{(1)} - \sqrt{3}h_x s_x \Psi_x^-}{\tilde{Q}^{(0)} + h_x \Psi_x^-} \right]. \quad (5.81)$$

Based on the positivity of the sources, such as  $\tilde{Q}^{(0)}$ ,  $\tilde{Q}^{(1)}$  and  $\Psi_x^-$  fulfill Eqs. 5.75 to 5.77, it can easily be deduced that the inequality

$$\left|\dot{Q}_x\right| \leq 3 \quad (5.82)$$

is strictly enforced. Solving the equation system given by Eq. 5.47, the zeroth moment of the flux is given by

$$\Psi^{(0)} = \frac{h_x Q_x (3 - \dot{Q}_x) + 1}{6Q_x h_x^2 + (3Q_x + 1)h_x + 1} Q^{(0)} \quad (5.83)$$

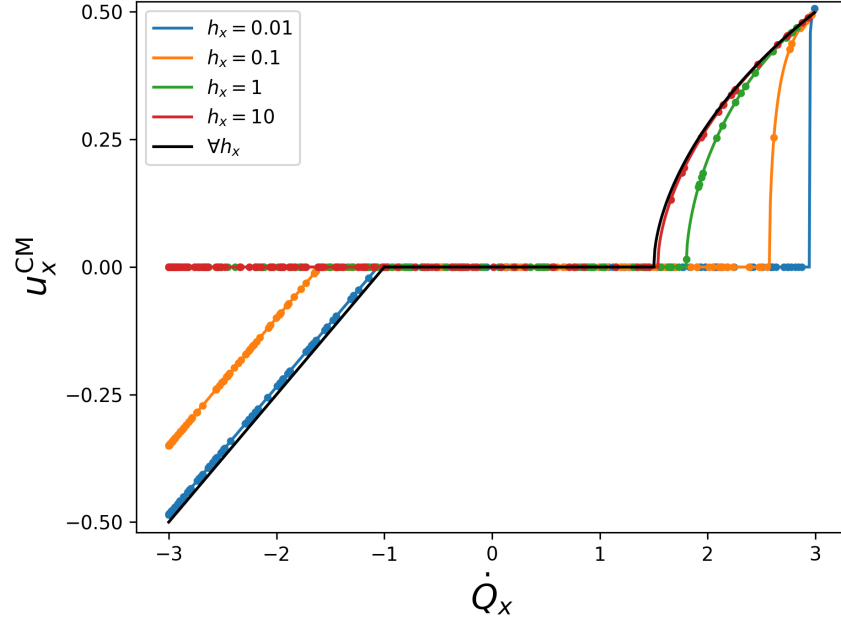


Figure 5.7 Centroid coordinates that enforce positivity as a function of parameter  $\dot{Q}_x$  and  $h_x$ . The continuous curves are given by Eq. 5.92, while the dots consists of the optimal solution with random  $\tilde{Q}^{(0)}$ ,  $\tilde{Q}^{(1)}$  and  $\Psi_x^-$  parameters using numerical optimization techniques. The black curve corresponds to the solution that depends solely on  $\dot{Q}_x$ .

and the ratio of the first to the zeroth moment of the flux is given by

$$\frac{\Psi^{(1)}}{\Psi^{(0)}} = \frac{s_x}{\sqrt{3}} \left[ \frac{h_x(3 + \dot{Q}_x) + \dot{Q}_x}{h_x Q_x(3 - \dot{Q}_x) + 1} \right]. \quad (5.84)$$

Following Ineq. 5.82, the condition  $\Psi^{(0)} \geq 0$  is fulfilled for any value of  $Q_x \geq 1/3$ . The fulfillment of the two other positivity conditions is analyzed based on the sign of  $\dot{Q}_x$ :

- **For  $\dot{Q}_x \geq 0$  :** The inequality

$$\frac{\Psi^+}{\Psi^{(0)}} = 1 + \sqrt{3}s_x Q_x \frac{\Psi^{(1)}}{\Psi^{(0)}} \geq 0, \quad (5.85)$$

which is equivalent to Ineq. 5.79, is always fulfilled. The only constraint left is

$$\left| \frac{\Psi^{(1)}}{\Psi^{(0)}} \right| \leq \sqrt{3}. \quad (5.86)$$

Substituting Eq. 5.84 in that expression, the following inequality is obtained

$$Q_x \geq \frac{h_x(3 + \dot{Q}_x) - (3 - \dot{Q}_x)}{3h_x(3 - \dot{Q}_x)}. \quad (5.87)$$

The intersection of this formula with  $Q_x = 1$  is given by

$$\dot{Q}_x^{\min} = \frac{6h_x + 3}{4h_x + 1} \quad (5.88)$$

and consists of the lower threshold of the region where correction should be applied.

- **For  $\dot{Q}_x < 0$  :** The Ineq. 5.85 can be rewritten as

$$\frac{|\Psi^{(1)}|}{\Psi^{(0)}} \leq \frac{1}{\sqrt{3}Q_x} \leq \sqrt{3}, \quad (5.89)$$

such as it encompass both Ineqs. 5.79 and 5.80. After some manipulation, the inequality can be expressed as

$$Q_x \leq \frac{-1}{6h_x + \dot{Q}_x}. \quad (5.90)$$

The intersection of this formula with  $Q_x = 1$  is given by

$$\dot{Q}_x^{\max} = -(6h_x + 1) \quad (5.91)$$

and consists of the upper threshold of the region where correction should be applied.

Consolidating these positivity-enforcing inequalities and establishing the suitable value that minimize the cost function, the value of  $Q_x$  that is a solution to the optimization problem is given by

$$Q_x = \begin{cases} \frac{h_x(3 + \dot{Q}_x) - (3 - \dot{Q}_x)}{3h_x(3 - \dot{Q}_x)} & \dot{Q}_x > \frac{6h_x + 3}{4h_x + 1} \\ -\frac{1}{6h_x + \dot{Q}_x} & \dot{Q}_x < -(6h_x + 1) \\ 1 & \text{otherwise} \end{cases} \quad (5.92)$$

or equivalently, using Eqs. 5.45 and 5.46,

$$u_x^{\text{CM}} = \begin{cases} \frac{2h_x(2\dot{Q}_x - 3) + (\dot{Q}_x - 3) + \sqrt{\Delta_x}}{8(\dot{Q}_x + 3)h_x + 8(\dot{Q}_x - 3)} & \dot{Q}_x > \frac{6h_x + 3}{4h_x + 1} \\ \frac{6h_x + (\dot{Q}_x + 1)}{4} & \dot{Q}_x < -(6h_x + 1) \\ 0 & \text{otherwise} \end{cases}, \quad (5.93)$$

with  $\Delta_x = 12(4\dot{Q}_x^2 - 9)h_x^2 + 12(4\dot{Q}_x^2 - 15\dot{Q}_x + 9)h_x + 9(\dot{Q}_x - 3)^2$ . A general expression, independent of  $h_x$ , can be found by taking the limit case such as  $h_x \rightarrow \infty$  if  $\dot{Q}_x > 0$  and  $h_x = 0$  if  $\dot{Q}_x < 0$ , which results in

$$Q_x = \begin{cases} \frac{(3 + \dot{Q}_x)}{3(3 - \dot{Q}_x)} & \dot{Q}_x > \frac{3}{2} \\ -\frac{1}{\dot{Q}_x} & \dot{Q}_x < -1 \\ 1 & \text{otherwise} \end{cases} , \quad (5.94)$$

or equivalently,

$$u_x^{\text{CM}} = \begin{cases} \frac{2\dot{Q}_x - 3 + \sqrt{12\dot{Q}_x^2 - 27}}{4(3 + \dot{Q}_x)} & \dot{Q}_x > \frac{3}{2} \\ \frac{\dot{Q}_x + 1}{4} & \dot{Q}_x < -1 \\ 0 & \text{otherwise} \end{cases} . \quad (5.95)$$

These solutions are shown in Fig. 5.7 for different value of  $h_x$ . Solution of numerical optimization techniques, using random  $\tilde{Q}^{(0)}$ ,  $\tilde{Q}^{(1)}$  and  $\Psi_x^-$  parameters and used to verify that the solution is indeed the optimal solution, is also shown. The optimization package *Optimization.jl* [209] is used to solve the minimization problem. The solution given by Eq. 5.92 is an improvement of the scheme by Voloschenko [199] since it strictly enforces positivity and 2<sup>nd</sup>-order accuracy. Contrary to his adaptive scheme, the 4<sup>th</sup>-order accurate linear diamond difference scheme is not employed in the presented scheme.

#### 5.4.2 2D linear weighted schemes

The 2D optimization problem

$$\min_{u_x^{\text{CM}}, u_y^{\text{CM}} \in [-\frac{1}{2}, \frac{1}{2}]} \left( u_x^{\text{CM}} \right)^2 + \left( u_y^{\text{CM}} \right)^2 , \quad (5.96)$$

subject to the positivity constraints such as

1. the mean in-cell source is positive, i.e.

$$Q^{(0,0)} \geq 0 , \quad (5.97)$$

2. the mean flux at each incoming boundary is positive, i.e.

$$\Psi_x^{-(0)} \geq 0 \quad \text{and} \quad \Psi_y^{-(0)} \geq 0 , \quad (5.98)$$

3. the second moment(s) of the in-cell source is bounded such as

$$\left|Q^{(1,0)}\right| \leq \sqrt{3}Q^{(0,0)}, \left|Q^{(0,1)}\right| \leq \sqrt{3}Q^{(0,0)}, \quad (5.99)$$

and

$$\left|Q^{(1,1)}\right| \leq \sqrt{3} \min \left\{ \sqrt{3}Q^{(0,0)}, \left|Q^{(1,0)}\right|, \left|Q^{(0,1)}\right| \right\}, \quad (5.100)$$

4. the second moment(s) of the incoming flux is bounded such as

$$\left|\Psi_x^{-(1)}\right| \leq \sqrt{3}\Psi_x^{-(0)} \quad \text{and} \quad \left|\Psi_y^{-(1)}\right| \leq \sqrt{3}\Psi_y^{-(0)}, \quad (5.101)$$

then

1. the mean in-cell source is positive, i.e.

$$\Psi^{(0,0)} \geq 0, \quad (5.102)$$

2. the mean flux at each incoming boundary is positive, i.e.

$$\Psi_x^{+(0)} \geq 0 \quad \text{and} \quad \Psi_y^{+(0)} \geq 0, \quad (5.103)$$

3. the second moment(s) of the in-cell source is bounded such as

$$\left|\Psi^{(1,0)}\right| \leq \sqrt{3}\Psi^{(0,0)}, \left|\Psi^{(0,1)}\right| \leq \sqrt{3}\Psi^{(0,0)}, \quad (5.104)$$

and

$$\left|\Psi^{(1,1)}\right| \leq \sqrt{3} \min \left\{ \sqrt{3}\Psi^{(0,0)}, \left|\Psi^{(1,0)}\right|, \left|\Psi^{(0,1)}\right| \right\}, \quad (5.105)$$

4. the second moment(s) of the incoming flux is bounded such as

$$\left|\Psi_x^{+(1)}\right| \leq \sqrt{3}\Psi_x^{+(0)} \quad \text{and} \quad \left|\Psi_y^{+(1)}\right| \leq \sqrt{3}\Psi_y^{+(0)}. \quad (5.106)$$

These constraints are more numerous than in the 1D case and establishing an expression for the weighting factors to enforce positivity is way harder. The flux moments are given by the solution of the  $4 \times 4$  matrix system, explicated in Eq. 5.72, and the complicated relations between  $(Q_x, Q_y)$  and  $(T_x, T_y)$  makes it really hard to obtain positivity-enforcing inequalities. Investigations to find centroid coordinates  $(u_x^{\text{CM}}, u_y^{\text{CM}})$  that strictly enforces positivity have, unfortunately, failed. Yet, expressions were found to improve greatly positivity and

monotonicity, and finding weights that stricly enforce positivity remains an open question.

The parameters

$$\dot{Q}_x = \sqrt{3}s_x \frac{\mathcal{Q}^{(1,0)}}{\mathcal{Q}^{(0,0)}} = \sqrt{3}s_x \left[ \frac{\tilde{Q}^{(1,0)} - \sqrt{3}h_x s_x \Psi_x^{-(0)} + h_y \Psi_y^{-(1)}}{\tilde{Q}^{(0,0)} + h_x \Psi_x^{-(0)} + h_y \Psi_y^{-(0)}} \right] \quad (5.107)$$

and

$$\dot{Q}_y = \sqrt{3}s_y \frac{\mathcal{Q}^{(0,1)}}{\mathcal{Q}^{(0,0)}} = \sqrt{3}s_y \left[ \frac{\tilde{Q}^{(0,1)} + h_x \Psi_x^{-(1)} - \sqrt{3}s_y h_y \Psi_y^{-(0)}}{\tilde{Q}^{(0,0)} + h_x \Psi_x^{-(0)} + h_y \Psi_y^{-(0)}} \right] \quad (5.108)$$

can be interpreted as the derivative of the source terms. It is assumed that the determination of centroid coordinate  $u_k^{\text{CM}}$  can be chosen from  $\dot{Q}_k$ , and only that value, for  $k \in \{x, y\}$ . It is also presumed that the required weights are given by the same rules as in the 1D case, such that  $\dot{Q}_k > 0$  requires  $u_k^{\text{CM}} > 0$  and vice-versa, based on Eq. 5.95. The value of the centroid coordinates are inflated by translating the positive and negative correction threshold in Eq. 5.95 to  $\dot{Q}_k = 0$ , to compensate the lack of a strictly positive method, such as

$$u_k^{\text{CM}} = \begin{cases} -\frac{1}{2} & \dot{Q}_k < -2 \\ \frac{\dot{Q}_k}{4} & -2 < \dot{Q}_k < 0 \\ \frac{\dot{Q}_k + \sqrt{3\dot{Q}_k(\dot{Q}_k + 3)}}{2\dot{Q}_k + 9} & 0 < \dot{Q}_k < \frac{3}{2} \\ \frac{1}{2} & \frac{3}{2} < \dot{Q}_k \end{cases} \quad (5.109)$$

This method is used for the results in Sect. 5.5.2, but also the ones in Sect. 3.14. An alternative expression to evaluate weights is used for the results in Sect. 5.5.1, but it relies on similar hypothesis and can be found in Bienvenue et al. [158].

## 5.5 Results and Discussion

### 5.5.1 Energy spectrum of electrons

Reproducing the energy spectra of charged particles in matter poses a significant challenge in deterministic transport, even with high-order energy discretization [47]. Lazo et Morel have applied the DG<sub>1</sub> scheme to the discretization of the CSD operator [48]. While improvement is observed where the classical DD<sub>0</sub> scheme produces oscillation, this scheme produces a negative flux dip at a high-energy part of the spectrum. This is, therefore, a valuable benchmark to evaluate the performance of the 2D adaptive scheme. These results were presented at M&C 2023 conference [158].

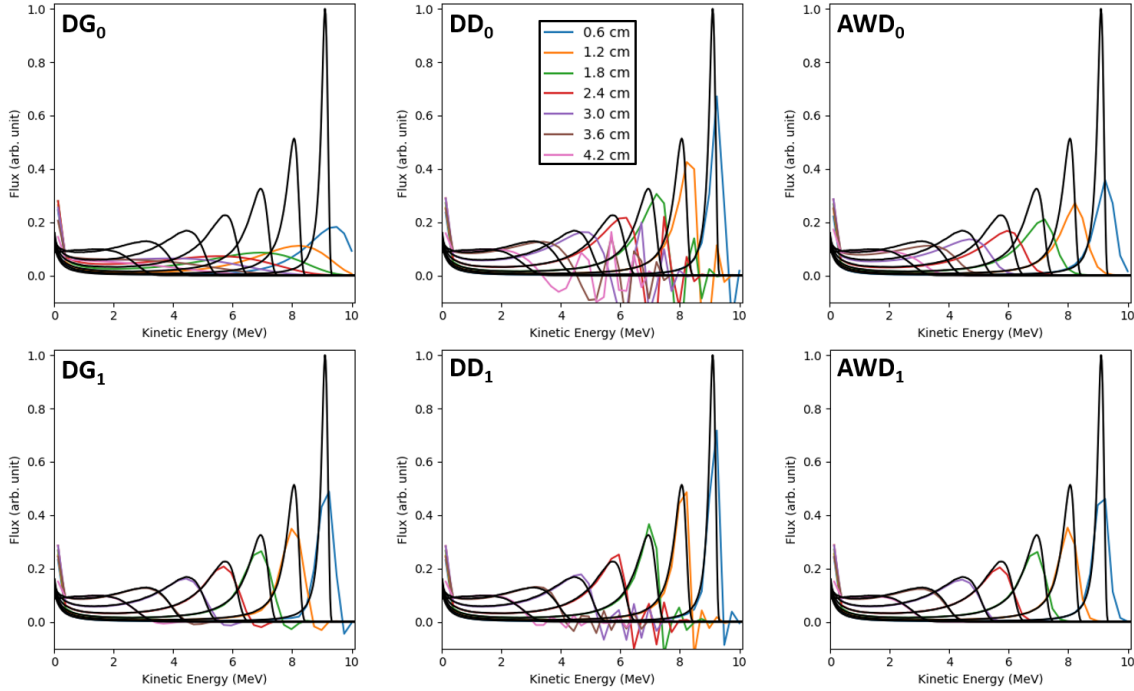


Figure 5.8 Electron energy spectra at various depths: comparison of different closure relations with 40 energy groups and 40 voxels. Reference curves, shown in black, correspond to the Monte Carlo solutions, while colored spectra denote results from the BFP solver. Figure reproduced from [158].

The benchmark comprises a 10 MeV electron beam incident normally on water in a 1D slab geometry. Therefore, the 1D Boltzmann transport equation generates a 1D finite element, while the 1D BFP equation generates a 2D finite element. The electron cross-sections and stopping powers are obtained from CEPXS-BFP [16, 210]. A  $P_{15}$  Legendre order and a 1 keV cutoff energy are employed. In the geometry, the water slab has a length of 8 cm. An  $S_{16}$  Gauss-Legendre quadrature and a convergence criterion of  $10^{-7}$  are used for the discrete ordinates computational scheme. The constant and linear DD, DG and AWD schemes are compared in coarse (40 energy groups and 40 voxels) and fine (300 energy groups and 160 voxels) discretization at different depths. The energy and spatial domains are discretized in meshes of the same size. They are presented in Fig. 5.8 and Fig. 5.9. The reference curves are obtained using GEANT4 [42] Monte Carlo calculations, simulating 1 million incident particles, using 80 and 400 scoring cells in space and energy, respectively. The PENELOPE physics model is used [211]. The  $AWD_0$  is the scheme of Carlson [177] with the monotonicity parameters from Voloschenko et Germogonova [197], chosen to be  $b = 3$ . The higher this parameter is, the lower the accuracy, but the higher the monotonicity.

While enforcing monotonicity and positivity, the step scheme ( $DG_0$ ) cannot replicate the



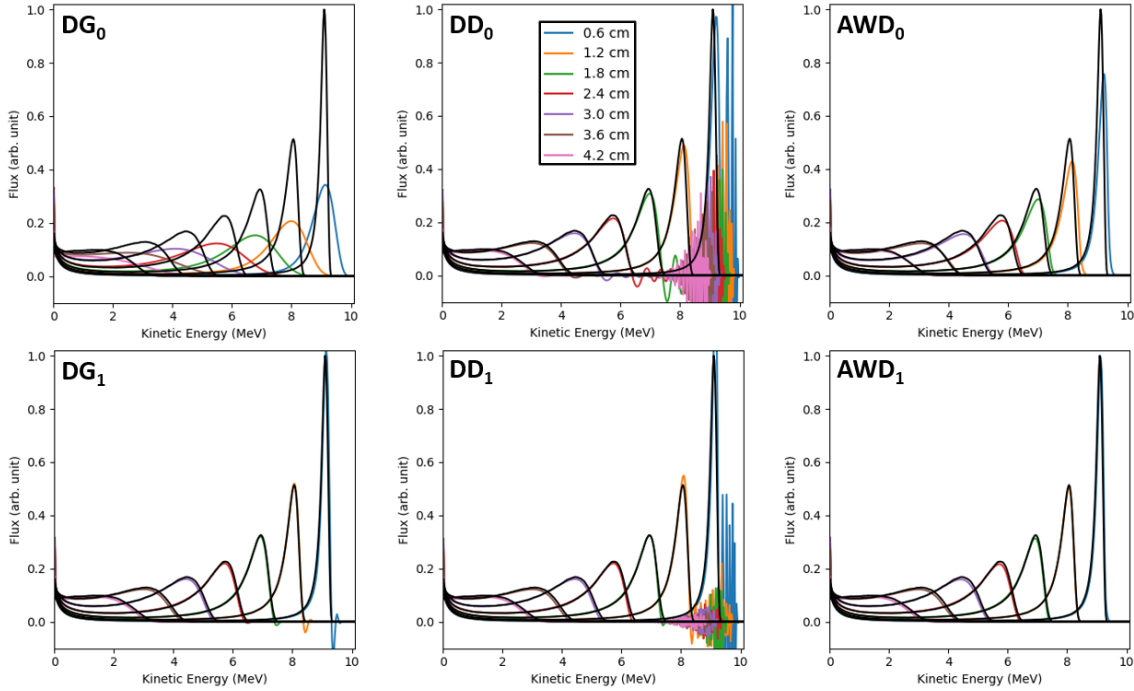


Figure 5.9 Electron energy spectra at various depths: comparison of different closure relations with 300 energy groups and 160 voxels. Reference curves, shown in black, correspond to the Monte Carlo solutions, while colored spectra denote results from the BFP solver. Figure reproduced from [158].

energy spectra, even with very fine meshes. The constant and linear DD schemes are better at reproducing the spectra peaks, which is expected for the best accuracy scheme for their respective order [157, 204], but they suffer from spurious oscillations. The  $DD_1$  scheme oscillations are, as expected, less predominant than the one of the  $DD_0$ . Unexpectedly, they are not lessened by a finer discretization but rather the opposite. This non-intuitive behaviour is noted by Petrović et Haghghat [208] that proved that these oscillations, for the  $DD_0$  scheme, remain important for any mesh refinement, even as  $h_x \rightarrow 0$ . It can be expected that the high-order DD schemes share this property with the  $DD_0$  scheme. The  $DG_1$  and  $DD_2$  exhibit less oscillation than the DD schemes, but they generate a negative flux dip at the higher-energies part of the spectrum. As seen in the following section, this can have consequences when this solution is used to estimate energy or charge deposition. The DG scheme is also prone to oscillation when the flux strongly decreases. The  $AWD_0$  strictly enforces positivity, but it lacks accuracy, which makes it unable to converge the energy spectra, even using very thin meshes. Still, it is a valuable alternative to the DD and DG schemes if one can afford the computational burden of increasing the flux polynomial expansion order in space and energy. The  $AWD_1$  scheme produces a positive and monotone solution on this challenging

benchmark, even if the proposed scheme is neither positive nor monotone. It can be seen that the scheme keeps most of the  $DG_1$  scheme while correcting the negative dip at the right of the energy spectra peak. The  $AWD_1$  scheme was also used to produce the energy spectrum in Figs. 3.10 to 3.12. It can be seen that the blue curve on the electron energy spectra in Fig. 3.12-C exhibits a non-physical oscillation around 100 MeV, which shows that there are a few cases where the scheme does not lead to a strictly positive and monotone solution. The  $AWD_1$  scheme remains very useful for energy spectrum comparison with Monte Carlo since it eliminates non-physical artifacts.

### 5.5.2 Energy deposition

The choice of scheme also has a significant impact on energy deposition calculations. The proposed benchmark comprises a 10 MeV electron beam incident normally on water in a 1D slab geometry. The electron cross-sections and stopping powers are obtained from the cross-sections developed in Chap. 3. A  $P_{15}$  Legendre order and a 1 keV cutoff energy are employed. In the geometry, the water slab has a length of 9.95 cm. An  $S_{16}$  Gauss-Legendre quadrature and a convergence criterion of  $10^{-7}$  are used for the discrete ordinates computational scheme. The energy domain is divided into 20 or 100 logarithmically spaced energy groups, while the spatial domain is divided into 20 or 100 linearly spaced voxels. The reference curves are obtained using GEANT4 Monte Carlo calculations and the PENELOPE physics model. The energy deposition solutions, based on the DD, DG, SM and AWD schemes up to linear order, are shown in Fig. 5.10.

The positive and monotone  $DG_0$  scheme is, as expected, highly inaccurate in all cases. The energy deposition profile is better characterized by constant  $DD_1$  scheme, but its solution is contaminated by intense spurious oscillations. Predicting the oscillatory behavior of the  $DD_0$  solution for a given discretization is not an easy task and, therefore, this method should be used very carefully. The  $AWD_0$  scheme, the compromise between the  $DG_0$  and  $DD_0$  schemes, damped most of the  $DD_0$  oscillations while retaining most of its accuracy. However, as shown in the case  $100g-20x$ , it can still lead to inaccurate results because it does not enforce 2<sup>nd</sup>-order accuracy. The linear  $SM_1$  offer such accuracy while being free of the inherent DD oscillations, but it exhibits intense negative flux dip near  $x = 6$  cm. The linear  $DG_1$  scheme gives similar results, but the negative flux dip is lower and accuracy is better. The linear  $DD_1$  scheme improve accuracy even more, but spurious oscillations, typical of DD schemes, are observable (rightmost graph for case  $20g-100x$  and middle one for case  $100g-20x$ ). The proposed  $AWD_1$  scheme is positive and monotone for every benchmark. It is the only 2<sup>nd</sup>-order accurate scheme to avoid the negative flux dip near  $x = 6$  cm.

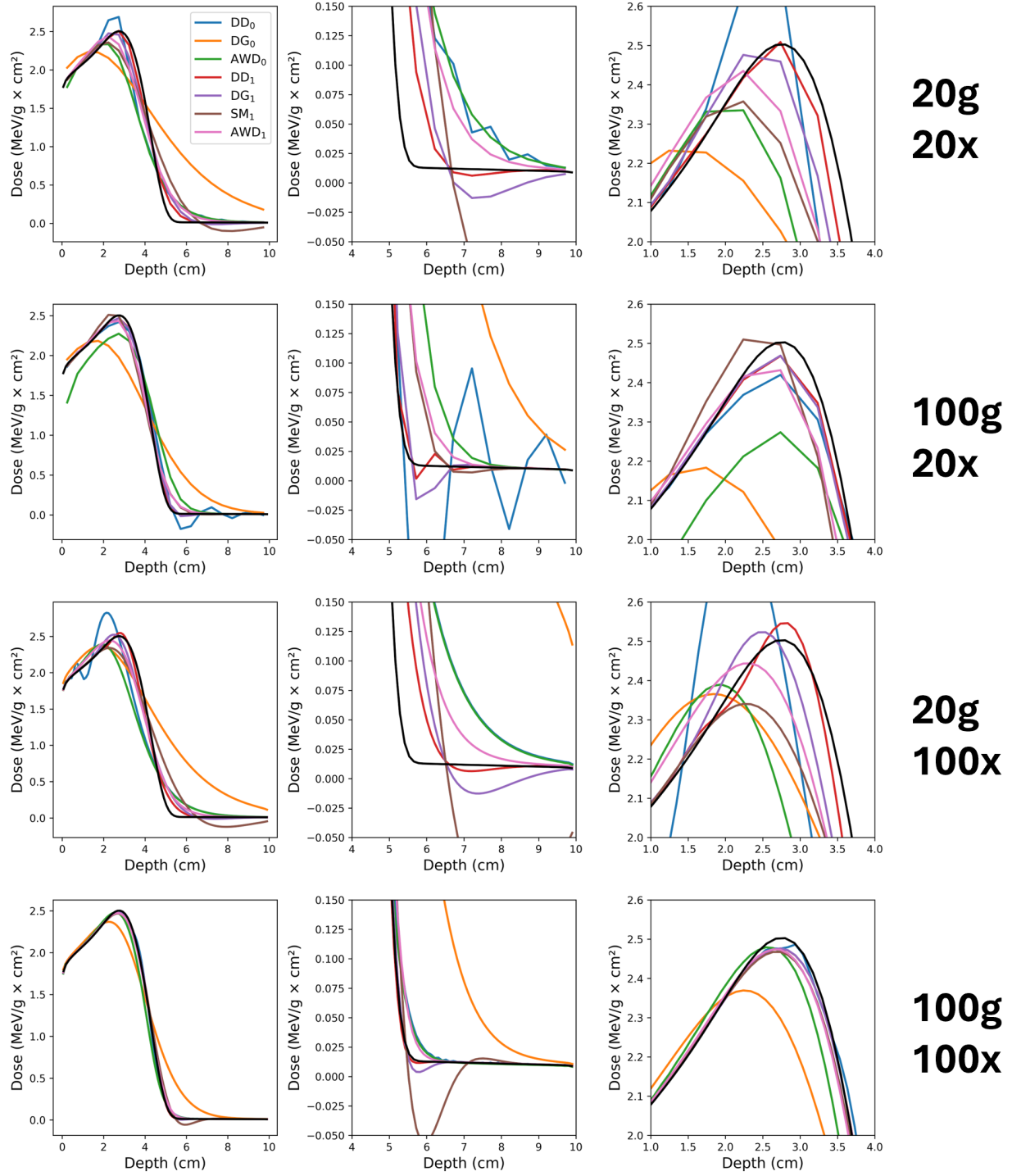


Figure 5.10 Comparison of discretization refinements and closure relations for energy deposition in water by 10 MeV incident electron beam. The black line is the Monte Carlo reference.

## 5.6 Conclusion and Perspectives

In this part of the thesis, the Boltzmann and the BFP transport equations are discretized using the Galerkin method of weighted residuals for any polynomial order expansion of the flux in space and energy. Linear 2<sup>nd</sup>-order accurately weighted schemes are developed based on constant-linear flux representation in 1D and 2D meshes. An adaptive choice of weights is proposed, leveraging the properties of these schemes. In the 1D case, the maximum accuracy positivity-enforcing weighting factors are found. In the 2D case, the relation between sources and flux moments is way more intricate than in 1D, and positivity-enforcing weighting factors are still to be discovered. Nevertheless, improved positivity and monotonicity can be obtained by extrapolating the conclusion of the 1D case to the 2D case. The resulting scheme is neither strictly positive nor monotone, but it significantly improves the non-adaptive scheme while enforcing strict 2<sup>nd</sup>-order accuracy.

Finding a positive and monotone 2<sup>nd</sup>-order accurate scheme for the transport equation is a long-standing problem [47, 162]. The proposed 2D weighted scheme seems to have the potential to address this challenge, as shown by its uses throughout this thesis. Proving that positivity can or cannot be enforced strictly by this 2D weighted scheme remains an open question. The methodology to develop this 1D and 2D weighted scheme, using linear-constant flux expansion, could be used to develop similar schemes on 3D meshes (for 3D Boltzmann, along x, y and z axis, and 2D BFP equation, along x, y and E axis) and in 4D meshes (for 3D BFP equation, along x, y, z and E axis). It is unclear if the resulting scheme can be written analytically as for the 1D and 2D schemes. Likewise, developing mixed schemes, linear along some axes and constant along others, and adaptive schemes for them could be interesting. For example, based on very fine 3D voxels such as the one expected from CT or MRI images, it could be sufficient to use a constant expansion for the flux in space while using a linear expansion in energy. Finally, while high-order expansion of the flux in energy was considered in this section, higher-order expansion of the stopping powers and total cross-sections in each energy cell could be considered, which would further increase the accuracy with coarse energy meshes. However, it should be noted that while the weighted scheme is fully compatible with the general polynomial expansion of these stopping powers and total cross-sections in each energy cell, the adaptive choice of weights proposed in this section depends on it. This would deserve further investigation if one wants the adaptive schemes to be compatible with the generalized multigroup approach.

## CHAPTER 6 CONCLUSION

### 6.1 Summary of Works

In this dissertation, algorithms for the BFP equation were developed to address identified shortcomings in producing coupled photon-electron-positron multigroup cross-sections in the angular discretization and the choice of closure relation. The main goal was to propose a tool to make determinist transport more reliable for RTP applications.

The production of accurate coupled photon-electron multigroup cross-sections was, until then, monopolized by the CEPXS code. Since 1989, most innovative research has come from the transport solver, but improvement in the produced cross-sections has yet to be made, whereas Monte-Carlo physics models have significantly evolved. Nonetheless, multiple issues within its multigroup methodology were identified, and its proprietary nature hinders the implementation of newer models and methods. A novel coupled photon-electron-positron multigroup cross-sections code for the BFP equation, RADIANT, was developed. It includes improved physics models for impact ionization, elastic scattering of electrons and positrons, bremsstrahlung, annihilation, Rayleigh scattering, Compton scattering, photoelectric effect, pair production and relaxation cascades. Explicit atomic data for positrons is defined. A novel definition for the soft and catastrophic domains was proposed to give an unambiguous definition of soft-stopping powers at boundaries. An updated and more accurate energy deposition formula is proposed. These methods were then used for BFP transport calculations, and their solutions, which consisted of energy deposition profiles and energy spectrum at various depths per particle species, have shown, compared to Monte-Carlo calculations, the capabilities of these cross-sections to replicate the distribution of particle and of energy in the medium.

Discretizing the angular domain of the transport equation, notably in multidimensional geometry, can be very challenging for classical discrete methods such as the one used in RTP. Electrons and positrons have highly forward-peaked scattering, and such scattering can lead to inaccurate results or even divergence of the SI process. The Galerkin quadrature method, which solves the leading issues with the  $S_N$  method, has been implemented and is compatible with any quadrature choice. Nonetheless, it was also observed that such scattering leads to significant monotonicity issues that can contaminate the energy deposition solution. To solve that issue, a monotone and moment-preserving finite-difference scheme has been developed for the AFP operator, based on a Voronoi tessellation of the unit sphere and compatible with nonorthogonal quadrature, to treat the forward-peaked component of the scattering.

These methods were shown to be very successful in tackling issues related to forward peaked scattering while enabling the use of efficient optimal quadrature.

The distribution of particles in space and energy varies enormously over small distances or energy changes in electron and positron transport problems. This is numerically troublesome, even using high-order DG-FEM, leading to negative energy deposition values and the inability to replicate energy spectra. Adaptive second-order accurate linear schemes have been developed and defined over 1D and 2D meshes, addressing non-adaptive schemes' monotonicity and positivity issues. Compared to calculations with non-adaptive schemes and Monte Carlo references their results show that adaptive schemes can give positive and monotone solutions, whereas second-order non-adaptive schemes fail.

In summary, this work proposed improved atomic data for particles of interest in RTP, a robust and efficient angular discretization for multidimensional transport, and accurate adaptive schemes for space and energy to mitigate parasite oscillations and negativities in solution.

## 6.2 Future Research

This work is not a dead end; on the contrary, it is a springboard toward developing new capabilities. While providing key advancements, the presented work is not without flaws, nor could it be directly applied for usage in clinical RTP systems.

For cross-section production, there are many limitations to the presented work. The leading one is the treatment of annihilation when positrons scatter under the cutoff. The absence of annihilation photons for soft positrons absorption with positron beams, could lead to substantial errors. Tackling this problem will require further investigations into developing better impact ionization models for small energy losses or some under-the-cutoff transport capabilities. The RADIANT package provides an open-source environment that will facilitate the development of improved physics models. More realistic cross-sections can be obtained for Compton scattering based on the subshell-dependant relativistic impulse models of Brusa et al. [146], with the related relaxation cascades. Its decomposition in soft and catastrophic components could also be investigated to see if it improves the calculations of high-order moments. The quality of the elastic cross-section should be further explored and compared to Monte Carlo calculations relying on state-of-the-art models. It could also be interesting to extend the RADIANT solver to generalized multigroup cross-sections, including high-order moments of the cross-sections in energy since high-order expansion in energy would require only minor changes in the development presented in Chap. 5. Finally, the development of

cross-sections for low-energy ( $< 1$  keV) applications or very-high energies ( $> 200$  MeV) and for other particles like protons, neutrons, and pions would extend the range of application of deterministic methods. The development of a coupled cross-section library including protons could be beneficial for proton therapy, which is likely to become more common in the years to come.

For the transport solver, many challenges remain toward an efficient general-purpose tool for RTP. The proposed adaptive schemes are beneficial for testing cross-section models, but 3D and 4D extensions would be necessary, which is not straightforward. An adaptive mixed linear (energy) and constant (in 3D space) scheme could, however, be of interest for RTP since 3D images are already composed of small voxels, and developing a strictly positivity-enforcing scheme should not cause too many difficulties. Ray effect remains an outstanding challenge with the discrete ordinates, and new ideas will be required to offer a satisfying solution to that problem. Until then, it still can be mitigated using conservative First Collision Source (FCS) methods. Another critical problem not addressed in this thesis is inner-iteration acceleration with highly-forward-peaked scattering. Improving the convergence of such methods in multidimensional geometries could help to make calculations faster. For clinical usage, parallelization over multiple CPUs or GPUs could be necessary to accelerate the calculations, and the development of such capabilities should be further investigated. Another crucial development would be a tool to estimate the error of the deterministic calculations, which is currently lacking. Some applications, such as MRI-guided radiotherapy, can require the inclusion of external magnetic and electric fields. St-Aubin et al. [23], and Pautz et al. [34] have proposed additional terms to add to the transport equation. Developing moment-preserving schemes, as the one for the AFP, is also a fascinating subject of study.

## REFERENCES

- [1] J. C. Garth, “Electron/photon transport and its applications,” *The Monte Carlo Method: Versatility Unbounded in a Dynamic Computing World*, Chattanooga, Tennessee, pp. 17–21, 2005.
- [2] J. L. Liscum-Powell, *Finite element numerical solution of a self-adjoint transport equation for coupled electron-photon problems*. The University of New Mexico, 2000.
- [3] M. Barberio, S. Veltri, M. Sciscio, and P. Antici, “Laser-accelerated proton beams as diagnostics for cultural heritage,” *Scientific Reports*, vol. 7, no. 1, p. 40415, 2017.
- [4] P. Reuss, *Précis de neutronique*. EDP sciences, 2003.
- [5] F. M. Khan and J. P. Gibbons, *Khan’s the physics of radiation therapy*. Lippincott Williams & Wilkins, 2014.
- [6] N. Papanikolaou, J. Battista, A. Boyer, C. Kappas, E. Klein, T. Mackie, M. Sharpe, and J. Van Dyk, *Tissue inhomogeneity corrections for megavoltage photon beams. AAPM Report No 85; Task Group No. 85; Task Group No. 65*, 01 2004.
- [7] K. A. Gifford, J. L. Horton, T. A. Wareing, G. Failla, and F. Mourtada, “Comparison of a finite-element multigroup discrete-ordinates code with Monte Carlo for radiotherapy calculations,” *Physics in Medicine & Biology*, vol. 51, no. 9, p. 2253, 2006.
- [8] A. F. Bielajew and D. W. Rogers, “PRESTA: the parameter reduced electron-step transport algorithm for electron Monte Carlo transport,” *Nuclear Instruments and Methods in Physics Research Section B: Beam Interactions with Materials and Atoms*, vol. 18, no. 1-6, pp. 165–181, 1986.
- [9] O. N. Vassiliev, *Monte Carlo methods for radiation transport*. Springer, 2017.
- [10] E. Boman, “Radiotherapy forward and inverse problem applying Boltzmann transport equation (Sädehoidon suora ja käänteisongelma boltzmannin siirtoyhtälön avulla),” Ph.D. dissertation, Kuopion yliopisto, 2007.
- [11] E. Spezi and G. Lewis, “An overview of Monte Carlo treatment planning for radiotherapy,” *Radiation protection dosimetry*, vol. 131, no. 1, pp. 123–129, 2008.
- [12] J. Seco and F. Verhaegen, *Monte Carlo techniques in radiation therapy*. CRC press Boca Raton, 2013.



- [13] P. Andreo, D. T. Burns, A. E. Nahum, J. Seuntjens, and F. H. Attix, *Fundamentals of ionizing radiation dosimetry*. John Wiley & Sons, 2017.
- [14] C. Börger, “Complexity of Monte Carlo and deterministic dose-calculation methods,” *Physics in Medicine & Biology*, vol. 43, no. 3, p. 517, 1998.
- [15] K. Przybylski and J. Ligou, “Numerical analysis of the Boltzmann equation including Fokker-Planck terms,” *Nuclear Science and Engineering*, vol. 81, no. 1, pp. 92–109, 1982.
- [16] L. Lorence Jr, J. Morel, and G. Valdez, “Physics guide to CEPXS: a multigroup coupled electron-photon cross-section generating code,” Sandia National Lab.(SNL-NM), Albuquerque, NM (United States), Tech. Rep., 1989.
- [17] J. E. Morel, “A hybrid collocation-Galerkin-Sn method for solving the Boltzmann transport equation,” *Nuclear Science and Engineering*, vol. 101, no. 1, pp. 72–87, 1989.
- [18] O. N. Vassiliev, T. A. Wareing, I. M. Davis, J. McGhee, D. Barnett, J. L. Horton, K. Gifford, G. Failla, U. Titt, and F. Mourtada, “Feasibility of a multigroup deterministic solution method for three-dimensional radiotherapy dose calculations,” *International Journal of Radiation Oncology, Biology and Physics*, vol. 72, no. 1, pp. 220–227, 2008.
- [19] O. N. Vassiliev, T. A. Wareing, J. McGhee, G. Failla, M. R. Salehpour, and F. Mourtada, “Validation of a new grid-based Boltzmann equation solver for dose calculation in radiotherapy with photon beams,” *Physics in Medicine & Biology*, vol. 55, no. 3, p. 581, 2010.
- [20] A. Fogliata, G. Nicolini, E. Vanetti, A. Clivio, and L. Cozzi, “Dosimetric validation of the anisotropic analytical algorithm for photon dose calculation: fundamental characterization in water,” *Physics in Medicine & Biology*, vol. 51, no. 6, p. 1421, 2006.
- [21] T. Han, J. K. Mikell, M. Salehpour, and F. Mourtada, “Dosimetric comparison of Acuros XB deterministic radiation transport method with Monte Carlo and model-based convolution methods in heterogeneous media,” *Medical Physics*, vol. 38, no. 5, pp. 2651–2664, 2011.
- [22] C. Yan, A. G. Combine, G. Bednarz, R. J. Lalonde, B. Hu, K. Dickens, R. Wynn, D. C. Pavord, and M. Saiful Huq, “Clinical implementation and evaluation of the Acuros dose calculation algorithm,” *Journal of Applied Clinical Medical Physics*, vol. 18, no. 5, pp. 195–209, 2017.

- [23] J. St. Aubin, A. Keyvanloo, O. Vassiliev, and B. Fallone, “A deterministic solution of the first order linear Boltzmann transport equation in the presence of external magnetic fields,” *Medical Physics*, vol. 42, no. 2, pp. 780–793, 2015.
- [24] J. St. Aubin, A. Keyvanloo, and B. Fallone, “Discontinuous finite element space-angle treatment of the first order linear Boltzmann transport equation with magnetic fields: Application to MRI-guided radiotherapy,” *Medical Physics*, vol. 43, no. 1, pp. 195–204, 2016.
- [25] O. Zelyak, B. G. Fallone, and J. St-Aubin, “Stability analysis of a deterministic dose calculation for MRI-guided radiotherapy,” *Physics in Medicine & Biology*, vol. 63, no. 1, p. 015011, 2017.
- [26] R. Yang, O. Zelyak, B. Fallone, and J. St-Aubin, “A novel upwind stabilized discontinuous finite element angular framework for deterministic dose calculations in magnetic fields,” *Physics in Medicine & Biology*, vol. 63, no. 3, p. 035018, 2018.
- [27] R. Yang, D. Santos, B. Fallone, and J. St-Aubin, “A novel transport sweep architecture for efficient deterministic patient dose calculations in MRI-guided radiotherapy,” *Physics in Medicine & Biology*, vol. 64, no. 18, p. 185012, 2019.
- [28] J. Kópházi and D. Lathouwers, “A space-angle DGFEM approach for the Boltzmann radiation transport equation with local angular refinement,” *Journal of Computational Physics*, vol. 297, pp. 637–668, 2015.
- [29] A. Hennink and D. Lathouwers, “A discontinuous Galerkin method for the mono-energetic Fokker–Planck equation based on a spherical interior penalty formulation,” *Journal of Computational and Applied Mathematics*, vol. 330, pp. 253–267, 2018.
- [30] D. Lathouwers and Z. Perkó, “An angular multigrid preconditioner for the radiation transport equation with Fokker–Planck scattering,” *Journal of Computational and Applied Mathematics*, vol. 350, pp. 165–177, 2019.
- [31] T. Burlacu, D. Lathouwers, and Z. Perkó, “A deterministic adjoint-based semi-analytical algorithm for fast response change computations in proton therapy,” *Journal of Computational and Theoretical Transport*, vol. 52, no. 1, pp. 1–41, 2023.
- [32] C. R. Drumm, W. C. Fan, and S. D. Pautz, “Specializations in the SCEPTRE Code for Charged-Particle Transport.” Sandia National Lab.(SNL-NM), Albuquerque, NM (United States), Tech. Rep., 2018.

- [33] W. C. Fan, C. R. Drumm, S. D. Pautz, and C. D. Turner, “Modeling electron transport in the presence of electric and magnetic fields.” Sandia National Lab.(SNL-NM), Albuquerque, NM (United States), Tech. Rep., 2013.
- [34] S. D. Pautz, C. Drumm, W. C. Fan, and C. D. Turner, “A discontinuous phase-space finite element discretization of the linear boltzmann-vlasov equation for charged particle transport,” *Journal of Computational and Theoretical Transport*, vol. 43, no. 1-7, pp. 128–147, 2014.
- [35] R. E. MacFarlane and D. W. Muir, “The NJOY nuclear data processing system version 91,” Los Alamos National Lab., NM (United States), Tech. Rep., 1994.
- [36] A. Trkov and D. A. Brown, “ENDF-6 Formats Manual: Data formats and procedures for the evaluated nuclear data files,” Brookhaven National Lab.(BNL), Upton, NY (United States), Tech. Rep., 2018.
- [37] A. Naceur, C. Bienvenue, P. Romano, C. Chilian, and J.-F. Carrier, “Extending deterministic transport capabilities for very-high and ultra-high energy electron beams,” *Scientific Reports*, vol. 14, no. 1, p. 2796, 2024.
- [38] A. Hébert and A. Naceur, “Implementation of the ELECTR module in NJOY,” in *EPJ Web of Conferences*, vol. 284. EDP Sciences, 2023, p. 11001.
- [39] A. Naceur, P. Romano, C. Chilian, and J.-F. Carrier, “Granularity Level Requirements for Multigroup Evaluated Electron Data Library Use in Boltzmann-Fokker-Planck Codes: A Bremsstrahlung Case Study,” in *43rd Annual Canadian Nuclear Society Conference*, 2024.
- [40] H. Hensel, R. Iza-Teran, and N. Siedow, “Deterministic model for dose calculation in photon radiotherapy,” *Physics in Medicine & Biology*, vol. 51, no. 3, p. 675, 2006.
- [41] E. Olbrant and M. Frank, “Generalized Fokker–Planck theory for electron and photon transport in biological tissues: application to radiotherapy,” *Computational and Mathematical Methods in Medicine*, vol. 11, no. 4, pp. 313–339, 2010.
- [42] S. Agostinelli, J. Allison, K. a. Amako, J. Apostolakis, H. Araujo, P. Arce, M. Asai, D. Axen, S. Banerjee, G. Barrand *et al.*, “GEANT4—a simulation toolkit,” *Nuclear Instruments and Methods in Physics Research Section A: Accelerators, Spectrometers, Detectors and Associated Equipment*, vol. 506, no. 3, pp. 250–303, 2003.

- [43] F. Salvat, J. M. Fernández-Varea, J. Sempau *et al.*, “PENELOPE-2018: A Code System for Monte Carlo Simulation of Electron and Photon transport,” in *Nuclear Energy Agency (NEA) Data Bank*, 2019.
- [44] I. Kawrakow and D. Rogers, “The EGSnrc code system,” *NRC Report PIRS-701*, NRC, Ottawa, 2021.
- [45] S. D. Pautz and M. L. Adams, “An asymptotic study of discretized transport equations in the Fokker-Planck limit,” *Nuclear Science and Engineering*, vol. 140, no. 1, pp. 51–69, 2002.
- [46] G. A. Failla, T. Wareing, Y. Archambault, and S. Thompson, “Acuros XB advanced dose calculation for the Eclipse treatment planning system,” *Palo Alto, CA: Varian Medical Systems*, vol. 20, p. 18, 2010.
- [47] Y. Azmy, E. Sartori, E. W. Larsen, and J. E. Morel, “Advances in discrete-ordinates methodology,” *Nuclear Computational Science: A Century in Review*, pp. 1–84, 2010.
- [48] M. S. Lazo and J. Morel, “A linear discontinuous Galerkin approximation for the continuous slowing down operator,” *Nuclear Science and Engineering*, vol. 92, no. 1, pp. 98–109, 1986.
- [49] M. D. Wilkinson, M. Dumontier, I. J. Aalbersberg, G. Appleton, M. Axton, A. Baak, N. Blomberg, J.-W. Boiten, L. B. da Silva Santos, P. E. Bourne *et al.*, “The FAIR Guiding Principles for scientific data management and stewardship,” *Scientific Data*, vol. 3, no. 1, pp. 1–9, 2016.
- [50] A. Hébert, *Applied reactor physics*. Presses Internationales Polytechnique, 2009.
- [51] E. E. Lewis and W. F. Miller, *Computational methods of neutron transport*. John Wiley and Sons, Inc., New York, NY, 1984.
- [52] I. K. Attieh, “Generalized Multigroup Method,” Ph.D. dissertation, University of Tennessee, 2004.
- [53] M. J. Berger and R. Wang, “Multiple-scattering angular deflections and energy-loss straggling,” in *Monte Carlo Transport of Electrons and Photons*. Springer, 1988, pp. 21–56.
- [54] J. Morel, “Fokker-Planck calculations using standard discrete ordinates transport codes,” *Nuclear Science and Engineering*, vol. 79, no. 4, pp. 340–356, 1981.

- [55] G. Pomraning, “The Fokker-Planck operator as an asymptotic limit,” *Mathematical Models and Methods in Applied Sciences*, vol. 2, no. 01, pp. 21–36, 1992.
- [56] S. B. Uilkema, “Proton therapy planning using the SN method with the Fokker-Planck approximation,” *Delft University of Technology*, 2012.
- [57] G. Pomraning, “Higher order fokker-planck operators,” *Nuclear Science and Engineering*, vol. 124, no. 3, pp. 390–397, 1996.
- [58] K. S. Beling, A. K. Prinja, and J. S. Warsa, “Generalized Fokker-Planck Approximations for Fast-Ion Slowing Down,” in *International Conference on Mathematics and Computational Methods Applied to Nuclear Science and Engineering (M&C 2023)*, 2023.
- [59] A. A. Calloo, “Parallel Discontinuous Finite Element SN Solver in Cartesian and Hexagonal Geometries for the Boltzmann Transport Equation in DRAGONS5,” Ph.D. dissertation, Polytechnique Montréal, 2022.
- [60] E. Gelbard, “Application of spherical harmonics method to reactor problems,” *Bettis Technical Review*, p. 73, 1960.
- [61] C. R. Drumm, “Spherical Harmonics (PN) Methods in the SCEPTRE Radiation Transport Code.” Sandia National Lab.(SNL-NM), Albuquerque, NM (United States), Tech. Rep., 2015.
- [62] H. Greenspan, C. Kelber, and D. Okrent, *Computing methods in reactor physics*. Gordon and Breach, 1972.
- [63] A. C. Oliveira, M. G. Santana, F. R. Lima, and J. W. Vieira, “Monte Carlo simulation of a medical linear accelerator for generation of phase spaces,” in *2013 International Nuclear Atlantic Conference - INAC 2013*, 2013.
- [64] K. D. Lathrop, “Ray effects in discrete ordinates equations,” *Nuclear Science and Engineering*, vol. 32, no. 3, pp. 357–369, 1968.
- [65] R. E. Alcouffe, “A first collision source method for coupling Monte Carlo and discrete ordinates for localized source problems,” in *Monte-Carlo Methods and Applications in Neutronics, Photonics and Statistical Physics: Proceedings of the Joint Los Alamos National Laboratory-Commissariat à l’Energie Atomique Meeting Held at Cadarache Castle, Provence, France April 22–26, 1985*. Springer, 2006, pp. 352–366.

- [66] J. E. Morel, T. A. Wareing, R. B. Lowrie, and D. K. Parsons, “Analysis of ray-effect mitigation techniques,” *Nuclear Science and Engineering*, vol. 144, no. 1, pp. 1–22, 2003.
- [67] W. Filippone, J. E. Morel, and W. F. Walters, “An extended first collision source method for electron beam source problems,” *Nuclear Science and Engineering*, vol. 112, no. 1, pp. 1–15, 1992.
- [68] C. R. Drumm, W. C. Fan, L. Lorence, and J. Liscum-Powell, “An analysis of the extended-transport correction with application to electron beam transport,” *Nuclear Science and Engineering*, vol. 155, no. 3, pp. 355–366, 2007.
- [69] M. Voloschenko and A. Dubinin, “ROZ-6.5: One-dimensional Discrete-ordinates Neutron, Photon and Charged Particles Transport Code, User’s Guide,” Keldysh Institute of Applied Mathematics, Moscow, Russia, Tech. Rep. 7-25, 2004.
- [70] A. B. Christensen, A. Kunen, J. Loffeld, P. Brown, and M. Fratoni, “A conservative first-collision source treatment for ray effect mitigation in discrete-ordinate radiation transport solutions,” *Journal of Computational Physics*, vol. 509, p. 113049, 2024.
- [71] T. A. Wareing, J. E. Morel, and D. K. Parsons, “A first collision source method for ATTILA, an unstructured tetrahedral mesh discrete ordinates code,” Los Alamos National Lab.(LANL), Los Alamos, NM (United States), Tech. Rep., 1998.
- [72] T. Camminady, M. Frank, K. Küpper, and J. Kusch, “Ray effect mitigation for the discrete ordinates method through quadrature rotation,” *Journal of Computational Physics*, vol. 382, pp. 105–123, 2019.
- [73] M. Frank, J. Kusch, T. Camminady, and C. D. Hauck, “Ray effect mitigation for the discrete ordinates method using artificial scattering,” *Nuclear Science and Engineering*, vol. 194, no. 11, pp. 971–988, 2020.
- [74] T. A. Wareing, J. M. McGhee, J. E. Morel, and S. D. Pautz, “Discontinuous finite element SN methods on three-dimensional unstructured grids,” *Nuclear Science and Engineering*, vol. 138, no. 3, pp. 256–268, 2001.
- [75] R. E. Alcouffe, “Diffusion synthetic acceleration methods for the diamond-differenced discrete-ordinates equations,” *Nuclear Science and Engineering*, vol. 64, no. 2, pp. 344–355, 1977.

- [76] J. E. Morel and T. Manteuffel, “An angular multigrid acceleration technique for Sn equations with highly forward-peaked scattering,” *Nuclear Science and Engineering*, vol. 107, no. 4, pp. 330–342, 1991.
- [77] K. R. Koch, R. S. Baker, and R. E. Alcouffe, “Solution of the first-order form of the 3-D discrete ordinates equation on a massively parallel processor,” *Transactions of the American Nuclear Society*, vol. 65, no. 108, pp. 198–199, 1992.
- [78] S. D. Pautz, “An algorithm for parallel Sn sweeps on unstructured meshes,” *Nuclear Science and Engineering*, vol. 140, no. 2, pp. 111–136, 2002.
- [79] A. A. Calloo and A. Hébert, “Parallel transport sweeps on two-dimensional cartesian and hexagonal grids,” American Nuclear Society-ANS, La Grange Park, IL 60526 (United States), Tech. Rep., 2022.
- [80] S. Moustafa, I. Dutka-Malen, L. Plagne, A. Ponçot, and P. Ramet, “Shared memory parallelism for 3D Cartesian discrete ordinates solver,” *Annals of Nuclear Energy*, vol. 82, pp. 179–187, 2015.
- [81] J. Morel, L. J. Lorence Jr, R. P. Kensek, J. A. Halbleib, and D. Sloan, “A hybrid multigroup/continuous-energy Monte Carlo method for solving the Boltzmann-Fokker-Planck equation,” *Nuclear Science and Engineering*, vol. 124, no. 3, pp. 369–389, 1996.
- [82] C. Bienvenue, A. Naceur, A. Hébert, and J.-F. Carrier, “Toward Highly Accurate Multi-group Coupled Photon-Electron-Positron Cross-Sections for the Boltzmann Fokker-Planck Equation,” submitted to *Journal of Computational Physics* (May 2024).
- [83] C. DesRosiers, V. Moskvina, A. F. Bielajew, and L. Papiez, “150-250 MeV electron beams in radiation therapy,” *Physics in Medicine & Biology*, vol. 45, no. 7, p. 1781, 2000.
- [84] L. Papiez, C. DesRosiers, and V. Moskvina, “Very high energy electrons (50–250 MeV) and radiation therapy,” *Technology in Cancer Research & Treatment*, vol. 1, no. 2, pp. 105–110, 2002.
- [85] K. Kokurewicz, E. Brunetti, G. Welsh, S. Wiggins, M. Boyd, A. Sorensen, A. Chalmers, G. Schettino, A. Subiel, C. DesRosiers *et al.*, “Focused very high-energy electron beams as a novel radiotherapy modality for producing high-dose volumetric elements,” *Scientific Reports*, vol. 9, no. 1, p. 10837, 2019.

- [86] S. Incerti, G. Baldacchino, M. Bernal, R. Capra, C. Champion, Z. Francis, P. Guèye, A. Mantero, B. Mascialino, P. Moretto *et al.*, “The geant4-dna project,” *International Journal of Modeling, Simulation, and Scientific Computing*, vol. 1, no. 02, pp. 157–178, 2010.
- [87] J. D. Boice Jr, “The linear nonthreshold (LNT) model as used in radiation protection: an NCRP update,” *International Journal of Radiation Biology*, vol. 93, no. 10, pp. 1079–1092, 2017.
- [88] J. A. Siegel, C. W. Pennington, and B. Sacks, “Subjecting radiologic imaging to the linear no-threshold hypothesis: a non sequitur of non-trivial proportion,” *Journal of Nuclear Medicine*, vol. 58, no. 1, pp. 1–6, 2017.
- [89] A. W. Chao, M. Tigner, H. Weise, and F. Zimmermann, *Handbook of accelerator physics and engineering*. World scientific, 2023.
- [90] F. N. Fritsch and R. E. Carlson, “Monotone piecewise cubic interpolation,” *SIAM Journal on Numerical Analysis*, vol. 17, no. 2, pp. 238–246, 1980.
- [91] J. M. Fernández-Varea, F. Salvat, M. Dingfelder, and D. Liljequist, “A relativistic optical-data model for inelastic scattering of electrons and positrons in condensed matter,” *Nuclear Instruments and Methods in Physics Research Section B: Beam Interactions with Materials and Atoms*, vol. 229, no. 2, pp. 187–218, 2005.
- [92] C. Møller, “Zur theorie des durchgangs schneller elektronen durch materie,” *Annalen der Physik*, vol. 406, no. 5, pp. 531–585, 1932.
- [93] S. Perkins, *Tables and Graphs of Atomic Subshell and Relaxation Data Derived from the LLNL Evaluated Atomic Data Library (EADL),  $Z = 1-100$* . Lawrence Livermore National Laboratory, 1991.
- [94] M. J. Berger and S. M. Seltzer, “Stopping powers and ranges of electrons and positrons,” Center for Radiation Research, National Bureau of Standards, Washington D.C., Tech. Rep., 1982.
- [95] R. M. Sternheimer, “The density effect for the ionization loss in various materials,” *Physical Review*, vol. 88, no. 4, p. 851, 1952.
- [96] H. Kolbenstvedt, “Simple theory for K-ionization by relativistic electrons,” *Journal of Applied Physics*, vol. 38, no. 12, pp. 4785–4787, 1967.



- [97] M. Gryziński, “Two-particle collisions. I. General relations for collisions in the laboratory system,” *Physical Review*, vol. 138, no. 2A, p. A305, 1965.
- [98] H. Bhabha, “The scattering of positrons by electrons with exchange on Dirac’s theory of the positron,” *Proceedings of the Royal Society of London. Series A-Mathematical and Physical Sciences*, vol. 154, no. 881, pp. 195–206, 1936.
- [99] S. M. Seltzer, “Cross sections for bremsstrahlung production and electron-impact ionization,” in *Monte Carlo Transport of Electrons and Photons*. Springer, 1988, pp. 81–114.
- [100] S. Perkins and D. Cullen, “The Livermore electron impact ionization data base,” Lawrence Livermore National Lab.(LLNL), Livermore, CA (United States), Tech. Rep., 1989.
- [101] F. Salvat and J. Fernández-Varea, “Semiempirical cross sections for the simulation of the energy loss of electrons and positrons in matter,” *Nuclear Instruments and Methods in Physics Research Section B: Beam Interactions with Materials and Atoms*, vol. 63, no. 3, pp. 255–269, 1992.
- [102] F. Salvat, “Bethe stopping-power formula and its corrections,” *Physical Review A*, vol. 106, no. 3, p. 032809, 2022.
- [103] F. Salvat, L. Barjuan, and P. Andreo, “Inelastic collisions of fast charged particles with atoms: Bethe asymptotic formulas and shell corrections,” *Physical Review A*, vol. 105, no. 4, p. 042813, 2022.
- [104] J. H. Scofield, “K-and L-shell ionization of atoms by relativistic electrons,” *Physical Review A*, vol. 18, no. 3, p. 963, 1978.
- [105] F. Salvat and J. M. Fernández-Varea, “Overview of physical interaction models for photon and electron transport used in Monte Carlo codes,” *Metrologia*, vol. 46, no. 2, p. S112, 2009.
- [106] F. Salvat and P. Andreo, “SBETHE: Stopping powers of materials for swift charged particles from the corrected Bethe formula,” *Computer Physics Communications*, vol. 287, p. 108697, 2023.
- [107] S. M. Seltzer and M. J. Berger, “Evaluation of the collision stopping power of elements and compounds for electrons and positrons,” *The International Journal of Applied Radiation and Isotopes*, vol. 33, no. 11, pp. 1189–1218, 1982.

- [108] S. Seltzer, J. Fernandez-Varea, P. Andreo, P. Bergstrom, D. Burns, I. Krajcar Bronić, C. Ross, and F. Salvat, “Key data for ionizing-radiation dosimetry: measurement standards and applications, ICRU Report 90,” 2016.
- [109] F. Rohrlich and B. Carlson, “Positron-electron differences in energy loss and multiple scattering,” *Physical Review*, vol. 93, no. 1, p. 38, 1954.
- [110] U. Fano, “Atomic theory of electromagnetic interactions in dense materials,” *Physical Review*, vol. 103, no. 5, p. 1202, 1956.
- [111] M. Inokuti and D. Y. Smith, “Fermi density effect on the stopping power of metallic aluminum,” *Physical Review B*, vol. 25, no. 1, p. 61, 1982.
- [112] N. F. Mott, “The scattering of fast electrons by atomic nuclei,” *Proceedings of the Royal Society of London. Series A, Containing Papers of a Mathematical and Physical Character*, vol. 124, no. 794, pp. 425–442, 1929.
- [113] E. Rutherford, “LXXIX. The scattering of  $\alpha$  and  $\beta$  particles by matter and the structure of the atom,” *The London, Edinburgh, and Dublin Philosophical Magazine and Journal of Science*, vol. 21, no. 125, pp. 669–688, 1911.
- [114] G. Moliere, “Theorie der streuung schneller geladener teilchen i. einzelstreuung am abgeschirmten coulomb-feld,” *Zeitschrift für Naturforschung A*, vol. 2, no. 3, pp. 133–145, 1947.
- [115] M. E. Riley, C. J. MacCallum, and F. Biggs, “Theoretical electron-atom elastic scattering cross sections: Selected elements, 1 keV to 256 keV,” *Atomic Data and Nuclear Data Tables*, vol. 15, no. 5, pp. 443–476, 1975.
- [116] J. A. Kulesza, T. R. Adams, J. C. Armstrong, S. R. Bolding, F. B. Brown, J. S. Bull, T. P. Burke, A. R. Clark, R. A. A. Forster III, J. F. Giron *et al.*, “MCNP® code version 6.3.0 theory & user manual,” Los Alamos National Lab. (LANL), Los Alamos, NM (United States), Tech. Rep., 2022.
- [117] M. Boschini, C. Consolandi, M. Gervasi, S. Giani, D. Grandi, V. Ivanchenko, P. Nieminen, S. Pensotti, P. Rancoita, and M. Tacconi, “An expression for the Mott cross section of electrons and positrons on nuclei with  $Z$  up to 118,” *Radiation Physics and Chemistry*, vol. 90, pp. 39–66, 2013.
- [118] S. M. Seltzer, “An overview of ETRAN Monte Carlo methods,” *Monte Carlo Transport of Electrons and Photons*, pp. 153–181, 1988.

- [119] L. Urbán, “A model for multiple scattering in Geant4,” RMKI Research Institute for Particle and Nuclear Physics, Budapest, Hungary, Tech. Rep., 2006.
- [120] V. Ivanchenko, O. Kadri, M. Maire, and L. Urban, “Geant4 models for simulation of multiple scattering,” in *Journal of Physics: Conference Series*, vol. 219, no. 3. IOP Publishing, 2010, p. 032045.
- [121] F. Salvat, A. Jablonski, and C. J. Powell, “ELSEPA—Dirac partial-wave calculation of elastic scattering of electrons and positrons by atoms, positive ions and molecules,” *Computer Physics Communications*, vol. 165, no. 2, pp. 157–190, 2005.
- [122] I. Kawrakow, “Improved modeling of multiple scattering in the voxel Monte Carlo model,” *Medical Physics*, vol. 24, no. 4, pp. 505–517, 1997.
- [123] T. Lijian, H. Qing, and L. Zhengming, “Analytic fitting to the Mott cross section of electrons,” *Radiation Physics and Chemistry*, vol. 45, no. 2, pp. 235–245, 1995.
- [124] U. Fano, “Inelastic collisions and the Moliere theory of multiple scattering,” *Physical Review*, vol. 93, no. 1, p. 117, 1954.
- [125] X. A. Li and D. Rogers, “Electron mass scattering powers: Monte Carlo and analytical calculations,” *Medical Physics*, vol. 22, no. 5, pp. 531–541, 1995.
- [126] W. Koepf, “Hypergeometric summation,” *Vieweg, Braunschweig/Wiesbaden*, vol. 5, no. 6, 1998.
- [127] I. S. Gradshteyn and I. M. Ryzhik, *Table of integrals, series, and products*. Academic press, 2014.
- [128] M. Landesman and J. Morel, “Angular Fokker-Planck decomposition and representation techniques,” *Nuclear Science and Engineering*, vol. 103, no. 1, pp. 1–11, 1989.
- [129] J. Morel, “On the validity of the extended transport cross-section correction for low-energy electron transport,” *Nuclear Science and Engineering*, vol. 71, no. 1, pp. 64–71, 1979.
- [130] H. Koch and J. Motz, “Bremsstrahlung cross-section formulas and related data,” *Reviews of Modern Physics*, vol. 31, no. 4, p. 920, 1959.
- [131] M. J. Berger and S. M. Seltzer, “Bremsstrahlung and photoneutrons from thick tungsten and tantalum targets,” *Physical Review C*, vol. 2, no. 2, p. 621, 1970.

- [132] S. M. Seltzer and M. J. Berger, “Bremsstrahlung energy spectra from electrons with kinetic energy 1 keV–10 GeV incident on screened nuclei and orbital electrons of neutral atoms with  $Z=1-100$ ,” *Atomic Data and Nuclear Data Tables*, vol. 35, no. 3, pp. 345–418, 1986.
- [133] E. Acosta, X. Llovet, and F. Salvat, “Monte Carlo simulation of bremsstrahlung emission by electrons,” *Applied Physics Letters*, vol. 80, no. 17, pp. 3228–3230, 2002.
- [134] L. Kissel, C. Quarles, and R. Pratt, “Shape functions for atomic-field bremsstrahlung from electrons of kinetic energy 1–500 keV on selected neutral atoms  $1 \leq Z \leq 92$ ,” *Atomic Data and Nuclear Data Tables*, vol. 28, no. 3, pp. 381–460, 1983.
- [135] L. Kim, R. Pratt, S. Seltzer, and M. Berger, “Ratio of positron to electron bremsstrahlung energy loss: an approximate scaling law,” *Physical Review A*, vol. 33, no. 5, p. 3002, 1986.
- [136] F. Salvat, J. Fernández-Varea, J. Sempau, and X. Llovet, “Monte Carlo simulation of bremsstrahlung emission by electrons,” *Radiation Physics and Chemistry*, vol. 75, no. 10, pp. 1201–1219, 2006.
- [137] A. Pořkus, “Shape functions and singly differential cross sections of bremsstrahlung at electron energies from 10 eV to 3 MeV for  $Z=1-100$ ,” *Atomic Data and Nuclear Data Tables*, vol. 129, p. 101277, 2019.
- [138] W. R. Nelson, H. Hirayama, and D. W. Rogers, “EGS4 code system,” Stanford Linear Accelerator Center, Menlo Park, CA (USA), Tech. Rep., 1985.
- [139] W. Heitler, *The quantum theory of radiation*. Courier Corporation, 1984.
- [140] Collaboration, GEANT and others, “Physics reference manual,” CERN, Switzerland, Tech. Rep., 2016.
- [141] J. H. Hubbell, W. J. Veigele, E. Briggs, R. Brown, D. Cromer, and d. R. Howerton, “Atomic form factors, incoherent scattering functions, and photon scattering cross sections,” *Journal of Physical and Chemical Reference Data*, vol. 4, no. 3, pp. 471–538, 1975.
- [142] D. T. Cromer, “Anomalous dispersion corrections computed from self-consistent field relativistic Dirac–Slater wave functions,” *Acta Crystallographica*, vol. 18, no. 1, pp. 17–23, 1965.

- [143] L. Kissel, B. Zhou, S. Roy, S. Sen Gupta, and R. Pratt, “The validity of form-factor, modified-form-factor and anomalous-scattering-factor approximations in elastic scattering calculations,” *Acta Crystallographica Section A: Foundations of Crystallography*, vol. 51, no. 3, pp. 271–288, 1995.
- [144] O. Iwamoto, N. Iwamoto, S. Kunieda, F. Minato, S. Nakayama, Y. Abe, K. Tsubakihara, S. Okumura, C. Ishizuka, T. Yoshida *et al.*, “Japanese evaluated nuclear data library version 5: JENDL-5,” *journal of nuclear science and technology*, vol. 60, no. 1, pp. 1–60, 2023.
- [145] D. E. Cullen, M. Chen, J. Hubbell, S. Perkins, E. Plechaty, J. Rathkopf, and J. Scofield, “Tables and graphs of photon-interaction cross sections from 10 eV to 100 GeV derived from the LLNL evaluated photon data library (EPDL),” Lawrence Livermore National Lab., CA (USA), Tech. Rep., 1989.
- [146] D. Brusa, G. Stutz, J. Riveros, J. Fernández-Varea, and F. Salvat, “Fast sampling algorithm for the simulation of photon Compton scattering,” *Nuclear Instruments and Methods in Physics Research Section A: Accelerators, Spectrometers, Detectors and Associated Equipment*, vol. 379, no. 1, pp. 167–175, 1996.
- [147] F. Biggs and R. Lighthill, “Analytical approximations for x-ray cross sections III,” Sandia National Lab.(SNL-NM), Albuquerque, NM (United States), Tech. Rep., 1988.
- [148] D. E. Cullen, J. H. Hubbell, and L. Kissel, “EPDL97: the evaluated photo data library97 version,” Lawrence Livermore National Lab.(LLNL), Livermore, CA (United States), Tech. Rep., 1997.
- [149] F. Sauter, “Über den atomaren photoeffekt in der k-schale nach der relativistischen wellenmechanik diracs,” *Annalen der Physik*, vol. 403, no. 4, pp. 454–488, 1931.
- [150] F. Biggs and R. Lighthill, “ANALYTICAL APPROXIMATIONS FOR TOTAL PAIR-PRODUCTION CROSS SECTIONS.” Sandia Corp., Albuquerque, N. Mex., Tech. Rep., 1968.
- [151] J. Baró, M. Roteta, J. Fernández-Varea, and F. Salvat, “Analytical cross sections for Monte Carlo simulation of photon transport,” *Radiation Physics and Chemistry*, vol. 44, no. 5, pp. 531–552, 1994.
- [152] Y.-S. Tsai, “Pair production and bremsstrahlung of charged leptons,” *Reviews of Modern Physics*, vol. 46, no. 4, p. 815, 1974.

- [153] H. Davies, H. Bethe, and L. Maximon, “Theory of bremsstrahlung and pair production. II. Integral cross section for pair production,” *Physical Review*, vol. 93, no. 4, p. 788, 1954.
- [154] C. Bienvenue, “Radiant (v0.1.2),” 2024. [Online]. Available: <https://github.com/CBienvenue/Radiant.jl>
- [155] J. Bezanson, A. Edelman, S. Karpinski, and V. B. Shah, “Julia: A fresh approach to numerical computing,” *SIAM review*, vol. 59, no. 1, pp. 65–98, 2017.
- [156] M. Poinot, “Five good reasons to use the hierarchical data format,” *Computing in Science & Engineering*, vol. 12, no. 5, pp. 84–90, 2010.
- [157] C. Bienvenue and A. Hébert, “High-order diamond differencing schemes for the Boltzmann Fokker–Planck equation in 1D and 2D Cartesian geometries,” *Annals of Nuclear Energy*, vol. 171, p. 109032, 2022.
- [158] C. Bienvenue, A. Naceur, J.-F. Carrier, and A. Hébert, “Adaptive gradient-driven coupled linear schemes and their usefulness for charged particle transport,” in *International Conference on Mathematics and Computational Methods Applied to Nuclear Science and Engineering (M&C 2023)*, 2023.
- [159] J. E. Morel, “An improved Fokker-Planck angular differencing scheme,” *Nuclear Science and Engineering*, vol. 89, no. 2, pp. 131–136, 1985.
- [160] J.-F. Carrier, L. Archambault, L. Beaulieu, and R. Roy, “Validation of GEANT4, an object-oriented Monte Carlo toolkit, for simulations in medical physics,” *Medical Physics*, vol. 31, no. 3, pp. 484–492, 2004.
- [161] P. Andreo and A. Brahme, “Restricted energy-loss straggling and multiple scattering of electrons in mixed Monte Carlo procedures,” *Radiation Research*, vol. 100, no. 1, pp. 16–29, 1984.
- [162] J. S. Warsa and A. K. Prinja, “p-adaptive numerical methods for particle transport,” *Transport Theory and Statistical Physics*, vol. 28, no. 3, pp. 229–270, 1999.
- [163] M. Asai, M. A. Cortés-Giraldo, V. Giménez-Alventosa, V. Giménez Gómez, and F. Salvat, “The PENELOPE physics models and transport mechanics. Implementation into Geant4,” *Frontiers in Physics*, vol. 9, p. 738735, 2021.
- [164] J. H. Renken, “Legendre Polynomial Expansion for the Klein-Nishina Formula,” *Journal of Applied Physics*, vol. 38, no. 12, pp. 4925–4927, 1967.

- [165] J. Hubbell and S. M. Seltzer, “Cross section data for electron–positron pair production by photons: a status report,” *Nuclear Instruments and Methods in Physics Research Section B: Beam Interactions with Materials and Atoms*, vol. 213, pp. 1–9, 2004.
- [166] D. Bote and F. Salvat, “Calculations of inner-shell ionization by electron impact with the distorted-wave and plane-wave Born approximations,” *Physical Review A*, vol. 77, no. 4, p. 042701, 2008.
- [167] D. Bote, F. Salvat, A. Jablonski, and C. J. Powell, “Cross sections for ionization of K, L and M shells of atoms by impact of electrons and positrons with energies up to 1 GeV: Analytical formulas,” *Atomic Data and Nuclear Data Tables*, vol. 95, no. 6, pp. 871–909, 2009.
- [168] G. J. Lockwood, L. E. Ruggles, G. H. Miller, and J. Halbleib, “Calorimetric measurement of electron energy deposition in extended media. Theory vs experiment,” Sandia National Lab.(SNL-NM), Albuquerque, NM (United States), Tech. Rep., 1980.
- [169] T. Tabata, “Backscattering of electrons from 3.2 to 14 MeV,” *Physical Review*, vol. 162, no. 2, p. 336, 1967.
- [170] T. Tabata, R. Ito, S. Okabe, and Y. Fujita, “Charge distribution produced by 4-to 24-MeV electrons in elemental materials,” *Physical Review B*, vol. 3, no. 3, p. 572, 1971.
- [171] T. Tabata, R. Ito, and S. Okabe, “An empirical equation for the backscattering coefficient of electrons,” *Nuclear Instruments and Methods*, vol. 94, no. 3, pp. 509–513, 1971.
- [172] C. J. Josey, A. R. Clark, J. A. Kulesza, E. J. Pearson, and M. E. Rising, “MCNP® Code Version 6.3. 0 Verification & Validation Testing,” *Los Alamos National Laboratory, Los Alamos, New Mexico, USA, Tech. Rep. LA-UR-22-32951*, p. 20, 2022.
- [173] A. Lechner, M. G. Pia, and M. Sudhakar, “Validation of geant4 low energy electromagnetic processes against precision measurements of electron energy deposition,” *IEEE Transactions on Nuclear Science*, vol. 56, no. 2, pp. 398–416, 2009.
- [174] C. Bienvenue, A. Naceur, J.-F. Carrier, and A. Hébert, “A Flexible, Moment-Preserving and Monotone Discretization of the Multidimensional Angular Fokker-Planck Operator,” submitted to *Nuclear Science and Engineering* (August 2024).

- [175] W. H. Reed, “Spherical harmonic solutions of the neutron transport equation from discrete ordinate codes,” *Nuclear Science and Engineering*, vol. 49, no. 1, pp. 10–19, 1972.
- [176] A. McLaren, “Optimal numerical integration on a sphere,” *Mathematics of Computation*, vol. 17, no. 84, pp. 361–383, 1963.
- [177] B. G. Carlson, “A method of characteristics and other improvements in solution methods for the transport equation,” *Nuclear Science and Engineering*, vol. 61, no. 3, pp. 408–425, 1976.
- [178] V. I. Lebedev, “Values of the nodes and weights of ninth to seventeenth order gauss-markov quadrature formulae invariant under the octahedron group with inversion,” *USSR Computational Mathematics and Mathematical Physics*, vol. 15, no. 1, pp. 44–51, 1975.
- [179] ———, “Quadratures on a sphere,” *USSR Computational Mathematics and Mathematical Physics*, vol. 16, no. 2, pp. 10–24, 1976.
- [180] V. I. Lebedev and D. N. Laikov, “A quadrature formula for the sphere of the 131st algebraic order of accuracy,” *Doklady Mathematics*, vol. 59, no. 3, pp. 477–481, 1999.
- [181] C. Ahrens and G. Beylkin, “Rotationally invariant quadratures for the sphere,” *Proceedings of the Royal Society A: Mathematical, Physical and Engineering Sciences*, vol. 465, no. 2110, pp. 3103–3125, 2009.
- [182] S. Heo and Y. Xu, “Constructing fully symmetric cubature formulae for the sphere,” *Mathematics of Computation*, vol. 70, no. 233, pp. 269–279, 2001.
- [183] J.-B. Bellet, M. Brachet, and J.-P. Croisille, “Quadrature and symmetry on the Cubed Sphere,” *Journal of Computational and Applied Mathematics*, vol. 409, p. 114142, 2022.
- [184] R. Sanchez and J. Ragusa, “On the construction of Galerkin angular quadratures,” *Nuclear Science and Engineering*, vol. 169, no. 2, pp. 133–154, 2011.
- [185] J. E. Morel, J. S. Warsa, B. C. Franke, and A. K. Prinja, “Comparison of two Galerkin quadrature methods,” *Nuclear Science and Engineering*, vol. 185, no. 2, pp. 325–334, 2017.
- [186] C. Drumm, W. Fan, A. Bielen, and J. Chenhall, “Least-squares finite-element algorithms in the SCEPTRE radiation transport code,” in *International Conference on*



*Mathematics and Computational Methods Applied to Nuclear Science and Engineering (M&C 2011)*, 2011.

- [187] J. S. Warsa and A. K. Prinja, “Moment-Preserving SN Discretizations for the One-Dimensional Fokker-Planck Equation,” Los Alamos National Lab.(LANL), Los Alamos, NM (United States), Tech. Rep., 2012.
- [188] J. E. Morel, A. Prinja, J. M. McGhee, T. A. Wareing, and B. C. Franke, “A discretization scheme for the three-dimensional angular Fokker-Planck operator,” *Nuclear Science and Engineering*, vol. 156, no. 2, pp. 154–163, 2007.
- [189] L. A. Poveda and P. Peixoto, “On pointwise error estimates for voronoï-based finite volume methods for the poisson equation on the sphere,” *Advances in Computational Mathematics*, vol. 49, no. 3, p. 36, 2023.
- [190] G. Dziuk and C. M. Elliott, “Finite element methods for surface PDEs,” *Acta Numerica*, vol. 22, pp. 289–396, 2013.
- [191] D. Zwillinger, *CRC standard mathematical tables and formulas*. Chapman and Hall, CRC, 2018.
- [192] C. Bienvenue and A. Hébert, “High-order diamond differencing schemes for the Boltzmann Fokker–Planck equation in 3D Cartesian geometries,” in *International Conference on Physics of Reactors (PHYSOR 2022)*, 2022.
- [193] J. S. Hesthaven and T. Warburton, *Nodal discontinuous Galerkin methods: algorithms, analysis, and applications*. Springer Science & Business Media, 2007.
- [194] G. B. Arfken, H. J. Weber, and F. E. Harris, *Mathematical methods for physicists: a comprehensive guide*. Academic press, 2011.
- [195] E. W. Larsen, J. E. Morel, and W. F. Miller Jr, “Asymptotic solutions of numerical transport problems in optically thick, diffusive regimes,” *Journal of Computational Physics*, vol. 69, no. 2, pp. 283–324, 1987.
- [196] P. G. Maginot, J. E. Morel, and J. C. Ragusa, “A non-negative moment-preserving spatial discretization scheme for the linearized Boltzmann transport equation in 1-D and 2-D Cartesian geometries,” *Journal of Computational Physics*, vol. 231, no. 20, pp. 6801–6826, 2012.

- [197] A. Voloschenko and T. Germogenova, “Numerical solution of the time-dependent transport equation with pulsed sources,” *Transport Theory and Statistical Physics*, vol. 23, no. 6, pp. 845–869, 1994.
- [198] R. Alcouffe, “An adaptive weighted diamond differencing method for three-dimensional, XYZ geometry,” Los Alamos National Lab.(LANL), Los Alamos, NM (United States), Tech. Rep., 1993.
- [199] A. M. Voloschenko, “Some improvements in solving the transport equation by the use of the family of weighted nodal schemes,” in *International Conference on Mathematics and Computational Methods Applied to Nuclear Science and Engineering (M&C 2011)*, 2011.
- [200] W. H. Reed and T. R. Hill, “Triangular mesh methods for the neutron transport equation,” Los Alamos Scientific Lab., N. Mex.(USA), Tech. Rep., 1973.
- [201] B. Neta and H. Victory, Jr, “A new fourth-order finite-difference method for solving discrete-ordinates slab transport equations,” *SIAM Journal on Numerical Analysis*, vol. 20, no. 1, pp. 94–105, 1983.
- [202] A. Hébert, “High order diamond differencing schemes,” *Annals of Nuclear Energy*, vol. 33, no. 17-18, pp. 1479–1488, 2006.
- [203] N. Martin and A. Hébert, “A three-dimensional SN high-order diamond differencing discretization with a consistent acceleration scheme,” *Annals of Nuclear Energy*, vol. 36, no. 11-12, pp. 1787–1796, 2009.
- [204] T. Germogenova, A. Shwetsov, and A. Voloschenko, “Adaptive positive nodal method for transport equation,” *Transport Theory and Statistical Physics*, vol. 23, no. 7, pp. 923–970, 1994.
- [205] S. Hamilton, M. Benzi, J. Warsa *et al.*, “Negative flux fixups in discontinuous finite element SN transport,” in *International Conference on Mathematics, Computational Methods and Reactor Physics (M&C 2009)*, American Nuclear Society, LaGrange Park, Illinois, USA. Citeseer, 2009.
- [206] R. S. Varga, “On higher order stable implicit methods for solving parabolic partial differential equations,” *Journal of Mathematics and Physics*, vol. 40, no. 1-4, pp. 220–231, 1961.

- [207] B. L. Ehle, “A-stable methods and padé approximations to the exponential,” *SIAM Journal on Mathematical Analysis*, vol. 4, no. 4, pp. 671–680, 1973.
- [208] B. G. Petrović and A. Haghighat, “Analysis of inherent oscillations in multidimensional SN solutions of the neutron transport equation,” *Nuclear Science and Engineering*, vol. 124, no. 1, pp. 31–62, 1996.
- [209] V. K. Dixit and C. Rackauckas, “Optimization.jl: A unified optimization package,” Mar. 2023. [Online]. Available: <https://doi.org/10.5281/zenodo.7738525>
- [210] A. M. Voloschenko, “CEPXS-BFP. User’s Guide.” Keldysh Inst. of Appl. Math., Tech. Rep., 2004.
- [211] J. Sempau, J. Fernández-Varea, E. Acosta, and F. Salvat, “Experimental benchmarks of the Monte Carlo code PENELOPE,” *Nuclear Instruments and Methods in Physics Research Section B: Beam Interactions with Materials and Atoms*, vol. 207, no. 2, pp. 107–123, 2003.
- [212] Á. Elbert and A. Laforgia, “An inequality for Legendre polynomials,” *Journal of Mathematical Physics*, vol. 35, no. 3, pp. 1348–1360, 1994.
- [213] F. G. Tricomi, “Sugli zeri dei polinomi sferici ed ultrasferici,” *Annali di Matematica Pura ed Applicata*, vol. 31, no. 1, pp. 93–97, 1950.
- [214] N. Hale and A. Townsend, “Fast and accurate computation of Gauss–Legendre and Gauss–Jacobi quadrature nodes and weights,” *SIAM Journal on Scientific Computing*, vol. 35, no. 2, pp. A652–A674, 2013.

## APPENDIX A    POLYNOMIALS

### Legendre polynomials

The Legendre polynomials, noted  $P_\ell(x)$  for  $\ell \geq 0$ , are a complete and orthogonal system defined over  $x \in [-1, 1]$  such as

$$\int_{-1}^1 dx P_\ell(x) P_{\ell'}(x) = \frac{2}{2\ell + 1} \delta_{\ell, \ell'} \quad (\text{A.1})$$

where  $\delta_{\ell, \ell'}$  is the Kronecker delta. They also can be defined as the eigenfunctions of the Legendre's differential equation

$$\frac{d}{dx} \left[ (1 - x^2) \frac{d}{dx} \right] P_\ell(x) = -\ell(\ell + 1) P_\ell(x) \quad (\text{A.2})$$

The Legendre polynomials can be calculated using the Bonnet's recursion formula with

$$P_\ell(x) = \begin{cases} 1 & \ell = 0 \\ x & \ell = 1 \\ \left[ \frac{2\ell - 1}{\ell} \right] x P_{\ell-1}(x) - \left[ \frac{\ell - 1}{\ell} \right] P_{\ell-2}(x) & \ell \geq 2 \end{cases} \quad (\text{A.3})$$

It can be shown that the Legendre polynomials are bounded by [212]

$$|P_\ell(x)| \leq 1 \quad (\text{A.4})$$

The  $\ell$ -order Legendre moments of a function  $f(x)$  can be defined as

$$f_\ell = \int_{-1}^1 dx P_\ell(x) f(x) \quad (\text{A.5})$$

and, if the function  $f(x)$  is positive, triangle inequality applied to integral and using the Legendre polynomial upper bound, we can show the following inequality for  $\ell \geq 1$  Legendre moments

$$\frac{|f_\ell|}{f_0} = \frac{\left| \int_{-1}^1 dx P_\ell(x) f(x) \right|}{f_0} \leq \frac{\int_{-1}^1 dx |P_\ell(x)| f(x)}{f_0} \leq 1 \quad (\text{A.6})$$

### Normalized Legendre polynomials

The normalized Legendre polynomials, noted  $\tilde{P}_\ell(x)$  for  $\ell \geq 0$ , are a complete and orthogonal system defined over  $x \in [-1/2, 1/2]$  such as

$$\int_{-1/2}^{1/2} dx \tilde{P}_\ell(x) \tilde{P}_{\ell'}(x) = \delta_{\ell, \ell'} \quad (\text{A.7})$$

They can be calculated using the following recursion formula [157]

$$\tilde{P}_\ell(x) = \begin{cases} 1 & \ell = 0 \\ 2\sqrt{3}x & \ell = 1 \\ 2\sqrt{\frac{2\ell+1}{2\ell-1}} \left[ \frac{2\ell-1}{\ell} \right] x \tilde{P}_{\ell-1}(x) - \sqrt{\frac{2\ell+1}{2\ell-3}} \left[ \frac{\ell-1}{\ell} \right] \tilde{P}_{\ell-2}(x) & \ell \geq 2 \end{cases} \quad (\text{A.8})$$

An upper bound for the size of the normalized Legendre polynomial can be derived from the one of the classical Legendre polynomial and is given by

$$|\tilde{P}_\ell(x)| \leq \sqrt{2\ell+1} \quad (\text{A.9})$$

The  $\ell$ -order normalized Legendre moments of a function  $f(x)$  can be defined as

$$f_\ell = \int_{-1}^1 dx \tilde{P}_\ell(x) f(x) \quad (\text{A.10})$$

and, if the function  $f(x)$  is positive, triangle inequality applied to integral and using the normalized Legendre polynomial upper bound, we can show the following inequality for  $\ell \geq 1$  Legendre moments

$$\frac{|f_\ell|}{f_0} = \frac{\left| \int_{-1/2}^{1/2} dx \tilde{P}_\ell(x) f(x) \right|}{f_0} \leq \frac{\int_{-1/2}^{1/2} dx |\tilde{P}_\ell(x)| f(x)}{f_0} \leq \sqrt{2\ell+1} \quad (\text{A.11})$$

### Associated Legendre polynomials (Ferrer definition)

The associated Legendre polynomials, using the Ferrer definition in which the factor  $(-1)^m$  is absent, is given by

$$P_\ell^m(x) = (1-x^2)^{m/2} \frac{d^m}{dx^m} P_\ell(x), \quad 0 \leq m \leq \ell \quad (\text{A.12})$$

To compute this term numerically, one can initially use the following identity (from [194], Eq. 15.93)

$$P_m^m(x) = (1 - x^2)^{m/2} (2m - 1)!! = (1 - x^2)^{m/2} \prod_{k=1}^m (2k + 1) \quad (\text{A.13})$$

If  $\ell = m$ , then computation is over, otherwise, one should use this second identity (from [194], Eq. 15.94)

$$P_{m+1}^m(x) = (2m + 1)xP_m^m(x) \quad (\text{A.14})$$

If  $\ell = m + 1$ , then computation is over, otherwise, this third identity (from [194], Eq. 15.88) iteratively can, since  $m \leq \ell$ , be use for all other case

$$P_\ell^m(x) = \frac{(2\ell - 1)xP_{\ell-1}^m(x) - (\ell + m - 1)P_{\ell-2}^m(x)}{\ell - m} \quad (\text{A.15})$$

### Real spherical harmonics

The real spherical harmonics, noted  $R_\ell^m(\mu, \phi)$  for  $\ell \geq 0$  and  $|m| < \ell$ , are a complete and orthogonal system defined over  $\mu \in [-1, 1]$  and  $\phi \in [0, 2\pi]$  such as

$$\int_{4\pi} d^2\Omega R_\ell^m(\Omega) R_{\ell'}^{m'}(\Omega) = \frac{4\pi}{2\ell + 1} \delta_{\ell, \ell'} \delta_{m, m'} \quad (\text{A.16})$$

They also can be defined as the eigenfunctions of the Laplace equation given by

$$\left[ \frac{\partial}{\partial \mu} \left[ (1 - \mu^2) \frac{\partial}{\partial \mu} \right] + \frac{1}{1 - \mu^2} \frac{\partial^2}{\partial \phi^2} \right] R_\ell^m = -\ell(\ell + 1) R_\ell^m \quad (\text{A.17})$$

The real spherical harmonics are given by [50]

$$R_\ell^m(\Omega) = \sqrt{(2 - \delta_{m,0}) \frac{(\ell - |m|)!}{(\ell + |m|)!}} P_\ell^{|m|}(\mu) \mathcal{T}_m(\phi) \quad (\text{A.18})$$

with

$$\mathcal{T}_m(\phi) = \begin{cases} \cos m\phi, & m \geq 0 \\ \sin |m| \phi, & m < 0 \end{cases} \quad (\text{A.19})$$

## APPENDIX B    QUADRATURES

### Gauss-Legendre quadrature

The  $N$ -order Gauss-Legendre quadrature is defined over  $x \in [-1, 1]$ . It gives exact result for polynomial of degree  $2N - 1$  or less. The  $i$ -th node  $x_i$  correspond to the  $i$ -th root of the Legendre polynomial  $P_N(x)$ . It can be found using Newton iteration method, if a good choice of initial node is done. Such a choice is proposed by Tricomi [213, 214]:

$$x_i^0 = \left[ 1 - \frac{N-1}{8N^3} - \frac{1}{384N^4} \left( 39 - \frac{28}{\sin^2(\phi_i)} \right) \right] \cos(\phi_i) \quad (\text{B.1})$$

with

$$\phi_i = \frac{\pi}{2} \left( \frac{4i-1}{2N+1} \right) \quad (\text{B.2})$$

The derivative of Legendre polynomial, needed for the Newton method, is given by

$$P'_N(x) = \frac{N(P_{N-1}(x) - xP_N(x))}{1-x^2} \quad (\text{B.3})$$

Finally, the weights are given by

$$\omega_i = \frac{2}{(1-x_i^2)(P'_N(x_i))^2} \quad (\text{B.4})$$

### Gauss-Lobatto quadrature

The  $N$ -order Gauss-Lobatto quadrature is defined over  $x \in [-1, 1]$ . It gives accurate result for polynomial of degree  $2N - 3$  or less. The  $i$ -th node  $x_i$  correspond to the  $(i-1)$ -th root of the Legendre polynomial derivative  $P'_{N-1}(x)$ . The first and last node are respectively  $x_1 = -1$  and  $x_N = 1$ . It can be found using Newton iteration method, if a good choice of initial node is done. A good choice of initial value is

$$x_i = \cos \left( (i-1) \frac{\pi}{N-1} \right) \quad (\text{B.5})$$

The second derivative of Legendre polynomial, needed for the Newton method, is given by

$$P''_N(x) = \frac{2xP'_N(x) - N(N+1)P_N(x)}{1-x^2} \quad (\text{B.6})$$

Finally, the weights are given by

$$\omega_i = \begin{cases} \frac{2}{n(n-1) (P_{N-1}(x_i))^2} & x_i \neq \pm 1 \\ \frac{2}{n(n-1)} & \text{otherwise} \end{cases} \quad (\text{B.7})$$

### Product quadrature with Chebychev azimuthal quadrature

The  $N$ -order product quadrature with Chebychev azimuthal quadrature is defined over the unit sphere. This method is symmetric over 8 octants and has no evaluation point along the reference frame axis. The points distribution over the sphere is uneven. The quadrature has  $N$  level containing  $2N$  points each. The total number of directions is

$$N_d = 2N^2 \quad (\text{B.8})$$

For a level  $n \in 1, \dots, N$  and the point  $m \in 1, \dots, 2N$  on that level, corresponding to an index  $i = 2N(n-1) + m$ , with  $\mu_n$  and  $w_n$  being the nodes and weights of the  $N$ -order quadrature over a line segment (e.g. Gauss-Legendre), the direction cosines are given by

$$\begin{aligned} \mu_i &= \mu_n \\ \eta_i &= \sqrt{1 - \mu_n^2} \cos(\phi_m) \\ \xi_i &= \sqrt{1 - \mu_n^2} \sin(\phi_m) \end{aligned} \quad (\text{B.9})$$

where

$$\phi_m = \frac{(2m-1)\pi}{2N} \quad (\text{B.10})$$

and the corresponding weight is given by

$$w_i = w_n \frac{\pi}{N} \quad (\text{B.11})$$

### Carlson quadrature

The Carlson quadrature [177] is defined over the unit sphere and require less evaluation point than product quadrature. This method is symmetric over 8 octants and has no evaluation point along the reference frame axis. In the octant with positive cosines, with  $N$ -order Carlson quadrature, the weight are given by

$$\omega_m = \frac{4(N-2n+2)}{N(N+2)} \quad (\text{B.12})$$



with  $m \in \{1, N/2\}$ . The main director cosine is given by

$$\mu_m = \bar{\mu}_m + f\mu_{m-1/2} \quad (\text{B.13})$$

with

$$\bar{\mu}_m = 1 - \frac{(N - 2n + 2)^2}{N(N + 2)} \quad (\text{B.14})$$

and

$$\mu_{m-1/2} = 1 - \frac{(N - 2n + 2)(N - 2n + 4)}{N(N + 2)} \quad (\text{B.15})$$

The factor  $f$  is determined by finding the root of the following equation

$$\sum_{m=1}^{N/2} \omega_m \mu_m^2 = 1/3 \quad (\text{B.16})$$

using the Newton-bisection presented in Section C. The two other director cosines are given

$$\eta_{m,k} = \sqrt{1 - \mu_m^2} \sin \theta_{m,k} \quad \text{and} \quad \xi_{m,k} = \sqrt{1 - \mu_m^2} \cos \theta_{m,k} \quad (\text{B.17})$$

where

$$\theta_{m,k} = \frac{\pi}{2} \left[ \frac{2m - 1}{N - 2k + 2} A_n + \frac{1 - A_n}{2} \right] \quad (\text{B.18})$$

with  $k \in \{1, N/2 - m + 1\}$ . The  $A_n$  factors are determined by finding the root of the following equation

$$\omega_0 \sum_{m=1}^{N/2} \sum_{m=1}^{N/2-m+1} \eta_{m,k} = \sum_{m=1}^{N/2} \omega_m \mu_m \quad (\text{B.19})$$

using the Newton-bisection presented in Section C.

## APPENDIX C    NEWTON-BISECTION METHOD

The Newton's method is a root-finding algorithm with quadratic convergence, meaning it is fast, but it is not guaranteed to converge without adequate estimate of the root. The bisection method is simple and robust, but convergence is slow. It is possible to combine Newton and bisection methods in order to retain most of the quadratic convergence while gaining the robustness of the bisection method.

First, we need to establish an interval containing the root of the function  $f(x)$ , i.e. an interval  $[a, b]$  such that  $f(a) \cdot f(b) < 0$ . The estimated root,  $r_0$ , is given by

$$r_0 = \begin{cases} a, & |f(a)| < |f(b)| \\ b, & \text{otherwise} \end{cases} \quad (\text{C.1})$$

Then, we try to perform a Newton iteration and compute

$$r = r_0 - \frac{f(r_0)}{f'(r_0)} \quad (\text{C.2})$$

and, if  $r \notin [a, b]$ , then we rather applied the bisection method and recompute  $r$  with

$$r = \frac{a + b}{2} \quad (\text{C.3})$$

Finally, we update our bounds substituting either  $a$  or  $b$  by the value of  $r$  such as  $f(a) \cdot f(b)$  stay lower than zero. We repeat the process until  $|f(r)| < \epsilon$ , where  $\epsilon$  is a tolerance criterion.